Mesoscale constitutive behavior of ferroelectrics

by

Mesut Varlioglu

A thesis submitted to the graduate faculty

in partial fulfillment of the requirements for the degree of

DOCTOR OF PHILOSOPHY

Major: Materials Science and Engineering

Program of Study Committee:
Ersan Ustundag, Major Professor
Vitalij K. Pecharsky
Matthew J. Kramer
Xiaoli Tan
Ashraf Bastawros

Iowa State University

Ames, Iowa

2009

TABLE OF CONTENTS

LIST OF FIGURES

LIST OF TABLES

ABSTRACT

The main goal of this study is the *in-situ* investigation of the ferroelectric domain structure inside polycrystalline $BaTiO_3$ under thermo-electro-mechanical loading conditions. The outcome is two-fold: (i) the characterization techniques were improved to study the polycrystalline ferroelectrics in the mesoscale; and (ii) the texture, lattice strain and volume fraction of domains were tracked under applied electric field and mechanical stress.

Two novel synchrotron-based characterization techniques, three-dimensional X-ray diffraction (3-D XRD) and Scanning X-ray Microdiffraction (μSXRD) were used in this study. The methodology and standards in both techniques differ from each other and the present study provides a framework to bridge these techniques. Although these methods have been developed earlier, their application and adaptation to ferroelectrics required some care. For instance, diffraction spots often overlapped and made it difficult to identify individual domains and/or grains. In order to eliminate the spot overlap, the polycrystalline $BaTiO_3$ sample was heated above the Curie temperature where the (tetragonal) domains disappear and attain the orientation of the grain. Next, the sample was cooled slowly to the room temperature and the evolution of the ferroelectric domains was studied at temperature and under electric field. The orientation relationships, volume fractions and lattice strain evolution of 8 domain systems were studied.

Whereas the orientation of the domains remained unchanged under electric field, the fraction of the energetically favorable domain variants increased. Due to local constraints, complete switching from one domain variant to another was not observed. The misorientation angles between domain variants slightly deviated from the theoretical value (=89.4°) by 0.2-0.3°. The deviation angle can be explained with the phase-matching angle developed during the cubic-tetragonal phase transformation to maintain strain compatibility of neighboring domains. The multiscale strain evolution of ferroelectric domains in a polycrystal was investigated quantitatively for the first time. Under electric field, lattice strains of up to 0.1% were measured along the applied field direction.

The present study offers a framework to characterize the polycrystalline materials with complex twin structures. By using the methodology described in this study, 3D-XRD

and μSXRD techniques can be employed to study texture and lattice strain evolution in polycrystalline materials in the mesoscale.

CHAPTER 1. INTRODUCTION

Ferroelectric ceramics have been extensively used in microelectronic and sensing applications for more than 50 years because of their excellent piezoelectric properties [Jona, F. (1962)]. As we live in an electronic age, a wide range of additional applications such as in transport and civil infrastructure will be built with more ferroelectric actuators and sensing devices. Therefore, more accurate prediction of ferroelectric properties will improve the efficiency and productivity of the design and reduce its environmental impact. To achieve this, more sophisticated constitutive models are needed.

Ferroelectric materials are widely produced with powder processing and other advanced manufacturing techniques [Rogan, R. (2003)]. The final microstructure is usually composed of grains containing several domains isolated from each other with domain boundaries. With an external stimulus such as electric field or mechanical stress, domains tend to orient along a uniform direction via a domain switching mechanism. Domain switching in one grain results in a change of stress and electric field in neighboring grains and this change generally leads to additional constraints on the original grain. The result is a complex three-dimensional stress state, which, when coupled with the low fracture toughness of ferroelectric ceramics, leads to degradation and failure. Therefore, proper quantification of ferroelectric constitutive behavior requires a technique capable of measuring internal stress/strain and domain switching (which leads to texture) at the inter- and intragranular level.

The current understanding of ferroelectric constitutive behavior is often based on either extreme of the microstructure scale, i.e. at the microscopic or macroscopic levels. While the former employs energy relations at the atomic level and requires a great number of parameters [Jordan, T. L. (2001)], the latter relies on various assumptions to describe the behavior of the bulk and ignores most microstructural parameters of the material. Both approaches also usually assume linear piezoelectric coefficients and employ a number of assumptions and parameters for the boundary conditions. Therefore, the improvement of the design and performance of ferroelectric ceramics cannot be achieved without a more sophisticated constitutive model, a model that needs to be multiscale bridging the

macroscopic and microscopic levels, and that takes into account appropriate microstructural parameters evolving at the intermediate mesoscale.

The main goal of the present study is to generate data at the mesoscale and help fill the gap between the atomistic and macroscopic scales. To this end, we have investigated the mesoscale behavior of ferroelectrics by studying domains in the bulk and at the surface. The bulk behavior has been studied using the "*three-dimensional X-ray diffraction* (3D-XRD)*"* method available at Sector 1 of the Advanced Photon Source (APS) in Argonne National Laboratory, Argonne, IL. For higher resolution, but closer to the surface, the "*Scanning X-ray microdiffraction* (μSXRD)" technique has been employed at Beamline 12.3.2 of the Advanced Light Source (ALS), Lawrence Berkeley National Laboratory, Berkeley, CA.

We have selected $BaTiO_3$ as the test material because of its well-known, simple and chemically stable crystal structure. Having been studied for more than 50 years, there exists a large body of literature on this material. Surprisingly, there are still some unknowns on $BaTiO_3$, e.g., the mechanism of 90° domain switching is still somewhat insufficiently described [Floquet, N. (1997)].

There are seven main chapters that describe the present study. *Chapter 1* provides the introduction and goal of this research. *Chapter 2* outlines the basic principles of piezoelectricity, ferroelectricity, ferroelectric domain structures in both single crystal and polycrystalline ferroelectrics. The texture evolution of ferroelectric domains is very important and it is crucial to have a fundamental knowledge on texture to interpret the results. *Chapter 3* fills this gap and describes the fundamentals of texture and explains why we selected the *Neo-Eulerian* method to represent the orientation of the ferroelectric domains. *Chapter 4 and 5* describe the general principles of the two non-destructive characterization techniques (3D-XRD and μSXRD) used. *Chapter 6* presents the experimental results and compares the domains in the bulk and those at the surface. The orientations of the ferroelectric domains in the same sample were also investigated with the EBSD technique and *Chapter 7* shows the results from this investigation. The experiments with both XRD techniques demonstrated that individual ferroelectric domains can be tracked as a function of applied electric field or temperature and *Chapter 8* summarizes the results of this investigation. Here, individual domains within a polycrystalline ferroelectric were

monitored under loading and their lattice strain evolution was measured for the first time. The present study offers methodology and a unique opportunity to study the constitutive behavior of ferroelectrics at the mesoscale.

CHAPTER 2. FERROELECTRICITY

This chapter will offer brief, fundamental basics on ferroelectric materials. The so-called active materials and their application areas will be described. The concepts of piezoelectricity, ferroelectricity and the microstructural features of these materials will be introduced. The response of ferroelectrics to outside stimuli alter their microstructural features, e.g., via domain switching. The basic mechanisms that dominate this process will be explained and the mesoscale behavior of polycrystalline ferroelectrics will be portrayed.

2.1. Active Materials

In modern materials science applications, there is a growing interest in materials that change shape or size under external stimuli such as electric or electromagnetic fields. These materials are called "active" or "smart" materials. The active materials are used in a wide variety of applications:

Thermo-elastic materials → Fiber optic sensors
Piezoelectric materials → Magneto-elastic damping, transducer/sensing applications
Magnetostrictive materials → Electro-acoustic devices
Shape memory alloys → Photo-elastic sensors

One of the most active research fields in materials science is dedicated to the characterization of active materials so that their properties can be enhanced due to a better understanding of the microstructural mechanisms that control the constitutive behavior of these materials.

2.2. Piezoelectricity

Piezoelectricity is defined as the coupling between mechanical stress and electricity. Lack of symmetry in the unit cell is important for the existence of piezoelectricity since a net movement of positive and negative ions with respect to each other as a result of stress produces an electric dipole, i.e., polarization. Out of the 32 point groups of symmetry, 21 do not possess a center of symmetry and 20 of them are piezoelectric [Haertling, G. H. (1999)]. Only 10 of these 20 groups can be polar in the absence of applied stress. These 10 polar

classes are also pyroelectric (the ability to generate an electric potential when heated or cooled). Many electronic devices employ piezoelectricity in a variety of applications such as actuators or sensors.

2.3. Ferroelectricity

Ferroelectric materials are a subgroup of pyroelectrics. Ferroelectrics must have a spontaneous polarization whose direction can be changed with an electric field. In other words, a ferroelectric material will still possess an electric polarization when the electric field is reduced to zero. Ferroelectrics differ from piezoelectric materials with their "spontaneous polarization". On a side note, there are analogous materials that couple different physical phenomena: a material showing a hysteresis between mechanical stress and strain is called *ferroelastic* (usually due to a stress-induced effect such as phase transformation or domain switching), while the one that couples magnetic field and strain is called *ferromagnetic*. If a material combines at least two of the properties mentioned above, it is called *multiferroic*.

Most commercial ferroelectrics have the perovskite crystal structure. This structure contains three ions of the form ABO_3. The *A* and *B* atoms posses +2 and +4 charges, respectively, while the *O* atom has a -2 charge. The *A* and *O* atoms are at the corners and faces of the unit cell, respectively, and the *B* atom is at the center. One of the most common ferroelectric materials is $BaTiO_3$ (Figure 2.1).

2.4. Ferroelectric Domains

Ferroelectric materials are known for their ability to convert mechanical energy to electric energy or vice versa. Upon cooling from a neutral or paraelectric phase, the material is called "ferroelectric" if it exhibits spontaneous polarization. The transformation temperature from the paraelectric to ferroelectric phase is called the Curie temperature (T_C). As the material is cooled below the Curie point, individual clusters of unit cells tend to orient along crystallographic directions (that depend on the crystal structure) to minimize internal energy. These individual clusters with uniform polarization vectors are called ferroelectric domains. Ferroelectric materials such as $BaTiO_3$ and $Pb(Zr,Ti)O_3$ (PZT) have perovskite-type ferroelectric phases below T_C and cubic crystal structure above. Figure 2.1 shows the

schematic displacive transformation of $BaTiO_3$ unit cell during the paraelectric-to-ferroelectric transformation.

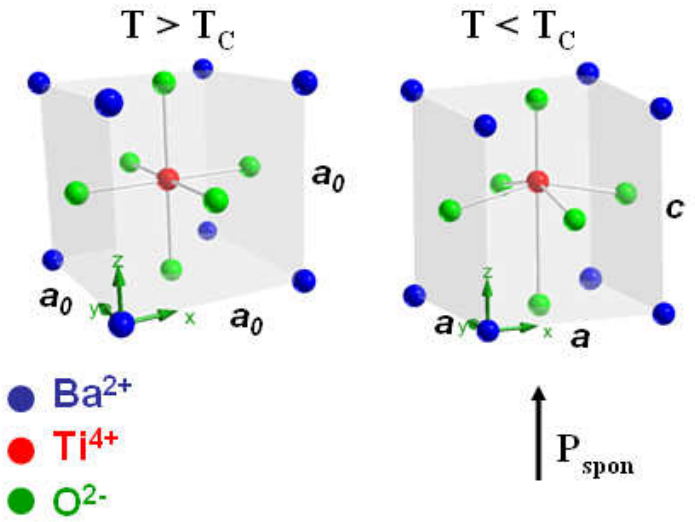

Figure 2.1. Left: Unit cell of $BaTiO_3$ in the paraelectric phase above the Curie temperature (T_C). The cubic symmetry does not allow for a spontaneous polarization. Right: Unit cell of $BaTiO_3$ in the ferroelectric phase (below T_C). The vector of the spontaneous polarization, P_{spon}, is oriented in the direction of the displaced titanium ion. [Kamlah M. (2001)]

The orientation of domains is crystal structure dependent leading to polar directions along a cube edge (6 variants), body diagonal (8 variants) and face diagonal (12 variants) for tetragonal, rhombohedral and orthorhombic symmetries, respectively [Li, F. X. (2006)]. The six domain variants of tetragonal $BaTiO_3$ are shown in Figure 2.2. A polycrystalline ferroelectric is typically an assembly of grains that contain several domain variants as in Figure 2.3.

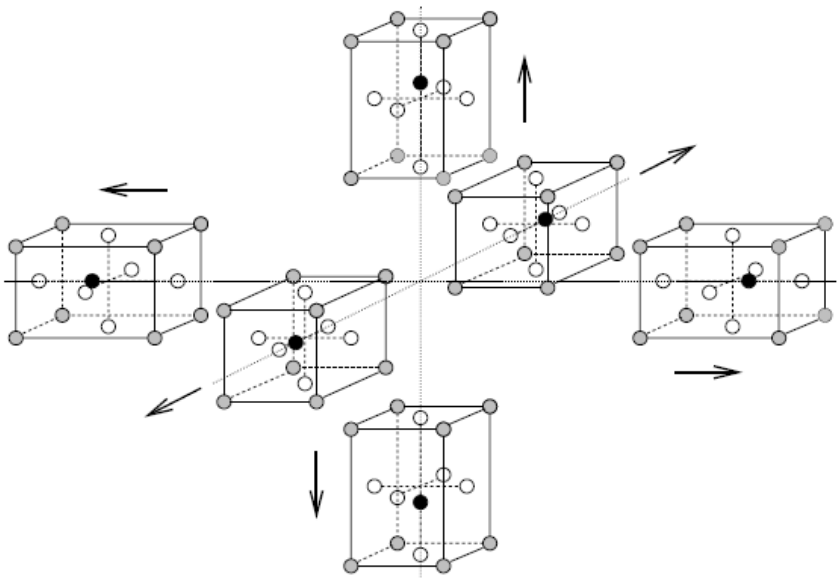

Figure 2.2. Following the paraelectric-to-ferroelectric phase transition, the spontaneous polarization vectors can choose among six equivalent directions in tetragonal perovskites. [Kamlah M. (2001)]

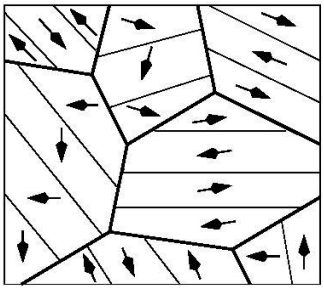

Figure 2.3. Grains in a ferroelectric material with sub-regions of equal spontaneous polarization – domain variants. [Kamlah M. (2001)]

Due to crystal symmetry, the direction of some of domains within the material can be equivalent. For example, cooling from the cubic to a tetragonal phase can form three kinds of domain structures [Cao W., Cross L. E. (1991)]: (1) 180° domains where the polarizations in the two domains will have the same magnitude but opposite directions, (2) 90° domains with a charge-neutral domain wall where for polarizations in the two domains are (almost) perpendicular to each other with a head-to-tail configuration, and (3) 90° domains with a charged domain wall, where the polarizations in the two domains are perpendicular to each other but in head-to-head or tail-to-tail configurations. It has been shown that the last kind of domain structure is not stable and tends to transform into the second kind with a zigzag twin

boundary. The 90° and 180° domains and the corresponding domain walls in $BaTiO_3$ are shown in Figure 2.4. The thickness of the 180° domain wall in $BaTiO_3$ is generally considered to be in the order of one unit cell although larger estimates have been made for the 90° domain walls [Subbarao E. C., *et al.* (1957)].

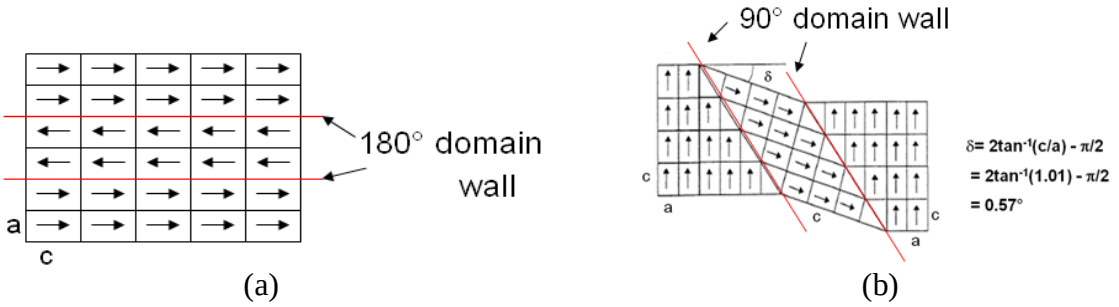

Figure 2.4. (a) 180° domains separated with domain walls. (b) 90° domains in $BaTiO_3$ where the angle between neighboring polarization vectors is 90° – 0.57° = 89.43°

Figure 2.5 shows the microstructure of a polycrystalline $BaTiO_3$ specimen. This complicated domain pattern makes it a challenge to accurately characterize the mesoscale domain mechanics. To date, most research has concentrated on averaging the bulk behavior and ignoring the contribution of the individual domains. In tetragonal symmetry, electric field can lead to both 180° and 90° domains while mechanical stress can cause only 90° domain switching [Berlincourt, D. *et al.* (1959)]. While Merz, W. J. (1952) indicated that the final domain structure must contain all 180° domains, Merz, W. J. (1954) later observed reoriented 90° domains as high electric fields. In another interesting research, Danielson, G. C. (1949) investigated the domain orientation in polycrystalline $BaTiO_3$ under applied electric field and found that 80% of the polycrystal consists of 180° domains while rest is 90° domains. Berlincourt, D. (1959) predicted that 2/3 of the total polarization occurs due to 90° domains switching, 1/6 occurs due to 180^o switching and the rest is due to the intrinsic piezoelectric effect. Since the 90° reorientation of domains requires more energy, the fraction of the 90° domains is not usually significant in the final microstructure. All of these studies, however, relied on bulk averaging or surface characterizations. The present study will attempt to offer more detailed information on domain switching in polycrystalline ferroelectrics.

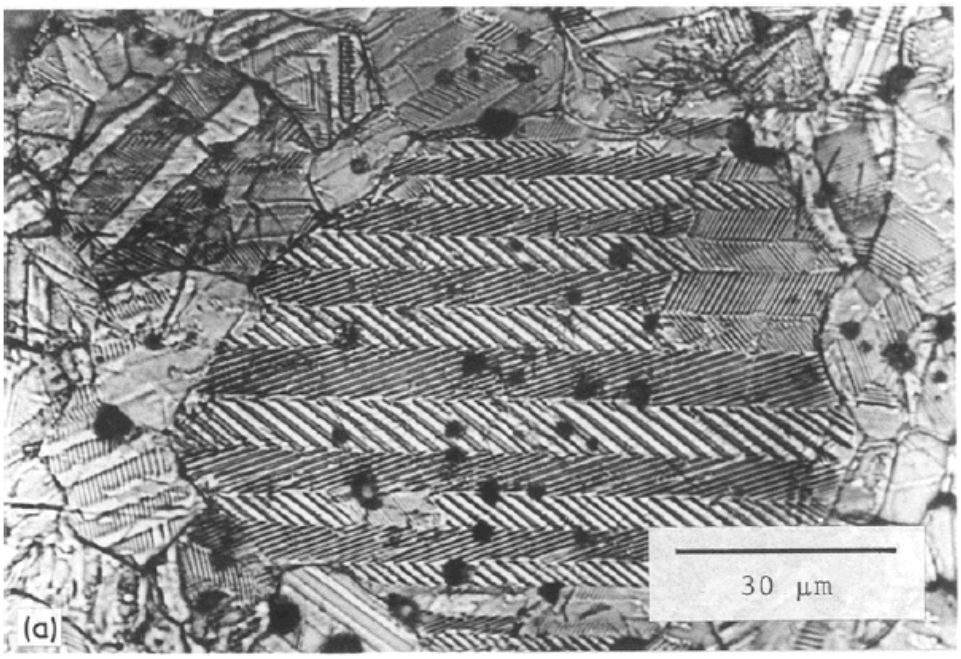

Figure 2.5. The microstructure of polycrystalline $BaTiO_3$ that shows domain variants within grains. [Arlt. G. (1990)]

2.4.1. Twinning vs. Domain Switching

Domain switching and twinning are similar mechanisms because they both require well-defined crystallographic orientation relationships across their boundaries.

Twinned crystals are produced in various ways. As a crystal grows from its initial nucleus some accident of growth may cause it to twin, such accidents being for a variety of reasons very much more probable in some structures than in others. Twinning may alternatively provide a means of relieving the strain induced by applied stress. Twinning may also be produced as the result of polymorphic transformations when a structure of higher symmetry is converted to a structure of low symmetry. These are the three principle types of twins and they are known respectively as *growth twins*, *deformation twins*, and *transformation twins* [Lee, C-C. (2004)]. The deformation twins are found in, e.g., BCC and FCC lattices. Growth twins are known in, e.g., $BaTiO_3$ and the formation of the twin can be understood as a shear operation with (111) planes successively translated by 1/3[11-2] vectors [Lee, C-C. (2004)]. The transformation twins are the dominant domain structure of $BaTiO_3$ and they are known as 180° and 90° domain variants.

2.4.2. Models of Domain Switching

Modeling the domain switching in polycrystalline ferroelectrics is a popular topic among the computational materials scientists. The existing models can be exemplified as a historical snapshot:

- *Indirect Observations of Domain Switching:* The early work on the domain switching of ferroelectrics was focused on the nucleation and growth of domains in single crystal $BaTiO_3$ under electric field and at high temperature [Merz, W. J. (1954)]. The domain wall thickness and energy were calculated in this study, the latter using the contributions of dipole-dipole interactions and anisotropy. The energy of dipole interactions was found as $10^{-14} / Na^2 erg/cm^2$ where N is the thickness of the wall in atomic separations and a is the lattice constant. The energy due to anisotropy can be calculated via the elastic energy per cm^3 which is stored when the unit cell deforms from tetragonal to cubic and is in the order of $\varepsilon_{elast} \cong \frac{1}{2} c_{33} z_z^2$ erg/cm^3 where c_{33} is a single crystal elastic constant and z_z is the spontaneous strain in $BaTiO_3$ at room temperature. In this assumption, the domain wall energy from the anisotropy is the function of spontaneous strain, z, crystal volume, V and domain wall thickness, t and electric field is acting along *33* direction. Then, the wall energy per cm^3 due to anisotropy becomes $\sigma_{anis} \cong \frac{1}{2} c_{33} z_z^2 Na$ erg/cm^3. The minimum wall energy is obtained when

$$\frac{\partial \sigma_w}{\partial N} = 0 = -\left(\frac{10^{-14}}{N^2 a^2}\right) + \frac{1}{2} c_{33} z_z^2 a \qquad (2.1)$$

or when

$$N = (2 \times 10^{-14} c_{33} z_z^2 a^3)^{1/2} \qquad (2.2)$$

From Equation 2.2, it is clear that N (wall thickness in atomic separations) must be small in $BaTiO_3$ because the dipole-dipole interaction is small and the anisotropy is large. N value at room temperature with c_{33}=2.0x10^{12} dyne/cm^2, z_z=7x10^{-3}, a=4.0x10^{-8} cm becomes ~1 as an atomic constant.

In Subbarao's work [Subbarao, E. C. (1957)], domain switching as a result of electric field or mechanical stress was observed by changes in x-ray patterns and dimensional changes in the polycrystalline $BaTiO_3$. Because of the difference in the c and a lattice

constants in tetragonal $BaTiO_3$, 90° domain switching should result in both dimensional changes and changes in the intensity of some x-ray peaks, e.g., (200) and (002). Meanwhile, 180° domain switching will not lead to any dimensional or x-ray pattern changes. During the depoling process, Subbarao, E. C. (1957) concluded that essentially all the 180° domain walls are removed and the polar axis of the domains lies within 90° of the applied field; in addition, about 12% of the domains switch by 90° under the influence of the poling field, but the about half of the these revert to their original orientation after removing the electric field. Subbarao also observed a strong inelastic effect in ceramic $BaTiO_3$ in the ferroelectric region. About the half of the strain, for a given stress, is inelastic; this is presumably due to domain reorientation under stress, since the strain is absent above the Curie point. For stresses approaching the breaking stress of the material, some 13% of the domains in the material are reoriented by 90° according to Subbarao, E. C. (1957).

In Berlincourt's work [Berlincourt, D. *et al.* (1959)], the amount of 90° reorientation during poling was determined from measured mechanical strains. It was found that within tetragonal symmetry electric field can cause both 180° and 90° domain reorientation but, mechanical stress can cause only 90° switching. The degree of the polarization in polycrystalline ferroelectric ceramics during poling was calculated for different crystal structures in Table 2.1. According to these calculations, the polarization vectors of the domains in a polycrystalline are one of the favorable directions and the degree of the polarization would be $(n-1)/n$ where n is the number of the polarization vectors allowed in the crystal symmetry.

Table 2.1. The portions of the polarization contributed by various domain-switching mechanisms in different crystal structures [Berlincourt, D. et al. (1959)]

Tetragonal		Rhombohedral		Orthorhombic	
1/6	No switching	1/8	No switching	1/12	No switching
1/6	180° switching	1/8	180° switching	1/12	180° switching
2/3	90° switching	3/8	71° switching	1/6	90° switching
		3/8	109° switching	1/3	60° switching
				1/3	120° switching

The following calculation shows how the data in Table 2.1 were extracted from experiments on single crystal and polycrystalline $BaTiO_3$ samples. The typical remnant

polarization for polycrystalline $BaTiO_3$ was measured as 5.314 $\mu C/cm^2$ while for a single crystal, this value was 26 $\mu C/cm^2$. For a perfect orientation of the ceramic along the poling direction, the maximum polarization will be crystal structure dependent and for tetragonal crystal, it is 26x0.83=21.6 $\mu C/cm^2$. The portion resulting 180° domain switching according to Table 2.1 is 1/6*21.6=3.6 $\mu C/cm^2$. The mechanical strain for the perfect 90° reorientation of a tetragonal $BaTiO_3$ ceramic in terms of the tetragonal distortion is 0.37% (*c/a* is 1.01) and the remnant axial strain was calculated as 0.047% by assuming the parallel and lateral strains are the same ratio of piezoelectric constants d_{33} and d_{31} [Berlincourt, D. et al. (1959)]. This indicates only 12% of the possible domain reorientations actually took place. With 12% of the 90° domain reorientation, its contribution to the ceramic polarization is 0.12*2/3*21.6=1.7 $\mu C/cm^2$. The total ceramic remnant polarization should then be 3.6+1.7=5.3 $\mu C/cm^2$. As will be shown later, this number is in perfect agreement with results obtained in the present study.

- *Phase-field Models:* Wang, J. et al (2005) investigated the microscopic domain structures in 2D ferroelectrics under biaxial strains using a phase-field model based on the time-dependent Ginzburg-Landau equation that takes both long-range electric and elastic interactions into account. In phase-field simulations, the spontaneous polarization vector, $\boldsymbol{P} = (P_1, P_2, P_3)$, is usually used as the order parameter, and the time-dependent Ginzburg-Landau equation, given as,

$$\frac{\partial P_i(r,t)}{\partial t} = -L\frac{\delta F}{\delta P_i(r,t)} \quad (i = 1,2,3) \qquad (2.3)$$

is generally used to calculate the temporal evolution, where L is the kinetic coefficient, F is the total free energy of the system, $\delta F / \delta P_i(\vec{r},t)$ represents the thermodynamic driving force of the spatial and temporal evolution of the simulated system, r denotes the spatial vector, $r = (x_1,x_2,x_3)$, and t denotes time. The total free energy of the system includes the bulk free energy, the domain wall energy, i.e., the energy of the spontaneous polarization gradient, the long-range electric and elastic interaction energies, and the elastic energy induced by

applied strains. The temporal evolution of the 2D polarizations at different temperatures and applied strains can be obtained by solving Eq. (2.3) with periodic boundary conditions in reciprocal space. In the cited research, there are some calculated results but this simulation is based on temperature dependent domain switching from a multi-domain state to a single domain state. The Curie temperature for this simulation is selected around 400°C which is close to the Curie's temperature of PZT. In this study, the simulation results are only at the steady state.

- *Thermodynamic Calculations:* Here, the macroscopic polarization states can be obtained by a nonlinear thermodynamic theory [Wang, J. et al (2005)]. The equilibrium polarization states are a function of the Helmholtz free energy of the system. This energy depends on several electromechanical parameters such as dielectric stiffness and coefficients, electrostrictive coefficients, and elastic compliances. The equilibrium polarization states under different biaxial strains and temperatures can then be determined by the minimization of the Helmholtz free energy.
- *Statistical Models:* Li et al [Li, F. X. (2006)] calculated the theoretical saturated domain orientation states in tetragonal, rhombohedral and orthorhombic ferroelectrics under electrical or mechanical loading by using a simple statistical method. In this model, the state of a cubic grain, which may contain several types of domains, is described by three Euler angles (θ, φ, ψ) in a fixed global Cartesian coordinate system (Figure 2.6).

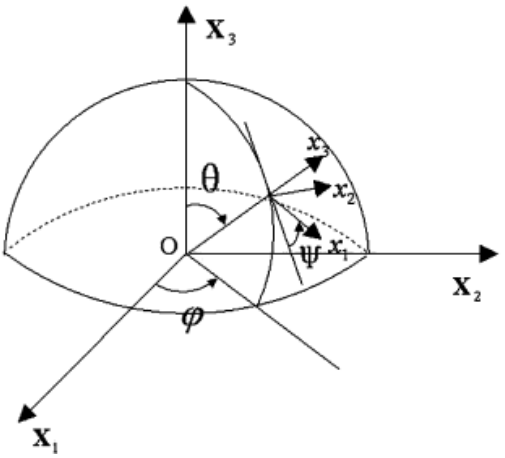

Figure 2.6. Illustration of the global Cartesian coordinate system [Li, F. X. (2006)]

The polar vector of each domain can be denoted by a vector that starts from the center of a unit sphere and ends at the spherical surface. In the proposed simple method, it is assumed that for a ferroelectric with *n* equivalent polar directions, an ideal poling treatment can make the end points of the polar vectors distribute uniformly on the spherical surface of a cone with its area equal to *1/n* that of the entire unit spherical surface. Thus, the saturated polarization and spontaneous strain of a poled ferroelectric can be obtained by the following equations:

$$P_{sat} = \frac{P_0 \int_0^{\theta_c} \cos\theta \sin\theta d\theta}{\int_0^{\theta_c} \sin\theta d\theta} = \frac{n-1}{n} P_0 \qquad (2.4)$$

$$\gamma_{sat} = \frac{\gamma_0 \int_0^{\theta_c} (\cos^2\theta - \frac{1}{2}\sin^2\theta) \sin\theta d\theta}{\int_0^{\theta_c} \sin\theta d\theta} = \frac{(n-1)(n-2)}{n^2} \gamma_0 \qquad (2.5)$$

where θ_c equals half of the central angle of the cone given by $\theta_c = \arccos\frac{n-2}{n}$. Cooling from paraelectric phase, the individual domains can orient in certain crystallographic orientations. These allowable directions are respectively along a cube edge (6), body diagonal (8) and face diagonal (12) for tetragonal, rhombohedral and orthorhombic symmetries, respectively. Therefore, the maximum spontaneous polarization of a poled ferroelectric will be $0.833P_0$, $0.875P_0$ and $0.917P_0$ for tetragonal, rhombohedral and orthorhombic crystal structures [Jaffe, B. (1971)], respectively, where P_0 is the polarization of an ideally poled sample.

- *Phenomenological Models:* These models (e.g., the Rayleigh model) try to describe the observed behavior without attempting to explain its physical origin. Hlinka, J. et al (2006) analyzed the properties of ferroelectric-ferroelastic twin boundaries in tetragonal $BaTiO_3$-like crystals in the framework of the phenomenological Ginzburg-Landau-Devonshire model. They assumed a proper ferroelectric crystal with a parent phase of macroscopically cubic O_h symmetry. The free energy of this system is assumed to be the sum of the part associated with a hypothetical reference cubic state F_r and the excess free

energy *F* arising due to the nonzero primary and secondary order parameters (polarization and strain fields).

- *Micromechanics Models:* In micromechanics models (e.g. the Preisach model) [Steinkopff, T. (1999)], a set of physical equations is solved on a small material volume from which the macroscopic behavior is calculated by averaging. The material behavior is described by means of physically meaningful variables. The main advantage of these models lies in their predictive capability. In a micromechanics model, domain switching occurs at sufficiently high stress, *T* or field levels, *E*. Switching is connected with changes of both the spontaneous strain, ΔS^S and the spontaneous polarization, ΔP^S . Favorably oriented domains grow at the expense of unfavorably oriented ones. Because of crystal symmetry (e.g., tetragonal) there are more than one possible new direction of spontaneous polarization. In the 3D micromechanics model used, the work done by switching is assumed to exceed a (positive) critical value:

$$\underline{T} \cdot\cdot \Delta \underline{S}^s + \vec{E} \cdot \Delta \vec{P}^s = \Delta w \leq \Delta w^c \tag{2.6}$$

which corresponds to critical stress or critical electric field under uncombined uniaxial loading. As a consequence of this combined energy criterion, the critical stress value is linearly dependent on the applied electric field. Unfortunately, this model fails to offer further insight into domain switching mechanisms in ferroelectrics.

- *Self-Consistent Model:* Huber et al [Huber, J. *et al.* (1999)] developed a constitutive model for the non-linear switching of ferroelectric polycrystals under a combination of mechanical stress and electric field. It was assumed that domain switching gives rise to a progressive change in remnant strain and polarization and to change in the average linear electromechanical properties. It is further assumed that switching is resisted by the dissipative motion of the domain walls. This model only gives the macroscopic response of tetragonal crystals and does not offer lattice-plane-specific information that could be useful in the present study. Meanwhile, a recent work by Motahari, M. S. (2007) enabled self-consistent model to increase the capability of studying crystal structures with a higher number of domain variants such as rhombohedral, orthorhombic, and even monoclinic structures and provide hkl dependent information from the domain variants.

In this chapter, the fundamental principles of the ferroelectric materials and the morphology of the ferroelectric domain structure were outlined. In a polycrystal ferroelectric, domain variants can present in a grain and the orientation of each domain variant can be obtained by the 3D-XRD and µSXRD techniques. Quantitative texture knowledge is necessary to identify the domain variants from the same grains and evaluate the evolution of those domains with external stimuli. Chapter 3 will describe the fundamentals of quantitive texture analysis and shows the standards to find misorientation between domain variants when crystal symmetry is present.

CHAPTER 3. TEXTURE

Most engineering materials are crystalline, and a majority of those are used in polycrystalline form. Depending on their crystal structures, materials can exhibit anisotropy in certain physical properties as both single crystals and polycrystals. Therefore, quantitative texture analysis is important in understanding material behavior. In this chapter, fundamentals of quantitative texture analysis, methods of defining the orientation of crystallites and finding misorientation between them will be described. This information will be valuable when the XRD techniques employed in this study are described in Chapter 4.

3.1. Definition

Each grain in polycrystalline materials is essentially a single crystal (while it is sometimes customary to also define sub-granular regions of slight misorientations). If the majority of grains are oriented along a certain direction, the material is considered "textured". Therefore, one can simply define texture as the "non-random distribution of the individual crystallites or "grains" (Note that the words "grain" and "crystallite" will be used interchangeably in this text, while strictly speaking, a "grain" can contain several "crystallites" as distinguished by diffraction analysis.). Figure 3.1(a) shows the schematic representation of two grains that are separated with a grain boundary. In order to define an orientation of a grain, a right-handed global coordinate system is introduced. The global coordinate system has the orthogonal axes ($\boldsymbol{s_1}$, $\boldsymbol{s_2}$, $\boldsymbol{s_3}$). The selection of orthogonal axes is important because it does not require any corrections when dealing with vector transformations. Every point in the global coordinate system can be expressed as a global vector:

$$s = l_1 s_1 + l_2 s_2 + l_3 s_3 \qquad (3.1)$$

where l_i ($i=1,2,3$) are the coefficients of the vector in the global coordinate system. Each unit cell, on the other hand, can be represented as a local coordinate system which has the orthogonal axes ($\boldsymbol{c_1}$, $\boldsymbol{c_2}$, $\boldsymbol{c_3}$) bound to the main crystal axes. A local vector in the crystal can then be defined as:

$$\mathbf{c} = m_1 c_1 + m_2 c_2 + m_3 c_3 \qquad (3.2)$$

where m_i (i=1,2,3) are the coefficients of the vector with respect to the local axes.

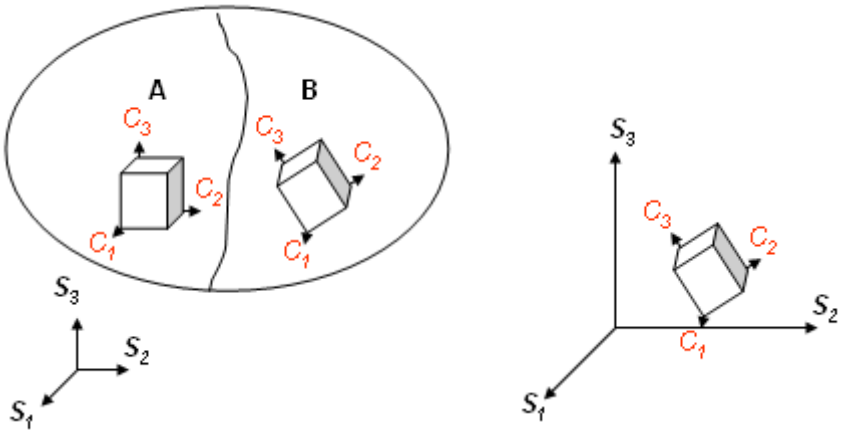

(a) (b)

Figure 3.1. (a) Schematic representation of two grains separated by a grain boundary. (b) A unit cell with attached local coordinates shown with respect to the global coordinates.

The local vectors can be transformed to the global coordinate system using:

$$\begin{aligned}
\mathbf{c}_1 &= \cos(\frac{c_1}{s_1})s_1 + \cos(\frac{c_1}{s_2})s_2 + \cos(\frac{c_1}{s_3})s_3 = g_{11}s_1 + g_{12}s_2 + g_{13}s_3 \\
\mathbf{c}_2 &= \cos(\frac{c_2}{s_1})s_1 + \cos(\frac{c_2}{s_2})s_2 + \cos(\frac{c_2}{s_3})s_3 = g_{21}s_1 + g_{22}s_2 + g_{23}s_3 \qquad (3.3) \\
\mathbf{c}_3 &= \cos(\frac{c_3}{s_1})s_1 + \cos(\frac{c_3}{s_2})s_2 + \cos(\frac{c_3}{s_3})s_3 = g_{31}s_1 + g_{32}s_2 + g_{33}s_3
\end{aligned}$$

where g_{ij} (i, j=1,2,3) is the direction cosine of the angle between the specified axis in local and global coordinates. For instance, g_{31} defines the direction cosine between the 3rd axis of the local system and the 1st axis of the global one. Since a coordinate system transformation can, in general, involve both rotation and translation, Equation (3.3) can also be written as:

$$\begin{bmatrix} c_1 \\ c_2 \\ c_3 \end{bmatrix} = \begin{bmatrix} g_{11} & g_{12} & g_{13} \\ g_{21} & g_{22} & g_{23} \\ g_{31} & g_{32} & g_{33} \end{bmatrix} \cdot \begin{bmatrix} s_1 \\ s_2 \\ s_3 \end{bmatrix} + \begin{bmatrix} t_1 \\ t_2 \\ t_3 \end{bmatrix} \qquad (3.4)$$

$$c_i = g_{ij} s_j + t_j \qquad (3.5)$$

where t_j ($j=1,2,3$) is the translational part of the transformation.The 3D-XRD and µSXRD techniques use different conventions for the transformation matrix. While µSXRD uses the same convention described above, 3D-XRD employs a matrix that transforms local vectors into global ones:

$$s_j = U_{ji} c_i \tag{3.6}$$

Therefore, the relation between the µSXRD and 3D-XRD transformation matrices becomes:

$$U = g^T \tag{3.7}$$

According to matrix algebra [Altmann, S. L. (1986)], the transformation matrix is a real square matrix whose transpose is its inverse and whose determinant is +1.

3.2. Description of Orientation

As discussed above, the orientation of a grain can be expressed as a transformation from the local coordinates into global coordinates. Since such a representation of the orientation with a tensor is not feasible and difficult when dealing with numerous grains, it is crucial to employ other methods to represent grain orientation such as Euler angles, angle-axis pairs, quaternions and Rodriguez vectors.

3.2.1. Bunge- Euler Angles

Bunge-Euler angles are the most commonly used technique to describe orientation. The crystal axes of a grain can be defined with respect to a fixed reference axis, which is called the orientation of the grain. The crystal orientation can then be described by consecutive rotation matrices. Euler angles define three consecutive rotations: first, an anticlockwise (positive) rotation around the [001] crystal direction; second, another rotation around the rotated [100] crystal direction, and finally, a third rotation around the new [001] direction. The corresponding rotation angles are called the φ_1, ϕ *and* φ_2 Euler angles. In this convention, a *positive rotation* is defined as anticlockwise and parallel to the specified axis. Figure 3.2 shows these rotations and the corresponding Euler angles.

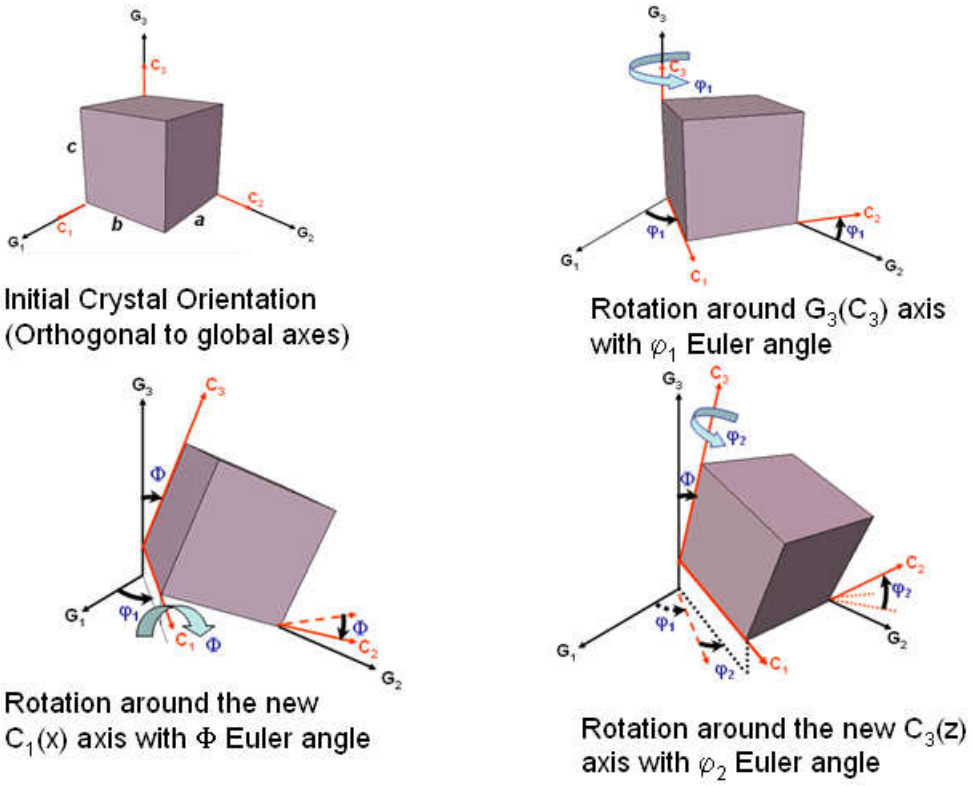

Figure 3.2. Euler angles and the corresponding rotations

The successive rotations in each Euler angle can be represented with the following matrices:

$$U(\phi_1)=\begin{pmatrix}\cos\phi_1 & \sin\phi_1 & 0\\ -\sin\phi_1 & \cos\phi_1 & 0\\ 0 & 0 & 1\end{pmatrix}$$

$$U(\Phi)=\begin{pmatrix}1 & 0 & 0\\ 0 & \cos\Phi & \sin\Phi\\ 0 & -\sin\Phi & \cos\Phi\end{pmatrix} \qquad (3.8)$$

$$U(\phi_2)=\begin{pmatrix}\cos\phi_2 & \sin\phi_2 & 0\\ -\sin\phi_2 & \cos\phi_2 & 0\\ 0 & 0 & 1\end{pmatrix}$$

The total rotation then becomes:

$$U(\phi_1,\Phi,\phi_2)=\begin{bmatrix}\cos\phi_1.\cos\phi_2-\sin\phi_1.\cos\Phi.\sin\phi_2 & \cos\phi_1.\sin\phi_2+\sin\phi_1.\cos\Phi.\cos\phi_2 & \sin\phi_1.\sin\Phi\\ -\sin\phi_1.\cos\phi_2-\cos\phi_1.\cos\Phi.\sin\phi_2 & -\sin\phi_1.\sin\phi_2+\cos\phi_1.\cos\Phi.\cos\phi_2 & \cos\phi_1.\sin\Phi\\ \sin\Phi.\sin\phi_2 & \sin\Phi.\cos\phi_2 & \cos\Phi\end{bmatrix} \qquad (3.9)$$

One can also employ a vector transformation, *g*, which rotates the crystal from the crystal frame into sample frame. We can construct *g* from three rotations about the sample axes:

$$g_1 = U(\phi_1)^T,\ g_2 = U(\Phi)^T,\ g_3 = U(\phi_2)^T \tag{3.10}$$

$$g = g_1 g_2 g_3 \tag{3.11}$$

By simple algebra, $U = g^T$.

Finally, the crystal orientation can also be represented as crystallographic planes and directions, i.e., *(hkl)[uvw]*. In this case, Bunge-Euler angles can be found as:

$$\Phi = \cos^{-1}\left(\frac{l}{\sqrt{h^2 + k^2 + l^2}}\right) \tag{3.12}$$

$$\phi_1 = \sin^{-1}\left(\frac{w}{\sqrt{u^2 + v^2 + w^2}}\right)\sqrt{\frac{l^2 + h^2 + k^2}{(h^2 + k^2)}} \tag{3.13}$$

$$\phi_2 = \cos^{-1}\left(\frac{k}{\sqrt{h^2 + k^2}}\right) \tag{3.14}$$

3.2.2. Angle-Axis Pairs

The orientation of a crystal can be expressed with an anticlockwise rotation (ψ) around a rotation vector (***n***). As shown in Eq. (3.9), the rotation matrix defines a proper rotation and its determinant is +1. This rotation matrix can be expressed as:

$$\mathbf{g} = \begin{bmatrix} g_{11} & g_{12} & g_{13} \\ g_{21} & g_{22} & g_{23} \\ g_{31} & g_{32} & g_{33} \end{bmatrix} \tag{3.15}$$

To solve for the rotation angle and axis, the rotation matrix above can be written as a sum of a symmetric and skew-symmetric matrix [Altmann, S. L. (1986)]:

$$g = \frac{1}{2}\{(g + g^T) + (g - g^T)\} \tag{3.16}$$

The last part of the matrix is called ***S***, corresponds to the skew-symmetric component (g-g^T) of g and can be written as:

$$S = g - g^T = \begin{bmatrix} 0 & g_{12} - g_{21} & g_{13} - g_{31} \\ g_{21} - g_{12} & 0 & g_{23} - g_{32} \\ g_{31} - g_{13} & g_{32} - g_{23} & 0 \end{bmatrix} = def \begin{bmatrix} 0 & c & b \\ -c & 0 & a \\ -b & -a & 0 \end{bmatrix} \qquad (3.17)$$

where, a, b and c stand for the virtual components of the rotation axis. Such a rotation axis (***n***) will be same after applying the rotation:

$$\mathrm{g}\,\boldsymbol{n} = \boldsymbol{n} \qquad (3.18)$$

From the orthogonality condition, $gg^T = 1$, we can obtain

$$n = g^T n \qquad (3.19)$$

$$gn = g^T n \qquad (3.20)$$

$$(g - g^T)n = 0 \qquad \Rightarrow \qquad Sn = 0 \qquad (3.21)$$

The skew-symmetrical matrix component (***S***) can be written from Equation (3.17):

$$Sn = \begin{bmatrix} 0 & c & b \\ -c & 0 & a \\ -b & -a & 0 \end{bmatrix} \begin{bmatrix} n_1 \\ n_2 \\ n_3 \end{bmatrix} = 0 \qquad (3.22)$$

From this equation, the components of the rotation axis can be expressed as the virtual components defined in Equation (3.17):

$$n_1 = an_3 / c \qquad n_2 = -bn_3 / c \qquad n_3 = \pm c(a^2 + b^2 + c^2)^{-1/2} \qquad (3.23)$$

The expression in the last component of the rotation axis can be easily written as the trace of SS^T:

$$SS^T = \begin{bmatrix} 0 & c & b \\ -c & 0 & a \\ -b & -a & 0 \end{bmatrix} \begin{bmatrix} 0 & -c & -b \\ c & 0 & -a \\ b & a & 0 \end{bmatrix} = \begin{bmatrix} c^2 + b^2 & ba & -ca \\ ba & c^2 + a^2 & cb \\ -ca & cb & b^2 + a^2 \end{bmatrix} \qquad (3.24)$$

and their relations are:

$$a^2 + b^2 + c^2 = \frac{1}{2} Tr(SS^T) \qquad (3.25)$$

On the other hand:

$$SS^T = (g - g^T)(g^T - g) = 2\mathrm{I} - g^2 - (g^T)^2 \tag{3.26}$$

where, I is the identity matrix. From the diagonalization of g and g^T,

$$g' = \begin{bmatrix} 1 & & \\ & e^{i\psi} & \\ & & e^{-i\psi} \end{bmatrix}, \qquad (g')^2 = \begin{bmatrix} 1 & & \\ & e^{i2\psi} & \\ & & e^{-i2\psi} \end{bmatrix} \tag{3.27}$$

so that the trace of g^2 must be $1 + 2\cos 2\psi$. The trace of $(g^T)^2$ must be the same since g^T being the reciprocal of g, its rotation angle is equal and opposite to that of g. Then, $Tr(SS^T)$ in Equation (3.26) is $8\sin^2\psi$, giving:

$$a^2 + b^2 + c^2 = 4\sin^2\psi \tag{3.28}$$

Then, the components of the rotation axis will be:

$$n_1 = \pm a(2\sin\psi)^{-1} \qquad n_2 = \pm b(2\sin\psi)^{-1} \qquad n_3 = \pm c(2\sin\psi)^{-1} \tag{3.29}$$

If we replace the virtual terms a, b and c with their real values in Equation (3.17), we will obtain:

$$\cos\psi = \frac{1}{2}(g_{11} + g_{22} + g_{33} - 1) \tag{3.30}$$

$$n_1 = \frac{g_{23} - g_{32}}{2\sin\psi} \quad n_2 = \frac{g_{13} - g_{31}}{2\sin\psi} \quad n_3 = \frac{g_{12} - g_{21}}{2\sin\psi} \tag{3.31}$$

The term $2\sin\psi$ in Equation (3.31) drops when normalizing the rotation axis components. The rotation angle and axis method is extremely useful when dealing with rotations of crystals with high lattice parameter ratios (e.g., hcp metals). Figure 3.3 shows the schematic representation of orientation with rotation axis and angle method. The rotation angle ψ is still an anticlockwise rotation parallel to the rotation axis.

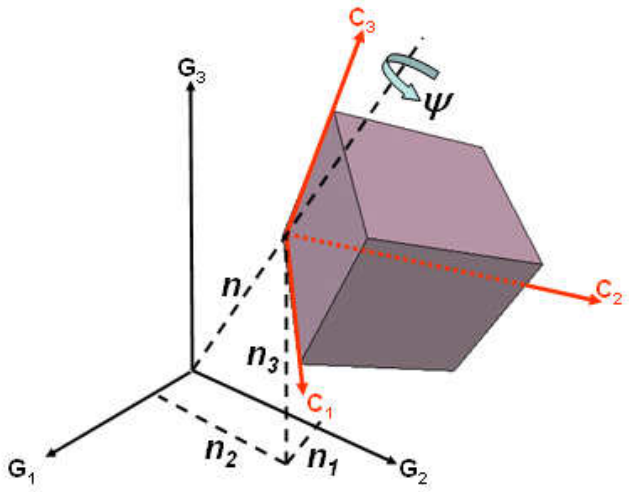

Figure 3.3. Schematic representation of orientation with the rotation angle and axis (a.k.a. angle-axis pair) method.

3.2.3. Quaternions

Quaternions are the non-commutative form of complex numbers. In this formalism, an orientation is represented by a quaternion that contains the rotation angle (ψ) $\psi \in [0, \pi]$ and the unit vector of the rotation axis ($\boldsymbol{n}$) (in the Cartesian coordinate system). In addition, for rotations, only quaternions of unit length are considered.

$$\mathbf{q} = [\cos(\frac{\psi}{2}),\ \mathbf{n}_1 \sin(\frac{\psi}{2}),\ \mathbf{n}_2 \sin(\frac{\psi}{2}),\ \mathbf{n}_3 \sin(\frac{\psi}{2})] \tag{3.32}$$

Note that the components of the quaternion can easily be obtained from the rotation angle and axis method. Adoption of the quaternion formalism in place of matrix representation of orientations makes it easier to calculate misorientation and will be discussed in Section 3.4.

3.2.4. Rodrigues Vectors

The division of the rotation axis components, $\boldsymbol{n}_1$, $\boldsymbol{n}_2$, and $\boldsymbol{n}_3$, by the rotation angle will create the Rodrigues vectors. The directions of the Rodrigues vectors are chosen parallel to the global axes. The relation between angle-axis pair and Rodrigues vectors is given as:

$$\mathbf{r} = \mathbf{n} \tan(\frac{\psi}{2}) \tag{3.33}$$

The Rodrigues vectors offer a major advantage by showing the rotation axis and angle components in their vector components.

3.3. Representation of Orientation

The methods to define grain orientations described above are three-dimensional representations. When a population of the grain orientations is interested, these methods are not easy to represent on a paper. As suggested by Frank, F. C. (1988), it can be accomplished by holograms, but that would be an expensive technique. Therefore, grain orientations are often mapped on a projection of a plane as will be described below.

Grain orientation mapping is basically “perspective projection”. Figure 3.12 shows the most widely used perspective projection methods that employ a reference sphere. The main distinction between these methods is the location of the viewpoint. Let us consider the point *P* as an orientation vector pointing from the center to the surface of the reference sphere. While the viewpoint from the center of the reference sphere to the projection plane gives the *gnomonic projection*, a viewpoint from an infinite distance parallel to the NS plane yields the *orthographic projection*. If the viewpoint is the surface of the other half of the sphere (e.g., point *S*), the result is the *stereographic projection*.

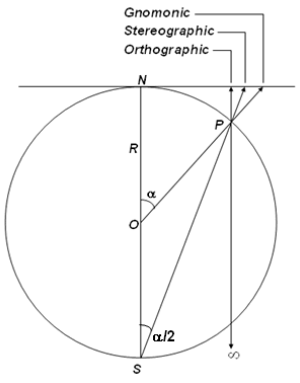

Figure 3.4. Different projections of a point *P* [redrawn from Amoros, J.L. et al (1975)]

While 3D-XRD uses stereographic projection, the µSXRD technique often employs gnomonic projection. In this section, orientation mapping will be described with respect to stereographic projection only because it is the most common method uses in quantitative

texture analysis. Mapping an orientation with the different projections is based on the same principles except the different projection angle, α as shown in Figure 3.4.

3.3.1. Pole Figure

As described in Equation 3.4, the orientation matrix of a grain defines the direction cosines of the angles between the local crystal and global vector components. The orientation of a grain on an (*hkl*) plane can be represented as a vector starting from the origin of a sphere to the surface of the sphere. The corresponding polar coordinates of this unit vector will be:

$$\begin{bmatrix} \sin\alpha\cos\beta \\ \sin\alpha\sin\beta \\ \cos\alpha \end{bmatrix} = \frac{1}{P}\begin{bmatrix} g_{11} & g_{12} & g_{13} \\ g_{21} & g_{22} & g_{23} \\ g_{31} & g_{32} & g_{33} \end{bmatrix} \cdot \begin{bmatrix} h \\ k \\ l \end{bmatrix} \tag{3.34}$$

where, $P = \sqrt{h^2 + k^2 + l^2}$ and α and ß are the polar angles described in Figure 3.5.

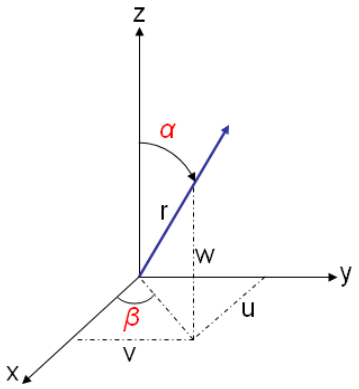

Figure 3.5. Orientation vector on an (*hkl*) plane within the unit sphere

Let us consider drawing a pole figure on the (001) plane. In this case, the components of the orientation matrix in Equation (3.34) can be reduced to g_{31}, g_{32} and g_{33}. The length of the orientation vector can be expressed as:

$$r = \sqrt{(g_{31}{}^2 + g_{32}{}^2 + g_{33}{}^2)} \tag{3.35}$$

which will be unity from the condition of orthogonality. The polar angles of the orientation vector can easily be found as:

$$\beta = \tan^{-1}\left(\frac{U_{32}}{U_{33}}\right) \qquad \alpha = \cos^{-1}\left(\frac{U_{31}}{r}\right) \tag{3.36}$$

And, the Cartesian coordinates of the orientation as a pole figure in stereographic projection will be:

$$x = \tan\left(\frac{\alpha}{2}\right).\cos\beta \qquad y = \tan\left(\frac{\alpha}{2}\right).\sin\beta \tag{3.37}$$

With the pole figure thus described, the orientation of a crystal direction can be mapped in the stereographic projection. The boundary of the pole figure describes the global coordinates. To view the distribution of crystallographic planes along a specific global direction, the inverse pole figure, described next is a very useful method.

3.3.2. Inverse Pole Figure

The orientation along a specific global direction can be drawn as an "inverse pole figure". The major advantage of this method is its ability to map crystallographic orientations within one figure along a fixed global direction. The plotting procedure of the inverse pole figure is very similar to the one described for the pole figure. The main difference is in which components of the orientation matrix are considered. For instance, for the distributions of crystallographic planes in the global *z* direction, one needs to take the g_{13}, g_{23} and g_{33} components of the orientation matrix as the corresponding vectors in the stereographic projection. Then the same procedure described in Equations (3.35) - (3.37) is used to plot the orientation of individual grains.

The size of the unique inverse pole figure depends on the crystallographic symmetry of the material (Figure 3.6). This non-repeated inverse pole figure is often called the "standard stereographic triangle (SST)". The complete circle of the projection plane can be divided using point symmetry operations. Starting with triclinic symmetry, one-fold rotation will cover the complete projection circle while the two-fold rotation symmetry in a monoclinic system will cover half of the area. Three mutually perpendicular symmetry elements in orthorhombic symmetry will define a quarter of the circular area; four-fold rotation and a mirror plane in tetragonal structures will lead to 1/8 of the area; trigonal

systems will have 1/6 due to their three-fold rotation and mirror plane; hexagonal crystals will need only 1/12 of the total area, and finally, cubic materials will suffice with 1/24 due to their four-fold and three-fold symmetries plus mirror planes.

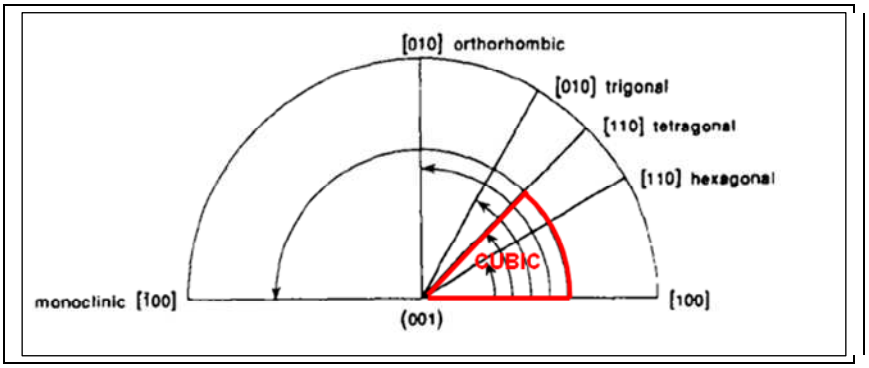

Figure 3.6. Size of the *unique* inverse pole figure depends on crystal symmetry [Dahms, M. (1992)].

3.3.3. Rodrigues Space

Rodrigues space is an extremely useful method to show orientation distributions. Its major advantage is its ability to show grain orientations a single plot unlike both types of pole figures. The Rodrigues space is mainly the three-dimensional reconstruction of the standard stereographic triangle shown in Figure 3.6 for different crystal symmetries. It is simply obtained by applying the symmetry operations at the boundaries of the standard stereographic triangle. The details of this procedure will be described in the Fundamental Region section (3.4.1).

3.4. Misorientation

The rotation (or orientation) difference between two grains is called misorientation and is defined as the smallest angle of rotation leading from one orientation to the other [Morawiec, A. (1995)]. There are several ways to calculate the misorientation between two grains. First, it can be calculated in a matrix form by multiplying the orientation matrix of a grain by the inverse of the orientation matrix of the other. If we denote two grains as *A* and *B*, the misorientation between these two grains will be given by:

$$\Delta g = g_A . g'_B \qquad (3.38)$$

$$\cos\psi = [(\sum_{i=1}^{3} \Delta g_{ii}) - 1] \Big/ 2 \tag{3.39}$$

$$< \hat{n}_1, \hat{n}_2, \hat{n}_3 > = < \Delta g_{23} - \Delta g_{32}, \Delta g_{13} - \Delta g_{31}, \Delta g_{12} - \Delta g_{21} > \tag{3.40}$$

where, $< \hat{n}_1, \hat{n}_2, \hat{n}_3 >$ and ψ represent the misorientation axis and angle, respectively. It is important to realize that misorientation is expressed in terms of the local crystal coordinates as opposed to the fixed sample coordinate system.

In the second method, the rotation between two orientations can be obtained by the product of their corresponding Rodrigues vectors [Frank, F.C. (1988)]:

$$r_B \circ r_A = \frac{(r_A + r_B - r_A \times r_B)}{(1 - r_A \cdot r_B)} \tag{3.41}$$

where, 'x' and '$.$' denote to vector and scalar products, respectively. The sign between r_B and r_A shows a special product of two Rodrigues vectors. Using this approach, the misorientation angle between two domains was calculated in the present study as:

$$\psi = 2\tan^{-1}[|r_B \circ (-r_A)|] \tag{3.42}$$

In the 3D-XRD technique, we use an orientation matrix that transforms local vectors to global vectors and its relation to the classical orientation matrix is (U=g^T). In the third method of representing misorientation, the dot products of each column of two orientation matrices (U_{ij}^A and U_{ij}^B) of grains A and B are calculated and the misorientation angle (ψ_{ij}) is defined by:

$$\psi_{ij} = \cos^{-1}\left\{ \frac{\sum_{i=1}^{3} U_{ij}^A U_{ij}^B}{\sqrt{\sum_{i=1}^{3} (U_{ij}^A)^2} \sqrt{\sum_{i=1}^{3} (U_{ij}^B)^2}} \right\} \tag{3.43}$$

In this study of ferroelectrics, for the two sets of the grains found at different applied electric fields, a misorientation matrix (S^{kl}) was created. From the calculated sets of misorientation angles, the ones between 0 and 1° and 89° and 90° are in close interest. The misorientation angles between 0 and 1° confirms the same orientations found between sets.

The misorientation angles between 89° and 90° are the candidates for the 90° domains where the misorientation angle for 90° domains is expected to be 89.4° ($2\tan^{-1}(\frac{a}{c})$). For M and N number of grains, the misorientation matrix, S^{kl} is given by:

$$S^{kl} = \left\{ \psi_{ij}^{kl} \mid 0 \le \psi_{ij}^{kl} \le 2\tan^{-1}(\frac{c}{a}) - 90° \wedge 2\tan^{-1}(\frac{a}{c}) \le \psi_{ij}^{kl} \le 90° \right\} \begin{matrix} k = 1,2,..N \\ l = 1,2,...,M \end{matrix} \quad (3.44)$$

This method requires manual inspection of columns of the orientation matrices because some orientations can be found as domains coincidentally.

Among the misorientation techniques described, the first method is more advantageous because it makes it possible to determine the misorientation axis components rather than just the misorientation angle. This gives crucial information about ferroelectric domains because it indicates the domain boundary between neighboring domain variants. We have used the first method to find the misorientation angles between the orientations found by both 3D-XRD and μSXRD methods.

3.4.1. Fundamental Region

Some of the orientation methods described above fail to show unique orientations. Figure 3.7 exhibits an object in inverse pole figures. For tetragonal symmetry (four-fold rotation, and two mirror planes), there will be 8 equivalent representations of the same object. For the cubic case (*43m*, i.e., four-fold rotation, three-fold inversion and a mirror plane) there will be 24 equivalent representations of the same object. The number of the equivalent representations increases substantially if the object locates near the symmetry elements and doubles for the misorientation calculations of two grains. When describing this orientation, Euler angles would fail to show the orientations with crystal symmetry because it is based on continuous rotations. The second major problem with Euler angles is that if the second Euler angle (ϕ) is zero and the sum of φ_1 and φ_2 are constant, all the orientations will be shown as the same orientations. [Morawiec, A. (1995)]. For example, the orientations shown with (45°, 0°, 45°) and (60°, 0°, 30°) Euler angles will be mapped to the same point in the stereographic projection while they will be different orientations.

The unique representation of orientation is not a simple task. Due to crystal symmetry, there is a multiplicity of different rotations from the reference orientation and the new orientations can be represented by different points in the stereographic projection [Frank, F. C. (1988)]. For instance, for two cubic crystals, there are 24 symmetrically equivalent points due to *43m* symmetry (4x3x2 symmetry points) and the misorientation between these crystals can have 24x24=576 equivalent designations. While all these orientations show physical identical orientations, it is important to select which one to use in the misorientation calculations. As shown in Figure 3.7, the orientations can be confined to a smaller section due to crystal symmetry. Among those projection areas, the area where there is only one unique representation in the stereographic projection is called the *fundamental region* and the orientation mapped to this area is used for calculation misorientation.

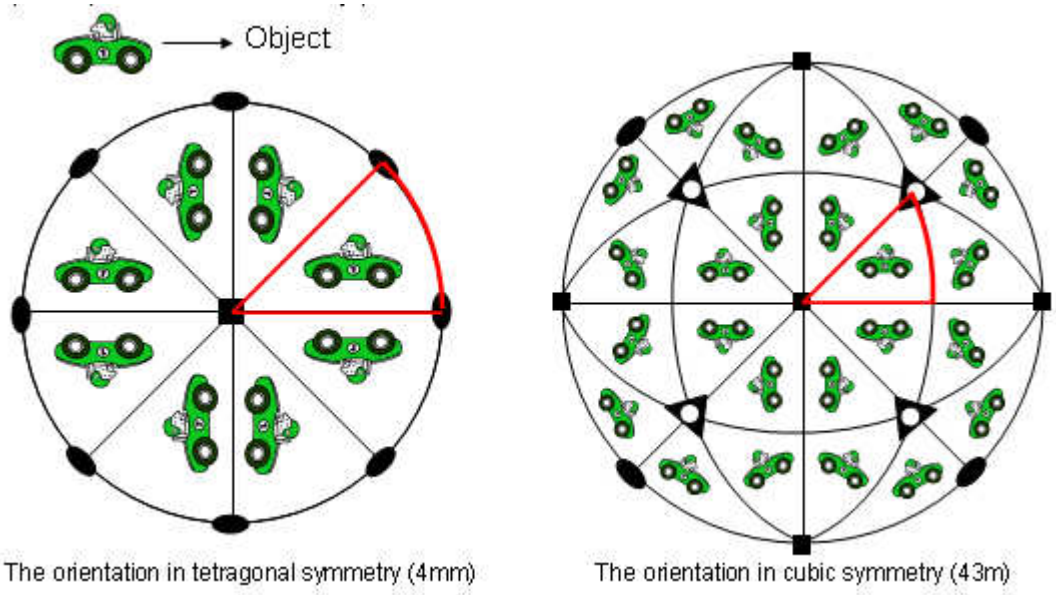

Figure 3.7. (a) Orientation representations in tetragonal (*4mm*), and (b) cubic (*43m*) symmetries. The red areas show the unique representations

A tetragonal (*P4mm*) crystal has a four-fold rotation and two mirror planes as symmetry operators. If we start with the standard stereographic triangle of the tetragonal crystal (Figure 3.6), we see that the maximum allowable rotation angle for [100] axis is 45° due to the four-fold symmetry. For the [001] and [110] axes, the maximum rotation angle is 180°. The corresponding Rodrigues vectors for these rotations will then be [0,0,1] for the [001] axis, $[\sqrt{2}-1,\sqrt{2}-1,0]$ for the [100] axis and $[\sqrt{2}-1,\sqrt{2}-1,0]$ for the [110] axis.

Figure 3.8(a) shows the representation of this standard stereographic triangle with Rodrigues vectors. By applying the tetragonal symmetry operators, the Rodrigues space can be constructed from the fundamental region. Figure 3.8(b) shows the corresponding Rodrigues space for tetragonal crystals. The maximum allowable angle in tetragonal Rodrigues space can be calculated with the maximum value of the components of the Rodrigues vector. Since the maximum Rodrigues vector for the tetragonal crystals is $[\sqrt{2}-1, \sqrt{2}-1, 1]$, the maximum rotation angle, θ will be:

$$\theta_{\max} = 2\tan^{-1}\left(\sqrt{(\sqrt{2}-1)^2 + (\sqrt{2}-1)^2 + 1^2}\right) = 98.42^\circ \qquad (3.45)$$

In sum, to calculate misorientations between individual grains, the following procedure can be applied:

- Find the standard stereographic triangle (SST) of the crystals
- Convert the SST boundaries into Rodrigues vectors
- Obtain Rodrigues space by applying the crystal symmetry operators
- Find the maximum rotation angle in the fundamental region of the Rodrigues space
- Apply the symmetry operators to the orientations after converting the orientation into a Rodrigues vector
- Select the orientation with the smallest rotation angle and closest to origin. For N symmetry operators and l_i being the vectors of the rotation axis of the i^{th} element of the symmetry operator, the fundamental region is described by:

$$\bigcap_{i=2}^{N} \{\mathbf{r}; \tan(\theta_i / 4) \pm \mathbf{r}.\mathbf{l_i} \geq 0\} \qquad (3.46)$$

where, $i=1$ corresponds to the identity rotation [Morawiec, A. (1995), Frank F.C. (1988)]. Each orientation found by 3D-XRD and µSXRD techniques was mapped to tetragonal fundamental region by using the steps outlined above.

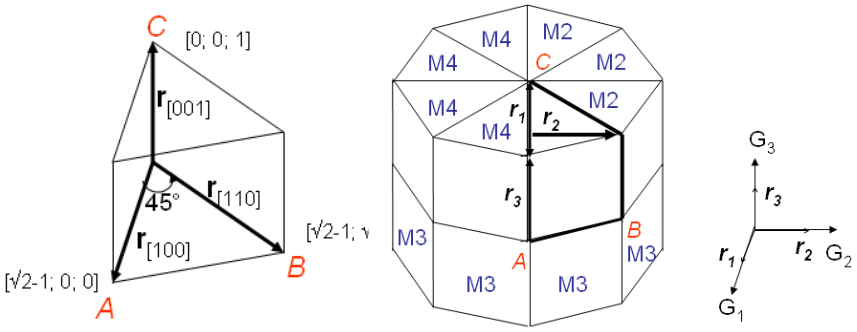

(a) (b)

Figure 3.8. (a) Representation of the fundamental region. (b) Construction of the Rodrigues space with the tetragonal symmetry operators {Identity (M1), four-fold rotation around [100] (M2) and two-fold rotation around [010] (M3) and [001] (M4)}.

CHAPTER 4. 3D-XRD TECHNIQUE

In this chapter, the 3D-XRD technique and data collection procedures will be described. Several new analysis methods have been created during the present study to interpret the results efficiently and these methods such as *phi-eta map*, *domain size*, *polarization angle* and *strain extraction* will also be described. 3D-XRD experiments were performed at Sector 1-ID of the Advanced Photon Source at Argonne National Laboratory, Argonne, IL. A detailed description of the $BaTiO_3$ 3D-XRD experiments is presented in Section 6.1.

4.1. Introduction

It is well known that most engineering materials are crystalline and their properties are greatly influenced by their crystal structure. Therefore, it is essential to characterize the internal structure of a material and link the results with performance. Selection of a non-destructive characterization technique allows a more reliable assessment of a material under various applied external stimuli. The most commonly used non-destructive characterization techniques are electron microscopy and standard laboratory X-ray diffraction. These techniques are considered surface probes [Lauridsen, E.M. (2000)] because the penetration depth of low energy X-rays and electrons is about a few μm. Due to various surface effects such as surface charges, strain relaxation, dislocations, samples have to be prepared carefully to represent the bulk behavior. Because of these surface effects, it is believed that such characterization techniques do not reveal the real material characteristics requiring most models to make sweeping assumptions on boundary conditions and average bulk properties. It is also believed that present models overestimate the texture development since grains undergo different crystallographic orientations with deformation [Margulies, L. *et al.* (2004)].

With high penetration depth and fast acquisition time, synchrotron radiation has lately become widely used in materials science. Several new characterization techniques such as 3D-XRD and μSXRD have been developed and applied to numerous problems. These

techniques allow *in-situ* measurements on mechanical behavior, temperature dependence or ferroelectric behavior by coupling a stress rig, furnace or high voltage supply, respectively.

The 3D-XRD technique has recently been developed by Risoe National Laboratory, Denmark [Lauridsen, E. M. (2001)] to study individual grains embedded in a bulk polycrystalline material. 3D-XRD allows the structural characterization of individual grains in polycrystals and yields the position, volume, orientation, and lattice (elastic) strain of these grains. The experimental setup consists of a monochromatic beam source, a sample holder, and a two-dimensional digital image plate detector to record the transmitted diffraction patterns. Figure 4.1 shows a schematic 3D-XRD setup. Typically high energy (50-80 keV) X-rays are employed to fully penetrate the sample which is rotated around the ϕ axis while collecting sequential diffraction patterns in small (<1º) ϕ steps. The scanned ϕ range is usually large enough (e.g., ϕ ±65º) to allow a fuller map of the reciprocal space.

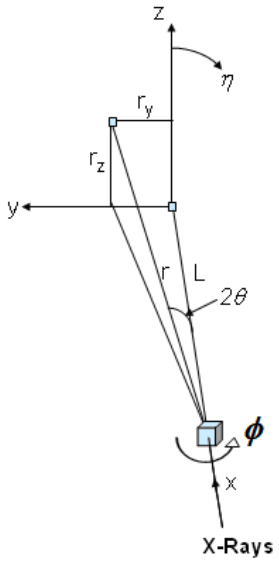

Figure 4.1. Simplified 3D-XRD setup. While x-rays are illuminating the region of interest (shown as a cube), the sample is rotated around the z axis with Δϕ angle steps. Each spot from different grains will diffract in a different 2θ and η location on the detector (shown as the y-z plane).

4.2. Data Analysis

The details of the data analysis were explained in the paper of Lauridsen, E.M. et al (2001). To summarize, the overall data analysis can be explained by one equation:

$$G_l = \Omega S g^{-1} B G_{hkl} \qquad (4.1)$$

where, the scattering vector $\boldsymbol{G_l}$ in the laboratory coordinate system (x,y,z) is converted into the reciprocal lattice system ($\boldsymbol{G_{hkl}}$). $\boldsymbol{\Omega}$ represents the rotation along z direction and has the following form:

$$\Omega = \begin{bmatrix} \cos(\phi) & -\sin(\phi) & 0 \\ \sin(\phi) & \cos(\phi) & 0 \\ 0 & 0 & 1 \end{bmatrix} \qquad (4.2)$$

$\boldsymbol{S}$, is the (sample) matrix that defines how the sample is mounted on the setup. If the sample is placed on the turntable, the resulting sample matrix will be:

$$S = \begin{bmatrix} 1 & 0 & 0 \\ 0 & 1 & 0 \\ 0 & 0 & 1 \end{bmatrix} \qquad (4.3)$$

Finally, $\boldsymbol{g^{-1}}$ defines the orientation of individual grains with respect to the sample coordinate system. Note that the original orientation matrix used in 3D-XRD transforms the crystal coordinate system into sample coordinate system. In order to be consistent with literature, this orientation matrix was represented with its inverse.

Figure 4.2 shows reciprocal lattice vectors in direct space together with the corresponding angles. In the 3D-XRD convention, the $\boldsymbol{a_1}$ is parallel to $\boldsymbol{b_1}$, $\boldsymbol{a_2}$ is in the plane of $\boldsymbol{b_1}$ and $\boldsymbol{b_2}$ and $\boldsymbol{a_3}$ is perpendicular to that plane. For tetragonal crystals, the reciprocal lattice vectors ($\boldsymbol{b_1, b_2, b_3}$) are parallel to the main axes of the crystal, and therefore, also the vectors in the Cartesian grain system ($\boldsymbol{G_c}$).

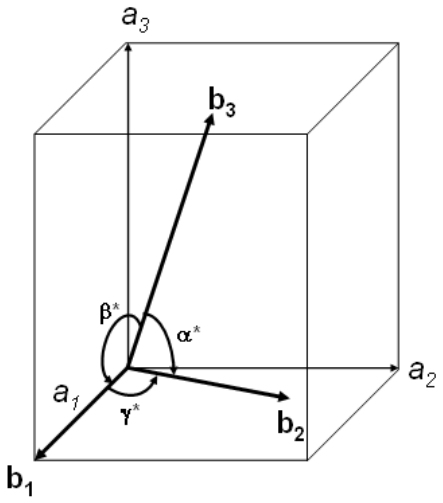

Figure 4.2. Reciprocal lattice vectors in real space and their corresponding angles.

The reciprocal lattice matrix transforms real space vectors (***a₁, a₂, a₃***) to reciprocal lattice vectors (***b₁, b₂, b₃***) and is given by:

$$B = \begin{bmatrix} b_1 & b_2\cos(\gamma^*) & b_3\cos(\beta^*) \\ 0 & b_2\sin(\gamma^*) & -b_3\sin(\beta^*)\cos(\alpha) \\ 0 & 0 & b_3\sin(\beta^*)\sin(\alpha) \end{bmatrix} \qquad (4.4)$$

where, α, β, γ and α^*, β^*, γ^* define the angles between real space and reciprocal vectors, respectively.

Assuming an X-ray is diffracted from position (x,y,z) in the sample system, with (x,y)=(0,0) along the rotation axis, the direction of the diffracted ray is determined by the Bragg 2θ and the azimuthal angle η (Figure 4.1). The intersection between the ray and the detector plane (L, r_y, r_z) is found from:

$$\begin{aligned} r_y &= -(L - x_l)\tan(2\theta)\sin\eta + y_l \\ r_z &= (L - x_l)\tan(2\theta)\cos\eta + z \end{aligned} \qquad (4.5)$$

where,

$$\begin{pmatrix} x_l \\ y_l \\ z \end{pmatrix} = \Omega \begin{pmatrix} x \\ y \\ z \end{pmatrix} = \begin{pmatrix} \cos(\phi) & -\sin(\phi) & 0 \\ \sin(\phi) & \cos(\phi) & 0 \\ 0 & 0 & 1 \end{pmatrix} \begin{pmatrix} x \\ y \\ z \end{pmatrix} \qquad (4.6)$$

Here, when r_y, r_z is at (0,0), the incoming beam and detector plane intersect. The normalized diffracted vector in the laboratory system can then be expressed as:

$$\frac{G_l}{\|G_l\|} = \Omega Sy = \Omega Sg^{-1}\mathbf{h} = \cos(\theta)\begin{pmatrix} -\tan(\theta) \\ -\sin(\eta) \\ \cos(\eta) \end{pmatrix} \qquad (4.7)$$

The standard coordinate system used at APS differs from the original coordinate system developed by Risoe. The APS coordinate convention is to identify the *Z* axis as the direction of beam propagation, the *Y* axis as up and the *X* axis as horizontal, orthogonal to the beam direction. The original system used by Risoe assumes the incoming beam direction as the *X* axis, while the *Y* and *Z* are the horizontal and vertical axes, respectively. For convenience, we will use the European Synchrotron Radiation Facility (ESRF) coordinate system to be consistent with the original setup by Risoe. The summary of these coordinate systems are given in Table 4.1:

Table 4.1. Coordinate systems used at APS and ESRF

APS	ESRF
Z: →Incoming Beam	*X*:→Incoming Beam
X: →Horizontal	*Y*:→Horizontal
Y:→Vertical	*Z*:→Vertical

The collection of 2D diffraction patterns for each phi oscillation were analyzed by the software called *Graindex* [Lauridsen, E.M. *et al.* (2001)]. *Graindex* is a multi-grain-indexing program that finds the orientation of grains based on monochromatic X-ray diffraction. The first version of this software runs as a subroutine in Image-Pro Plus 4.5.22 (Media Cybernetics, Silver Spring, MD) and the new version is a standalone freeware with a new name, Grainspotter. Since the optimization runs in progress, the data analysis routines were described according to Graindex. Figure 4.3 describes the flowchart during a typical 3D-XRDdata analysis. Three main steps are involved:

1. Data Preparation:

- *Any spatial distortion of the diffraction images is corrected.* The success in finding the grains accurately is highly dependent on the data preparation. If the diffraction patterns contain any spatial distortion, the data needs to be corrected before the grain analysis.
- *The beam center of the diffraction patterns is found within the Graindex convention.* It was found from experience that several programs such as *Fit2D, Matlab, Image-Pro Plus* use different conventions re. Coordinate systems. Therefore, it is important to perform a final tuning of the beam center by checking the 2θ locations of the peaks as a function of η. This helps eliminate misindexation of the neighboring spots from different *hkl*s such as (200) and (002) peaks.
- *Experimental parameters (sample-to-detector distance) are adjusted carefully.* The location of a diffraction spot should be well defined. The sample-to-detector distance directly affects 2θ location of spots. Theoretically, the sample-to-detector distance is refined until the difference in 2θ values between the theoretical predictions and those found by image processing is less than 10^{-4}.

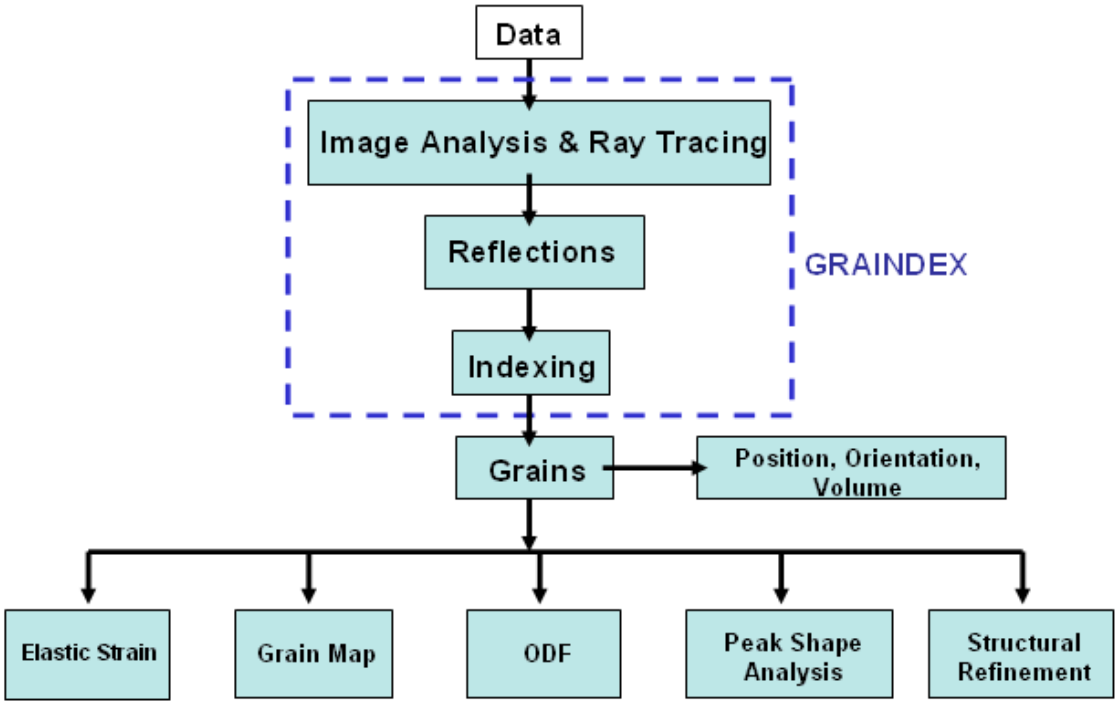

Figure 4.3. The flowchart in the data analysis of a typical 3D-XRD experiment [Lauridsen, E.M. (2001)]

2. Image Analysis and Ray Tracing:

- *All reflections on detector image are located after defining an intensity threshold.* The image processing is performed by creating a count setting file to define a desired intensity threshold. There are several advantages of the intensity threshold. First, it helps eliminate spots from weaker grains. Second. as the rotation of the sample approaches the phi angle limit (e.g., ±65°), some domains at high phi angle will diffract and the intensity threshold will also eliminate those domains. Third, it also helps eliminate overlapping it closely spaced spots.
- *List all reflections in a table.* The diffraction peaks and corresponding information such as their position on the detector plane (dety, detz), η, ϕ, 2θ and area of interest (AOI) are collected in a table.

- *Identify peak families based on their 2θ values and the diffraction families.* By using sample-to-detector distance and the X-ray energy etc., it is possible to categorize reflection families.

3. Indexing with the *Graindigger* Routine:

- *Convert the scattering vector orientation.* The scattering vectors in Eq. 4.12 is dependent on the phi rotation and it can be re-written as $G_s = g^{-1}BG_{hkl}$ by converting the scattering vectors of each reflection so they are dependent only on the orientation and reciprocal lattice matrices.

- *Increase Euler angles defining g^{-1} with finite steps using the following formula:*

$$\mathbf{U}_{mn} = \mathbf{U}^0_{mn} + \frac{\delta \mathbf{U}}{\delta \phi}(\mathbf{U}^0)_{mn}.\Delta\phi + \frac{\delta \mathbf{U}}{\delta \varphi_1}(\mathbf{U}^0)_{mn}\Delta\varphi_1 + \frac{\delta \mathbf{U}}{\delta \varphi_2}(\mathbf{U}^0)_{mn}\Delta\varphi_2 \qquad (4.8)$$

  where, U is the orientation matrix ($U=g^{-1}$). In order to find the orientation of all grains of interest, the full $[0,\pi]$ x $[0,2\pi]$ x $[0,2\pi]$ Euler space is searched and scattering vectors of the simulated and found reflections are compared using the least square method. For a given step ($\varphi_1^o, \Phi, \varphi_2^o$) and corresponding $\mathbf{U}^0 = \mathbf{U}(\phi, \varphi_1, \varphi_2)$, *Graindex* sorts the reflections whether there is no observation, matching observations or more than one observed reflections in the calculated detector location. The reflections with no observations are called “outliers”.

- *Find the observable reflections.* The number of observable *hkl*’s, M_{exp}, is found where there is at least one observation G_s that matches UBG_{hkl}. Among these reflections, grains are authenticated if:

  i. *The ratio of the observed reflections (M_{exp}) is higher than the completeness threshold.* Completeness is defined as the threshold ratio of the number of the calculated peaks to the observed peaks. The matching condition can be represented with $M_{\exp} \geq (1-\alpha)M_0$ where α is a small tolerance factor.

ii. *Uniqueness factor is satisfied.* Uniqueness factor defines the degree of which the set of matching *hkl'*s is not a sub-set of the matching *hkl'*s for another *U* setting.

iii. *Chi-square threshold is satisfied.* For a given step size of a few degrees in Euler angles, the fit can be weighted with respect to the estimated experimental errors in ω and η:

$$\chi^2 = \sum_{i,j} \frac{\{(G_s)_j - [U(\Delta\phi, \Delta\varphi_1, \Delta\varphi_2 B(G_{hkl})]_j\}_i^2}{\sigma_{ij}^2(\Delta\omega, \Delta\eta)} \qquad (4.9)$$

where, index *i* runs over the spatial coordinates, *i=1,2,3*, while *j* enumerates the members of group *B*. σ_{ij} is the error on G_s vector number *j* in the point U_0, calculated by error propagation using Eq. 4.1 and 4.7.

Noting that *Graindex* calculates the orientation matrices from the observed reflections, it is crucial to check whether there is a big difference between the positions of the calculated and observed reflections. The deviation should be as small as possible because large values suggest a discrepancy from the true orientation of the grains. Furthermore, the presence of a significant number of outliers makes the analysis questionable and further refinement of the *Graindex* parameters is necessary. Therefore, a minimum of 8 reflections are sought for each grain before it can be authenticated as a "real" grain.

Another "pitfall" [Lauridsen, E.M. (2001)] in studying ferroelectrics with the 3D-XRD technique is the overlapping spots of the domain variants. The misorientation between 90° domains within the polycrystal $BaTiO_3$ can be calculated by $2\tan^{-1}(c/a)$ where *a* and *c* denote the lattice parameters of tetragonal ferroelectric ceramics [Rogan, R. (2003)]. Since *c/a* ratio is 1.01 in $BaTiO_3$, the misorientation between the grains is very small (around 0.6°) and high resolution of domain peaks is necessary to deconvolute overlapping spots. To prevent this, the sample-to-detector distance is increased until one can observe the 200/002 rings near the outside edge of the CCD detector. This adjustment was found to yield sufficient resolution to deconvolute peaks from domain variants of $BaTiO_3$.

4.3. Phi-Eta Map

Due to the presence of domains in ferroelectrics, each grain contains "sub-grains" that are oriented by well defined, intrinsic crystal symmetry operations. The domains belonging to the same grain are called "domain variants". In $BaTiO_3$, these domains are arranged along the cube edges and the domains can have a configuration with six equal direction possibilities. Since *c/a* ratio in $BaTiO_3$ is different than unity, the orientations between domain variants can vary up to 1.2° (see Figure 6.7) and these domain variants diffract within proximity of each other. For this reason, the 3D-XRD experiments of $BaTiO_3$ employed smaller ϕ oscillations of 0.2° compared to the usual 1°.

To characterize the spots from individual domains, a given *hkl* ring was summed along η and then combined along ϕ. The map thus created is called "Phi-Eta" and it helps in the characterization and interpretation of diffraction patterns. Figure 4.4 shows the schematic procedure of creating an Phi-Eta map.

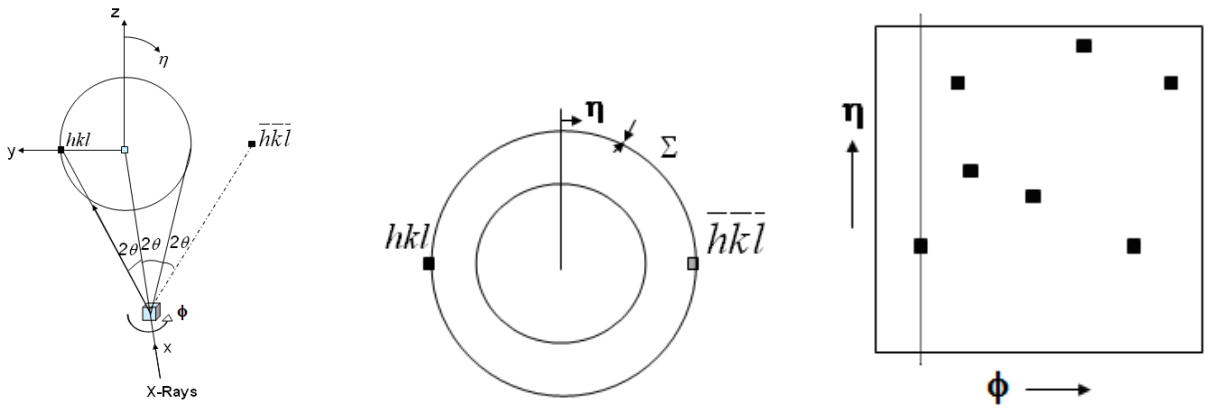

(a) (b) (c)

Figure 4.4. Schematic procedure of an Phi-Eta map. (a) The Friedel pair of a reflection diffracts with a 4θ angle. (b) The corresponding *hkl* rings are binned along η. (c) The binned rings are combined in ϕ.

There are several advantages of the *Phi-Eta map*. First, it is helpful in identifying the Friedel pair of any reflection. The Friedel pair of a given reflection will appear 180° further at η. The ϕ location of the Friedel pair is dependent on η. When η is close to 90° or 270°, the Friedel pair of the same reflection will diffract 2θ apart. When η is close to 0° or 180°, the

Friedel pair will diffract at more than 4θ apart. The second advantage of the Phi-Eta map is that it helps identify new spots appearing around original spots. If the new close spot does not appear in the Phi-Eta map of its Friedel pair, it can be confirmed as belonging to a neighboring grain.

This point can be further clarified as follows. Let us consider the spot from a grain that appears at η=90° and label it as *hkl* in Figure 4.5. The Friedel pair of this spot will appear at η 180° away. Since these pairs are 4θ apart from each other, the Friedel pair of the reflection will diffract after rotating the sample by 2θ degrees. For the spots diffracting parallel to the rotation axis (η=0° or 180°), the difference in 2θ between the Friedel pairs will be bigger than 2θ. Let's consider a scattering vector, ***A***. By inspecting Figure 4.5, the normalized scattering vector ***A*** in the diffraction cone can be found as:

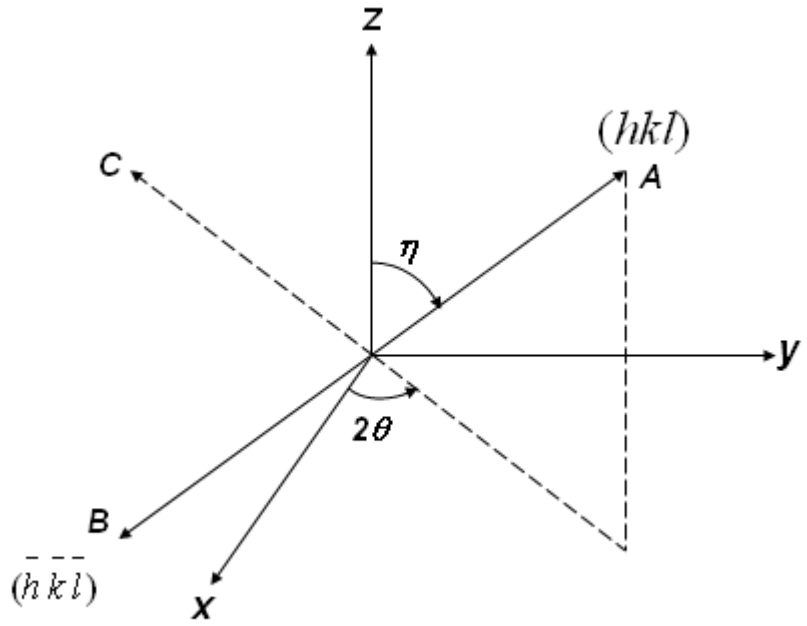

Figure 4. 5. Illustration of a scattering vector *A* and its Friedel pair, *B*. Since it is difficult to distinguish opposite directions with x-rays, the Friedel pair of *A* is mirrored on the –*YZ* plane.

$$\mathbf{A} = \frac{1}{N}\begin{pmatrix} 1 \\ \tan\theta \\ \dfrac{1}{\cos\theta\tan\eta} \end{pmatrix} \qquad (4.10)$$

where θ and η are the diffracting Bragg and azimuth angles and $N = \sqrt{1+\tan^2\theta+\tan^{-2}\eta}$ [Pecharsky, V. K. (2005)]. When the sample is rotated by ϕ, the scattering vector will also be rotated. The rotation of the sample can be expressed as in Eq. 4.2. After the rotation, the new scattering vector **B** will be given by

$$B = \Omega A \qquad (4.11)$$

If the rotation angle between Friedel pairs satisfying the Bragg condition is denoted as ξ, the relation between the Friedel pairs will be as follows:

The angle (ξ) between the two vectors, before and after the rotation can be calculated as:

$$\xi = 2\tan^{-1}\left(\frac{A_y}{A_x}\right)N = 4\theta\sqrt{1+\tan^2 2\theta+\tan^{-2}\eta} \qquad (4.12)$$

It can be easily seen that Friedel pairs diffract within an phi angle of $2\theta\sqrt{1+\tan^2 2\theta+\tan^{-2}\eta}$ from each other. A spot with an η value near the equator will experience the rotation that is equal to the actual rotation ϕ of the sample, while a diffraction spot near the poles (η=0 and π) will experience a smaller effective rotation of ξ.

4.4. Domain Size

According to diffraction theory, there is a correlation between the integrated intensity of a spot and the volume of the domain that generated it [Warren, B. E. (1990)]. The integrated intensities of diffraction spots were found by summing the pixel intensities and subtracting the background of the diffraction image. Appendix 2 develops the relationship between the diffracting volume and the integrated intensity in more detail. It was observed that several spots diffract within a range of ϕ which makes it difficult to find out which diffraction spots are the region of interest. Therefore, Phi-Eta maps were used to calculate the

integrated intensities of the diffraction spots. To convert the integrated intensities of the spots to grain volumes, the summed intensities of the (*002)* Phi-Eta map, I^{p}_{002}, at each electric field were used as an internal calibration. The relationship between the grain volume V_{grain} and the integrated intensity of a specific *hkl* reflection, I^{g}_{hkl} will then be:

$$V_{grain} = \frac{\Delta t_p}{\Delta t_g} \frac{m_{002}\left|F_{002}\right|^2}{\left|F_{hkl}\right|^2} \frac{\Delta\phi|\sin\eta|\sin 2\theta_{hkl}}{4\sin\theta_{002}} \frac{I^{g}_{hkl}}{I^{p}_{002}} V_{gauge} \qquad (4.13)$$

where, *F*, *m*, θ, and Δt refer to structure factor, multiplicity, Bragg angle and the acquisition times, respectively. However, this equation assumes a constant gauge volume during the phi oscillation. This is not true because the sample thickness changes during this oscillation and reaches a maximum at $\phi=\pm 45°$. To derive the transmission ratio of the X-ray beam in each phi value, beam intensity after a thickness of *x* is used:

$$I = I_0 e^{-\mu_l x} = I_0 e^{-(\mu_l/\rho)\rho x} \qquad (4.14)$$

where, I_0 is the incident beam intensity, μ_l is the linear absorption coefficient and $\mu_m = \mu_l/\rho$ is the mass absorption coefficient and ρ is the density. Therefore, the transmission ratio of a sample without rotation is:

$$\frac{I}{I_0} = e^{-\mu_l x} = e^{-(\mu_l/\rho)\rho x} \qquad (4.15)$$

Sample thickness, *x*, changes with the ϕ oscillation and the effective sample thickness can be denoted as x_0. Since $x_0 = x/\cos\theta$, the transmission ratio of the sample with ω oscillation will be:

$$\frac{I}{I_0} = e^{\frac{-\mu_l x}{\cos\omega}} = e^{\frac{-(\mu_l/\rho)\rho x}{\cos\phi}} \qquad (4.16)$$

Figure 4.6 shows the transmission ratio of the $BaTiO_3$ sample as a function of phi oscillation.

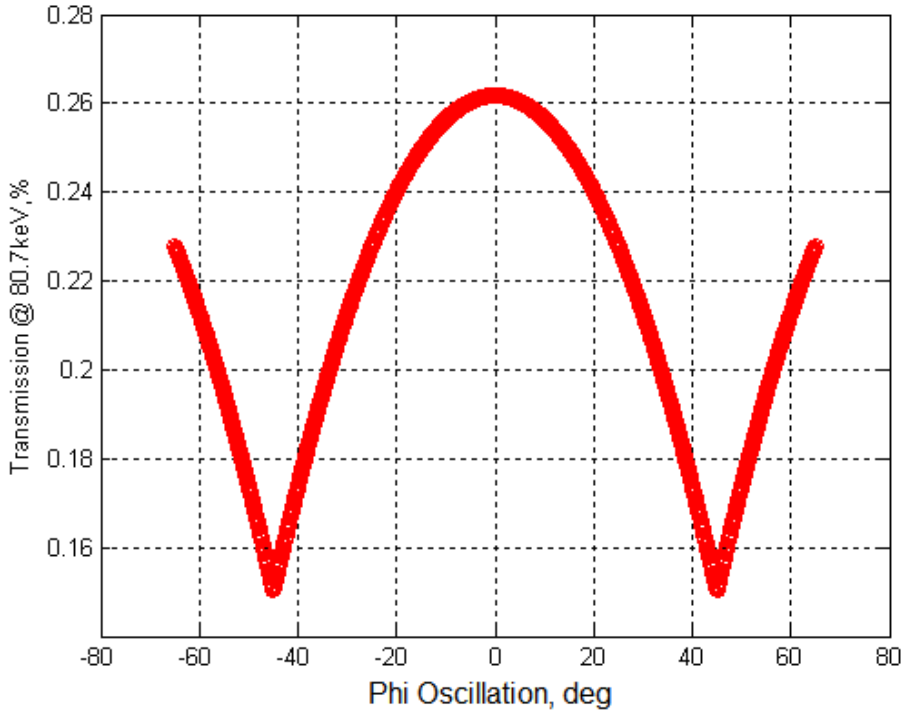

Figure 4.6. X-ray transmission fraction of the $BaTiO_3$ sample during ϕ oscillation.

Because the sample thickness changes with ϕ oscillation, the gauge volume in the equation above needs to be normalized with the phi oscillation. Equation 4.13 then becomes:

$$V_{grain} = \frac{\Delta t_p}{\Delta t_g} \frac{m_{002}|F_{002}|^2}{|F_{hkl}|^2} \frac{\Delta\omega|\sin\eta|\sin 2\theta_{hkl}}{4\sin\theta_{002}} \frac{I^g_{hkl}}{I^p_{002}} \frac{V_{gauge}}{\cos} \qquad (4.17)$$

The geometry of the diffracted domains is not known, but can be approximated by a cube or a sphere. The sphere radius can be found as $R = \sqrt{3V/(4\pi)}$ while the cube edge will be $a = \sqrt[3]{V}$. Since domains are arrangements of several tetragonal unit cells, the cube approximation of the shape of a domain may be a better representation of their shape.

4.5. Polarization Angle

Ferroelectric domains in a polycrystal will tend to orient along the electric field direction above the coercive field. The reorientation of these domains is called “poling” and the poling direction is the *c*-axis of the domains. The angle between the polarization vector of

a domain and the direction of the electric field is called the "polarization angle" and is expected to decrease as higher electric fields are applied. Figure 4.7 shows a schematic of a 3D-XRD experiment geometry. In order to track the orientation of the ferroelectric domains within the polycrystal as a function of electrical load, the polarization angle is calculated as the angle between the electric field in the sample coordinate system (i.e., the [010] direction or TD) and the polarization vector in crystal coordinates (i.e., the [001] direction in crystal coordinates). This angle corresponds to the direction cosine of the *y* sample axis and the *z* crystal direction (which show the electric field direction) and the *c* axis of the crystal. The U_{32} component of the orientation matrix (*U*) then becomes the polarization angle and these angles were tracked as a function of electric field.

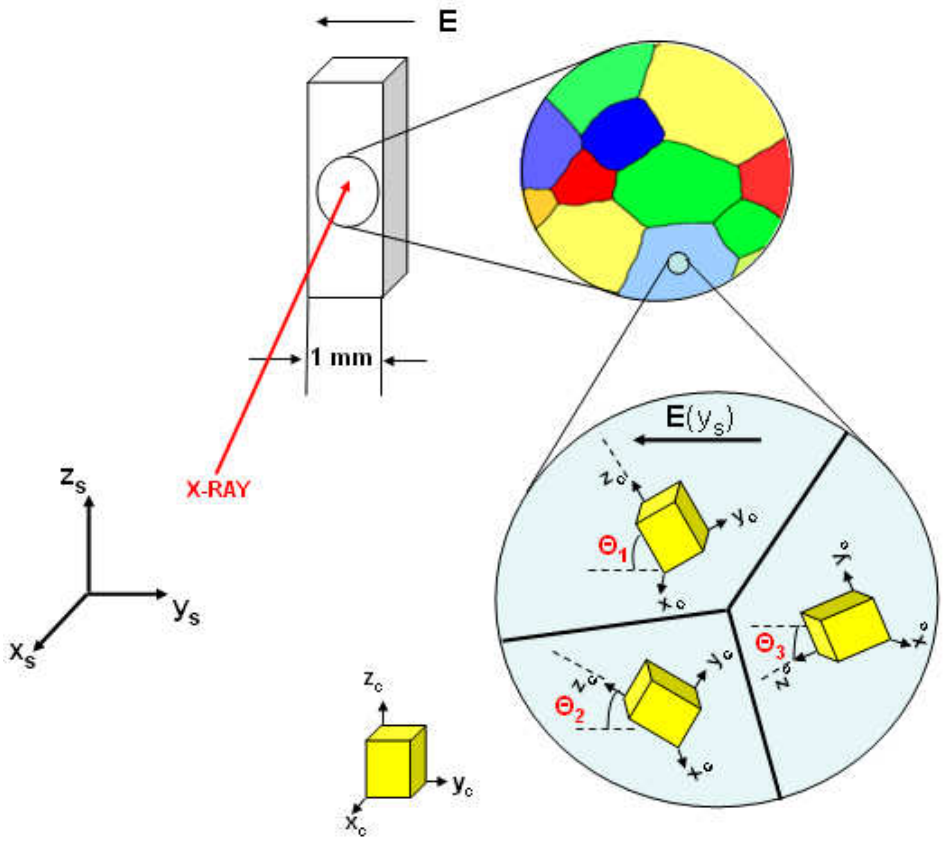

Figure 4.7. Schematic set-up in a 3D-XRD experiment. Each grain consists of ferroelectric domains that are arranged in three dimensions. Each crystallite (or domain) can be represented by a vector in the local coordinate system (x_c, y_c, z_c) and within a fixed sample coordinate system (x_s, y_s, z_s). The polarization angle, θ, defines the angle between the polarization vectors of the domains and the applied electric field direction.

4.6. Elastic Strain

In addition to the change in the orientation of domains, their elastic strain tensors can also be obtained from 3D-XRD data. To gather sufficient statistics, however, it is crucial to measure multiple domains and determine the strain tensor components of each grain and the offset (Δy, Δz) of its center of mass with respect to the phi axis [Margulies L. (2004)].

The relative shift in each spot with respect to the rotation ϕ axis can be calculated either from the detector images or the Phi-Eta map. While the spots from the detector images give a better fit, the Phi-Eta map is essential in the study of the orientation relationships of the neighboring spots. As a routine, the detector location of a spot from a domain was extracted from *Graindex* results at low voltage and the relative change of this spot as a function of electric field was calculated with 2D Gaussian fitting. If the location of the spot can be expressed as a function of *y* and *z* coordinates, the 2D Gaussian function of this spot is given by [Tamura, N. (2007)]:

$$f(y,z) = b + Ae^{-\frac{1}{2}\left(\left(\frac{(y-y_0)\sin\theta+(z-z_0)\cos\theta}{\sigma_y}\right)^2+\left(\frac{(y-y_0)\cos\theta-(z-z_0)\sin\theta}{\sigma_z}\right)^2\right)} \quad (4.18)$$

where b is the background value of the peak, the coefficient A is the peak value, x_o, y_o are the center of the peak and σ_x, σ_y are the full width half maximum (FWHM) of the spot. The 2D peak fitting can also be done with different profile functions and the corresponding 2D Lorentzian and Pearson functions are the following:

2D Lorentzian: $$f(y,z) = b + \frac{A}{\left(\frac{(y-y_0)\sin\theta+(z-z_0)\cos\theta}{\sigma_y}\right)^2+\left(\frac{(y-y_0)\cos\theta-(z-z_0)\sin\theta}{\sigma_z}\right)^2}$$

(4.19)

2D Pearson: $$f(y,z) = b + \frac{A}{(y_p^2 + z_p^2 + 1)^N} \quad (4.20)$$

$$y_p = 2\left(\frac{(y-y_0)\cos\theta-(z-z_0)\sin\theta}{\sigma_z}\right)\sqrt{2^{(1/N)}-1} \quad (4.21)$$

$$z_p = 2(\frac{(y-y_0)\sin\theta + (z-z_0)\cos\theta}{\sigma_y})\sqrt{2^{(1/N)}-1} \qquad (4.22)$$

where, N is the Pearson index.

After the initial guess for the peak location (y_o, z_o), FWHM of the peak (σ_y, σ_z), background value of the peak (b), it is possible to fit the 2D peak by using least square fitting. It is also possible to find the integrated intensity of the peak by summing the fitted function.

As with diffraction studies in general, 3D-XRD lattice strain characterization is based on measurements of relative changes in the d-spacing of selected lattice planes. For each diffraction spot, the lattice strain ε is found by measuring the shift in Bragg angle $\Delta 2\theta$. A specific measurement ε_i with a corresponding diffraction spot positioned at angles (ϕ, $2\theta_i$, η_i) and a scattering vector defined by the direction cosines l_i, m_i, n_i, is related to the components of the strain tensor ε_{hkl} by

$$\varepsilon_i = (l_i m_i n_i)\begin{bmatrix} \varepsilon_{11} & \varepsilon_{13} & \varepsilon_{13} \\ \varepsilon_{13} & \varepsilon_{13} & \varepsilon_{13} \\ \varepsilon_{13} & \varepsilon_{13} & \varepsilon_{13} \end{bmatrix}\begin{pmatrix} l_i \\ m_i \\ n_i \end{pmatrix} - [\cos(\phi_i) + \frac{\sin(\phi_i)\sin(\eta_i)}{\tan(\theta_i)}]\frac{\Delta x}{L} - [\sin(\phi_i) + \frac{\cos(\phi_i)\sin(\eta_i)}{\tan(\theta_i)}]\frac{\Delta y}{L}$$

(4.23)

where, Δx and Δy are the offsets in the sample system from the center of rotation and L is the sample-to-detector distance [Margulies, L. (2004)].

CHAPTER 5. MICRODIFFRACTION

The scanning X-ray microdiffraction (μSXRD) technique is based on back-scattering Laue diffraction. The technique and its data analysis procedure, together with its coordinate system conventions will be explained in this chapter. μSXRD allows the extraction of deviatoric lattice strain components; a process of obtaining two-dimensional strain maps will thus be described. All μSXRD experiments were performed at the X-ray microdiffraction end-station (first called, Beamline 7.3.3, recently it moved to Beamline 12.3.2) at the Advanced Light Source (ALS), Lawrence Berkeley National Laboratory. Further experimental details will be presented at Section 6.2.

5.1. The Scanning X-ray Microdiffraction Technique

A polychromatic ("white") X-ray beam offers a unique opportunity to sample a large fraction of the reciprocal space due to its ability to diffract from many lattice planes simultaneously. Figure 5.1 illustrates this process schematically.

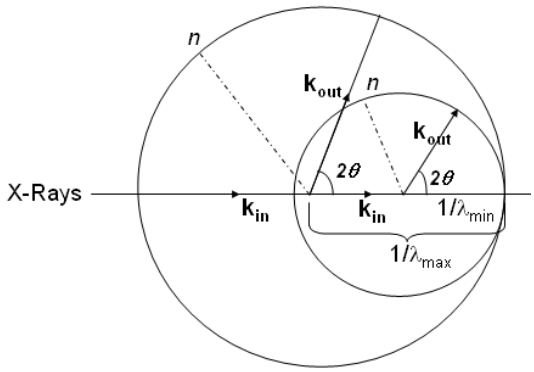

Figure 5.1. Diffraction from a polychromatic ("white") X-ray beam. The X-rays with the highest energy (i.e., lowest wavelength, λ) will yield the high end of the Ewald sphere, while the low energy X-rays will form the low end of the Ewald sphere.

The fundamental principles of the μSXRD technique are described elsewhere [Chung, J-S. (1999)]. Here, only a brief summary will be presented for completeness. By microfocusing the X-ray beam to a spot size of about 0.5-1 μm, the technique offers a unique opportunity to study local microstructure. The use of a white beam allows a fast scan of local

crystal orientations (i.e., local micro-texture) and three-dimensional strain fields (i.e., the deviatoric lattice strain tensor), all this without rotating the sample and/or the detector as is done on conventional (monochromatic) X-ray instruments. The analysis and interpretation of the multiple Laue patterns collected at each location requires sophisticated software: *XMAS* (X-Ray Micro Analysis Software) was developed for this purpose and has been successfully employed [Tamura, N. (2003)]. The relatively low X-ray energy of μSXRD (about 10-25 keV) compared to that of the 3D-XRD technique (>60 keV) limits the former to near surface regions, esp. with heavy elements

5.1.1. Coordinate Transformation

The μSXRD technique uses several coordinate systems that are similar to those employed in 3D-XRD. Figure 5.2 shows a typical μSXRD setup at ALS. The diffraction plane (*hkl*) is described in the laboratory coordinate system in real space and transformed to reciprocal space by the reciprocal lattice matrix (*B*):

$$B = \begin{pmatrix} a_1 & a_2 \cos\gamma & a_3 \cos\beta \\ 0 & a_2 \sin\gamma & -a_3 \sin\beta \cos\alpha^* \\ 0 & 0 & 1/b_3 \end{pmatrix} \qquad (5.1)$$

where, $a_{1,2,3}$ and $b_{1,2,3}$ and are the real and reciprocal lattice parameters while (α, ß, γ) and (α^*, ß*, γ^*) are the real and reciprocal lattice angles, respectively. The orientation of each grain can be expressed by a matrix transformation from reciprocal lattice to the sample coordinate system and can be expressed with the orientation matrix (*g*):

$$g = \begin{pmatrix} g_{11} & g_{12} & g_{13} \\ g_{21} & g_{22} & g_{23} \\ g_{31} & g_{32} & g_{33} \end{pmatrix} \qquad (5.2)$$

where, each component is the direction cosine between the reciprocal lattice vector and a vector in the sample coordinate system.

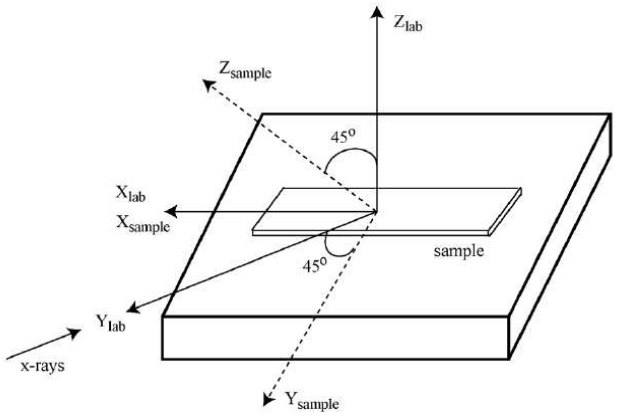

Figure 5.2. Laboratory and sample coordinate systems of the μSXRD technique as used at ALS [Valek, B. C. (2003)].

With the aid of the transformations described above, any diffraction spot on the detector can be linked with the normal [*hkl*] vector of a grain as follows:

$$n_{hkl} = \frac{\begin{bmatrix} 1 & 0 & 0 \\ 0 & \cos(45°) & -\sin(45°) \\ 0 & \sin(45°) & \cos(45°) \end{bmatrix} \mathbf{gB} \begin{pmatrix} h \\ k \\ l \end{pmatrix}}{\left| \mathbf{gB} \begin{pmatrix} h \\ k \\ l \end{pmatrix} \right|} \qquad (5.3)$$

Here, the first matrix transforms from the sample coordinate system to the laboratory coordinate system (the sample is mounted at a 45° angle with respect to the incoming X-ray beam). Additional diffraction angles are defined in Figure 5.3.

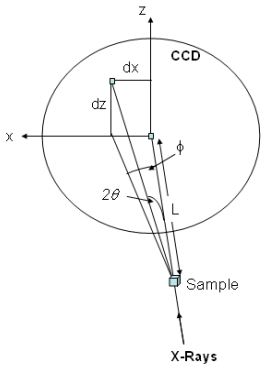

Figure 5.3. The coordinate and angle notations used at ALS

$$2\theta = \cos^{-1}(n_z) \text{ and } \Phi = \tan^{-1}(n_x / n_y) \qquad (5.4)$$

The location of a reflection on the image plate will then be:

$$dx = dx_0 + L \cdot \tan(90 - 2\theta) \cdot \sin(\Phi) / px \qquad (5.5)$$

$$dz = dz_0 + L \cdot \tan(90 - 2\theta) \cdot \cos(\Phi) / pz \qquad (5.6)$$

where, dx_0 and dz_0 define the center of the image, L is the sample-to-detector distance, px and pz is the pixel size of the detector horizontal and vertical directions, respectively. Figure 5.4 shows a simulated Laue pattern for $BaTiO_3$ using the X-ray energy range of 5-14 keV.

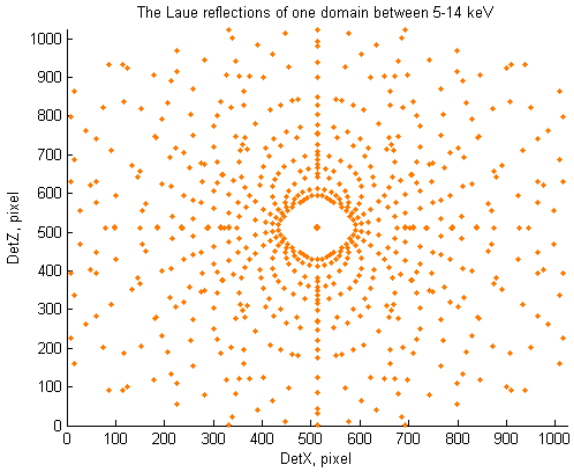

Figure 5.4. A simulated Laue diffraction pattern for a $BaTiO_3$ domain at X-ray energies between 5 and 14 keV (the former energy range of the ALS microdiffraction beamline 7.3.3).

5.1.2. Data Analysis

The X-ray microdiffraction end-station at the ALS is capable of delivering a focused X-ray white beam with a spot size slightly less than 1 μm using a pair of elliptically bent mirrors in the Kirkpatrick-Baez configuration. Diffraction data were collected in reflection mode using a large-area Bruker SMART 6000 CCD camera mounted on a vertical slide. The sample surface was set at 45° relative to the incoming beam. Figure 5.5 shows a typical experimental setup and a diffraction pattern.

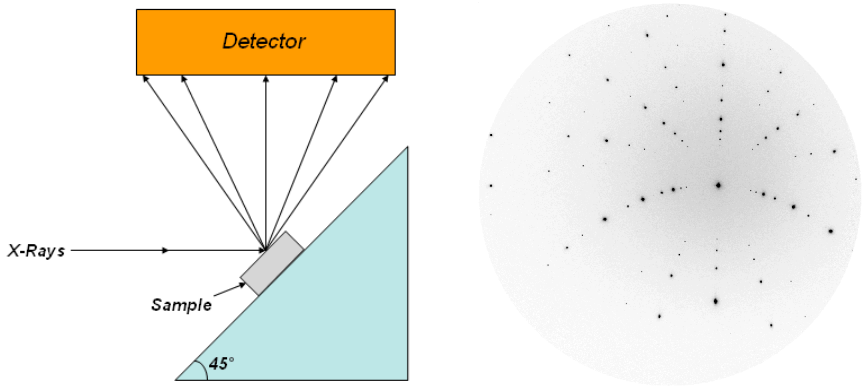

(a) (b)

Figure 5.5 (a) A typical schematic setup for the µSXRD experiments at ALS. (b) A typical diffraction pattern from single crystal $BaTiO_3$.

The diffraction patterns were analyzed by the custom software developed at the ALS (*XMAS*: X-ray Microdiffraction Analysis Software). The data analysis can be divided into three parts. First, the reflection positions in the patterns are determined within sub-pixel resolution by fitting their two-dimensional peak profiles with (two-dimensional) profile functions such as Gaussian, Lorentzian or Pearson VII. All the peaks in the diffraction pattern are sorted according to their integrated intensity values from the most intense to the weakest. After taking into consideration the first set of the strongest reflections, a virtual grain with a close orientation to this set of reflections is simulated using the measured peak positions and known lattice parameters. Next, additional matching reflections are identified until at least one spot matches with a spot of the simulated grain. If there is no match for the simulated spot, the search continues with the remaining reflections from the strongest to weakest. For the remaining unindexed reflections, new virtual grains are simulated and the search continues until a match is found. At the end of each search, the orientation matrix and the corresponding indexed reflections are saved if the simulated grain is authenticated as a real grain. Using the *sequential analysis* routine available in *XMAS*, additional (sequential) diffraction patterns can be analyzed automatically and the output of a given surface scan can be reported visually by using various subroutines available in *XMAS*.

5.1.3. Elastic Strain

To specify a position in sample coordinates [Chung, J-S. (1999)], one can use a vector either in crystal coordinates (v_a) or in sample coordinates (v_u). The relation between these vectors can be formulated as:

$$v_u = Av_a \qquad A = \begin{pmatrix} a_1 & a_2\cos\gamma & a_3\cos\beta \\ 0 & a_2\sin\gamma & -a_3\sin\beta\cos\alpha^* \\ 0 & 0 & 1/b_3 \end{pmatrix} \qquad (5.7)$$

where, $a_{1,2,3}$ and $b_{1,2,3}$ and are the real and reciprocal lattice parameters, respectively, and (α, ß, γ) and (α^*, ß*, γ^*) are the real and reciprocal lattice angles, respectively. Calculated refined lattice parameters (A_{meas}) for each grain and reference lattice parameters (A_o) form a matrix. Transformation of these vectors is possible with

$$A_{meas} = TA_0 \qquad (5.8)$$

where, T is the transformation matrix and finally deviatoric lattice strain can be found by:

$$\varepsilon'_{ij} = \frac{(T_{ij} + T_{ji})}{2} - I_{ij} \qquad (5.9)$$

where, I_{ij} is the identity matrix. The complete strain tensor is simply the sum of the deviatoric strain tensor and dilatational tensor ($\varepsilon_{ij} = \varepsilon'_{ij} + \Delta$) where $\Delta = \delta\mathbf{I}_{ij}$ and δ is the dilatational strain. The complete strain tensor can be measured with this technique by knowing the absolute lattice parameters of a single Laue reflection but the XMAS software currently calculates the deviatoric strain components. Since elastic strains play an important role in ferroelectric domain microstructures, finding the deviatoric strain components for each domain would be enough to study the ferroelectric domain switching in mesoscale.

5.1.4. Grain Map

The µSXRD technique, by not requiring a rotation of the sample/detector and by using a small beam size (below a typical grain size) enables detailed two-dimensional scans of the sample surface. Following data analysis that calculates, among other parameters, the orientation matrix (g) of a grain, one can create a 2-D grain map. The choice of creating the

grain map is arbitrary. For the ferroelectric domains, the angle between the direction of the polarization vector of the crystallites and global axes can be expressed as:

$$\theta_l = \cos^{-1}\left(\frac{g_{3l}}{\sqrt{g_{31}^2 + g_{32}^2 + g_{33}^2}}\right) \qquad l = 1, 2, 3 \tag{5.10}$$

where, l stands for x, y and z axes in global coordinates. This map will help to interpret the distribution of the polarization vectors along global coordinates. Grain map is very useful when mapping the distribution of the crystal properties with respect to the global coordinates.

5.1.5. Finding Precise Lattice Parameters

While the μSXRD technique is superb in obtaining the deviatoric lattice strain tensor, its use of a polychromatic X-ray beam makes it impossible to estimate *absolute* lattice parameters. However, there is a way to overcome this disadvantage. After indexing a diffraction pattern obtained from a polychromatic beam, one can perform an energy scan around one of the spots. This determines the absolute *d*-spacing of that spot, and by extension, the absolute lattice parameter. As a result, one can measure the complete three-dimensional lattice strain tensor of a sub-μm region using μSXRD.

5.1.6. Grain Depth

As mentioned before, μSXRD can routinely provide a list of grains that diffract from a specific sample location. In order to study the three-dimensional arrangement of these grains, a triangulation technique was developed [Larson, B. C. *et al.* (2000)]. Here, the diffraction patterns are collected from several sample-to-detector distances and the origins of the diffracted grains are traced back (Figure 5.6). While time consuming, this method offers unprecedented information about the geometrical arrangement of grains in real space. A detailed description of the triangulation technique can be found in Larson, B.C. *et al*'s article (2000).

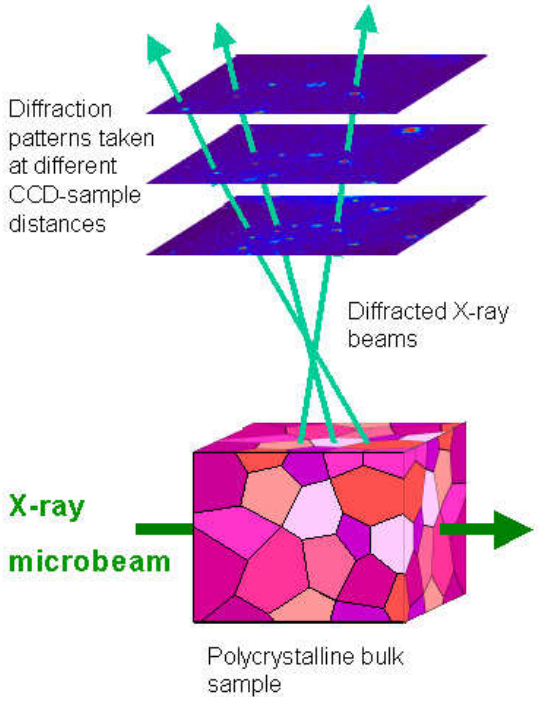

Figure 5.6. Schematic of the triangulation technique [Larson, B. C. *et al.* (2000)]

CHAPTER 6. RESULTS and DISCUSSION

The present study employed two complementary methods to investigate the mesoscale behavior of ferroelectrics:

- *3D-XRD technique* to track domains in multiple grains of a polycrystalline ferroelectric and to investigate their evolution as a function of electric field.
- *Scanning X-Ray Microdiffraction technique* to zoom on surface domains and to study their evolution with temperature.

6.1. 3D-XRD Experiments on $BaTiO_3$

$BaTiO_3$ ceramics were processed from a single batch of previously prepared stoichiometric $BaTiO_3$ powder (99.9% pure, with Ba/Ti ratio=1.00, from Ferro Corp., Transelco Division) to minimize the effects of stoichiometry variations between batches [Bryne, T. A. (2004)]. The initial powders were homogeneously mixed via vibratory milling for 5 h in zirconia media in ethanol. Approximately 4 wt% binder was added to the powder. Following binder burn-out at 500°C for 2 h, the well-mixed powder was calcined at 1300 °C for 2 h in an alumina crucible covered with zirconia powder. The final composition of the sample had approximately 95% of the theoretical density. For grain size measurements, samples were thermally etched at 1300°C for 2 h to reveal the grain structure. The grain size was calculated around 20 µm. The SEM micrograph of a typical microstructure of the $BaTiO_3$ ceramic is shown in Figure 6.1.

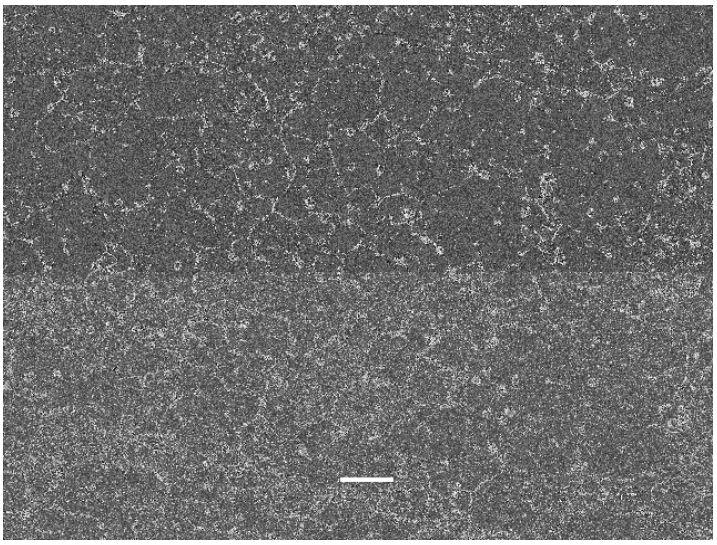

Figure 6.1. SEM image of $BaTiO_3$ sample used in 3D-XRD experiment. The grain size is typically around 20 µm.

Bulk polycrystalline $BaTiO_3$ samples were sectioned with a diamond saw into 1.2x1.2x5 mm dimensions to use in 3D-XRD experiments. After sectioning, the surfaces of the samples were polished with abrasive and finally with fine sandpaper until the dimensions would be 1x1x5 mm. Both 1x1 mm sides were sputtered with gold for 5 minutes and thin wires were attached using conductive epoxy. There are several advantages of selecting such sample dimensions. First, the X-rays can easily penetrate through the sample at high energy. Second, the applied electric field can be more than coercive field which leads to significant domain switching.

The polarization versus electric field hysteresis loops of the $BaTiO_3$ ceramics were measured with a RT66A standard ferroelectric test system (Radiant Technologies). Figure 6.2 shows a typical set of hysteresis loops. The remnant, spontaneous and saturation polarization of the sample were measured as 5.3, 8.5 and 22.2 $\mu C/cm^2$, respectively. The nominal coercive field was found to be 5.16 kV/cm.

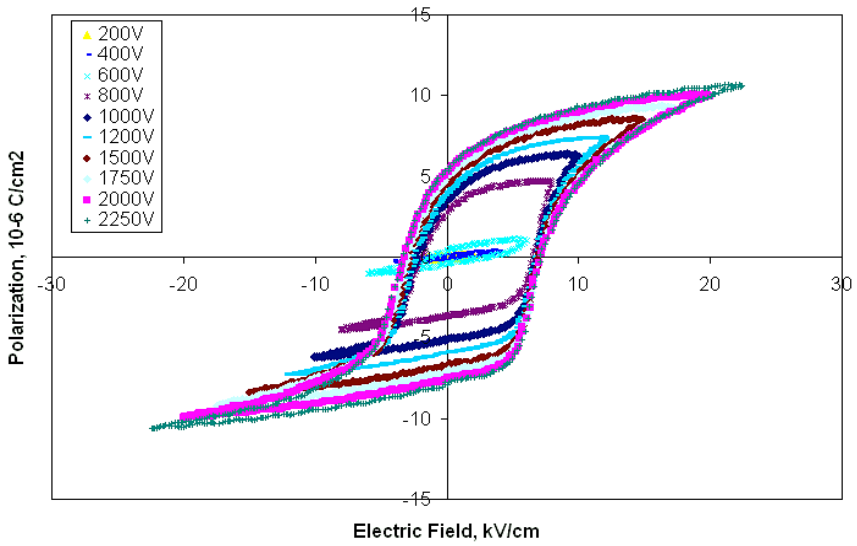

Figure 6.2. Polarization (*P*) vs. electric field (*E*) hysteresis loops of the $BaTiO_3$ sample used in 3D-XRD experiments.

3D-XRD experiments of $BaTiO_3$ were performed at beamline 1-ID-C of the Advanced Photon Source (APS), Argonne National Laboratory, Argonne, IL. This beamline not only provides dedicated high energy focusing optics but is specialized for 3D-XRD data acquisition and analysis.

Figure 6.3 shows a schematic setup of the $BaTiO_3$ experiments. High energy x-rays (80.72 keV, with wavelength $\lambda \sim 0.1535$ Å) in transmission mode were focused to a 30x30 μm^2 spot size. Since the grain size was estimated to be around 20 µm, this spot size was enough to illuminate roughly 100 grains. The samples were oscillated perpendicular to the beam with 0.2° ϕ steps up to ±65°; repeated at each applied electric field. The samples were not intentionally poled before the experiment but a high electric field was sometimes applied briefly to check the cable connections. The electric field was applied in-situ with a Trek 610D HV amplifier reaching up to ±20 kV/cm in 0.125 kV/cm steps and was perpendicular to the incoming beam (along the *y*-axis in Figure 6.3). The maximum applied electric field was high enough to trigger domain switching as the nominal coercive field of the material was previously measured as 5.16 kV/cm (Figure 6.2). The sample was aligned with the other 1 mm surfaces normal to the beam direction. Thus, the direction of the electric field was perpendicular to the X-ray beam (the *y*-axis in Figure 6.3). The rotation axis of the sample was carefully aligned by checking the same spot after rotating the sample for 180° along ω.

The sample-to-detector distance was adjusted as 952.70 mm. This distance enhanced the resolution of the diffraction spots on the Mar CCD detector (2048x2048 pixel size, MarUSA, Inc.) by increasing the resolutions of the variants of {001}, {011}, {111} and {002} diffraction planes. The lattice parameters of the $BaTiO_3$ were calculated as a=0.4000 nm and c=0.40314 nm.

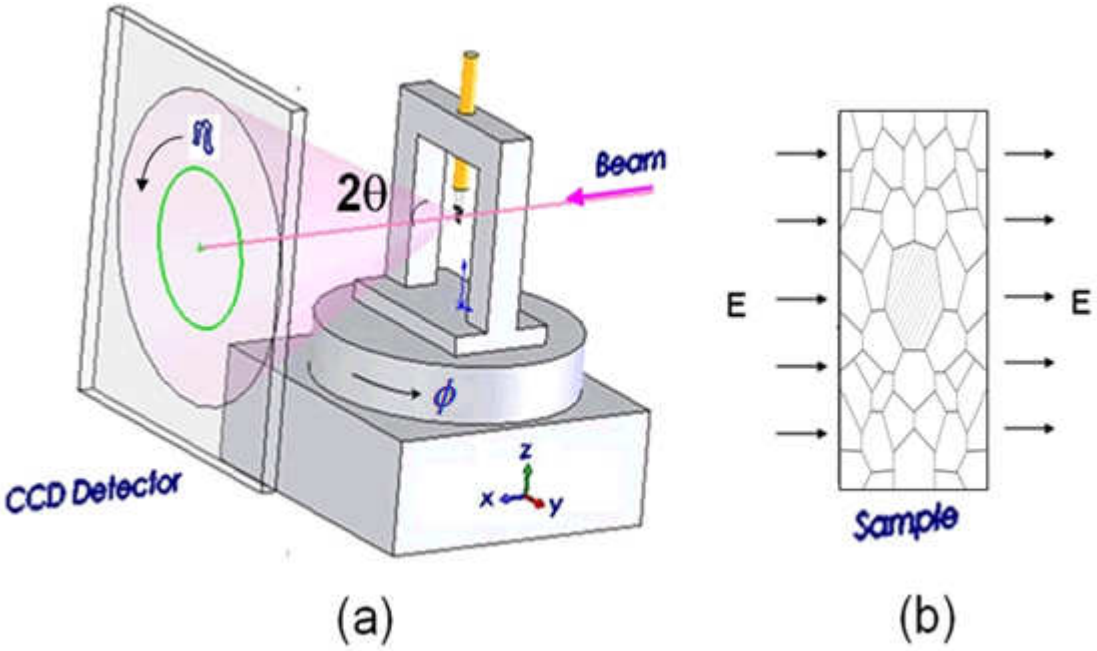

Figure 6.3. (a) Schematic 3D-XRD setup used at beamline 1-ID-C, APS. (b) A view along the X-ray beam (along the *x*-axis) at ϕ = 0°. The electric field direction is parallel to the *y*-axis which is perpendicular to the rotation axis (*z*)

6.1.1. Macroscopic Response to Electric Field

To make sure the sample experienced domain switching, the macroscopic (polycrystalline) response of ferroelectric domains within the polycrystalline $BaTiO_3$ was obtained by integrating diffraction images within ±10° of ϕ (where, ϕ=0° is perpendicular to the beam) and parallel to the electric field (η=90°±5°) using the *Fit2D.v12.077* software [Hammersley, A. P. (1997)]. Figure 6.4 also displays the results in terms of the MRD value (multiples of random distribution relative to an unpoled sample) obtained from this equation:

$$MRD = \frac{3I_{002}}{(I_{002} + 2I_{200})} \qquad (6.1)$$

The MRD is a better measure of texture evolution due to domain re-orientation and should be 1.0 for a random polycrystal. The electric field led to an increase of the (002) peak intensity due to a small portion of the domain alignment along the field direction. In Figure 6.1.4, while the initial state of the specimen is not random (MRD ~ 0.78), the applied field leads to slight domain re-alignment (MRD ~ 0.87 at 20 kV/cm). The most important contribution of this weak effect of the electric field may be the residual texture from the pre-poling the sample while checking the wire contacts.

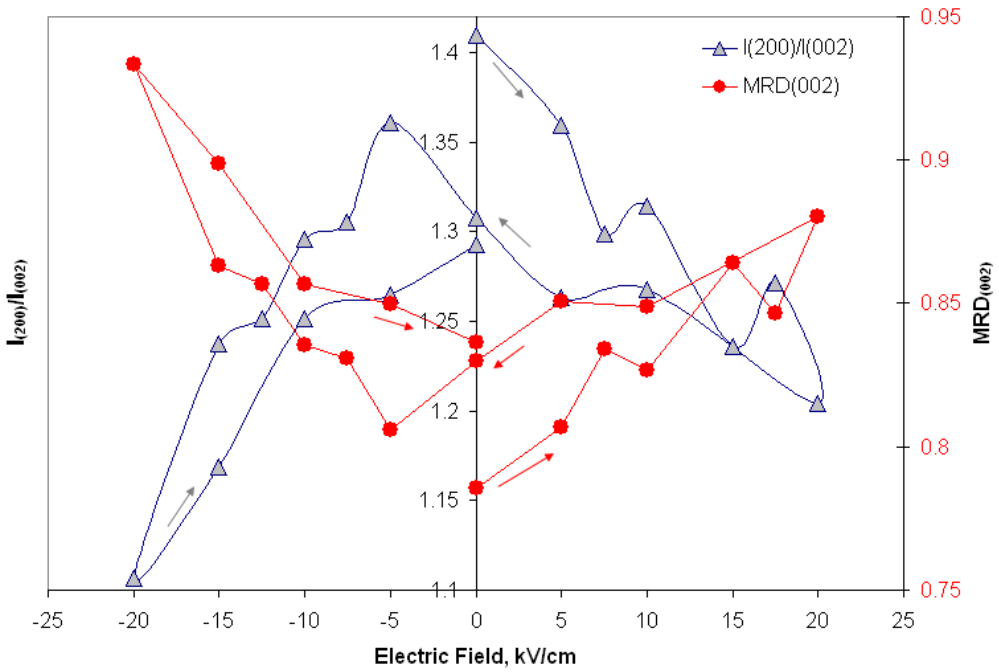

Figure 6.4. Variation of the integrated intensity ratio (I_{200}/I_{002}) and MRD_{002} as a function of electrical loading. Diffraction images within ±10° of the ϕ = 0° position and along the electric field were summed to obtain these macroscopic data. The arrows indicate the progression of the electrical loading.

6.1.2. Graindex Analysis

The diffraction patterns were analyzed using the *Graindex* software [Lauridsen, E. M. (2001)]. Table 6.1 shows the *Graindex* parameters employed. Section 4.2.1 explained all of these. To summarize, $2\theta_{max}$ is the maximum 2θ angle of the diffraction pattern, *Cloudfit Tolerance* defines the tolerance of a spot to be classified as the same spot at different sample detector distances, *G-vector Tolerance* sets the range of 2θ for each *hkl* family, *Eta*

Tolerance defines the eta limit during the image analysis, *Completeness* defines the ratio of number of theoretical reflections to identified reflections, *Uniqueness* requires that a set of matching *hkl*'s does not belong to another grain. *Angle Step*, *Delta Omega* and *Delta Eta* define the grid size of the Eulerian space when the *Graindigger* routine looks for a grain.

Table 6.1. Graindex parameters used in the $BaTiO_3$ 3D-XRD analysis

Parameters		***Value***
Rotation	ϕ_{start}	-64.9°
	ϕ_{end}	64.9°
	ϕ_{step}	0.2°
Experiment Parameters	Energy	80.57 keV
	Sample-to-Detector distance	952.7 mm
	Center Point of Image, Y_0	1028.7 pixel
	Center Point of Image, Z_0	1028.5 pixel
	Detector size	2048x2048
	Pixel size	0.08057 µm
Crystallography	a - *Lattice parameter (a)*	0.4000 nm
	b - *Lattice parameter (b)*	0.4000 nm
	c - *Lattice parameter (c)*	0.40314 nm
	α - *Unit cell angle (α)*	90°
	$ß$ - *Unit cell angle (ß)*	90°
	γ - *Unit cell angle (γ)*	90°
	Space Group - *The space group of the grain belongs to*	99 (P4mm)
	Number of Atoms in unit cell	5
	Atom Number of 1st Atom (Ba)	56
	Atom position (x,y,z)	0, 0, 1
	Atom Number of 2nd Atom (Ti)	22
	Atom position (x,y,z)	0.5, 0.5, 0.5
	Atom Number of 3rd Atom (O)	8
	Atom position (x,y,z)	0.5, 0.5, 0
	$2\theta_{max}$ - *Max. 2θ angle of the diffraction patterns*	4.7°
Ray Tracing	Cloudfit Tolerance	0.003
	G-vector Tolerance - *Range of allowable 2θ for each {hkl}*	0.003
	Eta Tolerance	0.2°
Graindigger	Completeness	0.7
	Uniqueness	0.3
	AngleStep - *The steps of the 1st Euler angle (φ_1),°*	0.2°
	Delta Eta - *The steps of the 2nd Euler angle (ϕ),°*	0.2°
	Delta Omega - *The steps of the 3rd Euler angle (φ_2),°*	0.2°

Table 6.2 shows the number of the domains found by Graindex at each applied electric field. *Graindex* compares the location of each spot in the diffraction pattern to those in the simulated pattern, and when sufficient overlap is found, it authenticates a domain (see Section 4.2 for further details). Typically, a discrepancy of about 0.2° was seen between measured and calculated ϕ and η locations of spots.

Table 6.2. Number of the orientations found by Graindex at each applied electric field.

Voltage, *kV/cm*	**2**	**3**	**5**	**7.5**	**10**	**12.5**	**15**	**17.5**	**20**	**10**	**5**	**0**
Number of Domains	34	28	36	36	34	36	35	40	37	36	37	33
Voltage, *kV/cm*	**-2**	**-3**	**-4**	**-5**	**-7.5**	**-10**	**-12.5**	**-15**	**-20**	**-10**	**-5**	**0**
Number of Domains	37	37	38	38	37	39	37	40	37	70	78	67

6.1.3. Domain Characterization

At this stage, it is important to note the fact that what *Graindex* identifies as a "domain" is simply a crystallite with a distinct orientation matrix. To determine special orientation relationships between any subset of these "domains" – as would be expected from the tetragonal structure of $BaTiO_3$ – the misorientation angles of the domains were compared. As was explained in Section 3.4, misorientation is the smallest rotation angle leading from one orientation to another [Morawiec, A. (1995)]. If we denote the orientation matrices of two domains as g_A and g_B, the rotation matrix that transforms *A* into *B* will be given by Δg:

$$g_B = \Delta g \cdot g_A \qquad \Delta g = g_B (g_A)^{-1} \tag{6.2}$$

The rotation angle and axis of this rotation will then be:

$$\cos\psi = \frac{[(\sum_{i=1}^{3} \Delta g_{ii}) - 1]}{2} \tag{6.3}$$

$$< \hat{n}_1, \hat{n}_2, \hat{n}_3 > = < (\Delta g_{32} - \Delta g_{23}), (\Delta g_{13} - \Delta g_{31}), (\Delta g_{21} - \Delta g_{12}) > \tag{6.4}$$

While the misorientation is described as the minimum rotation angle from one orientation to another, the orientation can also be described by finding a minimum rotation angle with respect to an orthogonal reference domain. If the same procedure described above

is repeated by taking an orthogonal reference domain, one obtains the orientation of the given domain. Table 6.3 lists the orientation of the domains found by Graindex at 2kV/cm together with their mutual misorientations. The orientations with respect to an orthogonal reference domain is shown as *angle-axis*, the misorientations of the domains of the domains are shown as *misorientation angle-axis* with the given domain.

Table 6.3. The list of orientation relationships between the domains found at 2 kV/cm

Domain*	Orientation Matrix	Angle Axis Misor. Angle Axis	Euler Angles ($\varphi_1 \phi \varphi_2$),°	Polar. Angle, °	Completeness	Chi-Square
33[a]	0.899 -0.429 -0.086 0.032 0.260 -0.965 0.437 0.865 0.247	78.28° <0.93 -0.27 0.24> 89.66° <1 0 0>	354.9 75.7 26.8	74.8	1	55.57
27[a]	0.898 0.084 -0.431 0.031 0.967 0.254 0.438 -0.242 0.866	30.06° <-0.5 -0.87 -0.05>	239.5 30 118.9	75.3	0.72	73.21
11[a]	0.430 0.092 0.898 -0.260 0.965 0.025 -0.865 -0.244 0.439	65.12° <-0.15 0.97 -0.2> 89.98° <0 -1 0>	91.6 63.9 254.2	88.6	0.83	29.29
1[b]	0.912 0.401 0.084 -0.189 0.595 -0.781 -0.363 0.697 0.618	55.76° <0.89 0.27 -0.36> 89.56° <1 0 0>	6.1 51.8 332.5	51.4	0.73	10.78
17[b]	0.911 -0.083 0.404 -0.189 0.7863 0.588 -0.366 -0.612 0.701	45.66° <-0.84 0.54 -0.07>	145.5 45.5 210.9	54	1	79.33
28[b]	0.397 -0.089 -0.913 0.594 0.784 0.182 0.699 -0.615 0.364	74.18° <-0.41 -0.84 0.36> 89.64° <0 1 0>	258.7 68.6 131.3	79.5	0.86	132.88
2[c]	0.949 -0.224 0.220 0.314 0.665 -0.678 0.006 0.713 0.701	48.88° <0.92 0.14 0.36> 89.4° <1 0 0>	18.0 45.5 0.44	42.7	0.7	84.39
14[c]	0.221 -0.211 0.951 -0.663 0.684 0.306 -0.716 -0.698 0.011	92.4° <-0.5 0.83 -0.23>	107.8 89.3 225.7	72.2	0.83	56.36
3[d]	0.318 -0.368 -0.874 0.232 0.924 -0.305 0.919 -0.106 0.379	71.94° <0.10 -0.94 0.32>	289.2 67.7 96.5	17.7	1	160.28
15[d]	0.873 -0.370 0.318 0.310 0.924 0.225 -0.378 -0.098 0.921	30.84° <-0.32 0.68 0.66> 89.9° <0 1 0>	125.3 22.9 255.4	77	0.94	68.72
13[e]	0.370 0.052 0.928 -0.743 0.615 0.262 -0.557 -0.786 0.266	82.76° <-0.53 0.75 -0.40>	105.8 74.57 15.3	74.8	0.86	115.44
34[e]	0.924 -0.378 -0.049 0.272 0.745 -0.609 0.267 0.549 0.792	43.08° <0.85 -0.23 0.48> 89.89° <1 0 0>	355.4 37.7 25.94	37.5	0.93	80.42

* The domains with the same superscript are variants of each other.

Table 6.3 shows that some domains are variants of each other since they transform into another by rotating around {100} or {010} planes by about 90°. For example, domains with *33* and *11* id numbers are found to be domain variants by rotation of domain 27 with

89.66° <1 0 0> and 89.98° <0 -1 0> rotation angle and axis respectively. This is the exact relationship to be expected from 90° domains in a tetragonal structure. These results demonstrate the power of the 3D-XRD technique to identify and track ferroelectric domains as well as their variants in situ. This is the first step towards quantifying the mesoscale constitutive response of ferroelectrics.

6.1.4. Domain Tracking

The domain tracking capability of 3D-XRD is illustrated in Figure 6.5: the progression of domains with electric field on the {001} pole figure. The numbering of domains at each electric field is exclusive, i.e., domains with the same numbers at two different voltage values are not necessarily the same domains. While there are no clear and drastic changes, some clustering is observed at high voltages along the field direction (the *Y*-axis of the pole figure). The results shows that very little 90° switching occurred like since the sample was pre-poled leading to a built-in texture.

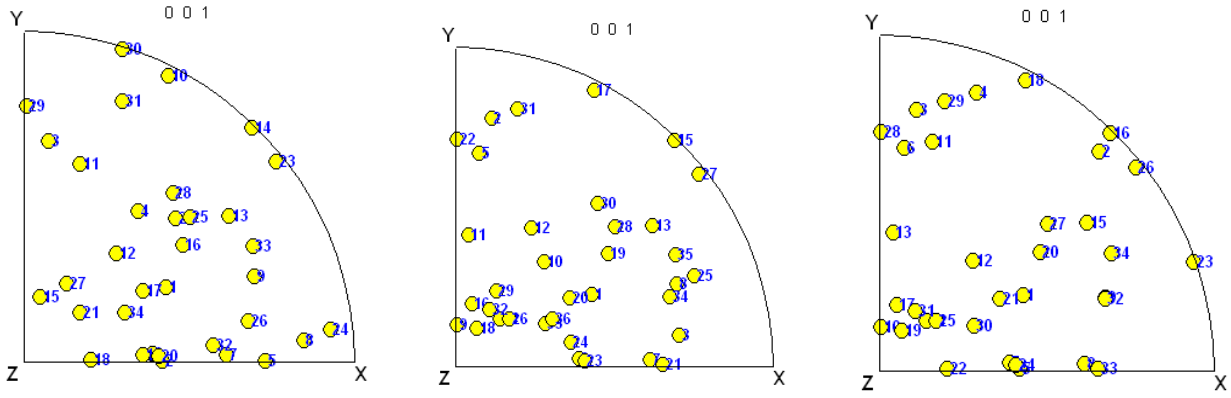

2 kV/cm 5 kV/cm 10 kV/cm

Figure 6.5. (Continued)

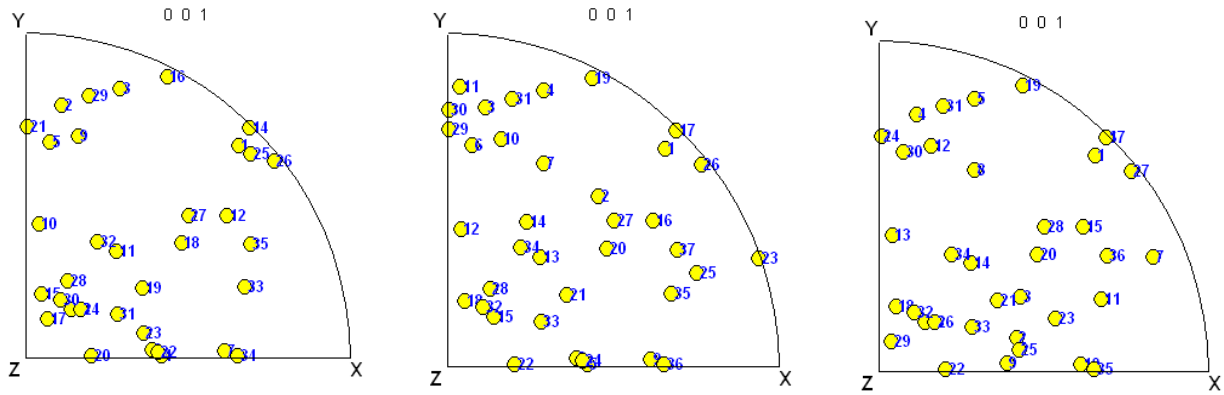

15 kV/cm | 20 kV/cm | 10 kV/cm unloading

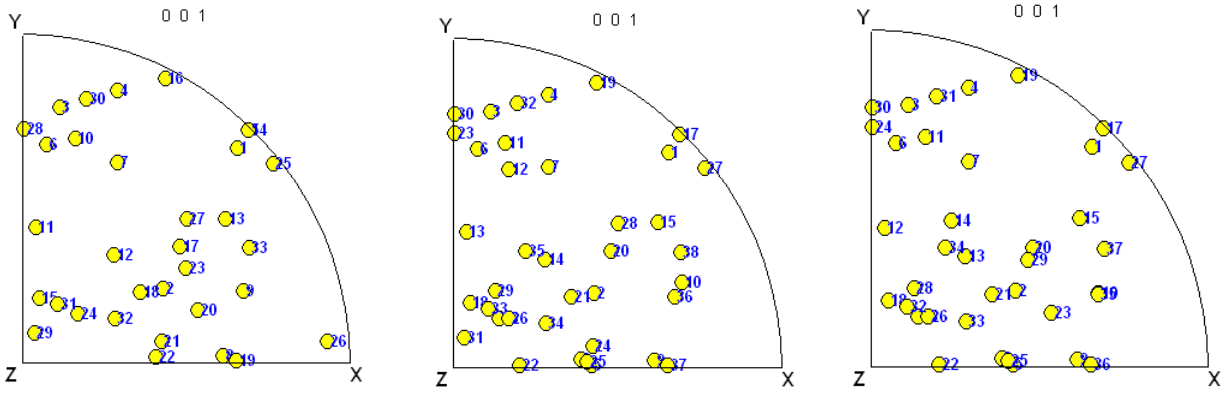

0V/cm unloading | -4 kV/cm loading | -12.5 kV/cm loading

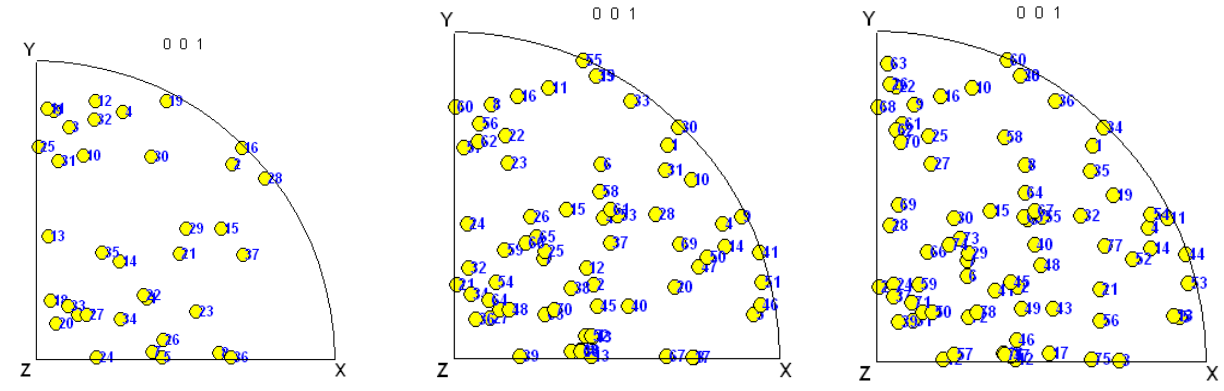

-20 kV/cm loading | -10 kV/cm unloading | -5 kV/cm unloading

Figure 6.5. [001] pole figure in stereographic projection of the orientations of ferroelectric domains as a function of electric field. Note that the numbering is unique to each electric field value.

The progression of the ferroelectric domains with the electric field can further be tracked by their polarization angles. As defined in section 4.2, the polarization angle is the angle between the polarization vector of the domains and direction of the electric field and is expected to decrease with the applied electric field. Table 6.4 shows the progression of the polarization angle of the domains as a function of electric field. With the applied electric field, some new domains were observed along and perpendicular to the electric field. To the contrary with the expected, the polarization angles of the ferroelectric domains don't change gradually with applied electric field. This is due to the fast dynamics and nature of the displacive transformation of the domain switching.

Table 6.4. The angle between polarization vectors of tracked ferroelectric domains in $BaTiO_3$ and the applied electric field vector as a function of electric field. Domains marked with the same superscript and color belong to the same subgrain/grain shown in Table 6.3. New domains (bold font) parallel and perpendicular to the electric field appear under electric loading while most of the domains remain unchanged due to residual texture from pre-poling. For instance, new parallel domains are 1.41, 1.87, 11.44° etc. while new perpendicular domains are 85.58 and 89.15° at 20 kV/cm.

θ (°)-rows vs. Electric Field (kV/cm)-columns								
2	***3***	***5***	***7.5***	***10***	***12.5***	***15***	***17.5***	***20***
			1.4	**1.5**	**1.5**	**1.5**	**1.5**	**1.5**
	1.9	1.9	1.9	1.9				
	11.4	11.3	11.3	11.4	11.4	11.4	11.3	11.3
		12.3	**12.4**	**12.5**	**12.4**	**12.4**	**12.4**	**12.4**
		12.8	**12.8**				**12.8**	**12.8**
			13.3	**13.3**	**13.3**	**13.4**	**13.4**	**13.5**
17.7[d]	17.7	17.8	17.8	17.8	17.8	17.8	17.8	17.8
27.8	27.9	27.9	27.9					
36.4	36.4	36.4	36.4	36.4	36.4	36.4	36.5	36.5
37.5[e]	37.6	37.5						
42.7[c]								
46.5	46.5	46.6	46.5	46.5	46.5	46.5	46.4	46.5
48.6	48.6	48.6	48.6	48.5	48.5	48.5	48.6	48.6
50.2	50.2	50.2	50.2	50.2	50.2	50.2	50.1	50.2
51.4[b]	51.3	51.3	51.4	51.3	51.3			
54[b]	54.0	54.0	54.0	54.0	53.9	53.9	53.9	53.9
56.8	56.8	56.7	56.7	56.7	56.7	56.7	56.7	56.7
64.8	64.8	64.8	64.8	64.8	64.8	64.8	64.7	
69.2	69.2		69.2	69.2	69.2	69.2	69.2	69.1
70.3	70.4	70.4	70.3	70.4	70.4	70.3	70.3	70.3
72.2[c]	72.2	72.2	72.2	72.1	72.1	72.2	72.2	72.2
74.8[e]	74.8	74.8	74.8	74.7	74.7	74.7	74.7	74.6
74.8[a]	74.8	74.8	74.8	74.8	74.8	74.7	74.7	74.8
75.3[a]	75.4	75.4	75.3		75.4	75.3	75.3	75.4
77[d]	76.9	76.9	76.9	76.9	76.9	77.0	77.0	76.9
79.5[b]	79.4	79.4	79.4	79.5	79.6	79.5		
83.7	83.7	83.7	83.7	83.7	83.7	83.7	83.7	83.6
			84.2	84.2	84.1	84.2	84.2	84.2
		84.7	84.8	84.7	84.7	84.7	84.7	84.7
							85.6	85.6
							89.2	89.2
86.2								
88.6[a]								

A close inspection of Table 6.4 shows that some domains could not be identified at the next electric field during the *Graindex* analysis. This may be due to the experimental parameters or the overlap of spots. In order to increase the efficiency of domain characterization and to better characterize closely positioned spots, a 90° domain switching model was developed.

6.1.5. 90° Domain Switching Model

Other than the previously described pseudo-cubic twinning of ferroelectric domains by 89.4° ($=2tan^{-1}(a/c)$) rotation around the cube edges, {100} (see Section 2.3 for details) , the crystallography of 90° domain switching in a tetragonal crystal can also be described by a 180° rotation around the {110} directions (Figure 6.6). The angle, α, is calculated as $tan(c/a)$ where a and c are the lattice parameters of the tetragonal unit cell.

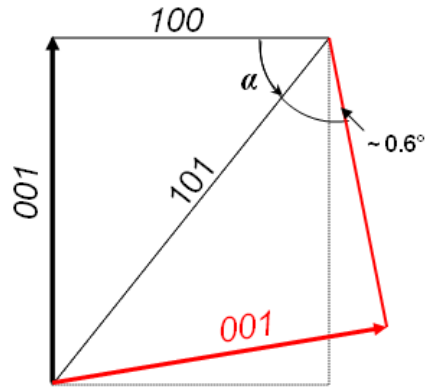

Figure 6.6. Schematic of 90° domain switching in a tetragonal crystal. The scale of the 100 and 001 directions is exaggerated for clarity.

This means, domain switching can happen on 6 crystallographic planes. For a tetragonal parent (with a polarization along [001]), the rotations around [101], [011], [0-11] and [-101] are equivalent to 90° switching while rotation around [110] and [1-10] for 180° domains. Figure 6.7 depicts the formation of a {100} quadruplet splitting by 90° domain switching.

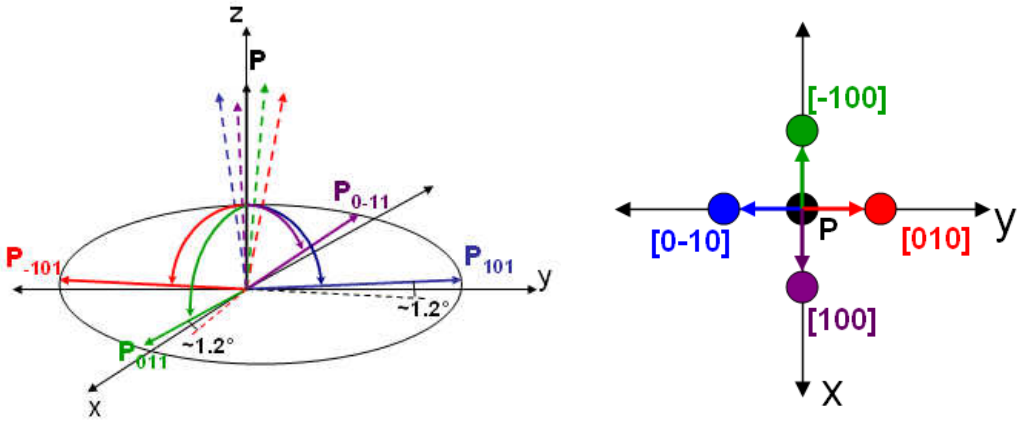

(a) (b)

Figure 6.7. (a) Schematic of 90° domain switching in a tetragonal crystal. (b) Projection from the *z* direction of the parent showing its corresponding {100} twin orientations. The angle between two domain variants corresponds to 1.2° when c/a ratio is taken as 1.01.

The transformation between the scattering vector in the laboratory coordinate system (G_l) and a crystallographic *hkl* plane (G_{hkl}) from a domain is given by:

$$G_l = \Omega UTBG_{hkl} \qquad (6.5)$$

where, Ω is the rotation matrix defining a rotation along *z* direction which is perpendicular to the incoming beam direction, *U* is the orientation matrix of the domain between crystallite and sample coordinate system, *T* is the twin transformation matrix in the crystallite coordinate system and *B* is the reciprocal lattice matrix (where crystallite axis x is parallel to b_1, y is in the plane of b_1 and b_2 and z is perpendicular to that plane) and G_{hkl} is the vector from the diffraction plane.

The twin transformation matrix (*T*) can be obtained by two methods. In the first method, the twinning happens by 180° rotation around the normal of (101), (-101), (011) or (0-11) planes. This rotation can be achieved by the transformation of the vectors by α rotation (in Figure 6.7) around the normal of the (101), (-101), (011) or (0-11) planes and an inverse symmetry operation around the non-negative axis. These rotations can be expressed as following:

$$M_{101}=\begin{vmatrix}\cos(\alpha) & 0 & \sin(\alpha)\\ 0 & 1 & 0\\ -\sin(\alpha) & 0 & \cos(\alpha)\end{vmatrix} \qquad T_{101}=M_{101}\begin{vmatrix}1 & 0 & 0\\ 0 & -1 & 0\\ 0 & 0 & -1\end{vmatrix}(M_{101})^{-1} \tag{6.6}$$

$$M_{011}=\begin{vmatrix}1 & 0 & 0\\ 0 & \cos(\alpha) & \sin(\alpha)\\ 0 & -\sin(\alpha) & \cos(\alpha)\end{vmatrix} \qquad T_{011}=M_{011}\begin{vmatrix}-1 & 0 & 0\\ 0 & 1 & 0\\ 0 & 0 & -1\end{vmatrix}(M_{011})^{-1} \tag{6.7}$$

$$M_{0\text{–}11}=\begin{vmatrix}1 & 0 & 0\\ 0 & \cos(-\alpha) & \sin(-\alpha)\\ 0 & -\sin(-\alpha) & \cos(-\alpha)\end{vmatrix} \qquad T_{0\text{–}11}=M_{0\text{–}11}\begin{vmatrix}-1 & 0 & 0\\ 0 & 1 & 0\\ 0 & 0 & -1\end{vmatrix}(T_{0\text{–}11})^{-1} \tag{6.8}$$

$$M_{\text{–}101}=\begin{vmatrix}\cos(-\alpha) & 0 & \sin(-\alpha)\\ 0 & 1 & 0\\ -\sin(-\alpha) & 0 & \cos(-\alpha)\end{vmatrix} \qquad T_{\text{–}101}=M_{\text{–}101}\begin{vmatrix}1 & 0 & 0\\ 0 & -1 & 0\\ 0 & 0 & -1\end{vmatrix}(M_{\text{–}101})^{-1} \tag{6.9}$$

The corresponding twin transformation matrices for these rotations will then be:

$$T_{101}=\begin{vmatrix}-\cos(\gamma) & 0 & \sin(\gamma)\\ 0 & -1 & 0\\ \sin(\gamma) & 0 & \cos(\gamma)\end{vmatrix} \qquad T_{\text{–}101}=\begin{vmatrix}-\cos(\gamma) & 0 & -\sin(\gamma)\\ 0 & -1 & 0\\ -\sin(\gamma) & 0 & \cos(\gamma)\end{vmatrix} \tag{6.10}$$

$$T_{011}=\begin{vmatrix}-1 & 0 & 0\\ 0 & -\cos(\gamma) & \sin(\gamma)\\ 0 & \sin(\gamma) & \cos(\gamma)\end{vmatrix} \qquad T_{0\text{–}11}=\begin{vmatrix}-1 & 0 & 0\\ 0 & -\cos(\gamma) & -\sin(\gamma)\\ 0 & -\sin(\gamma) & \cos(\gamma)\end{vmatrix} \tag{6.11}$$

where γ represents the angle between the polarization angle along polarization directions of parent domain and domain variants as shown in Figure 6.6 and $\gamma = 180 - 2\alpha = 180 - 2\tan^{-1}(\frac{d_{001}}{d_{100}}) = 89.43°$.

The second method to obtain twin transformation matrices is to use skew-symmetrical matrices. In this method, the transformation matrix can be obtained by a rotation around an axis. If ***n*** and ω are denoted as the rotation axis and angle respectively, the transformation matrix can be expressed as the combination of the identify matrix times

cos(ω), a matrix which is symmetrical about the leading diagonal and a matrix which is antisymmetrical (skew-symmetrical) about the leading diagonal (term on other side of diagonal is negative). This transformation matrix can be shown as [Euclid (2007)]:

$$T = \cos\omega \begin{bmatrix} 1 & 0 & 0 \\ 0 & 1 & 0 \\ 0 & 0 & 1 \end{bmatrix} + \sin\omega \cdot \begin{bmatrix} 0 & -n_3 & n_2 \\ n_3 & 0 & -n_1 \\ -n_2 & n_1 & 0 \end{bmatrix} + (1-\cos\omega) \cdot \begin{bmatrix} n_1^2 & n_1 n_2 & n_1 n_3 \\ n_1 n_2 & n_2^2 & n_2 n_3 \\ n_1 n_3 & n_2 n_3 & n_3^2 \end{bmatrix} \quad (6.12)$$

The combination of these matrices can be written in a single matrix form as follows:

$$T = \begin{bmatrix} (1-\cos\omega)n_1^2 + \cos\omega & (1-\cos\omega)n_1 n_2 - n_3 \sin\omega & (1-\cos\omega)n_1 n_3 + n_2 \sin\omega \\ (1-\cos\omega)n_1 n_2 + n_3 \sin\omega & (1-\cos\omega)n_2^2 + \cos\omega & (1-\cos\omega)n_2 n_3 - n_1 \sin\omega \\ (1-\cos\omega)n_1 n_3 - n_2 \sin\omega & (1-\cos\omega)n_2 n_3 + n_1 \sin\omega & (1-\cos\omega)n_3^2 + \cos\omega \end{bmatrix} \quad (6.13)$$

As discussed in Section 6.1.4, Graindex is not able to find all the domain variants from a grain due to experimental conditions such as shutter didn't open, beam lost etc. Therefore, one needs to look for the domain variants manually by starting a orientation matrix found by Graindex. By using the transformation matrix and diffraction equation in Eq (6.6), it is possible to simulate the possible domain variants, investigate the other domain variants and investigate the neighboring spots to confirm whether they are belong to same grain or not. By using both techniques described above, it is possible to mimic the domain switching and interpret the results better.

6.1.6. Characterization of Domain Variants

By combining the twin transformation matrices in Eq. (6.5), it is possible to study the variants of a domain found by *Graindex*. In order to accomplish this, a simulation package called *Diffsim* was used. *Diffsim* was written in *Matlab* by Risoe Lab researchers in Denmark to simulate 3D-XRD diffraction patterns from a set of grains with known orientations (its current name is *"Farfield Simulation"* [Schmidt, S. (2007)]). With the aid of this package, it is possible to predict the domain variants of a given domain and characterize the orientation of its variants. The best way to characterize the domain variants is to use the *Phi-Eta map* (Section 4.3) because the spots of the simulated domain variants can be easily observed. Several *Phi-Eta maps* were prepared from the (100), (001), (110), (011), (111), (200) and

(002) Debye rings using the *Fit2D.v12.077* software [Hammersley, A. P. (1997)] by integrating the rings along η (azimuth angle) and binning in 2θ and combining summed each ring along ϕ in *Matlab.*

Figure 6.8 shows an example of such a simulation for the domain variants no. 1, 17 and 28 (see Table 6.3). The corresponding locations of the (200) and (002) spots from domains no. 1, 17 and 18 are shown on the experimental data in Figure 6.8(a). As was shown in Eq. (4.12), it is possible to locate the Friedel pair of a given spot with the 3D-XRD technique and the shapes and morphologies of these pots are expected to be identical. Non-matching spots between Friedel maps are considered as some spots that diffract coincidentally in that given phi oscillation and they are discarded. Figure 6.8(b) shows the simulation by starting with domain no. 1 as the parent. The simulation identifies domains no. 17 and 28 as the variants of no. 1 rotated around the [011] (*) and [-101] (red>) directions, respectively.

As proved in Eq. (4.12), it is possible to locate the Friedel pair a given spot with the 3D-XRD technique and these two spots and surrounding spots are expected to be identical. Any new spots without its Friedel pair are considered as coincidence spots diffracting at that specific ω oscillation. Figure 6.8 (b) shows the simulation by starting with Domain 1 as a parent domain. With this simulation, the domain 17 and 28 are identified as the domain variants rotated around [011] (*) and [-101] (red>) direction.

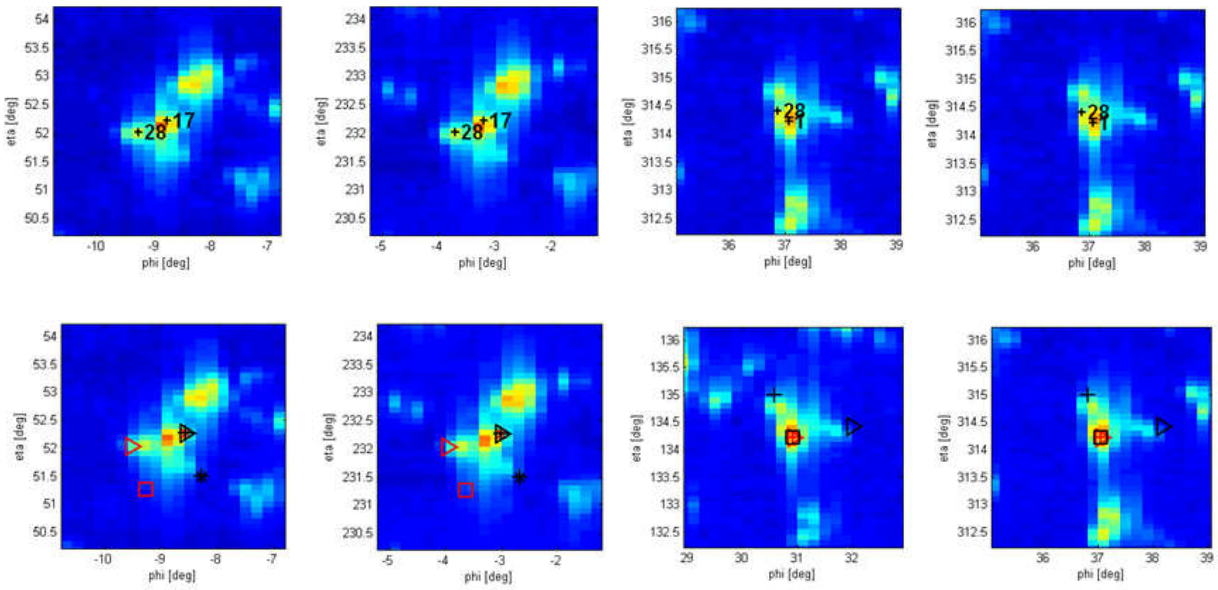

Figure 6.8. (a) *Phi-Eta* locations of the 200 and 002 peaks and their Friedel pairs of domain variants (1-17-28) in 200 and 002 at phi-eta map. The phi-eta map was prepared with the experiment data from 2kV/cm oscillation images from 2kV/cm. (b) The prediction of the spots by starting Domain 1 (red circle) and its domain variants. (red'o'→Parent, red+→101, red>→-101, red*→011, red□→0-11, black+→ 011&-101, black>→011&101, black*→0-11&-101, black□→0-11&101)

Table 6.5 shows the overall summary obtained from the 90° domain model for all the domain variants shown in Table 6.3. Note that [0-11] and [-101] directions in Table 6.3 correspond to successive 180° rotations around, first, the [0-11], and then [-101] directions.

Table 6.5. The summary of the relationships between some domains listed in Table 6.3. The crystallographic relation is defined as rotation around a specified axis of the parent domain. For example, among domain variants 33, 27 and 11, domains 27 and 11 can be obtained by the 180° rotation around [011] and [101] axes respectively.

Domain Group	Polarization Angle, °	Crystallographic relation
33, 27, 11	74.8, 75.3, 88.5	Parent(33), [011](27), [101](11)
1, 17, 28	51.4, 54, 79.5	Parent(1), [011](17), [-101](28)
13, 34	74.8, 37.5	Parent(13), [011](34)
3, 15	17.7, 77	Parent(3), [101](15)
2, 14	42.7, 72.2	Parent(14), [011](2)

Among the indentified groups of the ferroelectric domains, Domain 1, 17 and 28 is particularly interesting. While, the polarization angle of Domain 28 is almost perpendicular,

(79°), applied electric field reduces the intensity of this domain. Figure 6.9 and 6.10 show the evolution of this domain as a function of electric field.

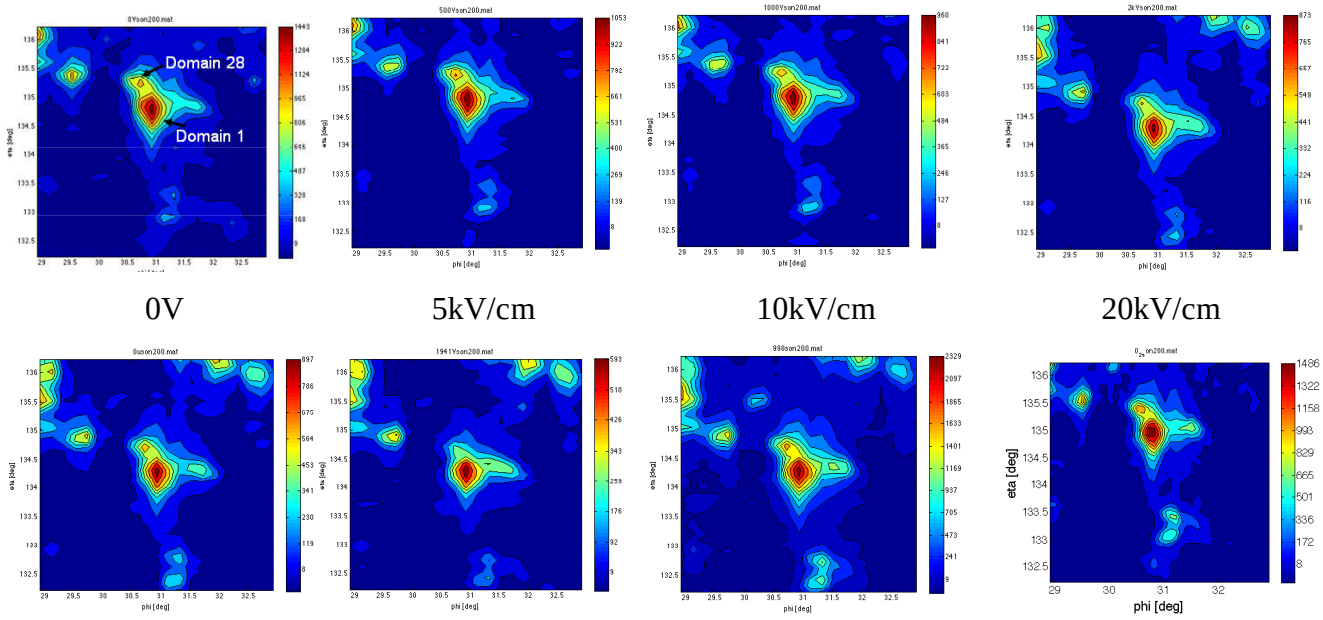

Figure 6.9. The evolution of the 200 reflections of Domain 1 and 28 as a function of electric field

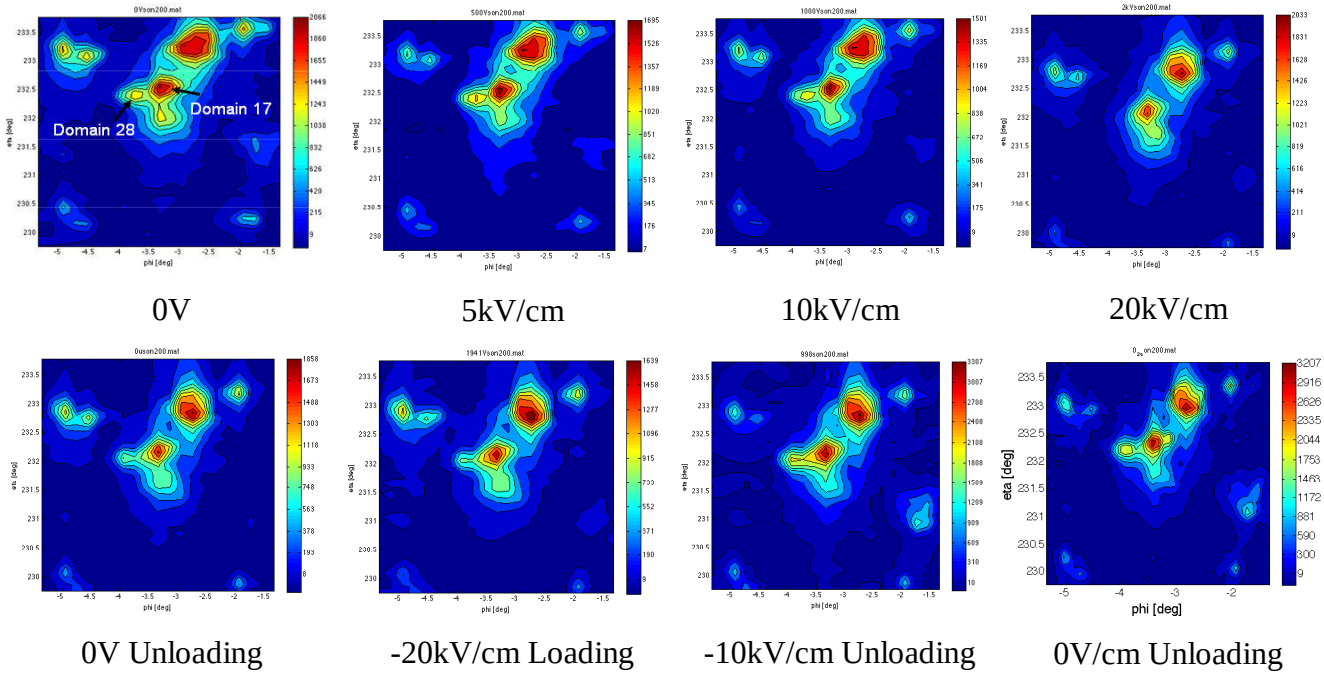

Figure 6.10. The evolution of the 200 reflections of Domain 1 and 28 as a function of electric field

The application of the electric field shows that the domains gradually experience domain switching and the domain switching can start around the coercive field (5 kV/cm).

6.1.7. Domain Intersections

A close inspection of the domains shown in Table 6.3 reveals that most of domain groups found are basically 90° variants of a parent domain twinned over (011) or (101) planes. These domain variants can be expressed with their polarization directions schematically. If we denote the parent domain as the [001] direction, then the (011) twin variant will have a polarization along the [010] direction. In the same way, the (101) variant will have a polarization along the [100] direction. The intersections of these domains can be shown schematically in Figure 6.11.

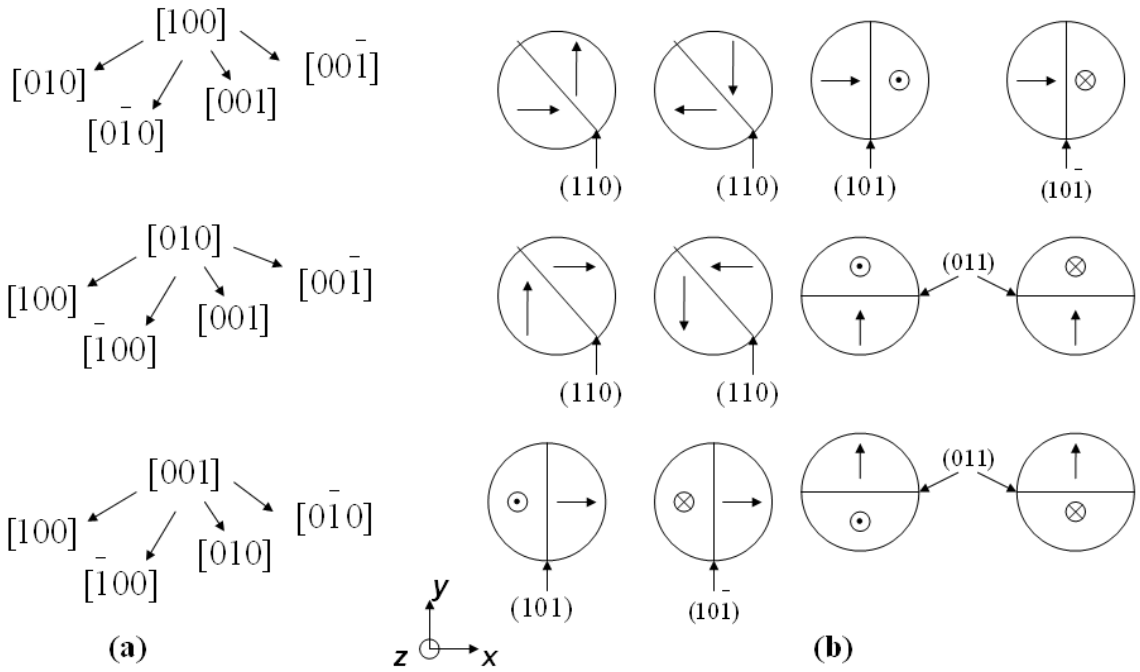

Figure 6.11. (a) The possible 90° variants of a parent domain with polarization vectors (from top to bottom) along [100], [010] and [001]. (b) Schematic intersection of these domains indicating the domain boundary planes. Each row shows the possible domain intersections of [100], [010] and [001] polarization vectors.

Combining the information on possible domain variants and the variants found by *Graindex*, one can draw a schematic of their arrangements in the microstructure. Figure 6.12 shows such a schematic [Tan, X. 2007)]. If we take our parent domain to be oriented along the *x*-direction, its variants can be obtained by twinning around (101) or (110) planes. These

domain variants can be either along the electric field or perpendicular to electric field and application of the electric field will yield the domains perpendicular to electric field to switch. Only two domain variants are seen in the domains embedded in the sample. The third domain variants are not seen as seen in the μSXRD experiments.

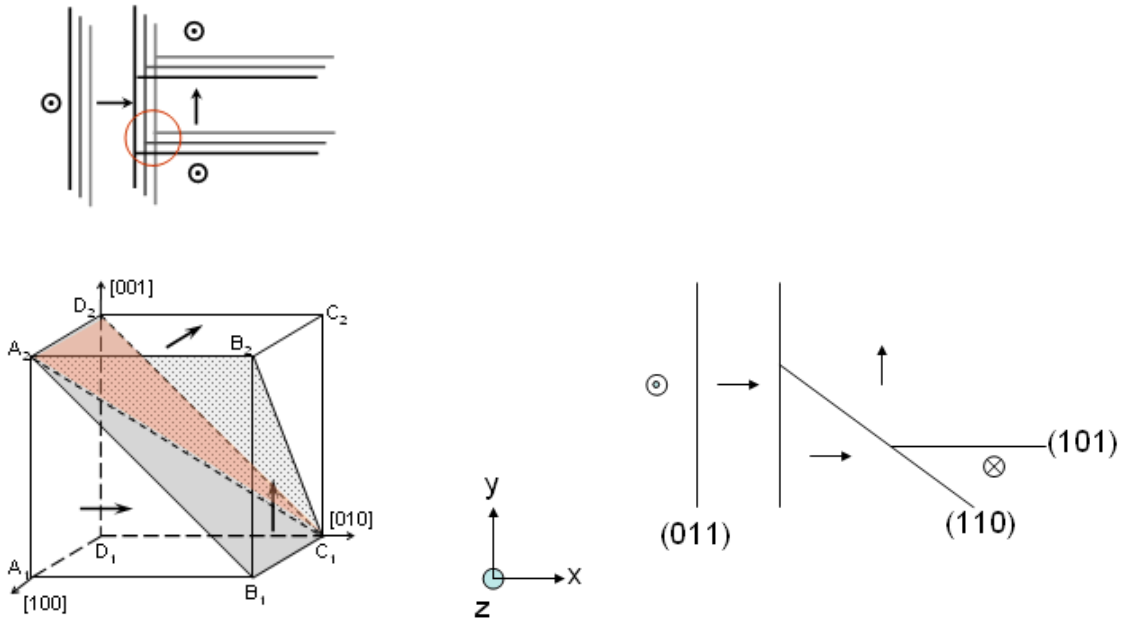

(a) (b)

Figure 6.12. Schematic of domain intersections. (a) Projection of these domains on the *z*-axis and the unit cell representation [Tan, X. (2007)]. The arrows show the intersections of the polarization vectors in a unit cell. (b) 2-D schematic of domain intersections. The [001] domain is neighbor with a [100] domain along the (011) domain boundary. The [100] domain is next to a [010] domain along (110). The fourth possibility is a [00-1] domain that borders a [010] domain along (101) and we didn't observe the fourth domain variant in 3D-XRD experiment [Tan, X. (2007)].

From the domain switching model and the results, most of the parent domains are found to be along the surface normal and the domain variants of the parent domains are produced by the rotation around either [100] or [010] direction with 89.4 or 89.6°. While the fraction of the domain variants that are perpendicular to the electric field reduces with the electric field, the parallel domains have higher intensity. This is consistent with the principles of the ferroelectric domain switching. With the new improvements, the configurations of the

domain variants can be predicted in three dimensions which give a unique opportunity to study the ferroelectric domain switching.

6.1.8. Domain Size

As discussed in Section 4.2.3, it is possible to find the volume of a diffracting domain based on measured intensity. Due to domain switching, the volumes of domains with larger polarization angles are expected to decrease while those of domains with smaller polarization angles to increase. To quantify domain volume evolution as a function of electric field, the integrated intensities of diffraction spots from domain variants were calculated with a 2-D Gaussian (Eq. 4.18). The intensity values were converted to domain volume by using Eq. (4.17). The same routine was repeated for the Friedel pair of a spot to get a better estimate for the domain volume. The *Phi-Eta* map was used in this effort because it is easy to isolate spots and observe its variants along ϕ and η. Figure 6.13 shows domain size evolution as a function of electric field for the domains listed in Table 6.3. The calculated domain sizes are based on the 200 reflections. The main reason of selecting 200 is that 200 peaks can have 4 variants (200, -200, 020, and 0-20) and it is possible to observe more variants on a 200 *Phi-Eta* map and compare their integrated intensity values.

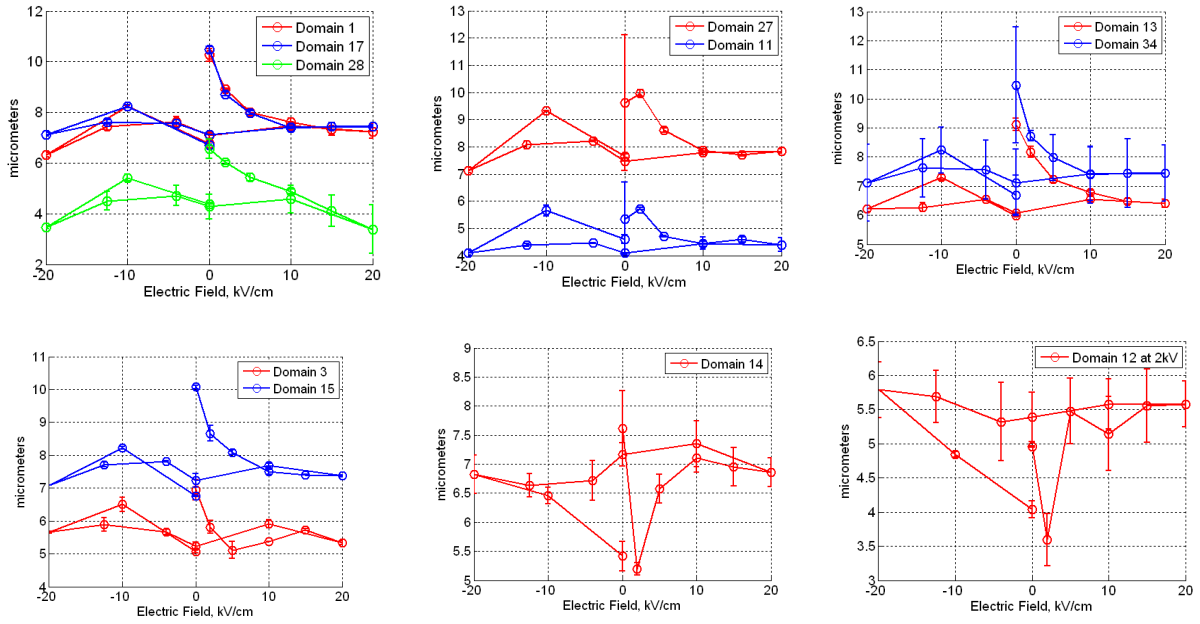

Figure 6.13. The domain size versus electric field as a function of electric field of the domain variants shown in Table 6.3

The data in Figure 6.11 is somewhat ambiguous and scattered. For instance, the volumes of some domains (Domain 1, 17, 28, 3-15) decrease with the increased electric field. An opposite trend should be observed as the volume of domains perpendicular to the electric field should decrease while that of the parallel ones should increase. Additional data is needed to clarify this issue. However, this exercise demonstrated the feasibility of tracking not only domain orientations, but also their volume as a function of loading.

6.2. Investigation of Mesoscale Behavior of Ferroelectrics in Response to Electric Field and Temperature

The evolution of the ferroelectric domains with electric field and temperature was studied by using 3D-XRD technique. The phase transformation from cubic to tetragonal and the distribution of the domain variants within the grain was studied. After cooling, the resultant domain variants are obtained by rotating 89.96° and 89.6° of the [100] or [010] axis of the cubic grain respectively. As response to electric field, the volume fraction change between the domains was observed. This volume fraction is favored on the domain that has a small angle between its c axis and the electric field direction. There is no such a significant grain rotation observed during domain switching. The improvements are explained to eliminate the major drawbacks of studying ferroelectrics: spot overlapping.

6.2.1. Experimental Procedures

$BaTiO_3$ ceramics were processed from a single batch of previously prepared stoichiometric $BaTiO_3$ powder (99.9% pure, with Ba/Ti ratio=1.00, from Ferro Corp., Transelco Division) to minimize the effects of stoichiometry variations between batches [Bryne, T. A. (2004)]. The initial powders were homogeneously mixed via vibratory milling for 5 h in zirconia media in ethanol. Approximately 4 wt% binder was added to the powder. Following binder burn-out at 500°C for 2 h, the well-mixed powder was calcined at 1300°C for 2 h in an alumina crucible covered with zirconia powder. The final composition of the sample had approximately 95% of the theoretical density. For grain size measurements, samples were thermally etched at 1300°C for 2 h to reveal the grain structure. The grain size was calculated around 20 μm.

Bulk polycrystalline $BaTiO_3$ samples were sectioned with a diamond saw into 1.2x1.2x5 mm dimensions. After sectioning, the surfaces of the samples were polished with abrasive and finally with fine sandpaper until the final dimensions would be 1x1x5 mm. During polishing, extra caution was shown not to introduce residual stress to the sample. Both 1x1 mm sides were sputtered with gold for 5 minutes and thin copper wires were attached using conductive epoxy. There are several advantages of selecting such sample dimensions. First, the X-rays can easily penetrate through the sample at high energy. Second, the applied electric field can be more than coercive field which leads to significant domain switching.

The 3D-XRD experimental setup mainly consists of a monochromatic high energy x-ray source, to enhance the penetration depth up to cm range, a sample holder with a rotating device in *x*, *y*, *z*, and ϕ axis to allow studying the grain rotations, and 2D CCD detector to record the diffraction patterns in each ω oscillation. Figure 6.3 shows the schematic 3D-XRD setup. With a typical range of 50-80 keV of micro-focused monochromatic x-rays, the crystallographic planes of each grain diffracts as Bragg peaks on the 2D detector. Rotation along *z* axis allows the grain to diffract as Bragg condition satisfies. For the ferroelectrics, domains diffract as population with a small degree and the technique requires smaller ϕ oscillation to resolve the domains, i.e. less than 0.6°. This angle can be resolved by 3D-XRD technique which gives a unique opportunity to study the ferroelectrics.

3D-XRD experiments of $BaTiO_3$ were performed at beamline 1-ID-C of the Advanced Photon Source (APS), Argonne National Laboratory, Argonne, IL. This beamline not only provides dedicated high energy focusing optics but is specialized for 3D-XRD data acquisition and analysis. By focusing vertically and using slits horizontally, high energy x-rays (80.72 keV, with wavelength $\lambda \sim 0.1535$ Å) in transmission mode were focused to a 20x20 μm^2 spot size. Since the grain size was estimated to be around 20 µm, this spot size was enough to illuminate roughly 50 grains. Among these grains, a few of those grains were illuminated with the x-ray beam during the sample rotation. The sample was centered on a vertically (phi) rotating fixture which heating capability is provided by a Thunderbolt electric cartridge heater that can heat up to 650°C with 172 W/in^2 power density. This device is

embedded to a sample holder which made of copper for high thermal conductivity. An electrically insulating and heat conductive epoxy was applied between the sample and the sample holder to prevent an electric arcing. The temperature profile on the copper plate was measured with Omega Model HH21 Microprocessor Thermometer and Fluke 87IV True RMS Multimeter. The temperature gradient within the sample was also monitored by using Inframetrics Model 760 IR imaging radiometer. While heating the sample stage, the positioning stage is prevented from heating by MACOR machinable glass ceramic posts.

Heating the sample above Curie temperature prior to electric field randomized the poling and preferred orientation became feasible with electric field. After cooling to room temperature, the sample was oscillated perpendicular to the beam with 0.25^{o} ϕ steps up to $\pm 60^{o}$; repeated at each applied electric field. The electric field was applied in-situ with a Canberra 3002 HV supply reaching up to +10 kV/cm (10mA) in 5 kV/cm steps and was perpendicular to the incoming beam (along the y-axis in Figure 6.3). The maximum applied electric field was high enough to trigger domain switching as the nominal coercive field of the material was previously measured as 5.16 kV/cm. The sample was aligned with the way where the electric field direction is normal to the incoming beam direction (Figure 6.3). The rotation axis of the sample was carefully aligned by checking the same spot after rotating the sample for 180° along η. The sample-to-detector distance was adjusted as 2274.3 mm. This distance enhanced the resolution of the diffraction spots on the GE 41RT amorphous silicon detector (2048x2048 pixel size, GE Healthcare Inc.) by increasing the radial angle resolutions of the variants of {001}, {011}, {111} and {002} diffraction planes. The lattice parameters of the $BaTiO_3$ were calculated as a=0.39986 nm at cubic region and a=0.39836 nm and c=0.40198 nm at room temperature. Using the on-the-fly scan mode in GE detector, collecting 480 images took less than 5 min. This fast acquisition speed of the GE detector made possible to automate the data acquisition process. The diffraction patterns collected at above Curie temperature were analyzed by Graindex [Lauridsen, E. M. (2001)]. The orientation with the highest number of observed reflections compared to simulated ones is selected as reference grain. The same grain was tracked while cooling the sample to room temperature and applying electric field.

After cooling to the room temperature, it is very difficult to find the orientations of the ferroelectric domains due to spot overlapping. The reflections with low multiplicity such as (001), (002), (110) and (112) don't experience spot overlapping and they are used to find the orientations of the domains by simulating the orientations using "diffsim" [Lauridsen, E. M. (2001)]. In order to find the misorientation between the tetragonal domains and the cubic grain, the orientations are first mapped to fundamental region respectively. While *m3m* point symmetry was used for cubic grain, *4mm* point symmetry was used for tetragonal domains and misorientation was calculated by using ODF/PF software package from Cornell University [Dawson, P., *et al.* (2005)]. As a convention, angle-axis pairs were used. This convention has a major advantage to show the misorientation angle and axis with respect to the reference grain and it is helpful when describing the misorientation angle between domains with the domain boundary.

6.2.2. Data Evaluation

In 3D-XRD technique, using high energy monochromatic x-rays makes possible to illuminate the grains embedded in a polycrystal. X-Ray beam can be focused to a desired area or grain. Among the illuminated area in the sample, each crystallographic plane of grains diffracts as a peak on the detector. The shape, distribution, and intensity of these peaks can be used to study the texture evolution of the material. Rotation along the ϕ axis, perpendicular the incoming beam direction, allows all the grains within the illuminated area to satisfy the Bragg condition and enable us to find the orientations of the grains. Typical oscillation angle for cubic materials is 1° and this angle needs to be small enough to resolve reflections if the sample has subgrain structure. The further details of the data analysis can be found from Lauridsen, E. M. (2001)'s paper. To summarize, the overall data analysis can be explained by one equation:

$$G_l = \Omega g^{-1} B G_{hkl} \qquad (6.14)$$

where the scattering vector $\boldsymbol{G_l}$ of each crystallographic planes in the laboratory coordinate system (x,y,z) is translated into reciprocal lattice system (G_{hkl}). For the translation, $\boldsymbol{\Omega}$ is the rotation matrix defining a rotation parallel to the z axis between laboratory system and the

sample system and $\mathbf{g^{-1}}$ is the orientation matrix defining a rotation between sample and crystal system (i.e. $\mathbf{G_l=\Omega.G_S}$, $\mathbf{G_S=g^{-1}.G_C}$). Note that the original orientation matrix used in 3D-XRD transforms the crystal coordinate system into sample coordinate system. In order to be consistent with literature, this orientation matrix was represented with its inverse. B is a second rank tensor which transforms the crystal coordinate system from reciprocal to real space. Each spot in the detector is converted to a scattering vector ($\mathbf{G_l}$) and these vectors are compared to simulated ones by using Euler angles. The reflections matching with the simulated ones with Euler angles are authenticated as orientations within the sample volume. For cubic materials, finding orientations are fairly easy compared to ferroelectrics since the reflections appear as distinct spots contrary to ferroelectric domains.

The polycrystalline ferroelectrics are usually composed of grains with several domains isolated by domain boundaries. Domain boundaries act as the twin boundaries and depending on the lattice parameters, the pseudo-cubic edges of the domains within a grain can have misorientation to each other. For the ferroelectrics where the c/a ratio is close to unity, the misorientation angle between the domains can be very small. For instance, c/a ratio of $BaTiO_3$ is 1.01 and the misorientation angle between the (100) and (001) planes of the individual domains can be calculated as i.e. around 0.6°. In order to resolve the domains, the sample needs to be oscillated with an angle smaller than theoretical misorientation angle. The typical oscillation step for the current investigation was 0.25° and this step was sufficient to resolve the domains from the same grain. The resolution of the spots along η was 0.1°. Due to tetragonal crystal structure in $BaTiO_3$, the distinction between (100) and (010) planes between the domains in the same grain is nearly impossible and it is difficult to resolve these reflections along ϕ and η. This drawback is known as spot overlap and it has been a limiting factor for finding the precise orientation of the domains.

One of the major advantages of the 3D-XRD compared to other characterization techniques is the capability to resolve the crystallographic planes with opposite directions. These planes are called as “Friedel pairs” in literature. If we assume one of these spots diffracting at ϕ_0 oscillation angle, η_0 azimuthal angle and 2θ diffracting angle at the detector, the Friedel pair of this spot will diffract at

$$\phi_1 = \phi_0 + 2\theta\sqrt{1 + \tan^2 2\theta + \tan^{-2}\eta_0} \quad ; \quad \eta_1 = \eta_0 + 180° \qquad (6.15)$$

where ϕ_1 and η_1 are the oscillation and azimuthal angle of its Friedel pair. The reflections that can be resolved from its Friedel pairs and don't experience spot overlap in *p4mm* tetragonal structure are (001), $(00\bar{1})$, (002) and $(00\bar{2})$. Since these reflections can be resolved in ϕ and η, they can represent the domains within the grain. Among these reflections, the radial separation of the (002) diffraction ring is the highest. Therefore, the (002) and $(00\bar{2})$ reflections are in great interest because they have the highest radial resolution achievable with the current detector. According to crystal structure of $BaTiO_3$, titanium atom is located in this crystal plane as well and this plane is more sensitive to study the strain and the orientation changes with applied electric field.

Indexation attempt of the ferroelectric domains needs to be done carefully. Because there are several domains diffract within a half degree, the indexation based on all reflection families may create a slight deviation from the real orientation of the domains. In addition, depending on the angle between its scattering vector and rotation axis, the same reflection can appear at sequential phi sets. To find the center-of-mass of the reflections, a given hkl ring was binned along η and then integrated along 2θ. The resultant map is called "Phi-Eta" and by using this map, it is possible to find the center-of-mass of the reflections at ω and η. As of interest, eta-phi map for the (002) reflections is prepared and the center of mass of 002 reflections is found based on the cubic grain and room temperature. Since (002) and $(00\bar{2})$ reflections will not be sufficient to find the orientation of the domains and (001) and $(00\bar{1})$ reflections will be linear to these reflections, other reflections are needed for finding the orientation. Because it has a high radial resolution and appears as a singlet along 2θ, (112) reflections can be used for candidate reflections. The normalized scattering vectors of these reflections in the sample system, G [Poulsen, H. F. *et al* (2004)] can be written as:

$$G = \Omega g^{-1} h = \begin{pmatrix} \cos(\phi) & -\sin(\phi) & 0 \\ \sin(\phi) & \cos(\phi) & 0 \\ 0 & 0 & 1 \end{pmatrix} g^{-1} \frac{\lambda}{4\pi\sin(\theta)} B \begin{pmatrix} h \\ k \\ l \end{pmatrix} = \cos(\theta) \begin{pmatrix} -\tan(\theta) \\ -\sin(\eta) \\ \cos(\eta) \end{pmatrix} \qquad (6.16)$$

where ϕ is the rotation angle, g^{-1} is the orientation matrix with direction cosine components, λ is the wavelength, η_0 is azimuthal angle and θ is half Bragg diffracting angle at the detector. Scattering vectors can also be written by a rotation from the crystal to sample coordinate systems by using Eq. (6.16):

$$G = g^{-1}\mathbf{h} = \begin{pmatrix} \cos(\phi) & -\sin(\phi) & 0 \\ \sin(\phi) & \cos(\phi) & 0 \\ 0 & 0 & 1 \end{pmatrix}' \cos(\theta) \begin{pmatrix} -\tan(\theta) \\ -\sin(\eta) \\ \cos(\eta) \end{pmatrix} \tag{6.17}$$

This equation allows one to calculate the angle (δ) between diffraction planes (G_1 and G_2) as:

$$\cos\delta = \cos(G_1 \cdot G_2) \tag{6.18}$$

This angle (δ) is also equivalent to interplanar angles [Pecharsky, V.K., Zavalij, P.Y. (2005)] and for tetragonal structure, ϕ angle can be calculated as:

$$\cos\delta = \frac{\frac{h_1h_2 + k_1k_2}{a^2} + \frac{l_1l_2}{c^2}}{\sqrt{\frac{h_1^2 + k_1^2}{a^2} + \frac{l_1^2}{c^2}}\sqrt{\frac{h_2^2 + k_2^2}{a^2} + \frac{l_2^2}{c^2}}} \tag{6.19}$$

To find the orientations of the domains, the reflections from cubic grains were used as reference. During the cooling, the tetragonal reflections transformed from those cubic reflections were tabulated. Among tabulated tetragonal reflections, (002) and (112) reflections were used for fitting. From these reflections, the angles between the tetragonal reflections are calculated via Eq. (6.17) and compared to theoretical interplanar angles for tetragonal structure Eq. (6.19). The angle between (002) and (112) reflections was found to be 35.51° by using Eq.(6.19) and the candidate reflections within a range of 0.1° of theoretical interplanar angles are fitted by using Eq. 6.19 and the orientations of the domains are found. The reflections from calculated orientations were also compared with the raw diffraction patterns by using "diffsim" software [Lauridsen, E.M. (2001), Schmidt, S. (2007)] and the orientations were verified for all reflections. The deviation between the reflections of the fitted orientations and raw diffraction patterns was less than 0.05° in *phi* and 0.1° in *eta*.

In order to find the misorientation between the tetragonal domains and the cubic grain, the orientations are first mapped to corresponding fundamental regions respectively. While m3m point symmetry was used for cubic grain, 4mm point symmetry was used for tetragonal domains and misorientation was calculated by using ODF/PF software package from Cornell University [Dawson, P. (2005), Frank, F. C. (1988)]. As a convention, angle-axis pairs were used. This convention has a major advantage to show the misorientation angle and axis with respect to the reference grain and it is helpful when describing the misorientation angle between domains with the domain boundary.

6.2.2.1. Box Scan

Intrinsic spot overlap is often a limiting factor in single grain investigations, esp. in ceramics. It has been demonstrated that this problem can be alleviated by taking repeated data sets while translating a smaller beam across the sample. Such 'box scans' also provide 2D spatial information about the center-of-mass of the scattering unit. With recent advances in detector technology, the acquisition of such large data sets has become reasonably fast for *in-situ* investigations. Figure 6.14 shows the schematic principles of box scan.

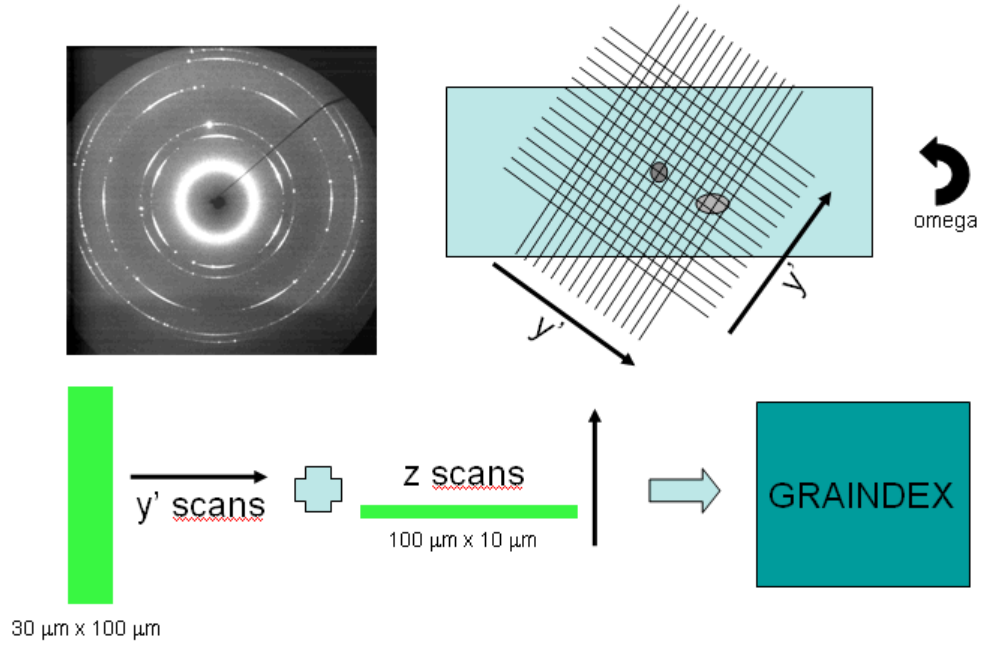

Figure 6.14. The "box scan" procedure: The sample is illuminated with a desired spot size. The spot size is further decreased to isolate overlapping peaks in the diffraction pattern and to locate the domains in 2D while changing the location of the sample. [Poulsen, H. F. (2004)]

From the previous 3D-XRD experiment, it is well observed that the domain switching doesn't involve a gradual domain rotation. In order words, the domains are switched to the most energetically favorable state by a displacive transformation. By combining the "box scan" technique, it is possible to study the local orientation distribution function of polycrystalline $BaTiO_3$. The procedure for studying the local orientation distribution function is described by Poulsen et al [Poulsen, H. F. (2005)]. It is crucial to boost the analysis by implementing the local distribution functions.

Box scan is the newly implemented routine to 3D-XRD technique to study the shape of the grain and distribution of the domain variants within the grain. In our experiment, the incoming beam is narrowed and sample was moved horizontally from -50 to 50 microns with 5 micron steps. At each image, the sample is rotated along phi from -60 to 60 deg with 0.25 deg steps. With box scan technique, it is possible to obtain 3D information of the tracked grains. We used this technique to track the morphology of the close spots along the sample and monitor the distribution of the domains within the grain. Figure 6.15 (a) shows the distribution o the close spots and their distribution as beam is moved out of the sample. The close spot appearing close to domain are shown at top left of the images stay diffract as the same behavior with the domain itself. The distribution of these close spots along the sample is shown Figure 6.15.b. This clearly shows that the close spot belongs to same grain and it is a subgrain feature. The detailed understanding of the subgrain feature is still underway and isn't included here.

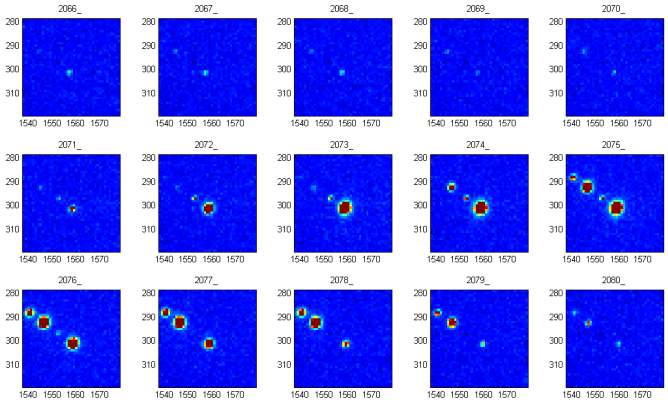

Figure 6.15 (a)

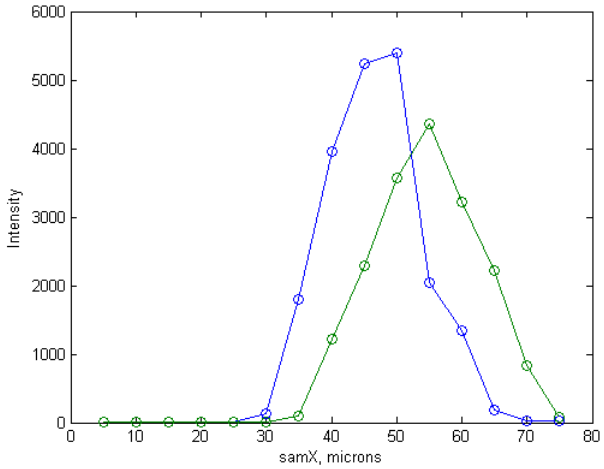

(b)

Figure 6.15. (a) The distribution of the close (200) spots along the sample coordinates. The spot at the center of the image belongs to the grain and the close spots appear at the top left portion of the image. (b) The distribution of the peak intensities when moving the sample. Blue color represent the spot belong to reference grain and green one is the close spot.

6.2.3. Results and Discussion

The phase transformation from cubic to tetragonal and the distribution of the domain variants within the grain was studied. The orientation relationship between the domains was revealed. As response to electric field, the volume fraction change between the domains was observed. The orientation changes with the electric change were studied. The distribution of the domains was also studied at above Curie temperature and room temperature.

The first study was to observe the evolution of the *hkl* cubic peaks when cooling down to room temperature. This study was carried on by cropping the locations of the cubic reflections from summed oscillation images at ±0.5° ϕ and observing the changes in the cubic reflections when cooling to room temperature. Figure 6.16 shows the locations of (200) cubic reflections and their transformation to the tetragonal (200), (020) and (002) reflections when cooling down to room temperature. The cubic reflections were observed to be sharp and intense at above Curie temperature. When cooling to room temperature, the centrosymmetric cubic phase (*pm3m*) transforms to noncentrosymmetric tetragonal phase by first transforming to an intermediate noncentrosymmetric tetragonal phase (*p4mm*). During the phase

transformation from *pm3m* to *p4mm*, the cubic unit cell slightly contracts along *a* axis and expands along *c* axis [Buttner, R. H. (1992)]. During the further cooling to room temperature, the tetragonality increases by cooling and domains form at room temperature.

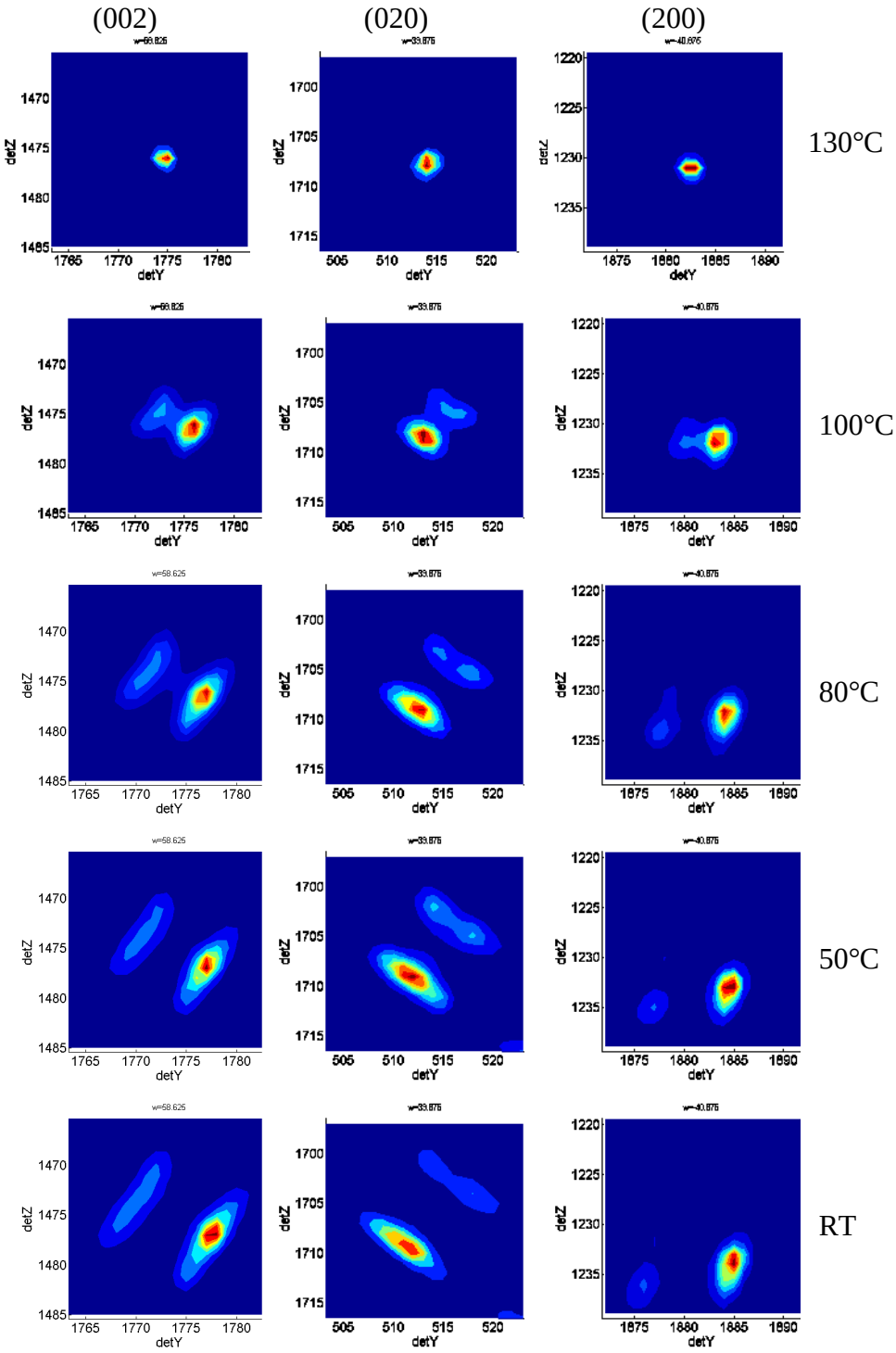

Figure 6.16. The evolution of 002 and 200 peaks by cooling to room temperature

Table 6.6 shows the orientations fitted with the routine described in Section 6.2.2 and misorientation angles of the domains with respect to cubic grain. The scattering vectors of the calculated orientations were compared with the experimental scattering vectors and the difference in ϕ and η was less than 0.1°. The domain A has the smallest misorientation with the cubic grain. Therefore, this domain can be considered as the parent domain. The orientation of Domain C can be obtained by rotating 89.74° around [0 1 0] axis of the cubic grain. This rotation is also equivalent to 180° rotation around the normal of tetragonal (101) plane. The theoretical misorientation angle of the domains can be calculated as $2\tan^{-1}(a/c)$ where *a* and *c* are the lattice parameters. For $BaTiO_3$, where c/a ratio is 1.0092, the theoretical misorientation angle between domains is 89.47°.

Table 6.6. The list of orientation relationships of the cubic grains and their domain variants as cooling to room temperature. The orientations were expressed as tensor and angle-axis pairs. The misorientation between domain variants was defined with respect to cubic grain.

Temperature		
130°C	RT	
Orientation Matrix	Orientation Matrix, Misor. Angle Orien. ID	
0.606 0.300 0.737 -0.753 0.516 0.408 -0.258 -0.802 0.538	0.607 0.295 0.738 -0.750 0.519 0.409 -0.262 -0.802 0.537 0.32° [-0.35 0.05 0.94]	A
	0.741 -0.604 -0.294 0.407 0.752 -0.518 0.534 0.265 0.803 89.9° [1 0 0]	B1
	0.738 -0.604 -0.300 0.403 0.752 -0.521 0.541 0.264 0.799 89.64° [-1 0 0]	B2
	0.740 0.295 -0.604 0.406 0.521 0.751 0.536 -0.801 0.266 89.74° [0 -1 0]	C

One of the striking finding from Table 6.6 is that there are four tetragonal domains formed from the cubic grain. We expect 3 domains as each of polarization vectors of the domains will form along the main cubic axes. The domains B1 and B2 are first considered as the subdomains inside the grain because the misorientation angle between these two domains is 0.4734°. The smallest misorientation angle between the domains can be 1.2° where two domains can rotate around a common plane with positive and negative rotation. The close inspection of the domain microstructure confirmed that these domains are actually c domains where their polarization vectors pointed along z and –z direction. Because of the ambiguity in xrays where the positive and negative directions are not detectable, we see two close spots diffracting from domains pointing opposite directions. The crystal directions of these close spots are opposite as well and we see (002) and $(00\bar{2})$ crystal directions as close spots.

Figure 6.17.a and b show the typical 3D arrangements of the ferroelectric domains in a grain and the schematic distribution of the polarization vectors of the domains respectively. The domains are separated from each other with domain boundaries. The microstructure in Figure 6.17.a is called “wedge shaped” in the literature [Merz, W. J. (1952)]. Arlt, G. (1990) discusses that this type of microstructure can have the minimum elastic energy. The domains in Figure 3.b is shown with their polarization vector directions with respect to sample coordinates. As shown in Table 1, domain A is pointed along x direction and this domain is more likely the parent domain due to its small misorientation angle with the cubic grain. The misorientation between domain A and domain B2 is 89.64° by rotation around [-100] axis of domain A. This clearly shows that the polarization vector of domain B2 is upwards along z direction. They are separated by (011) domain boundary. The misorientation angle and axis between domain A and C is 89.74° [0 -1 0]. The polarization vector of domain C is along y axis and these domains are separated by (-101) domain boundary. Finally, the misorientation between domain A and B1 is 89.9° around [100] axis of domain A. Based on this model, the misorientation angle between domain B1 and B2 was found as 0.52° and this angle is well matched with the misorientation angle found from the domains (i.e. 0.4734°). The three-dimensional arrangement of the domain variants is assumed to repeat itself inside the grain.

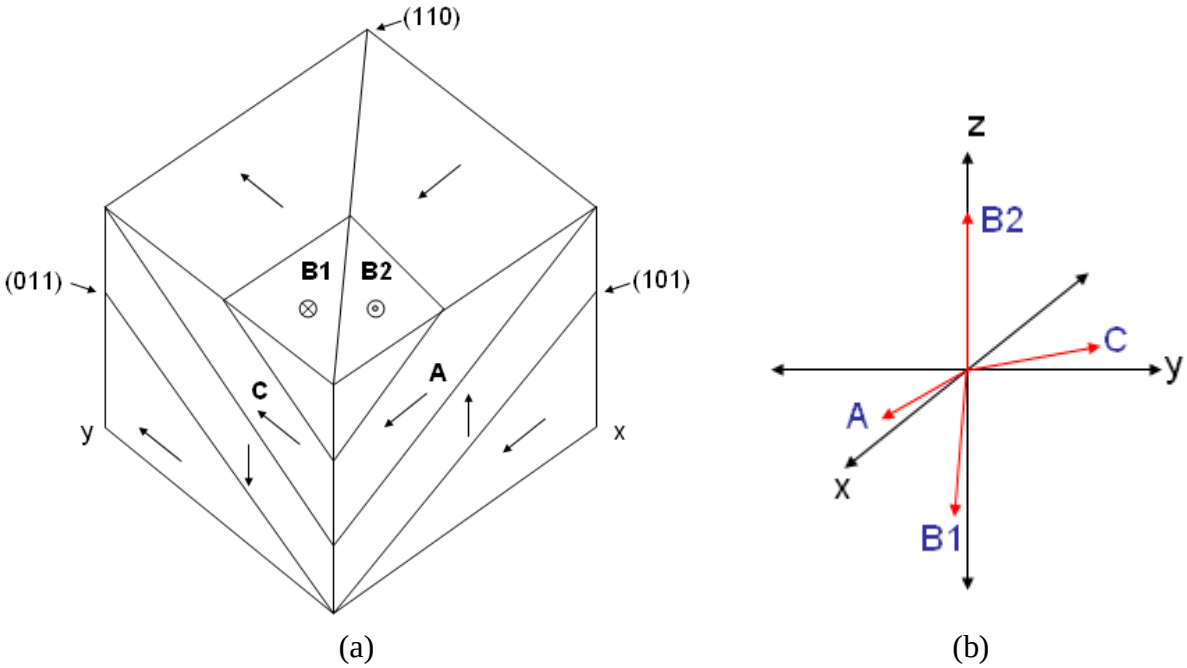

Figure 6.17. Schematic 3D arrangement of the ferroelectric domains. (b) The schematic distributions of the polarization vectors of the domains in sample coordinates.

When cooling from Curie temperature, each grain breaks up to domains to reduce the overall energy of the system [Arlt, G. (1990)]. Figure 6.18 shows the [100], [010] and [001] directions of the cubic grain and domain variants in pole figure as stereographic projection. For clarity, Wulf plot was overlaid to pole figure. The c axes of the domains are marked with red colors and the direction of the e-field was shown in Y axis as well. As clearly seen, the cubic crystal directions transform to tetragonal when cooling to room temperature and due to tetragonality, each cubic crystal directions break up to domains. For instance [100] cubic direction breaks up to [100], [010] and [001] tetragonal directions and each direction is shared by a domain. As shown in close-up view in Figure 4 the angle between the crystal directions of the domains is around 0.6° i.e. $2\tan^{-1}(c/a) - 90°$ where c/a ratio is 1.0092 for $BaTiO_3$. While forming the domains, it is also seen in Figure 6.18 that transformation from cubic to tetragonal is displacive and doesn't involve a significant grain rotation.

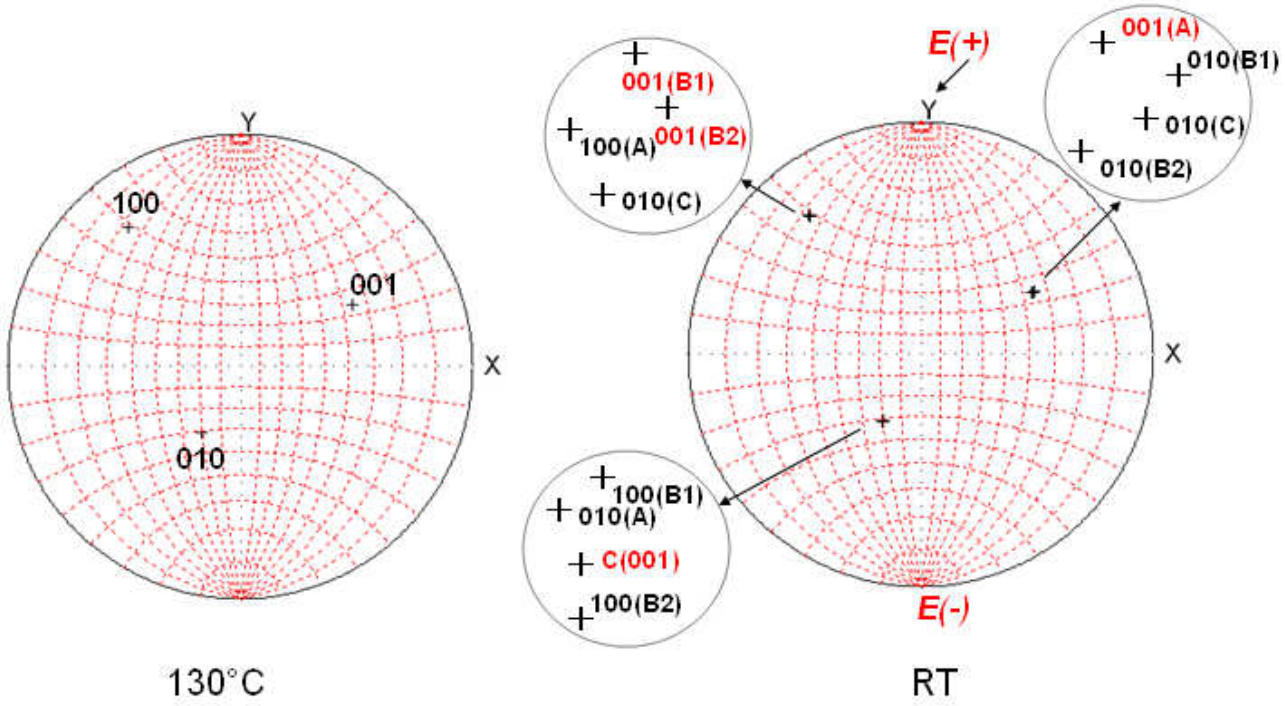

Figure 6. 18. {100} pole figures as a stereographic projection at above Curie and room temperature. The Wulf plot was overlaid for clarity. The orientations with letters at room temperature are shown in Table 1 and they are the domain variants within the grain. The electric field direction is Y-axis and the angles between c-axis of the domains (shown in red color) and the electric field are shown as well.

Figure 6.19 shows the ϕ-η distribution of the (002) reflections of the domain variants at above Curie temperature and room temperature. This distribution is obtained by binning (002) diffraction rings along η and integrating along 2θ. The markers at each map show the predictions of the calculated orientations found by technique described earlier and there is a good correlation between calculated and observed reflections. Figure 6.19 also shows the Friedel pair of the same reflections and Friedel pair of Domain A is missing because it diffracts out of oscillation range. From Table 1, Domain *A* has the same orientation with the cubic grain and appears as uniform domain with no close spots. Domain *B1 and B2* appear as close spots and one might consider them as directly in contact and separated by a coherent domain boundary. As described previously, these domains are actually pointing along the opposite directions and we observe them close spots due to ambiguity of detecting opposite directions in x-rays. The neighboring close spots are considered as not belonging to the same

grain because they have cubic reflections and they don't transform from the parent cubic reflections. The neighboring close spots that are not appearing at Friedel pairs are also considered as spots that diffract coincidentally at given ϕ and don't belong to same grain. Domain *C* appears as uniform domain as well. Between Domain A, B1, B2 and C, there are domain boundaries with a transition region and the orientation relationship of the domains is explained in Figure 6.18.

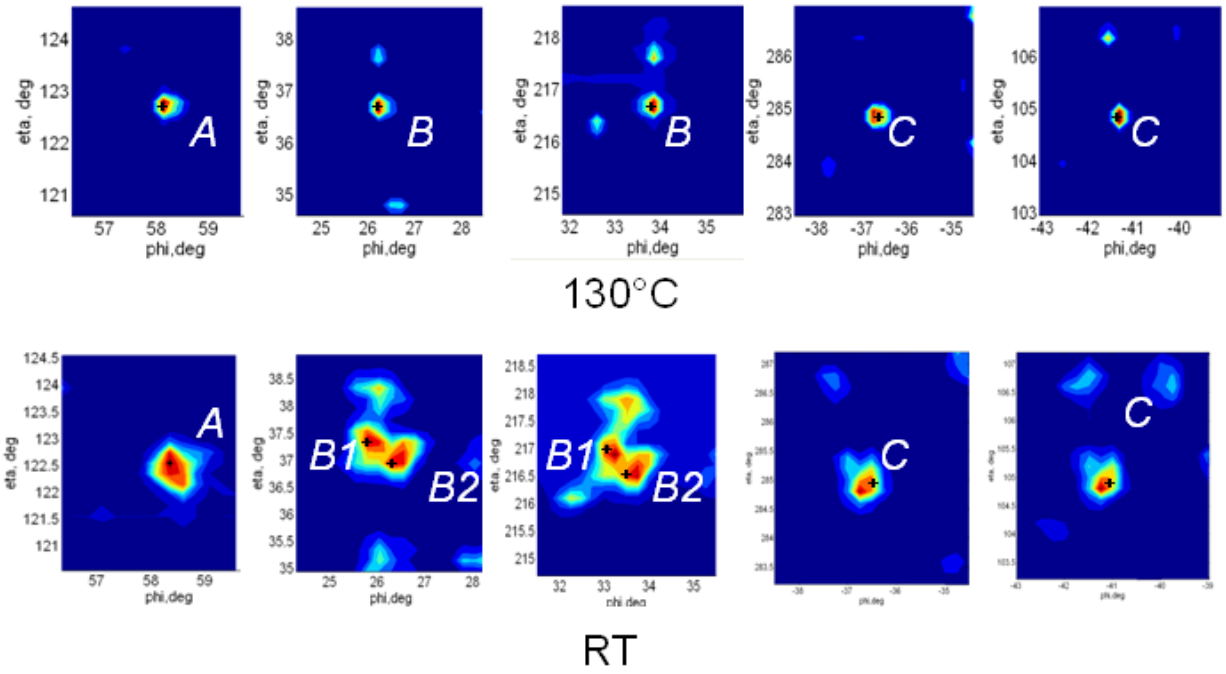

Figure 6.19. The phi-eta distribution of (002) reflections of the domains. The markers A, B and C represent the orientations shown at Table 1. The figures with a similar pattern are from Friedel pairs of the same reflections.

Electric field was applied to the sample up to 10kV/cm. Considering the coercive field of $BaTiO_3$ was measured as 5.14 kV/cm, the applied electric field was enough to trigger the domain switching. In order to quantify the overall change in the orientation of the domains, the orientations of the domains are calculated from its reflections at given electric field. The overall change was expressed with the misorientation angle between the domain at given electric field and the same domain with no electric field. Figure 6.20 shows the orientation change of the domains with applied electric field. Except the domain perpendicular to electric field, no significant domain rotation was observed.

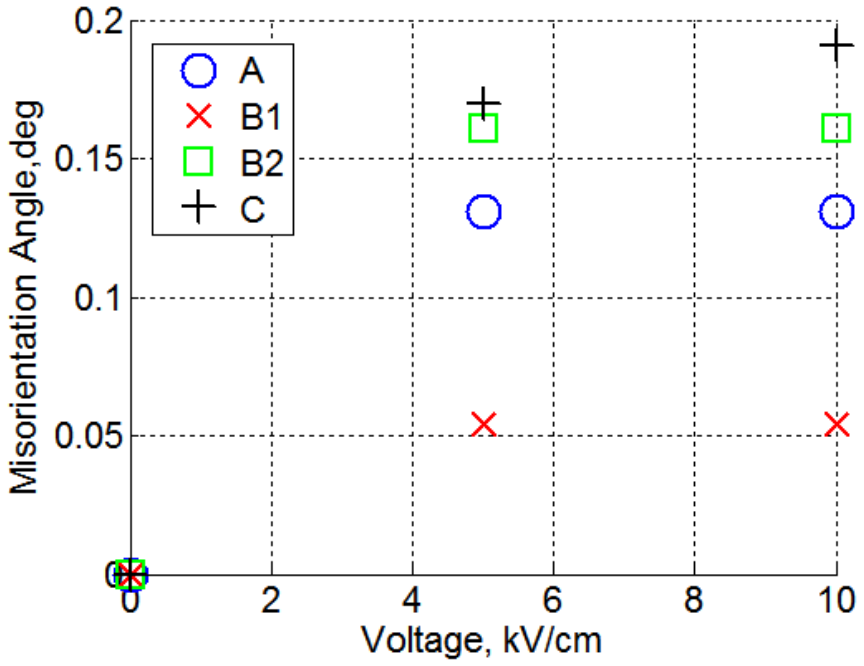

Figure 6.20. The orientation change of the domains with applied electric field

In order to understand why domains behave to the electric field differently, the angle between c axis of the domain and the electric field direction was calculated from the orientation matrices of the domains. We define this angle as "polarization angle". The polarization angles for Domain *A*, *B1*, *B2* and *C* are calculated as 65.8°, 58.8°, 58.6 and 41.3°. Since domain *A* has a large polarization angle, the application of the electric field is expected to cause the domain switching in greater scale in this domain. Therefore, the orientation change of this domain was observed to be the highest. This is also a proof that domains don't rotate during the poling process. The domain walls move as respond to electric field and the volume fraction of the domains will favor on the domain is the most energetically favorable.

There is a direct relation between the volume of the domain and the integrated intensity of the domain. In order to observe the volume fraction change between domain variants with applied electric field, the integrated intensities of the domains were calculated and the volume fraction of the domain within a grain (f_{002}^{d}) can be found as:

$$f_{002}^{d} = \frac{I_{002}^{d}}{(I_{200}^{dv} + I_{020}^{dv} + I_{002}^{d})} \tag{6.20}$$

where I_{002}^{d} is the integrated intensity of (002) spot from a domain and I_{200}^{dv} and I_{020}^{dv} are the integrated intensity of the (200) and (020) reflections of the remaining domain variants within the grain. The reflections are taken from the domain variants shown in Figure 4. To eliminate the effect of the Lorentz factor, the domain variants that diffract at the same η and ϕ are taken. For instance, (002) reflection of the domain A diffracting at η=122.5° and ϕ=58.4° is compared with the (200) and (020) reflections of the domain variants B1, B2 and C ant the same η and ϕ. For many cases, I_{200}^{dv} and I_{020}^{dv} are difficult to resolve due to spot overlap and the sum of these overlapped spots are taken in the calculation. To improve the statistics, the Friedel pair of the spot is measured as well.

Figure 6.21 shows the volume fraction change in the domain variants with applied electric field. The polarization angles for Domain *A*, *B1*, *B2* and *C* are calculated as 65.8°, 58.8°, 58.6 and 41.3°. The application of the electric field favors for the domain that is close the electric field direction. In this case, Domain B1 and B2 are the most favorable domain with its low polarization angle. Indeed, the volume fraction of Domain B1 and B2 increases with electric field up to 10kV/cm. This is due to lattice configuration and the polarization angle of the subdomains. With its high polarization angle, the volume fraction of Domain A decreases by around 50%. The volume fraction of domain C increases with electric field as well but this increase is not as significant as domain *B1* and *B2*. Beyond 10kV/cm, it is expected that the fraction of the energetically favorable domain variant increases. Due to grain boundaries and local boundary conditions, the overall switching from one domain is not complete. The higher electric field can be achieved by immersing the sample in a dielectric liquid but this has not been feasible in our setup because the sample needs to be exposed to heating prior to electric field to track the evolution of the same grain.

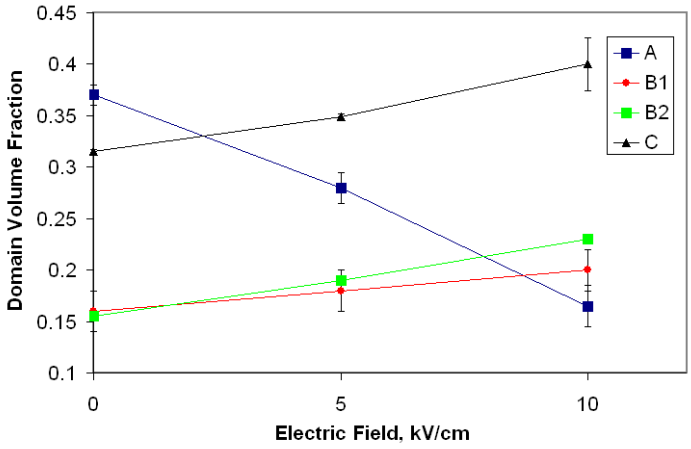

Figure 6. 21. The volume fraction change in the domains with the electric field. The error bars shows the independent measurements from Friedel pairs. The volume fraction was calculated from Eq. (6.20) which doesn't require a correction of Lorentz factor because the domain variants diffract at the close η and ϕ.

As seen in the orientation relationships of the domains, there is a slight deviation in the misorientation angles between domains and parent grain when cooling down to room temperature. This may come from the mismatch between the lattice parameters of the local domains and the creation of the spontaneous deformation during the cooling process. Figure 6.22 shows the schematic depiction of the pseudo-90° domains. The spontaneous deformation of the domains creates a mismatch in the domain walls and results in the rotation of the domains to reduce the spontaneous strain between the domains. This mechanism can also be considered as domain clamping effect during the cooling. As described with details in Appendix 7, Nepochatenko, V. A. (2006) modeled the mismatch angle between domains and this angle can be calculated as:

$$\Psi = \cos^{-1}\left(\frac{a_1 + c_1}{\sqrt{2(a_1^2 + c_1^2)}}\right) \qquad (6.21)$$

where a and c correspond to lattice parameters of the domains. Considering the lattice parameters for the $BaTiO_3$ sample were measured as a=0.39836 and c=0.40198 nm, the phase matching angle can be calculated as 0.314°. This angle is very close to the misorientation angle between the parent grain and domain. Most of the domains still deviate from the theoretical values which show the local lattice parameters of the domains that differ

from the average values. One explanation can be the Jahn-Teller effect which corresponds to a geometrical distortion in the oxygen tetrahedral due to deviations of the local domains.

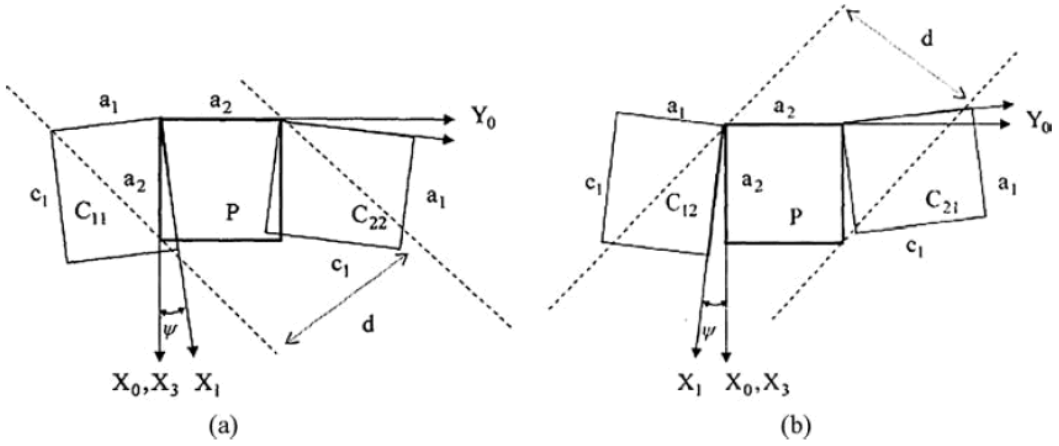

Figure 6.22. Schematic depiction of structure of pseudo-90° walls [Nepochatenko, V. A. (2006)]. ψ corresponds to phase matching angle between the domains.

The transformation mechanism of the cubic grain to tetragonal domains is further studied with more grains. Table 6.7 shows the grains investigated and the orientation relationships of the grains with the corresponding domains.

Table 6.7. The orientation relationships of the grains and domains when cooling down to room temperature

Grain Orientation	**Grain Number**	**Domain Orientations** **Misorientation Angle and Axis**
		0.416 0.909 0.028 0.791 -0.346 -0.505 -0.449 0.233 -0.863 B1 0.42° [0.91 0.2 0.36]
0.909 -0.029 -0.416 -0.344 0.511 -0.788 0.235 0.859 0.454	135	-0.903 0.429 0.030 0.355 0.783 -0.511 -0.243 -0.451 -0.859 B2 0.7° [0.06 -0.27 -0.96]
		-0.909 0.025 -0.416 0.346 -0.510 -0.787 -0.232 -0.859 0.455 A 89.95° [1 0 0]

Table 6.7 (Continued)

				0.417 0.908 0.022 0.785 -0.348 -0.512 -0.458 0.231 -0.859 C 0.34° [0.65 0.7 0.29]
				-0.410 0.912 -0.020 -0.791 -0.345 0.505 0.454 0.224 0.863 0.74° [0.2 0.67 0.72]
				0.880 0.238 -0.411 0.228 0.546 0.806 0.417 -0.803 0.427 89.93° [-1 0 0]
0.882 -0.412 -0.229 0.235 0.806 -0.543 0.409 0.425 0.808			208	0.883 0.222 -0.413 0.236 0.550 0.801 0.405 -0.805 0.434 89.46° [-1 0 0]
				0.883 -0.412 -0.227 0.235 0.805 -0.545 0.407 0.427 0.807 0.17° [0.73 0.54 -0.42]
				0.508 -0.564 -0.651 -0.227 0.641 -0.733 0.831 0.520 0.198 89.74° [0 -1 0]
-0.656 0.507 -0.559 -0.729 -0.232 0.644 0.197 0.830 0.521			218	-0.656 0.506 -0.560 -0.728 -0.229 0.646 0.199 0.831 0.519 89.85° [1 0 0]
				-0.995 -0.037 0.093 0.054 -0.982 0.180 0.085 0.184 0.979 0.36 [0.39 0.28 0.88]
0.091 -0.995 -0.043 0.178 0.058 -0.982 0.979 0.082 0.183			327	0.092 -0.995 -0.045 0.174 0.060 -0.983 0.980 0.082 0.179 89.79 [-1 0 0]
				0.092 -0.995 -0.041 0.171 0.056 -0.984 0.981 0.083 0.176 89.61° [-1 0 0]

One of the grains (#135) in Table 6.7 was further investigated. Figure 6.23 shows the (002) directions of four domains. (002) crystal direction of this grain gradually transforms to four domains.

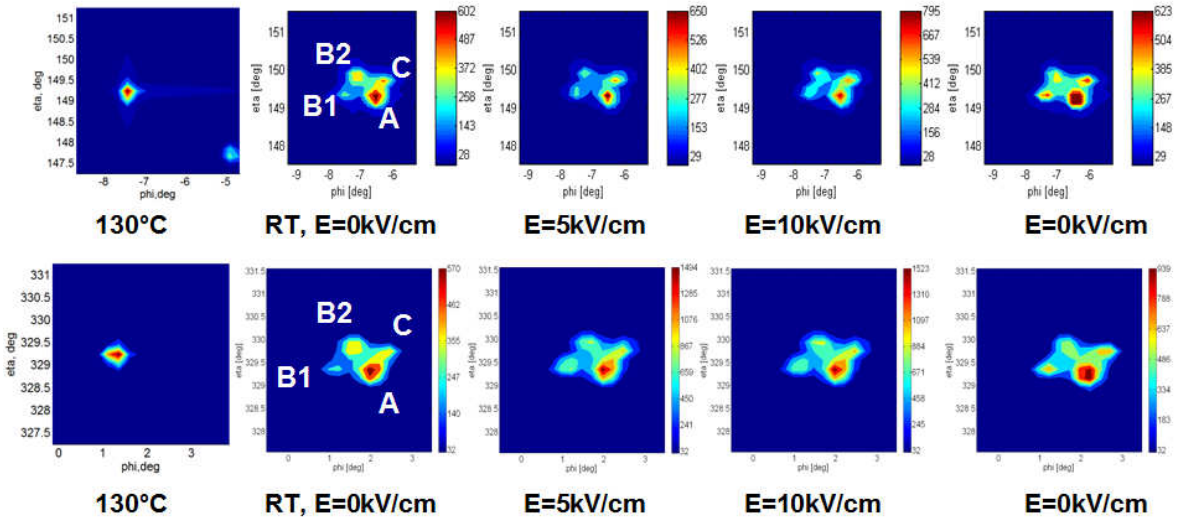

Figure 6. 23. Evolution of 002 reflections with temperature and electric field

The integrated intensity values of the domains shown in Figure 6.24 are calculated and the volume fractions of the domains are studied with the electric field. Figure 6.24 shows the evolution of the volume fraction of the domains with applied electric field. With application of electric field, the volume of the Domain A decreases while Domain C increases. Domain B1 and B2 remain unchanged with the application of electric field.

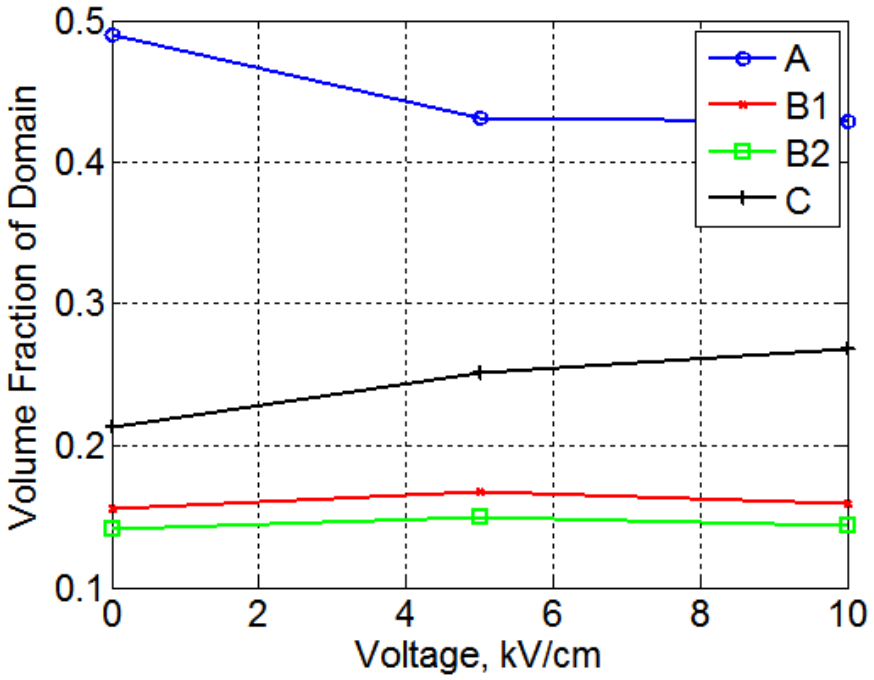

Figure 6. 24. The evolution of the volume fractions of the domains with the electric field

6.2.3.1. Lattice Strain by Domain Switching and Temperature

The evolution of the triaxial strain state of the polycrystalline $BaTiO_3$ as response to electric field was studied in macroscopic and mesoscopic scale. In macroscopic scale, the strain evolution was investigated from parallel to perpendicular direction of applied electric field. In mesoscale, the strain evolution of the domains within a grain was studied. The results were compared with the strains obtained from piezoelectric constants of $BaTiO_3$.

6.2.3.1.1. Macroscopic Strain

Figure 6.25 (a) shows the lattice strain evolution of the ferroelectric $BaTiO_3$ with applied electric field. The results were obtained by powder averaging the diffraction data and then observing the changes in the interplanar spaces of the diffraction planes. Since the direction of the applied electric field has a direct effect on the texture of the domains, the parallel direction to the applied field are studied because they will experience highest degree

of the domain switching. The position of the *hkl* peaks were found by single peak fitting. With the application of electric field, the highest strain was seen in (111) and (202) planes. While there is a compressive strain developed in (002) plane, no significant amount of strain was observed in (200) plane with applied electric field.

Figure 6.25(b) shows the lattice strain tensor evolution of the same sample with applied electric field. The lattice strain tensor was obtained from lattice strains shown in Figure 6.25(a). With the application of electric field, a tensile strain was observed along the *yy* and *xz* direction. *YY* direction corresponds to the applied electric field direction and a tensile strain is developed along the electric field. Development of a tensile strain was also observed along the shear direction (*XZ*) to the applied electric field direction.

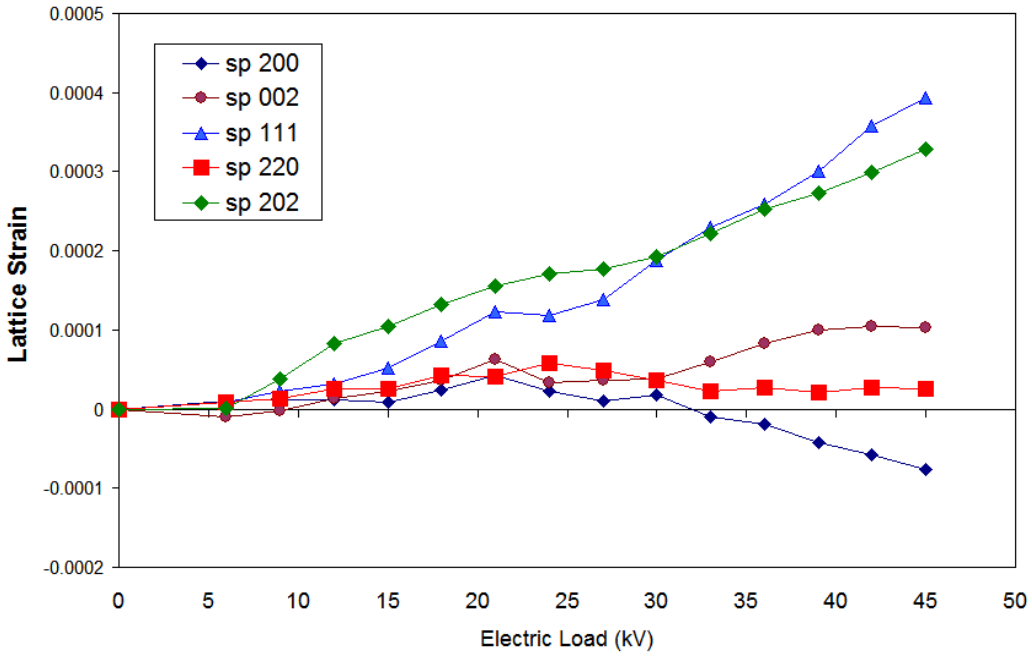

Figure 6.25 (a)

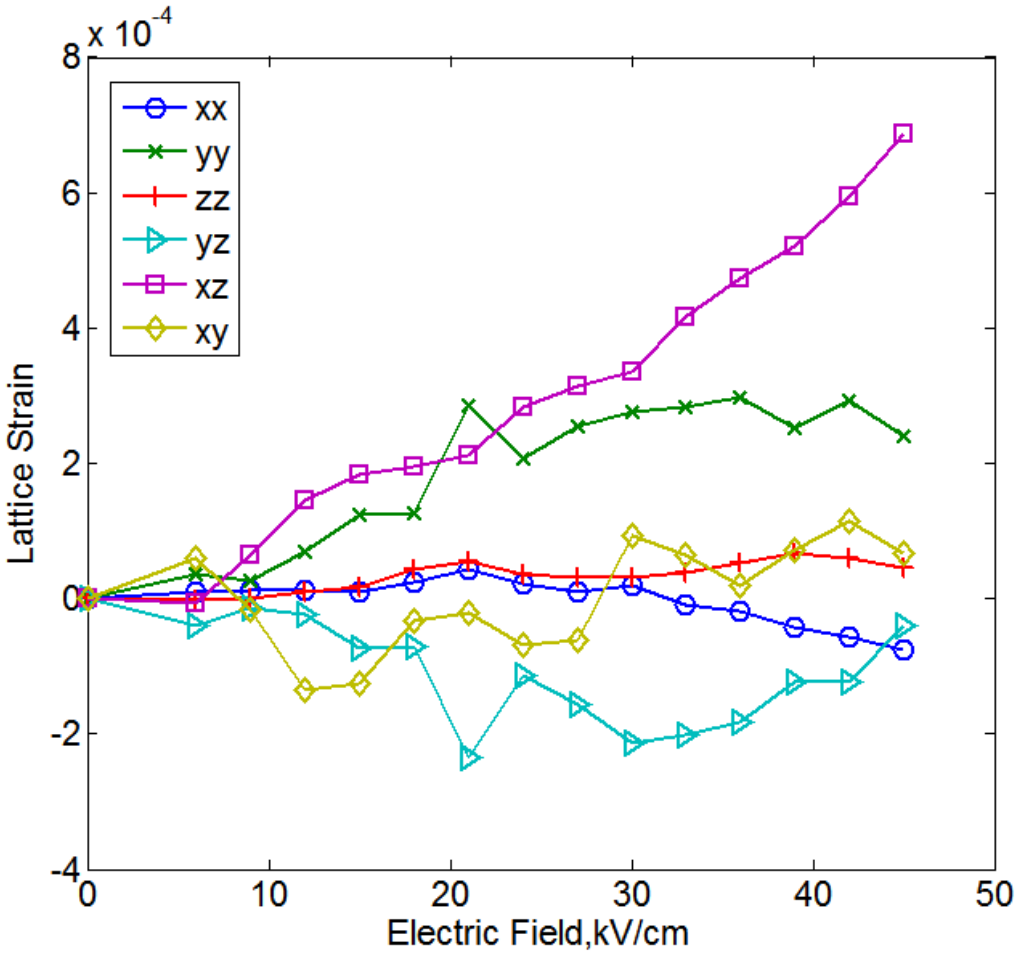

(b)

Figure 6. 25. (a) Lattice strain evolution of the ferroelectric $BaTiO_3$ with applied electric field. (b) Lattice strain tensor evolution of the same sample with applied electric field

6.2.3.1.2. Mesoscopic Strain

As the technique described above, the lattice strain tensor can be measured from powder average and domain variants. In order to confirm the strain free material as cooling down to room temperature, the first study was based on studying the evolution of the hkl cubic peaks when cooling down to room temperature. This study was carried on by summing oscillation images along phi and caking along radial direction from 0 to 360°. Figure 6.26 shows the caked diffraction patterns from different temperatures and the evolution of the peak splitting when cooling to room temperature. At each temperature, the positions of the diffraction peaks were found with Gaussian fitting function and spot strains were calculated

compared to cubic grain. We see the largest lattice change from [h00] and [00l] type peaks up to 5500 microstrain (=0.55%).

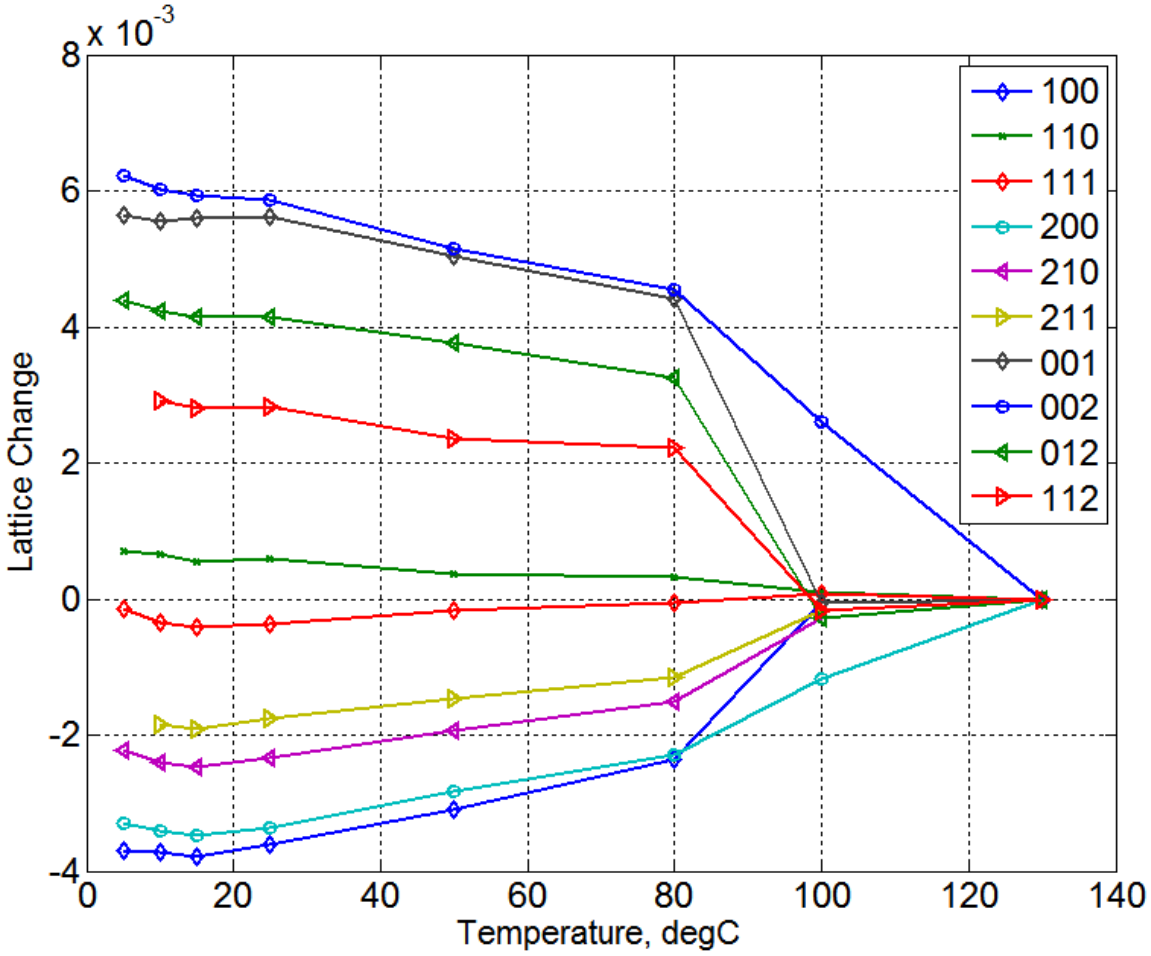

(b)

Figure 6.26. *hkl* lattice change of $BaTiO_3$ during the cooling from above Curie temperature to room temperature

With applied electric field up to 10 kV/cm, the overall lattice strain tensor for the powder average was found to be:

Applied Field, kV/cm Strain Tensor (ε_{ij})

5kV/cm $\begin{pmatrix} 56 & -40 & 0 \\ & 159 & 90 \\ & & 29 \end{pmatrix}$

10kV/cm $\begin{pmatrix} -75 & -292 & -40 \\ & 503 & -74 \\ & & 41 \end{pmatrix}$

As the lattice strain tensor are shown in microstrain (i.e. 10^{-6}). If the results are compared with the piezoelectric constants of the single crystal $BaTiO_3$, around 600 microstrain is expected along *yy* direction where the electric field direction is. Here the results are offers a good agreements with the calculated values when considering the strain resolution at APS Sector 1-ID is 10^{-4} (100 microstrain).

The lattice strain tensors of the ferroelectric domains are calculated by fitting the overall change of the diffraction peaks belong to the domains. As reference, the peak positions at room temperature and zero electric field are taken. To improve statistical errors, the Friedel pairs of the same spots are measured as well and the average values are taken as within 100 microstrain. With the application of the electric field up to 5kV/cm, the lattice strain tensors of the ferroelectric domains are found as:

Domain ID	Strain Tensor (ε_{ij})
B	$\begin{pmatrix} 13 & 0 & 0 \\ & 800 & 0 \\ & & -511 \end{pmatrix}$
C	$\begin{pmatrix} 0 & -292 & -40 \\ & 552 & -74 \\ & & -211 \end{pmatrix}$

where the marked domains are confirmed to be present in the grain tracked. As compared to powder average, the slightly higher normal strains along *yy* axis are observed with the application of electric field in these domains. This is due the local variation of the domains compared to powder average. One also can note that Domain B has slightly larger normal strain than Domain C. This can be explained by the angle between c-axis of the domains with respect to electric field, so-called “polarization angle”. The polarization angles for Domain B and C are calculated as 65.9° and 41.3°. Since the Domain B has larger angle with respect to electric field, we can expect slightly higher normal strain along electric field direction.

6.2.3.1.3. Comparison with Model

The measured strain values are the ones measured directly from the material. In order to compare the strain findings with the data itself, the strain values were calculated from the constitute relations. The three dimensional strain state will be directly proportional to the piezoelectric tensor, applied electric field and the applied stress. By assuming the material was stress free during the experiment, the strain tensor can be calculated from the piezoelectric coefficients of $BaTiO_3$ by applying electric field. The constitutive relations of the strain [Jaffe, B. (1971)] are

$$S_{ij} = d_{ijk} E_k + S^E_{ijkl} T_{kl} \qquad (6.22)$$

where S_{ij} is the strain tensor, d_{ijk} is the piezoelectric coefficient tensor, E_k is the applied electric field, S^E_{ijkl} is the compliance tensor and T_{kl} is the stress tensor. For $BaTiO_3$, piezoelectric coefficient parameters [Simmons, G. et al. (1971)] used were d_{15}=580, d_{13}=-50, d_{33}=191 in 10^{-12} C/N and compliance parameters are used as S_{11}=0.8050, S_{12}=-0.235, S_{13}=-0.524, S_{33}=1.57, S_{44}=1.84, S_{66}=0.884 in 10^{-12} m^2/N. Figure 6.27 shows the strain evolution of $BaTiO_3$ with applied electric field.

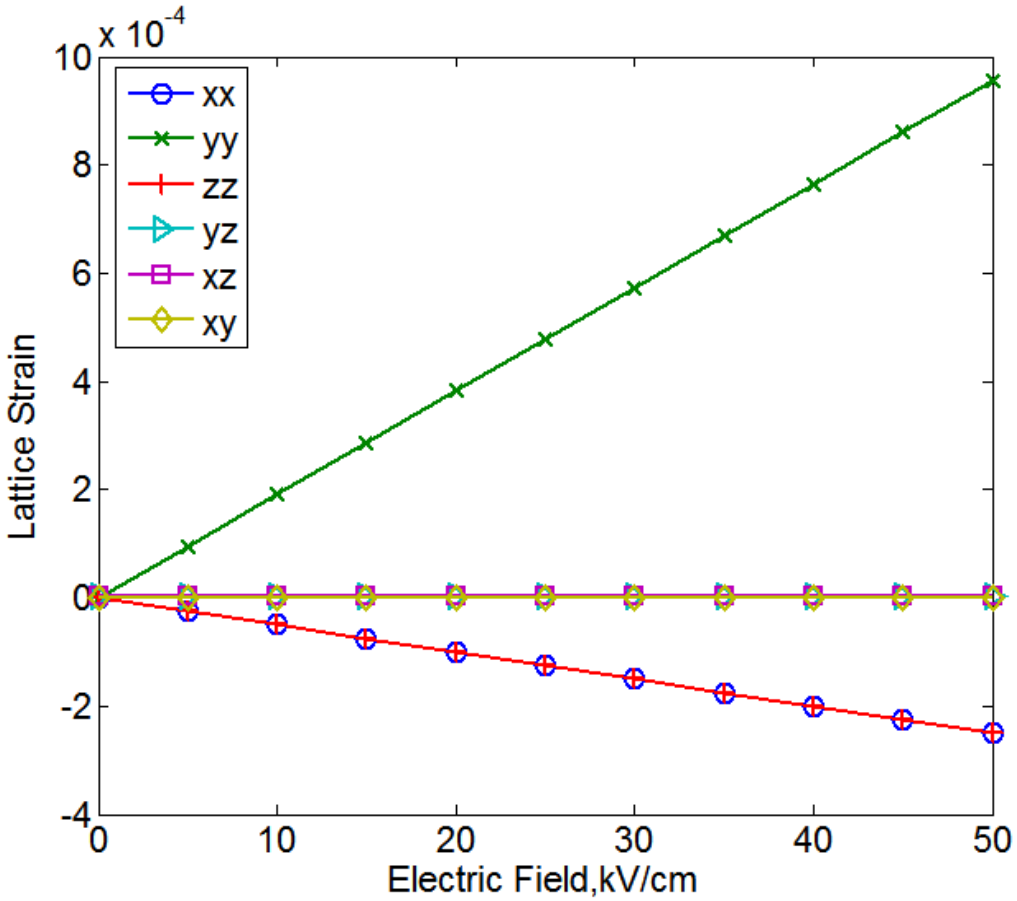

Figure 6.27. The strain evolution of $BaTiO_3$ with applied electric field

Compared to constitutive relations of the $BaTiO_3$ with the measured data, we can observe discrepancies in the strain evolution. Rather than a strain development suggested by the constitutive relations of $BaTiO_3$, we observe a shear strain development perpendicular to the applied field direction.

The overall strain measured from powder average and the ferroelectric domains suggest that the strain developed with applied electric field is rather small. The main source of the discrepancies is the complicated domain pattern which makes a challenge to accurately characterize the mesoscale domain dynamics. To date, most research has concentrated on averaging the bulk behavior and ignoring the contribution of the individual domains. As recalled, in tetragonal symmetry, electric field can lead to both 180° and 90° domains while mechanical stress can cause only 90° domain switching [Berlincourt, D. (1959)]. While Merz

[Merz, W. J. (1952)] indicated that the final domain structure must contain all 180° domains, Merz, W. J. (1952) later observed reoriented 90° domains as high electric fields. In another interesting research, Danielson, G. C. (1949) investigated the domain orientation in polycrystalline $BaTiO_3$ under applied electric field and found that 80% of the polycrystal consists of 180° domains while rest is 90° domains. Berlincourt, D. (1959) predicted that 2/3 of the total polarization occurs due to 90° domains switching, 1/6 occurs due to 180^o switching and the rest is due to the intrinsic piezoelectric effect. Since the 90° reorientation of domains requires more energy, the fraction of the 90° domains is not usually significant in the final microstructure. All of these studies, however, relied on bulk averaging or surface characterizations. Berlincourt, D. (1959) also predict the highest achievable strain in the single crystal ferroelectrics is c/a=0.37% when all the domains experience 90° domain switching. Since the remnant polarization of the polycrystalline ferroelectrics (around 8μC/cm) is one/third of the one in single crystal (26 μC/cm), the highest achievable strain in polycrystalline ferroelectric will be 0.12%. This value agrees well with the experimental findings. The present study attempts to offer more detailed information on domain switching in polycrystalline ferroelectrics.

6.3. Microdiffraction

The *Scanning X-Ray Microdiffraction* experiments were conducted at the microdiffraction end-station (initially at Beamline 7.3.3, lately at 12.3.2) of the Advanced Light Source at Lawrence Berkeley National Laboratory, Berkeley, CA. These experiments concentrated on the evolution of domains in polycrystalline $BaTiO_3$ with the temperature and electric field.

6.3.1. Evolution of Ferroelectric Domains around the Curie Temperature

The evolution of ferroelectric domains inside a single grain of a polycrystalline $BaTiO_3$ ceramic was investigated under quasistatic heating by using polychromatic scanning X-ray microdiffraction (μSXRD). Four domain orientations were observed from certain reflections and the 180° domain wall separating two domains was measured to be 180.47°. While heating the polycrystalline $BaTiO_3$ from room temperature to above the Curie temperature (125°C), the ferroelectric domains rotate towards the paraelectric cubic

orientation. The crystallographic relationships of the domains with respect to paraelectric phase were explained using a domain structure model by Nepochatenko, V. A. (2006). With the direct experimental observations, the technique was proved to be capable of studying ferroelectric domains embedded in polycrystalline ferroelectrics.

6.3.1.1. Introduction

Ferroelectric materials have been extensively used in microelectronic and sensing applications for more than 50 years because of their excellent piezoelectric properties [Jona, F. (1962)]. $BaTiO_3$ was one of the first commercially viable ferroelectrics [Jaffe, B. (1971)] and has been one of the most widely investigated ferroelectrics with its simple and well-known structure [Haertling, G. H. (1999)]. Upon cooling from a paraelectric phase, the polar axes of the individual clusters within a ferroelectric $BaTiO_3$ can orient in certain crystallographic directions to minimize the overall energy of the system [Arlt, G. (1990)]. These individual clusters are called ferroelectric domains. The orientation of the domains depends on the crystal structure and the spontaneous polarization of the ferroelectric domains can be parallel to a cube edge (6 possible directions in total), body diagonal (8) and face diagonal (12) for tetragonal, rhombohedral and orthorhombic symmetries, respectively [Li, F. X. (2006)]. For tetragonal ferroelectrics, the final microstructure is composed of 90° and 180° domains where the polarization vectors of adjacent domains are perpendicular and parallel to each other, respectively. Since the c/a ratio of $BaTiO_3$ is not unity, γ, the angle between c axes of two 90° domains is

$$\gamma = 2\tan^{-1}\left(\frac{a}{c}\right) \qquad (6.23)$$

For example, γ = 89.44° for polycrystalline $BaTiO_3$ with c/a=1.0098 [Harada, J. et al. (1970)]. Therefore, the angle between *a* and *c* axes of two adjacent domains is 0.54°.

Due to the relative ease of conventional ceramic processing [Jordan, T. L. (2001), Rogan, R. (2003)], the most commonly employed ferroelectrics are processed in polycrystalline form in which the material is composed of a collection of crystallographic grains with distinct orientations. In ferroelectric polycrystalline materials, each grain contains

domains that are oriented with respect to one another by specific crystal symmetry operations. The domains belonging to the same grain are referred to as domain variants. The domain structure in ferroelectric ceramics exhibits a more complex pattern compared to single crystals. Several techniques such as transmission electron microscopy (TEM) [Tan, X. (2004), Schönau, K. A. (2007)], White Beam Topography [Huang, X. R. (1996)], Electron Back Scattering Diffraction [Ernst, F. et al (2001)], optical microscopy and atomic force microscopy [Balakumar, S. et al (1997), Kalinin, S.V. (2001)], etc. have been used to characterize the ferroelectric domain structure but quantitive information on the orientation, strain and mesoscale dynamics within the ferroelectric domains are often lacking.

Temperature dictates both the formation of the ferroelectric phase from the paraelectric phase and the lattice aspect ratio of the ferroelectric phase, the latter of which affects the orientation relationships (Eq. 1). Experiments as a function of temperature can therefore be useful to measure the evolution of mesoscale domain patterns in polycrystalline ferroelectrics. During cooling from an elevated temperature, the domain variants experience a phase transformation from cubic to tetragonal and the orientation of the grain can be distinctly determined.

Ferroelectrics are extremely sensitive to the nature of the surface, defect structure, sample preparation [Chen, J-H, (2005), Chang, W. (2007)] and sample geometry [Lines, M. E. (1977)]. Therefore, surface-sensitive characterization techniques may measure behavior that is not representative of the bulk. Synchrotron-based polychromatic Scanning X-Ray Microdiffraction (μSXRD), on the other hand, is a promising non-destructive tool with greater penetration depth than these other techniques (25μm penetration depth in $BaTiO_3$ at 5-16 keV as compared to 5 μm using conventional laboratory X-rays or electron microscopy), adequate resolution in strain (0.02%) and crystallite orientation (0.01°) as well as microfocusing capability providing submicron spatial resolution [Goudeau, P. et al (2005)]. The fundamental principles of Laue or polychromatic X-Ray microdiffraction have been described elsewhere [Chung, J-S. Ice, G. E. (1999)] and only a brief introduction is provided here. Laue microdiffraction utilizes microfocused polychromatic X-rays to illuminate an area of the sample as small as 1 μm^2. Multiple diffracting planes then provide a Laue diffraction pattern of individual crystalline grains from a small region of material

embedded in a polycrystalline material. Laue microdiffraction can be used in scanning mode (polychromatic μSXRD) by raster-scanning the sample under the X-ray microbeam and measuring a Laue pattern at each step to obtain orientation and/or strain maps of the sample. Furthermore, the recent implementation of fast data acquisition and analysis programs such as XMAS (X-Ray Micro Analysis Software) [Tamura, N. (2003)] as well as the development of high-precision diffractometers [Tamura, N. (2003)] provides unique opportunities for μSXRD. In the present work, the μSXRD technique isused to study the local, microscale and mesoscale behavior of polycrystalline ferroelectric materials during heating.

6.3.1.2. Experimental Procedure

A polycrystalline $BaTiO_3$ ceramic was prepared using conventional high temperature sintering [Bryne T.A., (2004)] of $BaTiO_3$ powder (99.9% purity, with Ba/Ti ratio=1.00, Ferro Corp., Transelco Division). The nominal grain size was measured as approximately 20 μm as determined from an independent EBSD study with a $BaTiO_3$ sample from the same batch. The sample dimensions measured 1 mm x 1 mm x 5 mm and no electric field was applied prior to the experiment. The sample was attached on a heating element by using high temperature conductive glue (AA-Bond 200 Adhesive) to prevent sample movement during heating. The heating stage consists of a sample holder and a heating element bound by an Indium-Gallium coating to increase the conductivity. The temperature profile was monitored by one thermocouple attached to the surface of the sample (Fluke 87IV True RMS Thermometer), one from the heating element (Extech 421307 thermometer) and one with the IR thermometer (Extech Mini IR Thermometer 42500) pointed to the surface of the sample throughout the experiment. The sample was heated with steps up to and above the Curie temperature. The temperature variation between the thermometers did not exceed ±5°C for any temperature step.

For capacitance measurements, a sample was selected from the same batch and its surface was polished with fine paper to remove any surface contamination. The sample surfaces were sputtered with gold and a drop of silver paint was placed on the top of the electrodes to ensure a good electrical contact. Capacitance measurements were conducted using a Keithley 3330 LCZ meter at 0.1, 1, 10, and 100 kHz. Capacitance versus temperature

measurements took place in an environmental chamber by heating up to 150°C with 5°C/min heating rate and cooling back to room temperature. The capacitance response of the $BaTiO_3$ sample was recorded during the heating followed by cooling and only the heating part is included the present work because the measurements during cooling are identical to those measured during heating. The temperature was measured with a thermocouple placed in the vicinity of the sample.

μSXRD experiments were carried out on the X-ray microdiffraction end-station (7.3.3.) at the Advanced Light Source (ALS). The instrument has a capability of delivering X-ray white beam (5-14 keV) with less than 1 μm beam size by using a pair of elliptically bent mirrors in a Kirkpatrick-Baez configuration [Tamura, N. (2003)]. The diffraction patterns were collected with an area scan at room temperature and repeating at higher temperature steps. At each position of the area scans, the sample was exposed to X-rays for 2 seconds. The back-reflection Laue diffraction patterns produced by the white X-rays with 1 μm beam size were recorded using an X-ray CCD detector (MAR133) mounted on a vertical slide. The active area of the CCD camera had a diameter of 133 mm and we used the 1024x1024 pixels binned mode. The sample surface was set at 45° relative to the incoming beam and the detector. The distance from the CCD to the sample and the center of the diffraction patterns on CCD detector were determined to be 63.00 mm and 640.5, 514.2 pixels respectively.

The collected white-beam (Laue) diffraction patterns were analyzed with the custom XMAS software developed at the ALS. XMAS is capable of determining the positions of the reflections with subpixel resolution by using two-dimensional profile functions such as Gaussian, Lorentzian or Pearson VII. By using the peak positions and lattice parameters of $BaTiO_3$, each reflection was indexed with (hkl) indices. After indexing, the crystal orientations as an orientation matrix and the deviatoric strain tensor were obtained for each domain belonging to the illuminated area. The lattice parameter values of $BaTiO_3$ at room temperature used for the indexing procedure were a = 3.9947 Å and c = 4.0336 Å [Rogan, R. (2003)].

The orientation matrices in XMAS define the coordinates of the crystallites in the sample coordinate system unlike the standard definition of the orientation matrices as the

direction cosines between the crystallites and the sample axes. Therefore, the orientation matrices must be normalized with the corresponding lattice parameters to convert the standard orientation matrices. The resultant orientations are a set of rotations that are a function of crystal symmetry. A proper representation of the orientations is important because the misorientations between differing orientations should be independent of the crystal symmetry. Therefore, the orientations are required to be mapped to a unique solution, fundamental region [Frank, F. C. (1988), Morawiec, A. (1997)], in the orientation space. Fundamental region [Sundararaghavan, S. (2007)] represents a region in the orientation space where the all symmetrically equivalent orientations can be mapped into a uniquely determined one. In order to find the misorientation between the orientations of the domains, the orientations were mapped into the corresponding fundamental region with the symmetry operators in corresponding crystal structures. The fundamental regions of the cubic grain and tetragonal domains were determined with *m3m* and *4mm* point symmetry respectively. The misorientations between the grain-to-domains and domains-to-domains were calculated by using ODF/PF software package from Cornell University [Dawson, P. (2005), Frank, F.C. (1988)]. As the misorientation convention, angle-axis pairs were used. This convention has a major advantage to show the misorientation angle and axis with respect to the reference grain, information that is helpful when describing the misorientation angle between domains and the rotation axis between the domain variants.

6.3.1.3. Results and Discussion

Figure 6.28 shows the capacitance versus temperature profile of the $BaTiO_3$ sample measured at several different frequencies. The peak in capacitance was measured as 125.32 °C ± 0.06°C for all four frequencies.

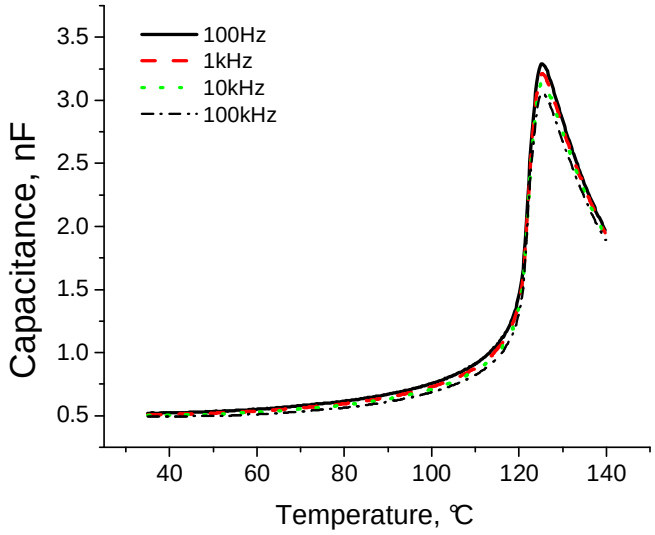

Figure 6.28. Capacitance change in $BaTiO_3$ as a function of temperature

Diffraction images were collected from the polycrystalline $BaTiO_3$ at each temperature step. At each temperature, an area of 50 μm^2 was scanned using 1.5 µm steps. At room temperature, the diffraction pattern shows four close spots. One of these grains was selected as reference and the diameter of this grain was found to be 16.5 µm by translating the stage and observing the distance required for significant changes in the diffraction pattern that are indicative of sampling a different grain orientation. Figure 6.29 shows the diffraction patterns of the reference grain recorded at room temperature (Fig. 6.29a) and 150°C (Fig. 6.29b), at temperature which is above the Curie temperature of $BaTiO_3$. During the heating cycle from room temperature to above the Curie temperature, the spots gradually converge to one. This is illustrated in an enlarged portion of the diffraction pattern in Figure 6.29c. Preceding the phase transformation from tetragonal to cubic, the ferroelectric domains rotate to the overall orientation of the grain. At a temperature of 125°C, only one spot can be distinguished in the diffraction pattern. The coalescence of the diffraction spots correlate with the capacitance measurements presented in Figure 6.28 and, therefore, the evolution of the ferroelectric domains within the grain. Furthermore, the relative positions of the spots as a function of temperature mimic the changes in the lattice parameters as a function of temperature. These observations suggest that the four different spots correspond to four

unique domain orientations in a tetragonal perovskite crystal, a result which is consistent with the expected domain wall orientations [Sapriel, J. (1975), Nepochatenko, V. A. (2006)].

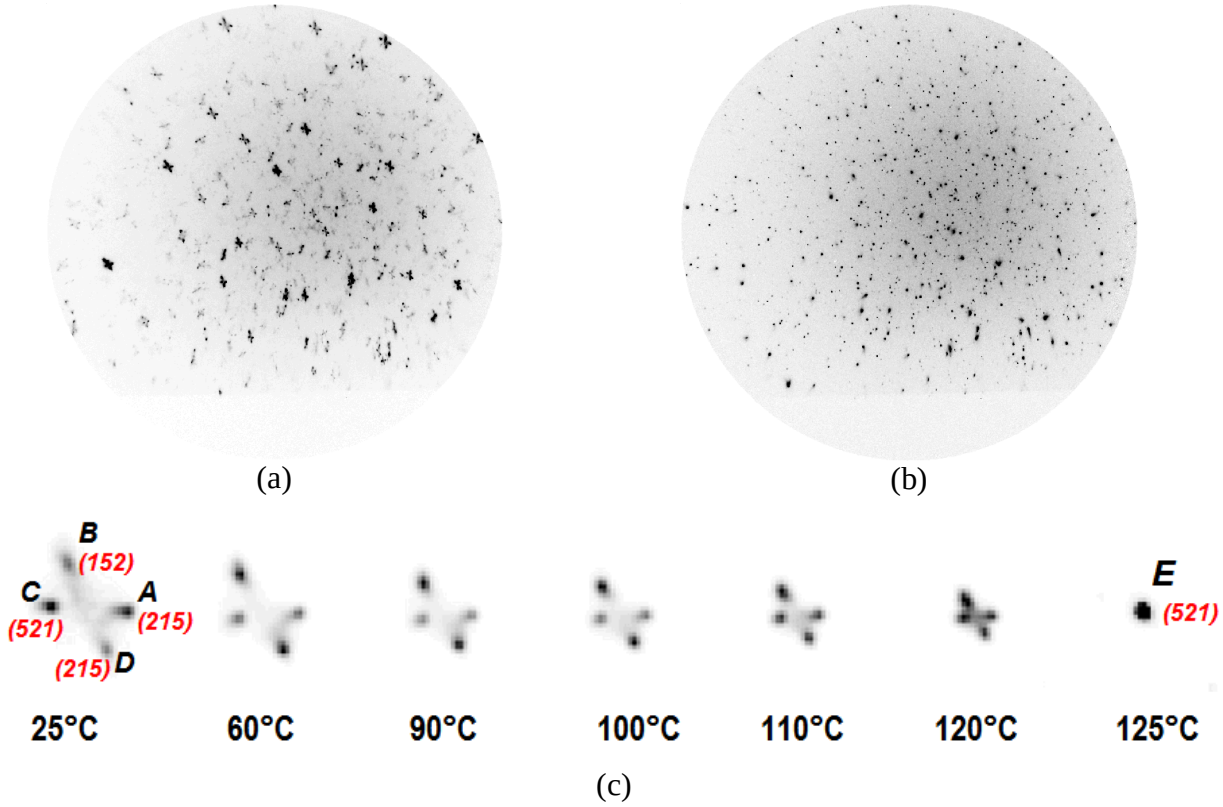

Figure 6.29. Laue diffraction patterns of $BaTiO_3$ recorded at (a) room temperature, (b) above Curie temperature (150°C). (c) The evolution of (215) spots of ferroelectric domains in $BaTiO_3$ sample as a function of temperature. Four spots become spot *E* at temperatures above the Curie temperature

The diffraction spots can be reconciled with the domain structures as follows. When the spontaneous polarization is formed with respect to a paraelectric cubic structure, several different 90° domain wall orientations can form. For instance, for a spontaneous polarization developed parallel to the [001] crystal direction, the domain walls can form parallel to $(101), (\bar{1}01)$, (011) and $(0\bar{1}1)$ planes, creating four domains with perpendicular polarization vectors relative to the [001] polarization direction. These four neighboring domains would have spontaneous polarization vectors parallel to [100], [010], $[\bar{1}00]$ and $[0\bar{1}0]$. In absence of a domain architecture model in which to reconcile the formation of such domains in real

space, the domain walls separating $[\bar{1}00]$ and [100] domains are typically referred to as 180° domain walls as their orientations can be reproduced from one another though a 180° crystallographic rotation. However, the domain architectures in real space can provide more information that is critical to interpreting the μSXRD measurement. A typical "wedge shaped" domain architecture in polycrystalline ferroelectrics is shown in Figure 6.30(b) [Merz, W. J. (1952)]. Arlt, G. (1990) discusses that this type domain architecture exhibits the minimum elastic energy. In Figure 6.30(a), the schematic distributions of the domain variants at room temperature are shown as crystal directions. The structure exhibits four domain variants with virtual polarization vectors pointed parallel to [001], [100], [010] and $[00\bar{1}]$ for domains *A*, *B*, *C*, and *D*, respectively. The domain walls between domain *A* and *C*, *C* and *B*, *B* and *D*, *D* and *A* are (101), (110), (011) and (110) respectively. The angle between the polarization axis of *A* and *C* is defined by Eq. (6.23) and will be equal to a value less than 90°. The angle between *C* and *B* is also an angle less than 90° as well as the angle between *B* and *D*. Thus, when describing the orientation of domains A, C, B, and D in sequence, the polarization direction of A is not found to be antiparallel to the polarization direction of D. Instead, the two domain orientations are related through an angle that will be referred to as the mismatch angle. The mismatch angle is developed during the cubic-to-tetragonal transformation and can be obtained by applying the spontaneous deformation transformation. The angle between the ferroelectric domain and the paraelectric phase corresponds to phase matching angle as described by Nepochatenko, V.A. (2006) and is given by the equation

$$\psi = \cos^{-1}\left(\frac{2+\varepsilon_{11}+\varepsilon_{22}}{\sqrt{2}\sqrt{(1+\varepsilon_{11})^2+(1+\varepsilon_{22})^2}}\right) = \cos^{-1}\left(\frac{a+c}{\sqrt{2}\sqrt{a^2+c^2}}\right) \qquad (6.24)$$

where ε_{11}, ε_{22} are the spontaneous strain components ($\varepsilon_{11} = (a-a_0)/a_0$, $\varepsilon_{22} = (c-a_0)/a_0$) that represent the lattice parameters for cubic phase (a_0) change to tetragonal (*a*, *c*). The mismatch angle between 180° domains corresponds to twice the phase matching angle between the ferroelectric and paraelectric phase developed during the cubic-to-tetragonal phase transformation to maintain the strain compatibility between neighboring domains [Sapriel, J. (1975), Nepochatenko, V. A. (2006)]. In order to satisfy the mechanical

compatibility, the neighboring domain must share a domain wall with the paraelectric phase. Considering the paraelectric phase doesn't change during the cubic-tetragonal phase transformation, the neighboring domain must share a domain wall with the paraelectric phase. The domain pairs then have domain walls that are perpendicular to each other. For instance, if a domain is separated with the paraelectric phase with (101) domain wall, the neighboring domain must be separated with $(\bar{1}01)$ domain wall with the paraelectric phase in order to have common and stable paraelectric phase that does not change during the phase transformation. Such domains develop a phase matching angle with respect to paraelectric phase with and separated with ($\pm\psi$) as described by Nepochatenko, V. A. (2006).

The crystallographic orientation of domain A is therefore not related to the orientation of domain D by a rotation of 180°, even though they are classically defined as 180° domains. Instead, their respective orientations can be calculated by a crystallographic rotation of approximately 180.55° (using values of a = 3.9947 Å and c = 4.0336 Å [Rogan, R. (2003)]). The structural nature of the interface between domains of this type is not considered in the present work, although it is noted that the lattice mismatch requires an elastic accommodation mechanism and the increasing lattice aspect ratio with decreasing temperature gradually changes this angle. Possible accommodation mechanisms may include a series of dislocations or elastic strain near the domain wall. The region of the diffraction pattern between the diffraction spots shows diffuse scattering (Fig. 6.29c) which may support either of these mechanisms.

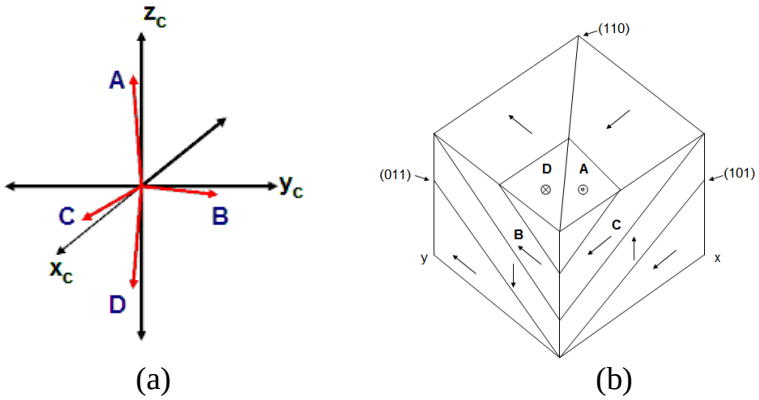

(a) (b)

Figure 6.30. (a) The schematic distributions of the domain variants in misorientation axes. The misorientation axes were based on the cubic grain and the angles were exaggerated for clarity. (b) The three dimensional arrangement of the domains.

By considering all the cube faces {100} as a possibility of spontaneous polarizations in tetragonal ferroelectrics, there can be four {110} 90° domain wall types relative to the cubic axis. However, since there are six possible domain variants in tetragonal structures, a total of 24 90° domains wall orientations can develop in a three dimensional arrangement. Due to the ambiguity of the directions in X-rays where the positive and negative directions are not detectable, a maximum of 12 domain wall types can be detected using X-ray diffraction.

The changes in the lattice parameters play an important role in the formation of the domains. During cooling, the lattice parameters in the tetragonal structure create an elastic driving force for the formation of the domain variants. Figure 6.29(c) shows the temperature evolution of the (215) spots in the heating regime. The close spots are marked with a letter. As the temperature is increased to a value near the Curie temperature, these diffraction spots begin to coalesce. These spots then become the same orientation (identified as E in Fig. 2c) at temperatures above the Curie temperature.

Table 6.8 shows the orientations of the domains at room temperature and the grain at above Curie temperature. The orientations are shown as direction cosines between the crystal lattice and global directions. Each column in the orientation matrices represents the direction cosines of the crystal lattice with respect to certain global direction. As seen in Table 6.8(a), the domain orientations are produced from the crystals pointing at different global directions. While domains A and D have similar crystal orientations in global coordinates, the orientations of domains B and C can be produced from domain A by rotating approximately 90° around [100] and [010], respectively. The misorientation angles of the respective domain orientations are also reported in Table 6.8. To obtain the misorientation angles, domain A was selected as the reference domain. The orientations of domains B and C are related to domain A by angles of 89.63° ($\approx 2\tan^{-1}(a/c)$) and 89.41°, respectively. Domain D appears as closely oriented to domain A with a 0.474° misorientation angle. The orientations of domains B and C were obtained by taking the domain A as reference orientation. By taking into account the varying c/a ratios of the domains (Table 6.8), the orientations of domain B

and C are related with twinning operations as m[011] and m[101] respectively. The orientation relations of the domains are confirmed to be consistent with Keeble, D. S. (2009)'s study on the tetragonal single crystal $BaTiO_3$.

As the temperature is increased to above the Curie temperature, the diffraction spots coalesce to a single spot, *E*. The transformation of these spots represents the disappearance of the domain structure within the grain as the Curie temperature is passed and the material becomes paraelectric. From the calculated misorientation between the orientations of the domain variants and the orientation of the grain with spot E shown in Table 6.8, none of the domains have an orientation that equals that of the grain in the paraelectric cubic state. Nepochatenko, V. A. (2006) has shown that the domains can rotate a small angle during the cubic-to-tetragonal phase transformation to maintain the strain compatibility as a function of changing lattice aspect ratio. This rotation is relative to the sample coordinate axes and represents a rotation of the entire domain crystal axes; such a rotation is not the same as a polarization rotation involving crystallographic distortions as described by Ahart, M. et al (2008). The rotation angle of the domain with respect to paraelectric phase is referred to as the "phase matching angle" and this angle was calculated as 0.28°±0.03° from the major axes between the domains and the grain by using Eq. (6.24). The comparison of the orientation of the grain and domains shows good agreement to the predicted phase matching angle.

Table 6.8. The orientations and misorientations of the domains seen at room temperature and above Curie temperature. The misorientations between the domains were calculated by selecting either domain A or domain E as the reference domain.

Domain*		Orientation Matrix			Misorientation Angle, [Axis]	Misorientation Angle, [Axis]	c/a Ratio
Room Temperature	A	0.846	0.193	-0.497	Reference	0.36°, [-0.23 0.6 0.77]	1.01
		0.119	0.8340	0.529			
		0.519	-0.507	0.687			
	B	0.842	-0.500	-0.200	89.63°, [1 0 0]	89.47°, [1 0 0]	1.088
		0.118	0.534	-0.8367			
		0.526	0.681	0.509			
	C	0.507	0.192	0.840	89.41°, [0 1 0]	89.67°, [0 1 0]	1.011
		-0.527	0.839	0.126			
		-0.681	-0.508	0.527			
	D	0.842	0.194	-0.502	0.47°, [0.59 -0.66 -0.47]	0.2°, [0.9 -0.41 0.18]	1.098
		0.119	0.843	0.525			
		0.525	-0.502	0.687			
$T > T_C$ (150° C)	E	0.842	0.194	-0.502	n/a	Reference	1
		0.119	0.841	0.526			
		0.524	-0.504	0.686			

The orientations demonstrate that the spontaneous polarization vectors of the domains form perpendicular to the cube faces, {100}, or parallel to the cube edges, <100>. To illustrate this further, Figure 6.31 shows the 001 pole figure for the domains inside of the reference grain at room temperature (Fig. 6.31a) and the 100 pole figure for the reference grain in the high temperature cubic phase (Fig. 6.31b). There is correlation between the [001] of the low temperature orientations and the <001> of the high temperature orientations.

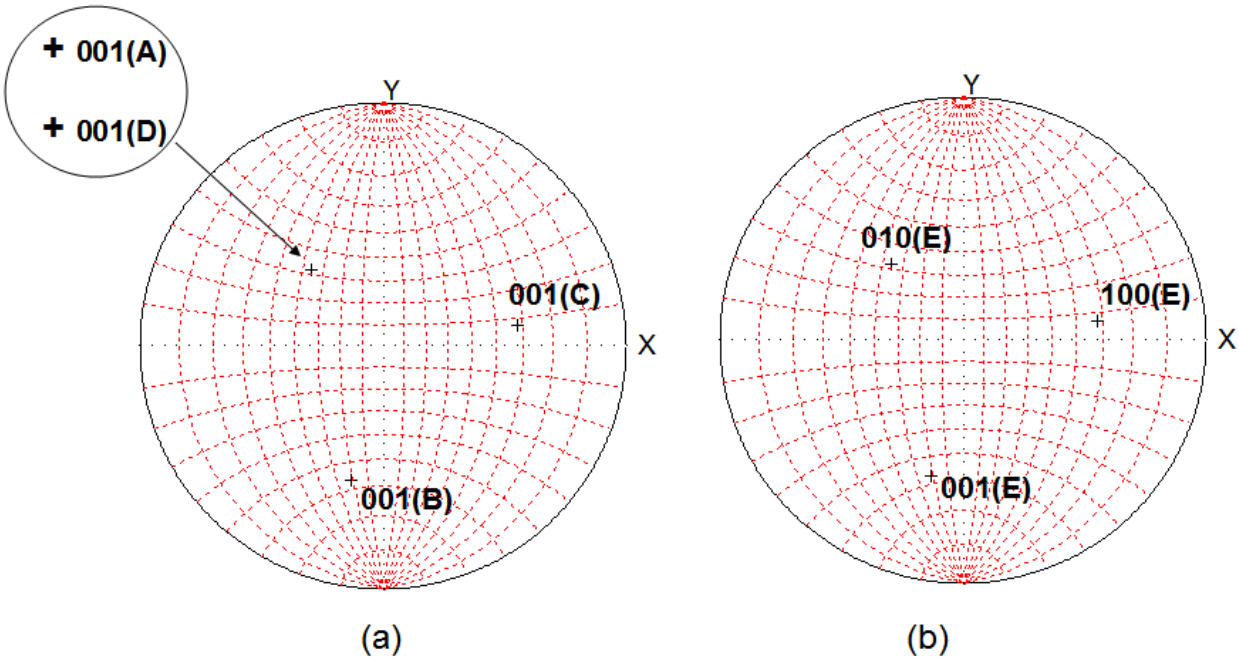

Figure 6.31. (a) 001 pole figure of the ferroelectric domain orientations at room temperature. (b) 100 pole figure of the grain at a temperature above the Curie temperature. Wulff net is overlaid for clarity. The orientations correspond to those presented in Table 6.8

A closer inspection of the diffraction patterns as a function of distance along the sample surface in 1.5 µm steps demonstrates that the spots representing different orientations have varying intensities. Because the thickness of the domains is smaller than the beam size (1 µm), different domains are being illuminated by the beam as the sample is moved. Since the same domain diffraction patterns are observed as the sample stage is moved, this three-dimensional arrangement of the domain variants is assumed to repeat itself inside the grain.

During heating from room temperature, the domains experience a gradual rotation and lattice parameter changes that result in the individual diffraction spots converging into a single diffraction spot at the Curie temperature. Figure 6.32(a) shows the evolution of the a/c ratio calculated as a function of temperature. The error bars were determined from independent a/c calculations of the domains at given temperature. The relatively different a/c ratios of the domains suggest that the local domains can show significant deviations from the from the local structure. During the phase transformation, the relative change in orientations of the domains can be calculated from the refinements of the peak position. These orientation relationships are related directly to the changes in the lattice parameter. For instance, the angles between domains A and C and between domains B and D have been calculated to be 89.61° and 89.58°, respectively, at a temperature of 90°C. The angles between these domain pairs were calculated for all the different temperature from the (251) and (351) diffraction peaks. Figure 6.32(b) shows the angular separations between the domain pairs A and C and B and D during heating. The orientation fitting was rather difficult at 120°C because the diffraction spots were very close to each other so it wasn't included. As the sample is heated to temperatures approaching the Curie temperature, the ferroelectric domains become more closely oriented to one another as well as become more closely oriented to the high temperature cubic orientation. The domains converge to a single orientation at temperatures near and above the Curie temperature. The comparison of the angular separation between the domains and theoretical misorientation angle calculated from c/a ratio by using Eq. (6.23) shows excellent correlations. The angular separation of the domain pairs is also well correlated with the capacitance versus temperature measurements as shown in Figure 6.28.

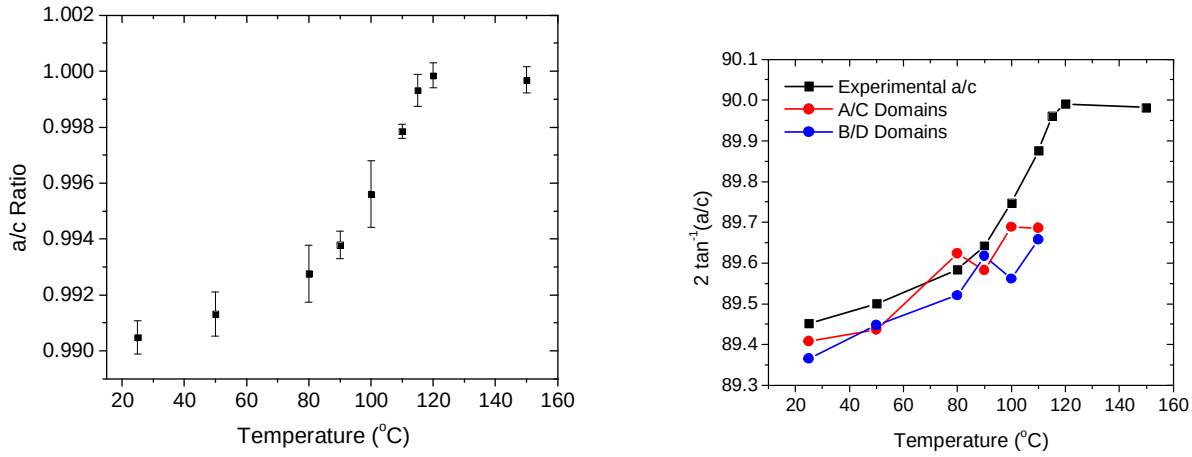

(a) (b)

Figure 6. 32 (a) The evolution of a/c ratio as a function temperature. (b) The angles between domain pairs (A/C and B/D) as a function of the temperature. Black curves were calculated by using tangent formula (Eq. 6.23)

The evolution of the ferroelectric domains inside the polycrystalline $BaTiO_3$ was investigated during quasistatic heating using scanning X-ray microdiffraction (μSXRD). Four domains are observed for certain reflections indicating that two domains that are classically defined as 180° domains may exhibit an orientation relationship that deviates from 180°. The crystallographic relationships of the domains are explained using a domain structure model by Nepochatenko, V. A. (2006). While heating the polycrystalline $BaTiO_3$ from room temperature to above the Curie temperature, the ferroelectric domains coalesce by gradual rotations that reflect their changing lattice aspect ratio. With the direct experimental observations, the technique is proved to be capable of studying ferroelectric domains embedded in polycrystalline ferroelectrics.

6.3.2. Ferroelectric domains in a polycrystalline $BaTiO_3$ under quasistatic heating and applied electric field

The evolution of the ferroelectric domains in a polycrystalline $BaTiO_3$ grain was studied as a function of applied electric field and heating by using Scanning Microdiffraction (μSXRD) technique. By cooling to room temperature, the cubic grain transform to tetragonal domains. By application of the electric field, polarization vectors of the domain rotated along the direction of the electric field. The changes in the volume fraction of the domains are

measured with the electric field. The complete domain switching to one domain variant is not observed with the application of the electric field. The local boundary conditions hindering the complete domain switching such as grain boundaries and surface charges are discussed.

6.3.2.1. Experimental Procedure

The polycrystal $BaTiO_3$ samples were manufactured with conventional powder processing techniques [Bryne, T. A. (2004)] from $BaTiO_3$ powder (99.9% pure, with Ba/Ti ratio=1.00, Ferro Corp., Transelco Division). The grain size of the sample was measured at approximately 20 µm and the sample dimensions were 1x1x5 $mm^{3.}$ During polishing, extra caution was shown not to introduce residual stress to the sample. The sides of the sample were coated with a conductive silver paint and copper wires were attached to the side with high temperature conductive glue (AA-Bond 200 Adhesive). No electric field was applied to sample prior to the experiment. Figure 6.33 shows the schematic setup for the experiment. The sample was attached on a heating stage by using high temperature conductive glue (AA-Bond 200 Adhesive) to prevent the sample moving due to heating. The heating stage consisted of a sample holder and a heating element bound by copper coating to increase the conductivity. To prevent a possible electric arcing between the heating stage and the sample, an insulating layer with captone tape was applied in the interface. The temperature profile was monitored by three thermocouples; one was attached to the surface of the sample (Fluke 87IV True RMS Thermometer), one from the heating element (Extech 421307 thermometer) and one with the IR thermometer (Extech Mini IR Thermometer 42500) pointed to the surface of the sample throughout the experiment. The sample was heated to above Curie temperature (150°C) where the tetragonal-to-cubic phase transformation was complete. The complete phase transformation was confirmed with the microdiffraction images. After an initial area scan with a coarse grid size to locate the grains, the sample was cooled to room temperature. The diameter of the reference grain was around 25µm. To make sure that the same sample location is scanned during cooling, a tiny lead piece was attached on the sample as a reference point. While cooling, the orientation evolution of the cubic grain was studied. At each cooling temperature steps, the location of the reference point was checked with fluorescence scan to make sure that polychromatic x-rays illuminates the same grain on the sample. After cooling to room temperature, the sample was exposed to a constant electric

field at 10, 15, 25 and 30 kV/cm. The amount of the applied electric field was above the coercive field which was measured as 5.14 kV/cm with hysteresis measurements. At each electric field, the 50x50 μm^2 area was scanned with 1µm step size. The evolution of the ferroelectric domains at the same grain was tracked with a final scan after reducing the electric field to zero. The orientation of the sample with respect to laboratory coordinates was calculated with the fluorescence scan and the angle between the sample edge and laboratory coordinates was found to be 0.3°.

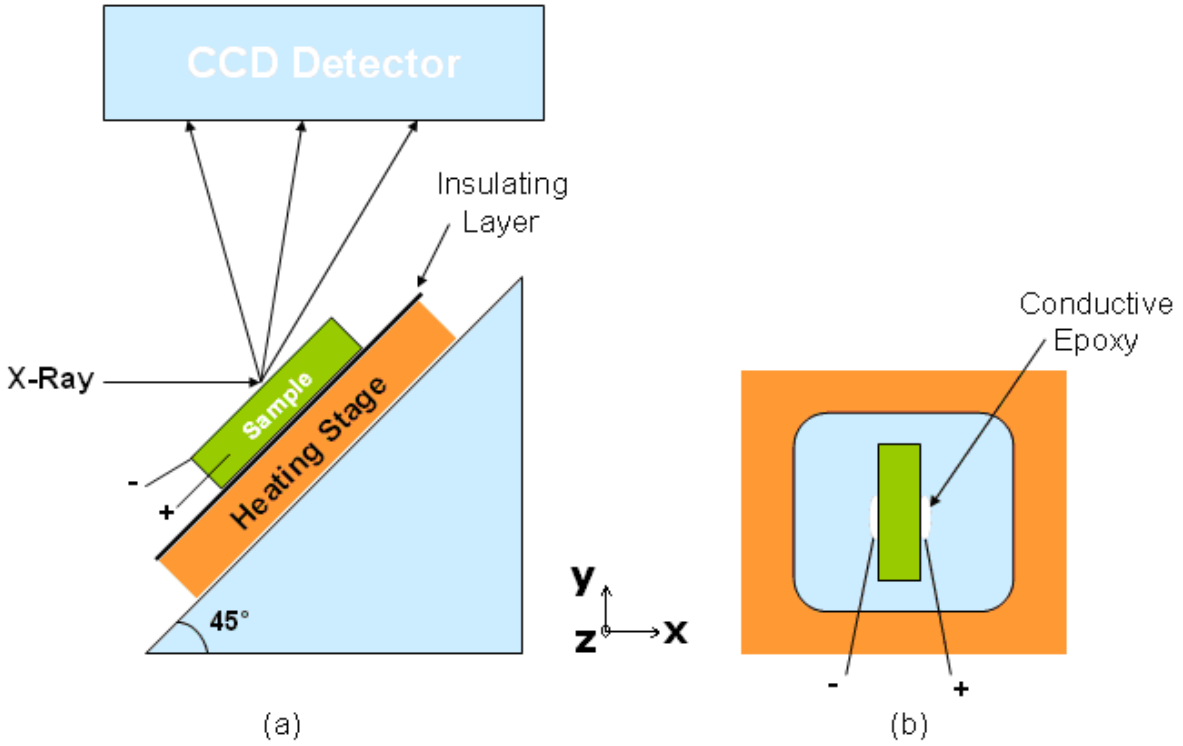

Figure 6.33. (a) Side view of the schematic experiment setup. (b) The view of the experiment setup from incoming x-rays. Sample dimensions are 1x1x5 mm^3

µSXRD experiments were carried out on the X-ray microdiffraction end-station (12.3.2) at the ALS. The instrument has a capability of delivering X-ray white beam (6-22 keV) with less than 1 µm beam size by using a pair of elliptically bent mirrors in a Kirkpatrick-Baez configuration [Savytskii, D. I. (2003)]. The diffraction patterns were collected with an area scan at various conditions described above. At each grid position of area scans, the sample was exposed to polychromatic x-rays for 1 second. The back-reflection Laue diffraction patterns produced by the white x-rays with 1µm beam size were

recorded using a CCD detector (Bruker 6000) mounted on the vertical slide. The active area of the CCD camera was 90x90 mm^2 and binning mode will be 1024x1024 pixels. The sample surface was set to be at 45° relative to the incoming beam and the detector. The nominal distance from the CCD to the sample and the center of the diffraction patterns on CCD detector will be determined to be 84.94 mm and 522.7, 512.3 pixels respectively. In order to study the grain depth, the detector is moved 65 mm upwards and the scans were repeated.

The collected white-beam (Laue) diffraction patterns were analyzed with the custom software developed at the ALS (X-MAS, X-ray Microdiffraction Analysis Software) [Tamura, N. (2003)]. XMAS is capable of determine the positions of the reflections with subpixel resolution by using two-dimensional profile functions such as Gaussian, Lorentzian or Pearson VII function. By using the peak positions and lattice parameters of $BaTiO_3$, the program simulates an orientation from three most intense spots. The simulated orientations are compared with the experimental reflections and the simulated orientation is authenticated as real grain if a sufficient amount of reflections are found. The typical number of the reflections found from the cubic grain was around 110. The orientation of the cubic grain was also validated from its reflections with a fitting routine written in Matlab (Ver. 7.2.0, The MathWorks, Inc.). The diffraction patterns recorded at room temperature were analyzed with XMAS software and the orientations sharing the cubic reflections are found. For the space group and lattice parameters, the literature values of the $BaTiO_3$ were used as *p4mm* (s.g. 99), a: 0.39947 nm and c: 0.40336 nm for tetragonal structure and *pm3m* (s.g. 221) and a: 0.4009 nm for cubic structure respectively [Rogan, R. (2003)].

In order to find the misorientation between the orientations at room temperature and the cubic grain, the orientations are first mapped fundamental region with corresponding symmetry operators. While *m3m* point symmetry was used for cubic grain, *4mm* point symmetry was used for tetragonal orientations and misorientation was calculated by using ODF/PF software package from Cornell University. The orientation matrices found by XMAS define the crystal coordinates instead of the standard definition as direction cosines between the crystallites and the sample axes. In order to obtain the orientation matrix with direction cosines, each orientation was normalized with the corresponding lattice parameters. As the misorientation convention, angle-axis pairs were used. This convention has a major

advantage to show the misorientation angle and axis with respect to the reference grain. It is helpful when describing the misorientation angle between domains and the rotation axis between the domain variants.

μSXRD technique is well capable of finding deviatoric strain components of the local crystallites. The method simply compares the calibration lattice parameters with the localized crystallites and finds strains from the mismatch between the lattice parameters between. However, this method has some pitfalls. Using a generalized lattice parameter for all structure can result in a big deviation from the local structure. For instance, such calibration lattice parameters having *aac* lattice configuration along the global coordinates can find a large strain in the domains that have *aca* or *caa* configuration along the global coordinates. Furthermore, using generalized calibration parameters can have deviation from the experimental conditions. All of these factors combined, it is important to eliminate the errors in the strain calculations.

The lattice strain tensor (ε_{ij}) of each domain was obtained by using technique described by Margulies [Margulies, L. (2001)]. The relation between the lattice strain tensor (ε_{ij}) of each domain and its spot strains (ε_i) and the direction cosines ($l_i m_i n_i$) of those spots can be described as [Poulsen, H. F. (2004)]

$$\varepsilon_i = \frac{d_i - d_0}{d_0} = -\frac{\sin(\theta_i) - \sin(\theta_0)}{\sin(\theta_0)} = (l_i m_i n_i)\varepsilon_{ij}\begin{pmatrix} l_i \\ m_i \\ n_i \end{pmatrix} \qquad (6.25)$$

After finding the orientations of the domains successfully, the center of mass of each peak belong to the domains is found by peak search routine [Blair, D. (2008)]. The peak search routine is based on searching image row by row and identifying connected pixels that are above the intensity threshold as a peak. The overall principles of the peak search routine were described at elsewhere [Vaughan, G. H. M. (2004)]. The spot strains for 15 reflections were calculated with Eq. 6.25. Due to using white beam, d-spacings of each plane are unknown. Instead of d-spacing, Bragg angle was used with the right hand side of Eq. 6.25. The spot strains were measured from the peak shifts as the electric field is applied. As a calibration, the peak positions (θ_0) as initial unpoled stage are taken. The peak shifts were

calculated from the peak positions at given electric field (θ_i) and initial stage (θ_0). In order to find the direct effect of domain switching, the unstrained sample was used as internal calibration. From Eq. 6.25, the lattice strain tensor can be easily calculated by using the direction cosines of the peaks but no further analysis is done considering that the spot strain would be enough at this time.

6.3.2.2. Results and Discussion

The phase transformation from cubic to tetragonal and the distribution of the domain variants within the grain was studied. The orientation relationship between the domains was studied. As response to electric field, the volume fraction change between the domains the orientation changes with the electric field at 10, 15, 25 and 30 kV/cm were studied. The distribution of the domains was also studied at above Curie temperature and room temperature. Figure 6.34 shows the typical microdiffraction patterns recorded at above Curie temperature, room temperature, applied electric field at 30kV/cm and finally with 0kV/cm. When the sample was in the above Curie region, we observed no peak broadening. This is a proof that the material in unstrained state. There were no close spots were observed above Curie temperature. This is due to cubic phase transformation. During the cooling, the peaks are gradually broadened and split to there to four spots depending on the hkl. This is a clear proof that the phase transformation is complete and material transformed to tetragonal. By application of the electric field, no visual change seen in the diffraction pattern up to 5 kV/cm. The previous hysteresis measurement showed that coercive field of this material is 5.16 kV/cm and the applied electric field was well below to cause domain switching. By applied field more than coercive field, the peaks are shifted along the electric field direction. This is caused by the rotation of the polarization vectors of the domains along the electric field. After removing the electric field, the peaks return to original position with a strained state.

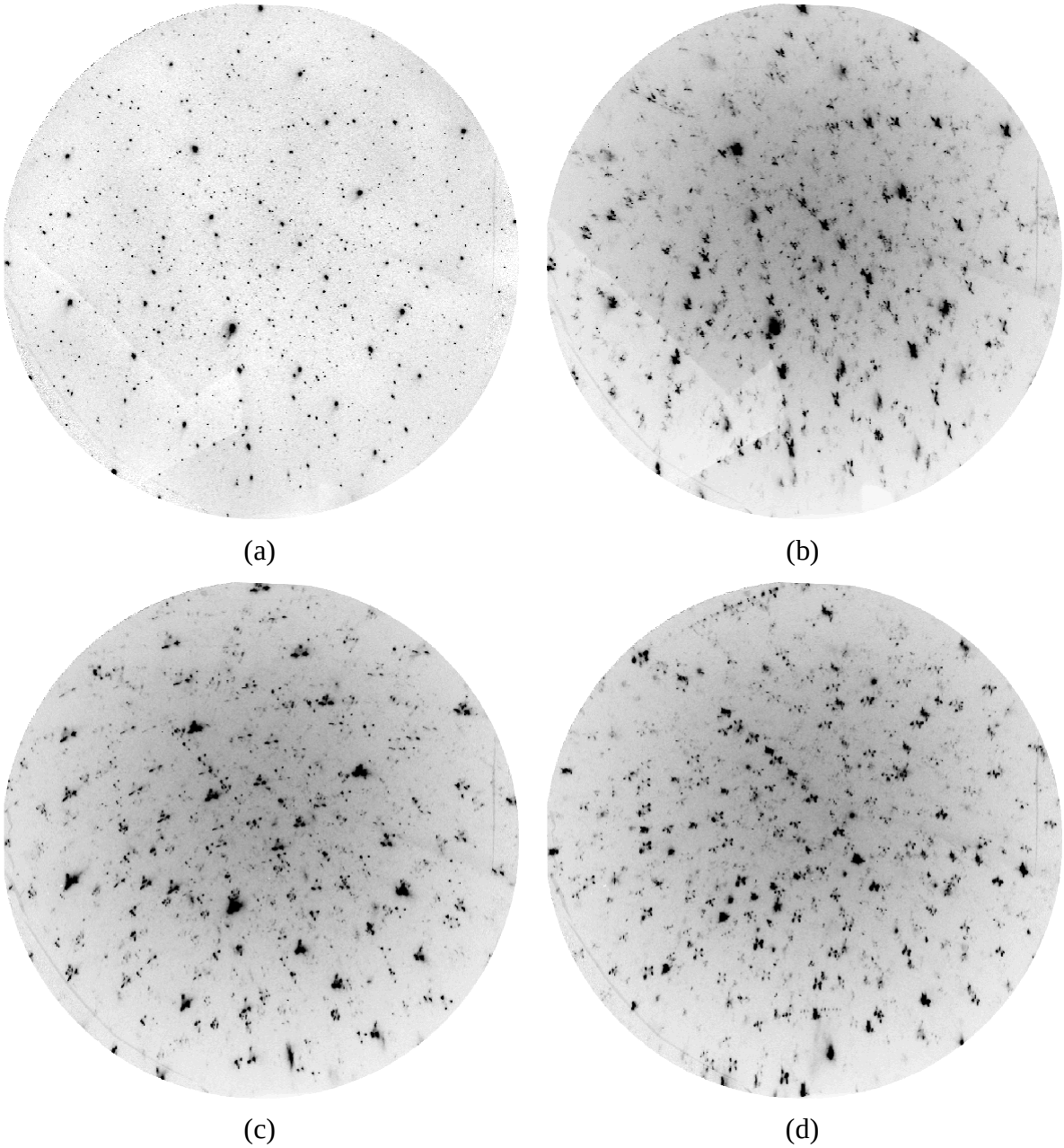

(a) (b)

(c) (d)

Figure 6.34. Microdiffraction patterns of $BaTiO_3$ sample recorded at (a) above Curie temperature (130°C), (b) 8 hours after cooling to room temperature (c) applied electric field at 30kV/cm (d) electric field turn down to zero.

Table 6.9 shows the orientation of the cubic grain at above Curie temperature and the orientations that formed when cooling to room temperature. The orientation of this cubic grain was found by XMAS [Tamura, N. (2003)]. Upon cooling, the cubic diffraction spots split into tetragonal reflections due to cubic-to-tetragonal phase transformation. The resultant

orientations are obtained by indexing the diffraction pattern recorded at room temperature and they are rotated 89.73° and 89.28° of the [100] or [010] axes of the cubic grain respectively. These [100] and [010] axes are pseudocubic and they are equivalent to 180° rotation around tetragonal [011] and [101] axes respectively. Since these orientations show specific crystallographic relations and are the subgroup of the cubic grain, they are called domain variants.

Table 6.9. The list of orientation relationships of the cubic grains and their domain variants as cooling to room temperature. The orientations were expressed as tensor and angle-axis pairs. The misorientation between domain variants was defined with respect to cubic grain.

Temperature	
130°C	RT
Orientation Matrix	Orientation Matrix, Misor. Angle Orien. ID
	0.812 -0.098 0.567 -0.228 0.856 0.468 -0.537 -0.507 0.678 0.13° < 0 0.15 0.22> A
0.809 0.089 -0.580 -0.236 -0.859 -0.459 -0.538 0.504 -0.673	-0.567 -0.815 -0.095 -0.467 0.235 0.853 -0.678 0.530 -0.514 89.73° <1 0 0> B -0.094 0.563 0.818 0.858 0.461 -0.232 -0.505 0.686 -0.527 89.28° <0 1 0> C

When cooling from Curie temperature, each grain breaks up to domains to reduce the overall energy of the system [Arlt, G. (1990)]. Figure 6.35 shows the [100], [010] and [001] directions of the cubic grain and domain variants in pole figure as stereographic projection. For clarity, Wulf plot was overlaid to pole figure. The *c* axes of the domains are marked with red colors and the direction of the e-field was shown in Y axis as well. As clearly seen, the crystal directions transform to tetragonal when cooling to room temperature and each crystal directions break up to domains. For instance [100] cubic direction breaks up to [100], [010] and [001] tetragonal directions and each direction is shared by a domain. As shown in close-

up view in Figure 6.35, the angle between {100} crystal directions of the domains is around 0.6° i.e. $2\tan^{-1}(c/a) - 90°$ where c/a ratio is 1.01 for $BaTiO_3$. While forming the domains, it is also seen in Figure 3 that no significant grain rotation was observed.

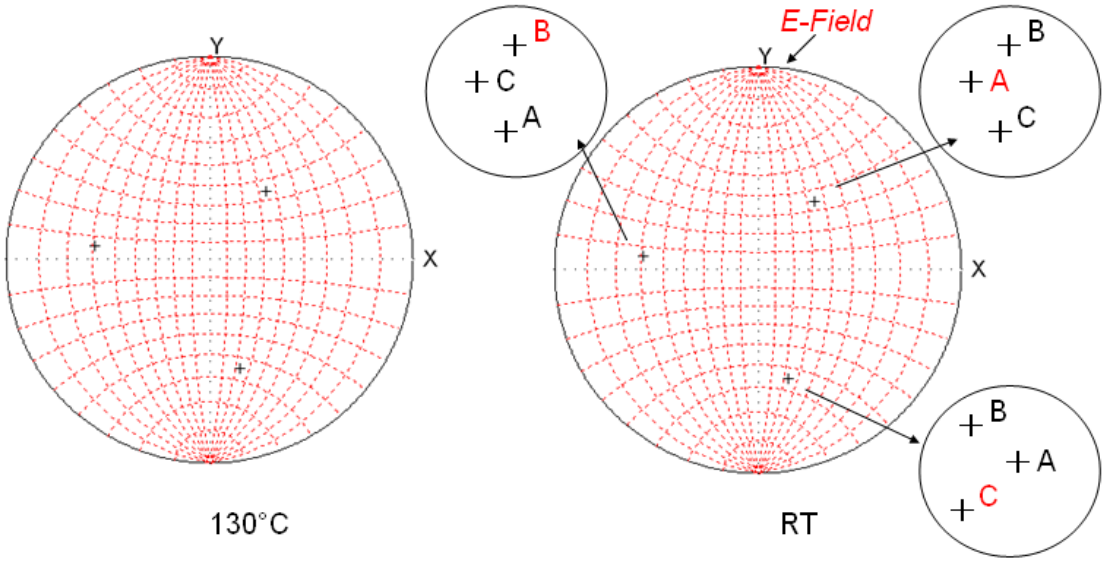

Figure 6.35. {100} pole figures as a stereographic projection at above Curie temperature and at room temperature. The Wulf plot was overlaid for clarity. The orientations with letters at room temperature are shown in Table 1 and they are the domain variants within the grain. The electric field direction is Y-axis and the angles between c-axis of the domains (shown in red color) and the electric field are shown as well

Figure 6.36 shows the evolution of the (211) peak as the temperature is cooled to room temperature. From Table 6.9, domain A has the same orientation with the cubic grain with a smallest misorientation to cubic grain. Domain *B* is obtained with the rotation b 89.32° along [100] axis or 180° along [011] direction of the cubic grain. Domain *C* is obtained with the rotation by 89.28° around [010] axis of the cubic grain. The close inspection showed that the domain C breaks up two subdomains. By the application of the electric field, these subdomains orient along the electric field and converge to one with 30kV/cm electric field. Between Domain A, B and C, there is a domain boundary with a transition region. These transition regions are considered as the regions where polarization vectors transform one direction to another [Floquet, N. (1997)]. The angle between c axis of the domain and the electric field direction was calculated from the orientation matrices of the domains. We define this angle as “polarization angle”. The polarization angles for Domain *A*, *B* and *C* are

calculated as 35.9°, 58.4° and 46.6°. Since domain *A* has a large polarization angle, the application of the electric field is expected to cause the domain switching in greater scale in this domain.

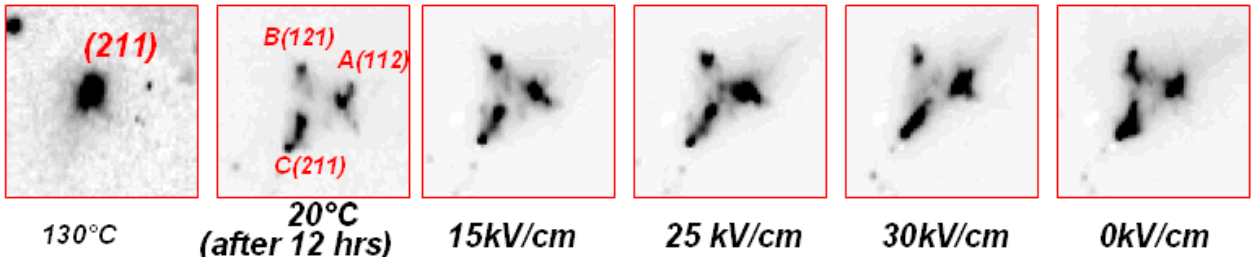

Figure 6.36. The evolution of the (211) peak from the above Curie temperature to cooling. (211), (121) and (112) peaks at room temperature belong to domains shown in Table 6.9 respectively

There is a direct relation between the volume of the domain and the integrated intensity of the domain. In order to observe the volume fraction change between domain variants with applied electric field, the integrated intensities of the domains were calculated and the volume fraction of the domain within a grain (f_{hkl}^{d}) can be found as:

$$f_{hkl}^{d} = \frac{I_{002}^{d}}{(I_{hkl}^{dv} + I_{hlk}^{dv} + I_{lhk}^{d})} \qquad (6.26)$$

where I_{hkl}^{d} is the integrated intensity of (hkl) spot from a domain and I_{hlk}^{dv} and I_{lhk}^{dv} are the integrated intensity of the (hlk) and (lhk) reflections of the remaining domain variants within the grain. The integrated intensities of the reflections are calculated with "automatic peak finding routine" of XMAS software. For fitting, Lorentzian type fitting was used. The reflections calculated from the domain variants are shown in Figure 4. To eliminate the effect of the Lorentz factor, the domain variants that diffract at the same detector location are taken. To improve the statistics, the {123} reflection family of the same grain are taken. Using white beam enables to resolve the domain variants on the detector.

Figure 6.37 shows the volume fraction change in the domain variants with applied electric field. The polarization angles for Domain *A*, *B* and *C* are calculated as 35.9°, 58.4° and 46.56°. The application of the electric field favors for the domain that has smaller angle with the electric field direction. In this case, Domain A is the energetically favorable domain with its low polarization angle. Indeed, the volume fraction of Domain A increases by 25%

with the electric field up to 30kV/cm. This is due to lattice configuration and the polarization angle of the subdomains. The volume fraction of domain C increases with electric field as well but this increase is not as significant as domain *A*. With its high polarization angle, the volume fraction of Domain B decreases by around 50%. Beyond 10kV/cm, it is expected that the fraction of the energetically favorable domain variant increases. Due to grain boundaries and local boundary conditions, the overall switching from one domain is not complete. The higher electric field can be achieved by immersing the sample in a dielectric liquid but this has not been feasible in our setup because the sample needs to be exposed to heating prior to electric field to track the evolution of the same grain.

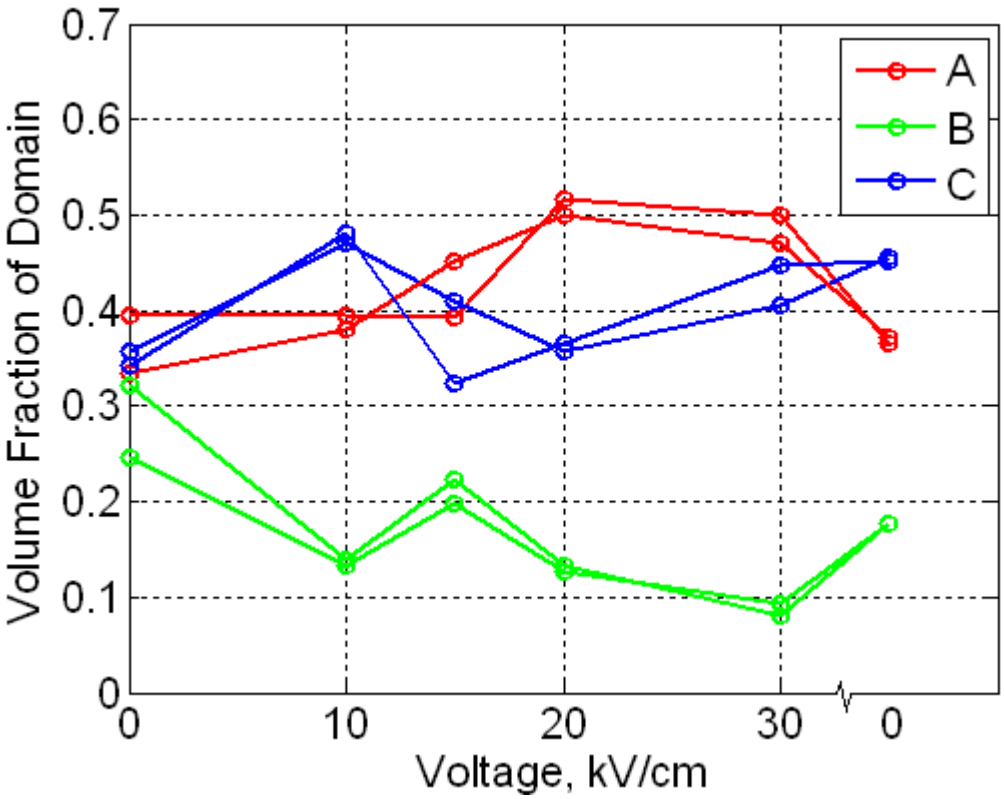

Figure 6.37. Volume fraction change in the domain variants with applied electric field.

During the poling process, the spontaneous polarization directions of the domains are expected to switch along the electric field. Due to tetragonal symmetry [Berlincourt, D. et al. (1959)], the poling process can lead either 90° or 180° domain switching. Among those, only 90° domain switching can create a strain in the body and this stress can calculated in theory.

Due to small tetragonality ratio in $BaTiO_3$, the overall strain in a single crystal $BaTiO_3$ due to complete domain switching can be calculated as 1-c/a (1%). The strain values for polycrystal are rather small than this value. To calculate the correlation, we can compare the spontaneous polarization of the single crystal and polycrystal $BaTiO_3$. The measured spontaneous polarization of single crystal and polycrystalline $BaTiO_3$ are 26 and 5.3 $\mu C/cm^2$ respectively. The maximum strain caused by the complete domain switching is expected to be 20% of the single crystal. Therefore, the application of the electric field can create around 0.2% strain (or 2000 microstrain).

The procedure on how to find the spot strains of each domain is outlined above. Table 6.10 shows the spot strains of the domains as the electric field is applied. For the reflections where hkl values are close to unity, it is very difficult to resolve the subdomains and the strain values of those domains were not included. The maximum spot strain with the electric field is 2000 microstrain and this is well correlated with the literature values [Cross00] and the calculation above. The highest strains were observed in the reflections that have high angle with the electric field. Considering electric field is applied along x axis of the sample (Figure 6.33), the crystallographic planes along x axis (such as 211 or 312) should experience less strain compared to other domains. Indeed, 211 planes experiences less strain compared (112) planes. Domain C1 and C2 are subdomains and they experience elastic deformation with applied electric field. With application of electric field at 30kV/cm, these subdomains showed tensile and compression strains. With removing the electric field, the domains return to their initial states with a residual stress.

Table 6.10. The spot strains of the domains as the electric field is applied

	hkl	**211**	**112**	**233**	**332**	**433**	**334**	**312**	**213**	**111**	**122**	**232**	**313**	**134**	**525**
E Field, kV/cm	**10**	494	16	889	16	28	893	322	39	107	51	44	5	936	24
	15	-68	-45	-9	-45	-28	11	-6	-363	-836	3	-2	-258	72	26
	25	-55	652	-32	652	-70	-983	-47	-331	-858	-47	-963	-219	-642	-315
	30	-46	-738	-143	-738	-847	-2000	-47	-901	-79	-1765	-2004	-652	78	-806
	0	-38	-755	-110	-755	-111	-1009	306	-425	-895	-68	-1051	-316	58	-350

Domain A

Table 6.10 (Continued)

	hkl	**211**	**112**	**233**	**332**	**433**	**334**	**312**	**213**	**111**	**122**	**232**	**313**	**134**	**525**
E-field, kV/cm	10	653	-20	-128	-12	-981	9	-464	3	920	-18	29	482	84	45
	15	613	-1134	-174	-1834	-1033	1588	-456	10	1795	-947	-1009	-8	-753	713
	25	620	-38	-110	-1004	-1044	1568	-912	635	1807	-978	2010	790	-780	325
	30	-91	-582	-238	1051	9	788	-432	-322	1706	2135	-1012	216	-1652	713
	0	-802	-629	1844	-967	-996	-14	1000	678	879	2065	-1020	215	-888	-48

Domain B

hkl		**112**	**213**	**225**	**211**	**313**	**134**
E-field, kV/cm	10	-29	-335	-1044	-630	50	909
	15	-33	45	-340	707	630	876
	25	-54	-439	0	-442	238	142
	30	2050	1239	-8	-1111	544	807
	0	-37	-344	-341	-442	-9	16

Domain C1

hkl		**112**	**213**	**225**	**211**	**313**	**134**
E-Field, kV/cm	10	-11	45	315	1223	-16	7
	15	9	71	281	2513	45	-832
	25	648	-1618	260	575	166	-909
	30	-1520	-928	-40	-42	-685	-1425
	0	-1398	-517	10	19	-340	-907

Domain C2

The evolution of the ferroelectric domains with electric field was studied by using μSXRD technique. The phase transformation from cubic (*pm3m*) to tetragonal (*p4mm*) and the distribution of the domain variants within the grain were investigated. After cooling, the resultant domain variants are obtained by rotating 89.73° and 89.28° of the [100] or [010] axes of the cubic grain respectively. As response to electric field, the volume fraction change between the domains was observed. This volume fraction is favored on the domain that has a small angle between its c axis and the electric field direction. There is no such a significant grain rotation during domain switching. Domains flip such without requiring a significant rotation from the initial orientation. During the domain switching, the domain walls move to decrease the energy of the system. The misorientation angles between domain variants deviate from the theoretical value (89.4°) by 0.2-0.3°. This shows the local variations from

the domain variants inside of the grain. This study clearly shows the μSXRD technique is capable of studying the mesoscale behavior of the ferroelectrics in polycrystalline state.

This chapter showed the results from the evolution of the ferroelectric domains both with 3D-XRD and μSXRD technique. The orientation relationships from 3D-XRD technique were confirmed with the μSXRD technique. The morphology of the domain variants is modeled and the 90° domain switching model was used to confirm the domain variants within the grains. Tetragonal-cubic phase transition used in μSXRD technique can help solving the severe overlap problem in 3D-XRD technique. The next chapter will discuss the results from EBSD experiments.

CHAPTER 7. DOMAIN CHARACTERIZATION WITH EBSD

The objective of this study is to characterize the orientation relationships in the ferroelectric domains of polycrystalline $BaTiO_3$ using the EBSD technique.

7.1. Experimental Procedure

The polycrystalline $BaTiO_3$ sample was prepared with the conventional ceramic processing techniques and a bulk sample with nominal 2x2x4 mm^3 dimensions was used in the Electron Backscatter Diffraction (EBSD) experiments. The nominal grain size of $BaTiO_3$ sample was measured around 20µm. The sample surfaces were fine ground with 320 and 600 grits and then fine polished with 0.5µm alumina powder. Next, the surface was coated with gold using sputtering and then polished with ion-milling.

In the EBSD technique, the sample is tilted by a 70° angle with respect to the incoming beam. A monochromatic electron beam with a 25 kV energy hits the tilted crystalline sample and interacts with the lattice planes. The diffraction planes satisfying the Bragg condition undergo backscatter diffraction and form Kikuchi lines on a fluorescent screen. Each intersecting diffraction planes define the zone axis of diffracted crystallographic planes. An area scan along the sample surface can be used the measure the crystal orientation and misorientation between neighboring grains. At 25 kV, the penetration depth of electrons in $BaTiO_3$ was calculated to be around 2.5µm.

An area of 4x11.7μm^2 with 0.1µm step size was scanned in the EBSD experiment. The step size was selected as rather small to detect the orientation between the domain variants within the grain. The collected EBSD diffraction patterns were analyzed by a commercial OIM software. For indexing, the crystallographic database from the International Centre for Diffraction (JCPDS) was used. The crystallographic parameters for $BaTiO_3$ were selected as a=0.3994 nm, c=0.40314 nm with the *p4mm* (no: 99) space group. In order to find the right zone axis, (103), (112) and (211) reflections were added to the solution. During the indexation, the free parameter being refined is the orientation angle of the crystal. The fitting parameter during the indexation is called “confidence index (CI)” and for the perfect solution, the confidence index is 1. For a very low (less than 0.1) confidence index, the results can be questionable and a special caution needs to be taken to interpret them.

Therefore, the lower threshold for the confidence limit in this experiment was 0.1 and the orientations found with lower confidence indeces were discarded. The Euler angles of each orientation from the area scan were exported to Matlab and each orientation was mapped into the tetragonal fundamental region. The misorientation between the domain variants was shown with angle axis pair notation.

For the grain map, a new procedure was created. When an inverse pole figure direction is taken along a sample direction, the corresponding direction constitutes a vector with components ranging from 0 to 1. This vector was directly used for the coloring in RGB mode where [001], [010] and [100] corresponds to red, green and blue colors, respectively. The standard inverse pole figure was also plotted by assuming that the orientation in EBSD experiments is defined with respect to crystal coordinates.

7.2. Results

The EBSD experiments of $BaTiO_3$ offer hope that this method can be used to correlate the domain structures found both by the 3D-XRD and µSXRD techniques. Figure 7.1(a) shows the typical EBSD pattern and it clearly proves that EBSD technique was successful on $BaTiO_3$. Figure 7.1(b) shows the indexed EBSD pattern where the zone axis was found to be along [-110].

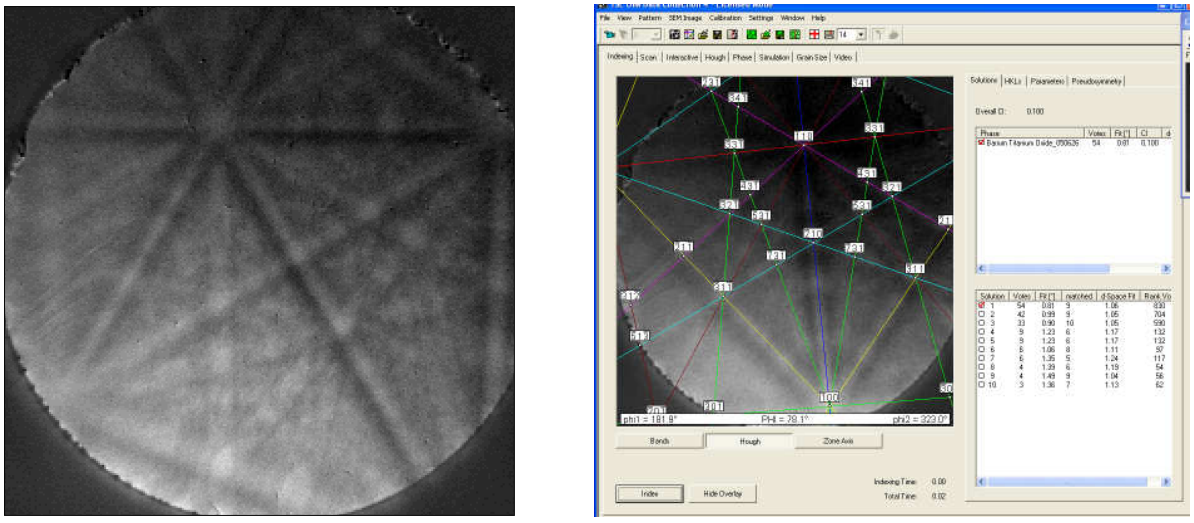

(a) (b)

Figure 7.1. (a) A schematic EBSD pattern from polycrystalline $BaTiO_3$. (b) The same pattern after indexation. The zone axis was found as [-110]

Figure 7.2 shows the orientation map with respect to the sample coordinates. The orientations found with a confidence limit of less than 0.1 were eliminated. The majority of the domains align along the [010] crystal direction with the sample surface normal. The regions with close red, blue and green colors show the orientations that are perpendicular to each other. These regions most likely are domain variants, but further proof is necessary. Notice that the surface scan in EBSD technique is performed in a honeycomb pattern and we see a gap between the successive points in every sample scan direction.

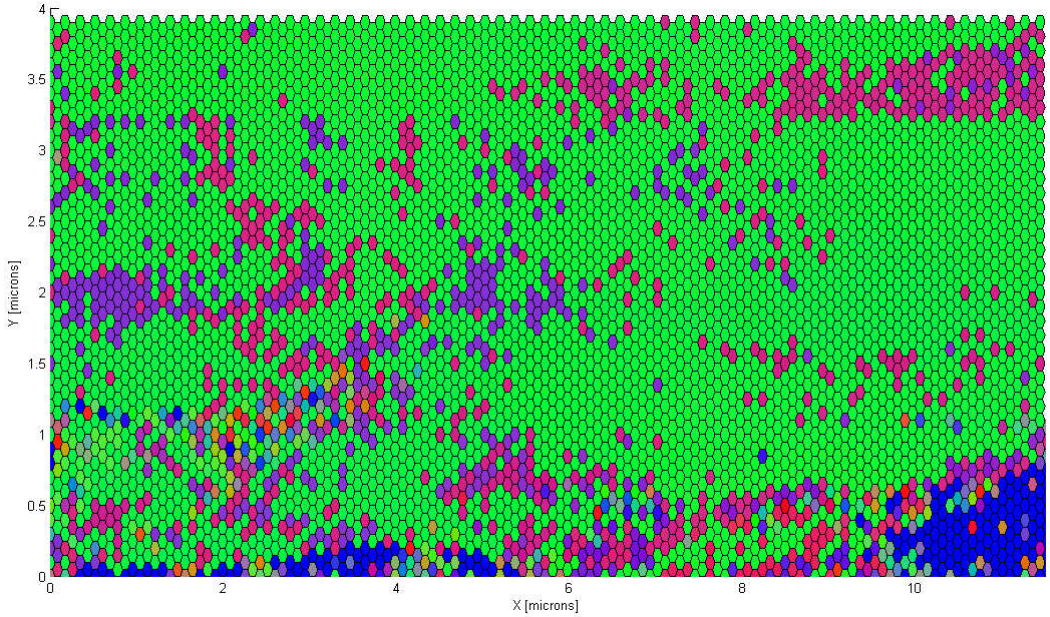

Figure 7.2. The grain map of the ferroelectric domains along sample normal. Each color shows the alignment of the crystal directions along the sample normal. While green shows the [010] direction, red and blue colors show the [100] and [001] crystal directions respectively. The confidence index threshold was 0.2 for this grain map

Figure 7.3 shows the close-up region with orientations that are perpendicular to each other. The regions are marked with different numbers to study the misorientation relationship between them.

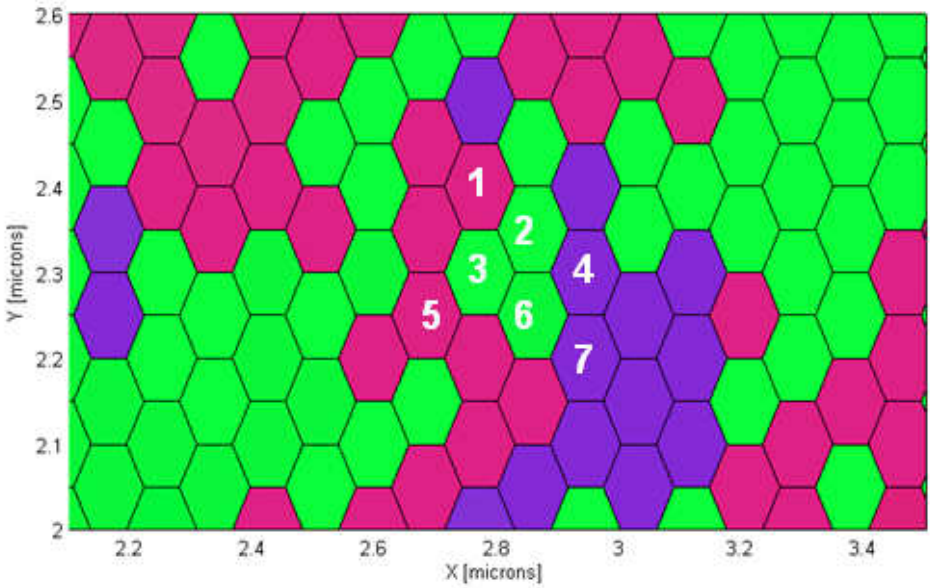

Figure 7.3. The domain variants in close-up view. While green shows the [010] direction, red and blue colors show the [100] and [001] crystal directions respectively. In black regions, either no grains or those with low confidence index were found.

Table 7.1 furnishes the marked orientations of the close-up region in Figure 7.3. The close inspection shows that these orientations are indeed domain variants to each other. The orientations 2, 3 and 6 basically come from the same domain. The orientations 1 and 5, 4 and 7 are also the same domains, respectively. The interesting misorientation relation is between domains 1 and 5 because they have a 0.4° misorientation. This may be due to twinning of 1 to 2 and then 2 to 5. We see a similar pattern in microdiffraction experiments and called these domains as “up and down” domains with respect to the spontaneous polarization direction. The domain boundaries between domains 1 and 2, 2 and 4, 3 and 5 are [100], [0-10] and [100] axes, respectively. This clearly shows the same orientation morphology of the parent domain that we found in the μSXRD technique.

Table 7.1. The orientations of the domains marked in Figure 3 and their misorientation relationships. * CI: Confidence index. Higher CI is the better.

ID No	Location, µm x	Location, µm y	CI*	Euler Angles, °	Angle Axis	Misorientation Angle Axis
1	2.4	2.771	0.1	100.3 59.4 254.3	59.6° [-0.08 0.97 -0.22]	Main Domain
2	2.35	2.858	0.117	2.5 76.3 31.5	82.44° [0.35 -0.23 0.90]	89.54° [100]
3	2.3	2.771	0.142	2.4 76.2 31.3	82.3° [0.35 -0.23 0.9]	89.65° [100]
4	2.3	2.944	0.247	251.3 33.8 115	34.3° [0.18 -0.9 -0.37]	89.74° [0-10]
5	2.25	2.685	0.192	100.2 59.4 253.9	59.6° [-0.09 0.97 -0.23]	0.4° [00-1]
6	2.25	2.858	0.125	2.3 75.9 31.1	81.94° [0.35 -0.23 0.91]	89.56° [100]
7	2.25	3.031	0.225	250.6 33.8 115.6	34.39° [0.18 -0.91 -0.38]	89.63° [0-10]

Figure 7.4 shows the inverse pole figures along sample directions. We see the same orientation relationship as we see in the grain map. Similarly, the crystals align along the [001] and [101] crystal directions respectively parallel to the sample surface directions.

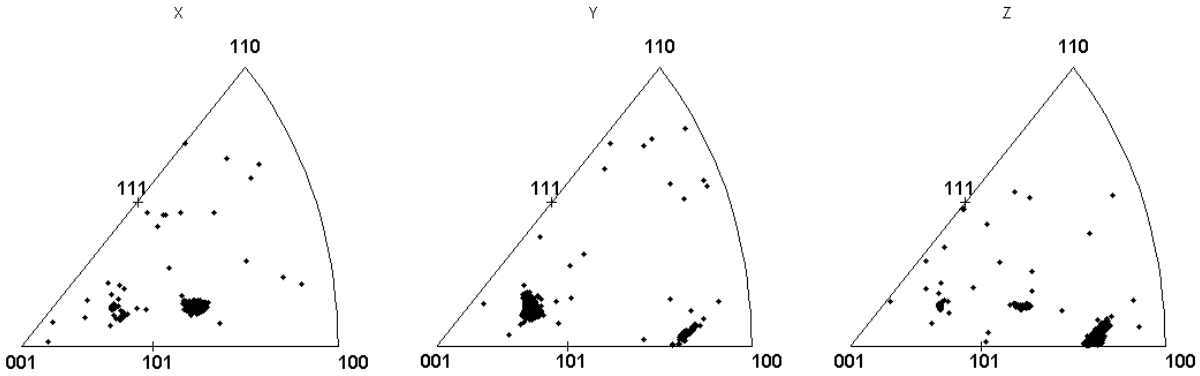

Figure 7.4.The inverse pole figures along sample directions (X, Y and Z)

During the area scan, it was realized that the EBSD diffraction patterns rotate as the scanned location is moved 0.1µm away. Figure 7.5 shows the change in the diffraction

patterns as we moved to a different area. The rotation of the diffraction patterns was measured as around 1° and this angle apparently corresponds to the angle between *c* and *a* axes of the domain variants since $2\tan^{-1}(c/a) - \pi = 0.6°$ where *a* and *c* refer to the lattice parameters of $BaTiO_3$. Therefore, a slight rotation in the EBSD diffraction patterns was considered as the domain variant of the given domain.

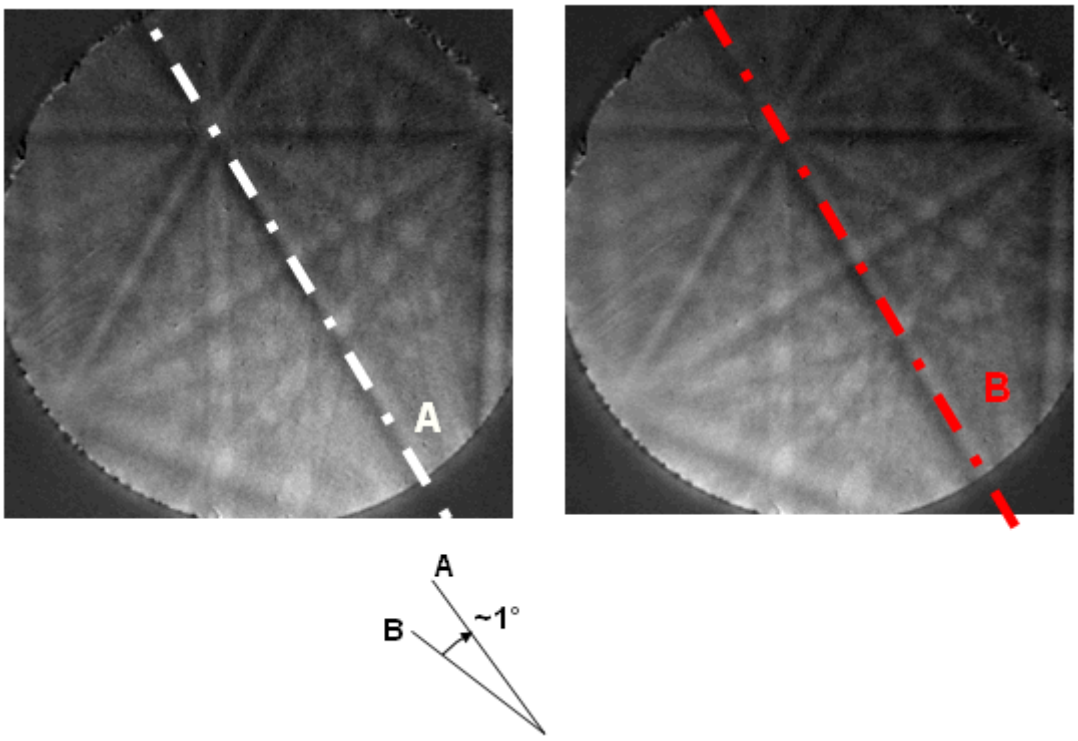

Figure 7.5. The small rotation in the EBSD diffraction pattern when scanning to the next domain

This study clearly shows that the ferroelectric domain structure can mapped with the EBSD technique. Meanwhile, there are several drawbacks to this technique. The penetration depth is not as deep as with the 3D-XRD and μSXRD techniques. Quantitative results on internal strain in the domain variants are almost impossible. Also, the misorientation angle between the domain variants is too close to the resolution of the EBSD technique. Therefore, EBSD can be used in a preliminary study to identify important regions before applying the XRD techniques.

CHAPTER 8. CONCLUSIONS AND FUTURE DIRECTIONS

The main goal of this study has been the *in-situ* investigation of the ferroelectric domain structures inside polycrystalline $BaTiO_3$ under thermo-electro-mechanical loading. The outcomes are two-fold: (i) the characterization techniques are improved to study the polycrystalline ferroelectrics in the mesoscale; and (ii) the texture, strain and volume fraction of the ferroelectric domains were tracked under applied electric field and mechanical stress.

Technique

3D-XRD, μSXRD and EBSD techniques were used in this study. The XRD techniques were improved and adapted to study domain mechanics for the first time. The details are explained in Appendices 1-6.

Results

The overlap of diffraction spots was a limiting factor in the study of the domains. In order to eliminate the spot overlap, the polycrystalline $BaTiO_3$ sample was heated above the Curie temperature where the tetragonal domains will disappear and attain the orientation of the grain. Next, the sample was cooled slowly to the room temperature and the evolution of the ferroelectric domains was studied at temperature and under electric field. The orientation relationships, volume fractions and lattice strain evolution of the domains were monitored. The following results were found:

- 8 groups of ferroelectric domains were identified and tracked with electric field. New domains were observed under high applied electric field.
- The orientation of the domains remained unchanged even under high electric field. However, by the application of electric field, the fraction of the energetically favorable domain variants increased. Due to local constraints, the overall switching from one domain variant to another was not complete.
- There was no significant grain or domain rotation during domain switching. Domains appeared to flip without requiring any measurable rotation from their initial orientation. During the domain switching, the domain walls move to decrease the energy of the system.

- The misorientation angles between domain variants slightly deviated from the theoretical value (=89.4°) by 0.2-0.3°. This deviation angle matches with the expected phase-matching angle described in Appendix 7.
- Lattice strain evolution of the ferroelectric domains was studied under electric field. Since the same grain was cooled down from the Curie temperature, the texture evolution of the domains was easily visible. The results were compared with the macroscopic strain results and a development of strains up to 0.1% was observed along the applied electric field direction. This way, the multiscale evolution of the ferroelectric domains in a polycrystal was investigated quantitatively for the first time.
- Data analysis was challenging due to the complex structure of ferroelectrics. It required an integrated approach that involves diffraction pattern simulation. The methodology to overcome the spot overlap in polycrystalline ferroelectrics was established and the results from the methodology were described.

Future Directions

The present study provides a framework to characterize the polycrystalline materials with complex twin (or domain) structures. By using the methodology described in this study, 3D-XRD and μSXRD techniques offer unique opportunities to study texture and strain evolution in the mesoscale nondestructively. It is now possible to employ these methods to perform a detailed study of the mesoscale constitutive behavior of materials with domains (or twins) as their main inelastic deformation mechanism. Especially important is to determine how the von Mises criterion [Hertzberg, R. W. (1995)] is satisfied in materials with fewer than 5 degrees of freedom (e.g., independent domain variants). Note that tetragonal $BaTiO_3$ has only 3 independent domain variants. As such, large intergranular stresses can be expected to develop in polycrystalline $BaTiO_3$ under high electric field. Other tetragonal active materials will suffer a similar faith. It is, therefore, important to quantify the evolution of lattice strain and texture within a cluster of grains under electromechanical loading. The newly developed box scan technique of 3D-XRD can be invaluable in this effort. However, such a study would yield a large amount of data and require new analysis procedures,

especially if integration to solid mechanics models is attempted. Nevertheless, the present study has laid the groundwork for this next step and offered a unique opportunity to truly quantify the mesoscale constitutive behavior of active materials.

Appendix 1. Scattering of x-rays from electrons, atoms and unit cells

When an x-ray beam hits an atom, the beam may be either absorbed with an ejection of electrons from the atom or scattered. X-rays are the electromagnetic waves with electric vector varying sinusoidally with time and directed perpendicular to the direction of the propagation of the beam [Warren, B. E. (1990]. Let's consider a single free electron at the origin with an unpolarized primary beam directed along the X-axis as in Figure A1.1. We would like to obtain the intensity of scattered radiation at point P which is at a distance R from the electron at an angle ϕ with X- axis. Since the primary beam is polarized, the electric vector takes with equal probability all orientations in the YZ plane.

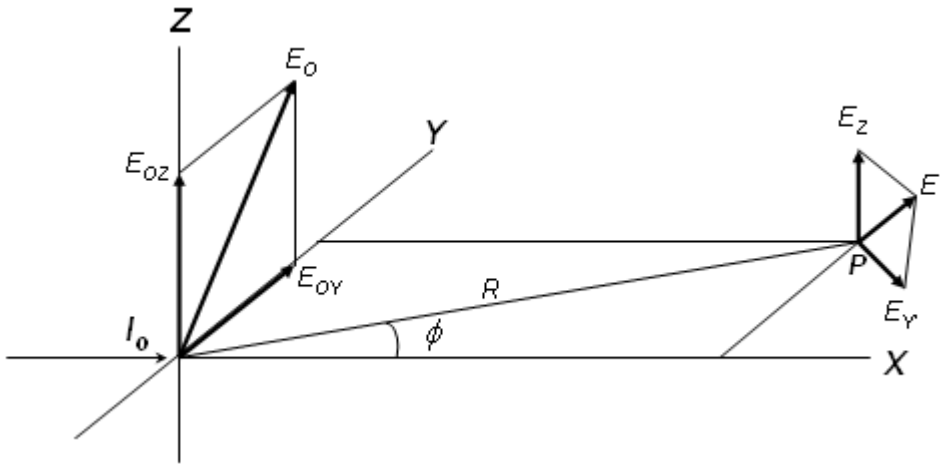

Figure A1.1. Classical scattering of an unpolarized primary beam by a single free electron at the origin [redrawn from Warren, B.E. (1990)]

We can choose one direction E_0 and later average over all directions. Since it is a vector, E_0 can be resolved into components E_{0Y} and E_{0Z}. If ν is the frequency of the primary beam, the instantaneous values of the electric fields are

$$\varepsilon_{OY} = E_{OY}\sin 2\pi\nu.t\,; \qquad \varepsilon_{OZ} = E_{OZ}\sin 2\pi\nu.t \qquad \text{(A1.1)}$$

Considering first the component ε_{OY}, a force is exerted on the electron which produces a *Y*-component of acceleration

$$a_Y = \frac{f_Y}{m} = \frac{eE_{0Y}}{m}\sin 2\pi\nu\, t \qquad \text{(A1.2)}$$

where *e* and *m* are the charge and mass of the electron.

From electromagnetic theory, an accelerated charge radiates. Figure A1.2 shows a charge q with an acceleration $\boldsymbol{a}$, and at a distance R, the electric field ε which results from the acceleration. In terms of cgs units, which for x-ray scattering are the simplest, the electric field is given by

$$\varepsilon = \frac{qa\sin\alpha}{c^2 R} \qquad \text{(A1.3)}$$

where c is the velocity of the light. The electric field is in the plane of R and a, and its magnitude depends on the component $a\sin\alpha$. This leads to a very simple and useful rule in considering problems of scattering and polarization. With the eye placed at the point of observation P, which is seen, determines the electric field produced.

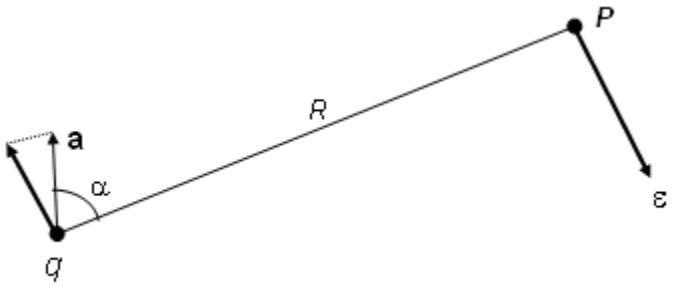

Figure A1.2. Illustration of electric field ε, produced by a charge q with acceleration a, according to classical electromagnetic theory

By means of Eq. 4.3, we can express the instantaneous value of the electric field due to the acceleration a_Y :

$$\varepsilon_{Y'} = \frac{e^2 E_{0Y}}{mc^2 R}\sin 2\pi\nu\, t\, \cos\varphi \qquad \text{(A1.4)}$$

Expressed in terms of amplitude, $\varepsilon_{Y'} = E_{Y'}\sin 2\pi\nu\, t$ where the amplitude is given by

$$E_{Y'} = \frac{e^2 E_{0Y}}{mc^2 R}\cos\varphi \qquad \text{(A1.5)}$$

Similar reasoning applied to the initial amplitude E_{0Z} leads to

$$E_Z = \frac{e^2 E_{0Z}}{mc^2 R} \qquad \text{(A1.6)}$$

The resultant amplitude E at the point of observation is then given by:

$$E = E_Z^2 + E_{Y'}^2 = \frac{e^4}{m^2c^4R^2}(E_{0Z}^2 + E_{0Y}^2\cos^2\varphi) \qquad \text{(A1.7)}$$

We now let E take with equal probability all orientations in the YZ-plane and consider the appropriate averages

$$< E_{0Y}^2 > + < E_{0Z}^2 > = < E_0^2 > \qquad \text{(A1.8)}$$

Since the Y and Z axes are equivalent,

$$< E_{0Y}^2 > = < E_{0Z}^2 > = \frac{1}{2} < E_0^2 > \qquad \text{and}$$

$$< E^2 > = < E_{0^2} > \frac{e^4}{m^2c^4R^2}(\frac{1+\cos^2\varphi}{2}) \qquad \text{(A1.9)}$$

The observable quantity is the intensity I, where by intensity we will always mean energy per unit area per unit time. In cgs units, the intensity is given by

$$I_e = \frac{c}{8\pi} < E^2 > \qquad \text{(A1.10)}$$

where E is the amplitude or maximum value of a sinusoidally varying field. Multiplying both sides of Eq. A1.2, we obtain

$$I_e = I_0 \frac{e^4}{m^2c^4R^2}(\frac{1+\cos^2\varphi}{2}) \qquad \text{(A1.11)}$$

Eq. A1.11 gives the intensity of classical scattering by a single free electron and it is often called "Thomson scattering equation". The factor $(1+\cos^2\varphi)/2$ is called the polarization factor for an unpolarized primary beam. If the primary beam is not polarized, the polarization factor takes a different form. The numerical value in Eq. A1.11 by using *SI* units is

$$K = \frac{e^4}{m^2c^4} = \frac{(4.802\times10^{-10})^4}{(9.107\times10^{-28})^2(2.998\times10^{10})^4} = 7.94\times10^{-30}\,m^2 \qquad \text{(A1.12)}$$

where R is expressed in meters. The equation A1.11 can be expressed as a simpler form if ϕ is taken as 2θ, Bragg angle in Figure A1.1:

$$I_e = I_0 \frac{K}{R^2}\left(\frac{1+\cos^2 2\theta}{2}\right) \quad \text{(A1.13)}$$

The scattering from the unit cell follows the same pattern with the Eq. A1.13 but the arrangement of the atoms in the unit cell needs to be considered. Structure factor, $|F_{hkl}|^2$, is the absolute value of the structure amplitude and includes several contributions determined by the arrangement of the atoms in the unit cell and other structural features [Pecharsky, V.T. (2005)]. Therefore, the scattering from the unit cell will be:

$$I_p = I_0 \frac{K}{R^2}|F_{hkl}|^2\left(\frac{1+\cos^2 2\theta}{2}\right) \quad \text{(A1.14)}$$

or in a simpler form

$$I_p = I_e|F_{hkl}|^2 \quad \text{(A1.15)}$$

A1.1. X-Ray Scattering Basics

3D-XRD technique is based on elastic Bragg scattering from crystals and restricted in the elastic limit of monochromatic x-rays. Therefore, the absorption of x-rays from the sample is neglected in this technique. The incident electrons scatter from the electrons in the crystal; this process is well described in elsewhere [Warren, B.E. (1990)].

A1.1.1. Basic Scattering Theory

The basic scattering from electrons, atoms and the unit cell is discussed in Appendix 1 with details. When monochromatic x-rays hit an object, the diffraction planes in the object satisfying the Bragg condition will diffract with 2θ angles. Direction and multitude of each diffraction plane will differ with the plane wave monochromatic X-ray beam defined by k_{in}. The scattering from x-rays are shown in Figure A1.3. Each diffraction plane will diffract with a different scattering vector. The length of the wave vector, k_{out}, is preserved due to assumption of elastic scattering, that is:

$$|k_{in}| = |k_{out}| = \frac{2\pi}{\lambda} \quad \text{(A1.16)}$$

where λ is the wavelength of the x-ray beam.

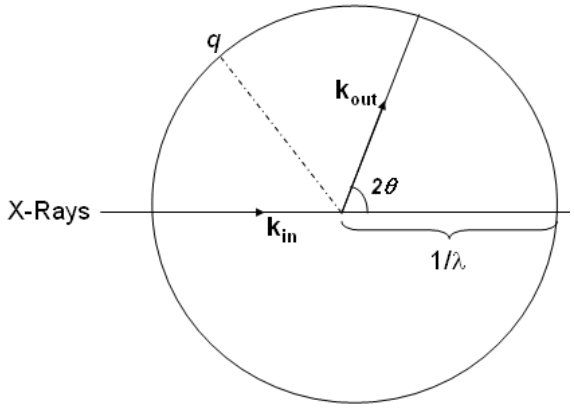

FigureA1.3. Scattering from x-rays

The scattering ability of the object is described by the complex scattering amplitude, *A*, which described both the amplitude and the phase of the observed scattered wave to the incoming wave. The phase difference, in the scattered wave, due to the different positions of *j* number of the atoms in the object can be found as:

$$(k - k_o).r_j = q.r_j \qquad \text{(A1.17)}$$

with the scattering vector, q, defined as

$$q = k - k_0 \qquad \text{(A1.18)}$$

The scattering amplitude from a collection of atoms can be written as:

$$A(q) = \sum_j f_j(q) e^{iq.r_j} \qquad \text{(A1.19)}$$

where $f_j(q)$ and r_j are the q-dependent atomic scattering factor and scattering vector for atom *j* respectively. Since x-ray detectors do not record both the phase and the amplitude of the scattered beam, but the only the intensity:

$$I(q) = AA* |A(q)|^2 \qquad \text{(A1.20)}$$

Therefore, the phase information is lost.

A1.1.2. Diffraction from a Perfect Crystal

The position of the atoms in a crystalline material is normally described by a lattice and a basis. A crystal lattice is characterized by the fact that it obeys certain translation symmetries. A 3D lattice can be described with three lattice basis vectors, a_1, a_2 and a_3, which have the property that looks the same if translated by an integer number of any of these.

The *lattice* is more formally described by vectors in the form:

$$R_n = n_1 a_1 + n_2 a_2 + n_3 a_3 , \qquad \text{(A1.21)}$$

with n=(n_1,n_2,n_3) all being integers.

These vectors give the positions of the unit cells of the crystal, the lattice points, each unit cell is populated by the same arrangement of atoms described by what is known as the basis. The basis can be described by vectors, r_j, relative to the lattice points. The position of any given atom in a crystal can be given as:

$$R_{n,j} = R_n + r_j = n_1 a_1 + n_2 a_2 + n_3 a_3 + r_j \qquad \text{(A1.22)}$$

for some *n, j*.

Scattering Amplitude

In the case of crystal, the general formula for the scattering amplitude can be separated into two parts as:

$$A(q) = \overbrace{\sum_j f_j(q) e^{iq.r_j}}^{unit\ cell\ sum} \overbrace{\sum_n e^{iq.R_n}}^{lattice\ sum} \qquad \text{(A1.23)}$$

where the "unit cell sum" is the sum over the atom configuration in the basis, and the 'lattice sum" is over all lattice points.

The reciprocal space and lattice

In conventional crystallography, the substances are assumed to have crystal structures repeating themselves with three-dimensional periodicity. The repeated crystals constitute the *direct lattice* and macroscopic geometric properties are the consequence of this crystal in microscale. Each faces of the crystal constitute a crystallographic plane and these faces are parallel to sets of lattice planes. The electron density of the crystal can be expressed as a periodic function of the lattice: $\rho(\mathbf{r} + \mathbf{t}_n) = \rho(\mathbf{r})$. The most general expression for a periodic function is the plane wave: $e^{i\varphi} = \cos\varphi + i\sin\varphi$. If we consider a function *f(**r**)* such that $f(\mathbf{r} + t_n) = f(\mathbf{r})$, i.e., the function has the total symmetry of the lattice. The most general way of writing this function is $f(r) = Ae^{i\varphi(r)}$. To be an argument of this exponential function, $\varphi(\mathbf{r}) = \mathbf{K}.\mathbf{r}$ needs to be where **K** has units (1/distance). The restrictions on **K**,

$f(\mathbf{r}+t_n) = Ae^{i\mathbf{K}(r+t_n)} = Ae^{i\mathbf{K}.\mathbf{r}}e^{i\mathbf{K}.t_n}$ which means that $e^{i\mathbf{K}t_n} = 1 \; or \; \mathbf{K}.\mathbf{t}_n = 2\pi N$

Since $\{t_n\}$ forms a lattice, then **K** is part of a set of vectors that also form a lattice – the *reciprocal lattice*. **K** can be expressed as $hb_1 + kb_2 + lb_3$; h, k and l are integers and b_1, b_2 and b_3 are the primitive vectors in reciprocal space. The conditions that define these vectors with respect to real space lattice are;

$$a_i.b_j = 2\pi\delta_{ij} \qquad \text{(A1.24)}$$

where δ_{ij} is the Kronecker delta.

The reciprocal space lattice is a set of imaginary points constructed in such a way that the direction of a vector from one point to another coincides with the direction of a normal to the real space planes. The separation of those points (absolute value of the vector) is equal to the reciprocal of the real interplanar distance. These reciprocal basis vectors are related to the crystal lattice basis vectors by:

$$b_1 = \frac{2\pi}{v_c}a_2 \times a_3, b_2 = \frac{2\pi}{v_c}a_3 \times a_1, b_3 = \frac{2\pi}{v_c}a_1 \times a_2 \qquad \text{(A1.25)}$$

with $v_c = a_1 \cdot (a_2 \times a_3)$ the volume of the unit cell. It can be seen that dimension of the reciprocal lattice vectors are reciprocal in length, hence the name.

The reciprocal basis vectors span, in a natural way, a lattice in reciprocal space, with a reciprocal lattice vector, ***G***, given as

$$G_{hkl} = hb_1 + kb_2 + lb_3 \qquad \text{(A1.26)}$$

with h, k, l integers.

Reciprocal lattice vectors have the following properties, relating them to the underlying crystal structure:

- G_{hkl} is perpendicular to the lattice plane with Miller indices hkl.
- $G_{hkl} = \frac{2\pi}{d_{hkl}}$, where d_{hkl} is the lattice spacing of the lattice planes with Miller indices hkl.
- G_{hkl} is bounded with the real lattice. When the real lattice is rotated, the reciprocal lattice is rotated too.

APPENDIX 2. The relation between diffracting volume and intensity

In the rotating crystal technique, the crystal is rotated with an angular velocity $\overset{o}{\omega}$ normal to the paper as shown in Figure A2.1.

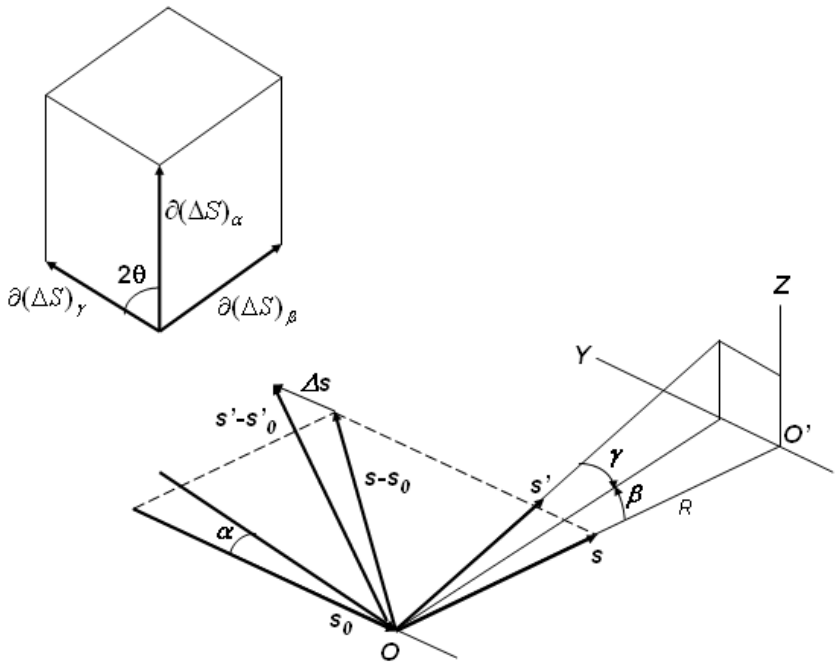

Figure A2.1. The geometry involved in calculating the integrated intensity from a small single crystal which is rotated at constant angular velocity ω about an axis normal to the paper

The intensity can be calculated as the energy per unit area and then the energy will be:

$$E = \iint I_p dt dA = \iiint I_p dt R^2 d\beta d\gamma \qquad \text{(A2.1)}$$

where I_p is the intensity from one unit cell (Eq. 4.14), *dt* is the unit data collecting time, *dA* is the unit area. Let the direction of the primary beam as a vector s_0' making angle with α. Then the time during the direction of primary beam α and α+dα

$$dt = \frac{(d\alpha)}{\omega}$$

The total diffracted energy

$$E = \frac{R^2}{\omega} \iiint I_p \, d\alpha \, d\beta \, d\gamma \qquad \text{(A2.2)}$$

Since the directions of primary and diffracted beams which differ from Bragg law directions, let $s'-s_0^{'} = s - s_0 + \Delta s$ where $s - s_0 = \lambda H_{hkl}$

Replacing one of sine functions with (s-s_0) by $\lambda H_{hkl} + \Delta S$

$$\sin^2 \frac{\pi}{\lambda}(\lambda H_{hkl} + \Delta s) \cdot N_1 \vec{a}_1 = \sin^2 \pi(hN_1 + \frac{\Delta S \cdot N_1 a_1}{\lambda}) \qquad \text{(A2.3)}$$

$$= \sin^2 \frac{\pi}{\lambda}(\Delta S \cdot N_1 \vec{a}_1)$$

It is convenient to represent ΔS as a vector in reciprocal space

$$\Delta S = \lambda(p_1 b_1 + p_2 b_2 + p_3 b_3) \qquad \text{(A2.4)}$$

where b_1, b_2, b_3 and p_1, p_2, p_3 are the reciprocal lattice vectors and coefficients of these vectors.

$$\sin^2 \frac{\pi}{\lambda} \Delta \vec{s} \cdot N_1 \cdot \vec{a}_1 = \sin^2 \pi(p_1 b_1 + p_2 b_2 + p_3 b_3) \cdot N_1 \vec{a}_1 = \sin^2 \pi N_1 p_1 \qquad \text{(A2.5)}$$

Total diffracted energy

$$E = \frac{I_e R^2}{\omega} |F_{hkl}|^2 \iiint \frac{\sin^2 \pi N_1 p_1}{\sin^2 \pi\ p_1} \cdot \frac{\sin^2 \pi N_2 p_2}{\sin^2 \pi\ p_2} \cdot \frac{\sin^2 \pi N_3 p_3}{\sin^2 \pi\ p_3}\, d\alpha\ d\beta\ d\gamma \qquad \text{(A2.6)}$$

$$|d(\Delta S)_\alpha| = d\alpha \quad |d(\Delta S)_\beta| = d\beta \quad |d(\Delta S)_\gamma| = d\gamma$$

$$dV = d(\Delta S)_\beta \cdot d(\Delta S)_\gamma \times d(\Delta S)_\alpha = \sin 2\theta\ d\alpha\ d\beta\ d\gamma \qquad \text{(A2.7)}$$

α, ß and γ can be expressed as volume integral

$$E = \frac{I_e R^2 |F_{hkl}|^2}{\omega \sin 2\theta} \iiint \frac{\sin^2 \pi N_1 p_1}{\sin^2 \pi\ p_1} \cdot \frac{\sin^2 \pi N_2 p_2}{\sin^2 \pi\ p_2} \cdot \frac{\sin^2 \pi N_3 p_3}{\sin^2 \pi\ p_3}\, dV \qquad \text{(A2.8)}$$

$$dV = \lambda b_1 dp_1 \cdot \lambda b_2 dp_2 \times \lambda b_3 dp_3 = \lambda^3 V_b dp_1 dp_2 dp_3$$

$$= \frac{\lambda^3}{V_a} dp_1 dp_2 dp_3$$

$$E = \frac{I_e R^2 \lambda^3 |F_{hkl}|^2}{\omega V_a \sin 2\theta} \int_{-\infty}^{\infty} \frac{\sin^2 \pi N_1 p_1}{(\pi\ p_1)^2} dp_1 \cdot \int_{-\infty}^{\infty} \frac{\sin^2 \pi N_2 p_2}{(\pi\ p_2)^2} dp_2 \times \int_{-\infty}^{\infty} \frac{\sin^2 \pi N_3 p_3}{(\pi\ p_3)^2} dp_3 \qquad \text{(A2.9)}$$

where $N=N_1.N_2 N_3$ (number of the unit cells in the crystal, diffracted energy

$$E = \frac{I_e R^2 \lambda^3 N \left|F_{hkl}\right|^2}{\omega V_a \sin 2\theta} \qquad \text{(A2.10)}$$

Since the volume is composed of unit cell with Avogadro numbers ($NV_a = \delta V$), the integrated intensity will be:

$$E = \frac{I_e R^2 \lambda^3 \delta V \left|F_{hkl}\right|^2}{\omega V^2{}_a \sin 2\theta} \qquad \text{(A2.11)}$$

The diffracted area will depend on the 2θ diffracting angle as shown in Figure A2.2. If we consider a volume element between z depth and z+dz and define δV as the number of the blocks in the volume element as the average volume, it will depend on

$$e^{-2\mu z/\sin\theta} \frac{A_0 dz}{\delta V \sin\theta} \qquad \text{(A2.12)}$$

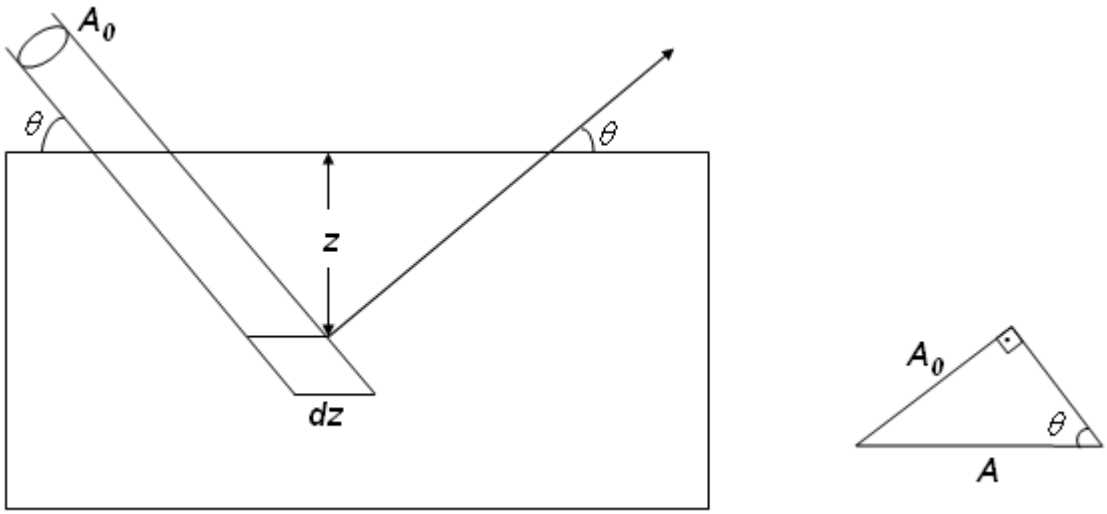

Figure A2.2. The geometry involved in calculating the integrated intensity for an extended face mosaic crystal.

Then, the final energy of the diffracted volume will be:

$$E = \frac{I_e R^2 \lambda^3 \delta V \left|F_{hkl}\right|^2}{\omega V_a^2 \sin 2\theta} \int_{z=0}^{\infty} e^{-2\mu z/\sin\theta} dz \qquad \text{(A2.13)}$$

$$E = \frac{I_e R^2 \lambda^3 \delta V \left|F_{hkl}\right|^2}{\omega V_a^2 \sin 2\theta} \frac{\sin\theta}{2\mu} \tag{A2.14}$$

Even though we related the energy of the diffracted volume, it will be related with the data collecting time. Moreover, the effect of the location of the spot is important and we can relate the diffraction spot with η and |sin(η)|. If we relate the diffracted total volume and diffracted specific hkl vector, they will related as:

$$E_{powder} = \frac{I_e R^2 \lambda^3 V_{gauge}}{V_a^2 \mu} \frac{\sin\theta_{hkl} \left|F_{hkl}^p\right|^2}{2\omega \sin 2\theta_{hkl}} \Delta t_{powder} \tag{A2.15}$$

$$E_{hkl} = \frac{I_e R^2 \lambda^3 V_{hkl}}{V_a^2 \mu} \frac{\sin\theta_{hkl} \left|F_{hkl}^g\right|^2}{2\omega \sin 2\theta_{hkl}} \Delta t_{hkl} \tag{A2.16}$$

$$\frac{E_{powder}}{E_{hkl}} = \frac{V_{gauge} \Delta t_{powder} \left|F_{hkl}^p\right|^2 m_{hkl} \Delta\omega \sin 2\theta_{hkl}}{V_{hkl} \Delta t_{hkl} \left|F_{hkl}^g\right|^2 \sin\theta_{hkl}} \tag{A2.17}$$

By the combination of the Eq. (A2.15) and (A2.16), the volume of the diffracting grain can be found as:

$$V_{hkl} = \frac{E_{hkl} V_{gauge} \Delta t_{powder} \left|F_{hkl}^p\right|^2 m_{hkl} \Delta\omega \sin 2\theta_{hkl}}{E_{powder} \Delta t_{hkl} \left|F_{hkl}^g\right|^2 \sin\theta_{hkl}} \tag{A2.18}$$

Appendix 3. Scanning microdiffraction principles

This section will describe the principles that scanning diffraction technique is relied on and shows the coordinate transformations in Scanning Microdiffraction technique. By using the principles described, one can characterize the twin orientations by starting from an indexed pattern.

Figure A.3.1 describes the Scanning Microdiffraction technique schematically. The incident beam is pointed along -y direction. The normal of the diffraction plane will be dependent on the orientation matrix (U), reciprocal lattice matrix (B) and diffraction plane. The diffraction equation will be:

$$n_{hkl} = \begin{vmatrix} 1 & 0 & 0 \\ 0 & \cos(45) & -\sin(45) \\ 0 & \sin(45) & \cos(45) \end{vmatrix} UB \begin{pmatrix} h \\ k \\ l \end{pmatrix} \qquad \text{(A3.1)}$$

From the vector addition, the diffracted beam vector will be:

$$k_{out} = k_i + n_{hkl} \qquad \text{(A3.2)}$$

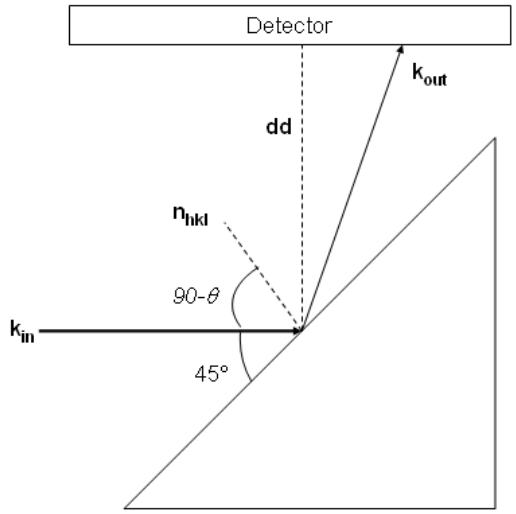

Figure A3.1. Scanning Microdiffraction Setup

The angle between the incident beam and the normal of the diffraction plane will be 90-2θ and

$$90 - \theta = \cos^{-1}\left(\frac{dot(k_i, n_{hkl})}{|ki||n_{hkl}|}\right) = \cos^{-1}\left(\frac{dot(k_{out}, n_{hkl})}{|k_{out}||n_{hkl}|}\right) \qquad \text{(A3.3)}$$

In order to obtain the diffracting vector (k_{out}), the locations of the diffracting spots on the detector are determined and each diffraction spots are converted to a diffracting vector (k_{out}) with the following formula:

$$k_{out} = \begin{pmatrix} (x - x_c)\cdot \mathrm{px} \\ (y - y_c)\cdot \mathrm{py} \\ \mathrm{L} \end{pmatrix} \qquad \text{(A3.4)}$$

where x and y are the location of the spot in the detector, x_c and y_c are the center of the image, *px* and *py* are the pixel size of the CCD detector in mm per pixel and *L* is the sample-to-detector distance. The normal of the diffraction plane (n_{hkl}) by Equation A3.2 can be found as:

$$n_{hkl} = \frac{k_{out} - k_{in}}{\left|k_{out} - k_{in}\right|} = \frac{\begin{pmatrix} k_{out}(1) \\ k_{out}(2) \\ k_{out}(3) \end{pmatrix} - \begin{pmatrix} 0 \\ 1 \\ 0 \end{pmatrix}}{\left|\begin{pmatrix} k_{out}(1) \\ k_{out}(2) \\ k_{out}(3) \end{pmatrix} - \begin{pmatrix} 0 \\ 1 \\ 0 \end{pmatrix}\right|} = \frac{\begin{pmatrix} k_{out}(1) \\ k_{out}(2) - 1 \\ k_{out}(3) \end{pmatrix}}{\sqrt{k_{out}(1)^2 + (k_{out}(2) - 1)^2 + k_{out}(3)^2}} \qquad \text{(A3.5)}$$

By considering the incoming beam direction is towards y. The normalized length of the diffracted beam, k_{out}, is 1 ($\sqrt{k_{out}(1)^2 + k_{out}(2)^2 + k_{out}(3)^2} = 1$) and if we put in the equation:

$$n_{hkl} = \frac{\begin{pmatrix} k_{out}(1) \\ k_{out}(2) - 1 \\ k_{out}(3) \end{pmatrix}}{\sqrt{1 - 2k_{out}(2) + 1}} = \frac{\begin{pmatrix} k_{out}(1) \\ k_{out}(2) - 1 \\ k_{out}(3) \end{pmatrix}}{\sqrt{2 - 2k_{out}(2)}} \qquad \text{(A3.6)}$$

Then, the components of the diffracted beam vector will be:

$$\begin{aligned} k_{out}(2) &= 1 - 2n_{hkl}(2)^2 \\ k_{out}(1) &= n_{hkl}(1)\sqrt{2 - 2k_{out}(2)} \\ k_{out}(3) &= n_{hkl}(3)\sqrt{2 - 2k_{out}(2)} \end{aligned} \qquad \text{(A3.7)}$$

If the detector has a tilt with respect to incoming beam plane, the components of a finalized diffraction vector (r) will be:

$$R_{tilt} = \begin{pmatrix} 1 & 0 & 0 \\ 0 & \cos(-\beta) & -\sin(-\beta) \\ 0 & \sin(-\beta) & \cos(-\beta) \end{pmatrix} \begin{pmatrix} \cos\gamma & -\sin\gamma & 0 \\ \sin\gamma & \cos\gamma & 0 \\ 0 & 0 & 1 \end{pmatrix} = \begin{pmatrix} \cos\gamma & -\sin\gamma & 0 \\ \cos(-\beta)\sin\gamma & \cos(-\beta)\cos\gamma & -\sin(-\beta) \\ \sin(-\beta)\sin\gamma & \sin(-\beta)\cos\gamma & \cos(-\beta) \end{pmatrix} \qquad \text{(A3.8)}$$

$$\begin{pmatrix} r_x \\ r_y \\ r_z \end{pmatrix} = R_{tilt} k_{out} = \begin{pmatrix} \cos\gamma & -\sin\gamma & 0 \\ \cos(-\beta)\sin\gamma & \cos(-\beta)\cos\gamma & -\sin(-\beta) \\ \sin(-\beta)\sin\gamma & \sin(-\beta)\cos\gamma & \cos(-\beta) \end{pmatrix} \begin{pmatrix} k_{out}(1) \\ k_{out}(2) \\ k_{out}(3) \end{pmatrix} =$$

$$\begin{pmatrix} \cos\gamma \cdot k_{out}(1) - \sin\gamma \cdot k_{out}(2) \\ \cos(-\beta)\sin\gamma \cdot k_{out}(1) + \cos(-\beta)\cos\gamma \cdot k_{out}(2) - \sin(-\beta) \cdot k_{out}(3) \\ \sin(-\beta)\sin\gamma \cdot k_{out}(1) + \sin(-\beta)\cos\gamma \cdot k_{out}(2) + \cos(-\beta) \cdot k_{out}(3) \end{pmatrix} \quad \text{(A3.9)}$$

where β and γ are the tilt angles defining a rotation along X and Z coordinates respectively. The diffraction vector is converted to the normal of the diffraction planes by using Equation A3.5 and the orientation matrices of each domain are found by using Equation A3.1.

Appendix 4. Computer Codes used in 3D-XRD Analysis

This section will describe the codes written to analyze the 3D-XRD experiment output.

A4.1. Orientation Fitting

Due to complexity and spot overlapping problems in ferroelectric materials, the orientation fitting in the tetragonal regime needs to be done with the following code. In order to do the fitting, first a grain indexing software is used to identify the orientations at cubic regime. Then, the distributions of these spots are found by Phi-Eta maps and center of mass of each candidate spot is found. The minimum number of the spots required for orientation fitting is 3 in this routine. By using quaternions, the minimum number of spots required for the orientation fitting can be reduced to 2 as well. Note that the reflections used in the orientation fitting need to be nonlinear reflections.

```
%Eta-Phi locations with hkl values go here.
etaPhi=[58.41   122.6   0   0   -2;
   -41.17  105.1   2   0   0;
   -36.63  285.1   -2  0   0;
   33.68   216.66  0   2   0;
   26.3    36.66   0   -2  0];

%Lattice parameters of BaTiO3 at room temperature.
ucell=[3.9836  3.9836 4.0198 90 90 90];

en=80.72; %Energy of the x-rays

 % Converting  energy to lambda
lambda=12.398427/en;

%Forming B matrix;
B=FormB(ucell);

%Getting hkls
Ghkl=etaPhi(:,3:5)';

%Producing Bhkls
Bhkl=B*Ghkl;

%Creating d-spacing
list=findDspace(en,ucell,99,200,2274);

% Formulations on finding the U matrix comes from Poulsen's book
% Chapter 3, page 26, Equation 3.6

for i=1:size(Bhkl,2)
   aa=find(list(:,1)==Ghkl(1,i)&list(:,2)==Ghkl(2,i)&list(:,3)==Ghkl(3,i));
   A(i)=2*pi*sind(list(aa,6))/lambda;
   gamma(:,:,i)=[cosd(etaPhi(i,1)) -sind(etaPhi(i,1)) 0;...
      sind(etaPhi(i,1)) cosd(etaPhi(i,1)) 0;...
      0 0 1];
   b(:,i)=A(i)*[-tand(list(aa,6)/2) -sind(etaPhi(i,2)) cosd(etaPhi(i,2))];
   bB(:,i)=b(:,i)'*gamma(:,:,i);
   Bhkl(:,i)=lambda*Bhkl(:,i)/(4*pi*sind(list(aa,6)/2));
end

U=bB/Bhkl;
```

```
%
U(1,:)=U(1,:)/norm(U(1,:));
U(2,:)=U(2,:)/norm(U(2,:));
U(3,:)=U(3,:)/norm(U(3,:))

% The determinant will determine whether the orientation is a real square
% matrix (determinant = 1)
determinant=det(U)
```

A4.2. Pole Figure

This function plots orientations as a pole figure. The code was originally written by Henning Poulsen and it was improved with overlaying Wulff plot.

```
function xy = plotU2pol(U,ucell,H,ttlFig,plotNum)

% Pole Figure from U Matrix
% A simple converter that plots a number of reflections in the corresponding pole-figure.
% The formalism follows the ID11-3DXRD specs
%
%  Written by: Henning Poulsen, Risoe 1/11 2000.
% Improved by: Mesut Varlioglu, ISU 10/12/2007
% By overlaying the Wullf plot.
%
% USAGE:  plotU2pol(uu,[3.9836 3.9836 4.0198 90 90 90],[1 0 0; 0 1 0; 0 0 1],'RT',1);
%

%Create B matrix; It uses farfield diffsim function which is avaliable
%online, type in google "fable farfield simulation" to obtain this package.
B=FormB(ucell);

figure;set(gcf, 'color', 'white');
%wulff;
for ij=1:size(U,3)

   % calculate the Bunge u,v,w then X and Y
   for i1 = 1:size(H,1)
      h = H(i1,1);
      k = H(i1,2);
      l = H(i1,3);

      Gs = U(:,:,ij)*B*[h k l]';
      Glen = (Gs(1)^2 + Gs(2)^2 + Gs(3)^2)^0.5;
      u = Gs(1)/Glen; v = Gs(2)/Glen; w  = Gs(3)/Glen;
      if w<0
         u = -u; v = -v; w = -w;
      end
      x(i1) = u/(w+1);
      y(i1) = v/(w+1);
   end


   %plot the data point
   hold all;
   plot(x,y,'k+','MarkerSize',6);
   xy{ij}=[x y];
   if plotNum==1
      text(x+0.01,y,num2str(ij),'Color','k','FontWeight','bold','FontSize', 14);
   else
      continue;
   end
   hold all;
   axis equal;
```

```
    axis off;
end

axis off; axis square;


text(1.3,1,ttlFig,'FontSize',8);
t=0:0.01:2*pi;
xcircle = cos(t);
ycircle = sin(t);
plot(xcircle,ycircle,'k-')
text(1.05,0,'X','FontSize',14)
text(0,1.05,'Y','FontSize',14)

t = -1:1/20:1;
hline1 = plot(t,0,'k');
hline2 = plot(0,t,'k');

N = 90;
cx = cos(0:pi/N:2*pi);                    % points on circle
cy = sin(0:pi/N:2*pi);
psi = [0:pi/N:pi];
for i = 1:8                               %plot great circles
    rdip = i*(pi/18);                     %at 10 deg intervals
    radip = atan(tan(rdip)*sin(psi));
    rproj = tan((pi/2 - radip)/2);
    x1 = rproj .* sin(psi);
    x2 = rproj .* (-sin(psi));
    y = rproj .* cos(psi);
    plot(x1,y,':r',x2,y,':r');
end

for i = 1:8                               %plot small circles
    alpha = i*(pi/18);
    xlim = sin(alpha);
    ylim = cos(alpha);
    x = [-xlim:0.01:xlim];
    d = 1/cos(alpha);
    rd = d*sin(alpha);
    y0 = sqrt(rd*rd - (x .* x));
    y1 = d - y0;
    y2 = - d + y0;
    plot(x,y1,':r',x,y2,':r');
end

hold off;

xy=[x y];
```

A4.3. Inverse Pole Figure

This function plots orientations as an inverse pole figure. The code can currently plot the orientations with cubic and tetragonal crystal symmetries.

```
function plotInvPoleFig(rmat,ttlFig,symOP)

% It plots the inverse pole figures of the orientations with their symmetry
% operations.
%
% USAGE: plotInvPoleFig(umat,'ttlFig1',1); For tetragonal
%        plotInvPoleFig(umat,'ttlFig1',2); For cubic
```

```
figure;
hold all;

ttl={'X','Y','Z'};
for ij=1:3
    subplot(1,3,ij);
    hold all;
    if symOP == 1
        for i = 1:size(rmat,3)

            u=rmat(1,ij,i);
            v=rmat(2,ij,i);
            w=rmat(3,ij,i);

            INVPF1(:,i)=acos(abs(w));  % ...(:,1) is alpha angle
            INVPF2(:,i)=atan(abs(u)./abs(v));%+45*pi/180; % ...(:,2) is beta angle
            bmax=45;
            if INVPF2(i) > (pi/4)
                INVPF2(i) = pi/2 - INVPF2(i); % enforcing a mirror about 45deg
            end
            % tan(alpha/2) incorporates stereographic projection
            xinv(i)=tan(INVPF1(i)/2).*cos(INVPF2(i));
            yinv(i)=tan(INVPF1(i)/2).*sin(INVPF2(i));
            % this line plots the data point
            plot(xinv(i),yinv(i),'k.')
            %plot(xinv(i),yinv(i),'ko', 'MarkerFaceColor', 'y', 'MarkerSize', 10)
            %text(xinv(i)+0.01,yinv(i),num2str(i),'Color','b','FontWeight','bold','FontSize', 10)
            axis square
            %title(PFtitle);
            axis off
            hold all;
        end
        hold on;

        plot([0 1], [0 0], 'k-')
        xinv2=tan([45 54.7 90]*pi/180/2).*cos([0 45 bmax]*pi/180);
        yinv2=tan([45 54.7 90]*pi/180/2).*sin([0 45 bmax]*pi/180);
        plot(xinv2(1),yinv2(1),'k+')
        plot(xinv2(2),yinv2(2),'k+')


        % these plot lines for the borders of the Inverse PF
        plot([0 xinv2(3)],[0 yinv2(3)],'k-')
        xinv3=ones(1,20).*cos(linspace(0,bmax,20)*pi/180);
        yinv3=ones(1,20).*sin(linspace(0,bmax,20)*pi/180);
        plot(xinv3,yinv3,'k-')

        text(0.38,-0.04,'101','FontWeight','bold','FontSize',12);
        text(0.31,0.41,'111','FontWeight','bold','FontSize',12);

        text(-0.1,-0.04,'001','FontWeight','bold','FontSize',12);
        text(1,-0.04,'100','FontWeight','bold','FontSize',12);
        text(0.67,0.75,'110','FontWeight','bold','FontSize',12);
        %text(1.02,0.04,'E Field','FontWeight','bold','Color','g','FontSize',12);

        % i= 1; plot(xinv(i),yinv(i),'ko', 'MarkerFaceColor', 'y', 'MarkerSize', 10)
        %text(xinv(i)+0.01,yinv(i),num2str(i),'Color','b','FontWeight','bold','FontSize', 10)
        hold off;
    elseif symOP == 2
        for i = 1:size(rmat,3)

            b(1)=rmat(1,ij,i);
            b(2)=rmat(2,ij,i);
            b(3)=rmat(3,ij,i);
```

```
        [A,INDEXA]=sort(abs(b));

        w=abs(b(INDEXA(3)));
        v=abs(b(INDEXA(2)));
        u=abs(b(INDEXA(1)));

        c = tan( acos(w)/2);

        alpha = acos(v/(v^2 + u^2)^.5);

        xinv(i) = c*cos(alpha);
        yinv(i) = c*sin(alpha);
        plot(xinv(i),yinv(i),'k.')
        %text(xinv(i)+0.01,yinv(i),num2str(i),'Color','b','FontWeight','bold','FontSize', 10)
        axis square
        %title(PFtitle);
        axis off
        hold all;
        bmax=45;
      end
   end

   % these lines plot extra points for reference
   hold on;
   plot([0,.5],[0,0],'k-',[0,.355],[0,.355],'k');

   % these plot lines for the borders of the Inverse PF
   %plot([0 .366],[0 .366],'k-')
   xinv3=ones(1,20)/2.*cos(linspace(0,bmax,20)*pi/180);
   yinv3=ones(1,20)/2.*sin(linspace(0,bmax,20)*pi/180);
   plot(xinv3,yinv3,'k-')

    text(0.34,0.38,'111','FontWeight','bold','FontSize',12);
   text(0.5,-0.02,'110','FontWeight','bold','FontSize',12);
   text(-0.03,-0.02,'100','FontWeight','bold','FontSize',12);


   % i= 1; plot(xinv(i),yinv(i),'ko', 'MarkerFaceColor', 'y', 'MarkerSize', 10)
   %text(xinv(i)+0.01,yinv(i),num2str(i),'Color','b','FontWeight','bold','FontSize', 10)
   hold off;
   set(gcf, 'color', 'white');
   title(ttl{ij});
end
text(0.5,0.5,ttlFig);
```

A4.4. Lattice Strain Matrix

This code finds the lattice strain tensor from the spot strains and direction cosines.

```
function strain=findLatticeStrain(lmn,epsilon)

%It finds the strain tensor components from the direction cosines and spot
%strains.
% USAGE: strain=findLatticeStrain(rand(3,18),rand(1,18))

for i = 1:size(lmn,2)
   fx(i,:)=[lmn(1,i)^2 lmn(2,i)^2 lmn(3,i)^2 lmn(1,i)*lmn(2,i) lmn(1,i)*lmn(3,i) lmn(2,i)*lmn(3,i)];
end

strain=fx\epsilon'; %It causes rank deficient results.
```

Appendix 5. Computer codes used in μSXRD analysis

This section will describe the codes written to analyze the μSXRD experiment output.

A5.1. Orientation Fitting

Due to complexity of the μSXRD technique and spot overlapping problems in ferroelectric materials, the orientation fitting of the ferroelectric domains was confirmed with this code. In this fitting, the information about the each orientation is extracted and the orientations are confirmed by using the output parameters from XMAS software.

```
function [usimCor,uxmas]=findOrienWB1(file)

% It finds and confirms the orientation from the XMAS outputs
%
% USAGE: [usimCor,uxmas]=findOrienWB1('BaTO130CLast_0392.STR')

[table,reflist]=readSTRv4(file);

% Converting XMAS orientations to direction cosine matrices.
[uxmas,OM1] = convertU2rmat(table);


% xc=522.7;
% yc=512.3;
% dd=83.94;

px=135/1024;
py=135/1024;

% figure;

% B=[1.567   0.00081035   -0.0018622
%    0      1.569         0.00089509
%    0      0             1.5674];

abc(:,1:3)=table(:,5:7)*10;
abc(:,4:6)=table(:,8:10);

table(:,5:7)*10;
%rot1=[-0.99993 -0.01146 0; -0.00806 0.70319 -0.71095; 0.00815 -0.71090 -0.70324]; %For ALSJan08
rot1=[0.99994 -0.01087 0; 0.00769 0.70735 -0.70682; 0.00769 0.70678 0.70739];
% rot2=[-1 0 0;
%       0 cosd(45) -sind(45);
%       -0 -sind(45) -cosd(45)];

for ij=1:size(reflist,2)
   xc=table(ij,24);
   yc=table(ij,25);
   dd=table(ij,23);
   for i=1:size(reflist{1,ij},1)
      k{ij}(i,:)=[ ((reflist{1,ij}(i,1)-xc)*px) ((reflist{1,ij}(i,2)-yc)*py) dd];
      k1{ij}(i,:)=k{ij}(i,:)/norm(k{ij}(i,:));

      theta{ij}(i,:)=acosd(dot([0 -1 0],k1{ij}(i,:)))/2;
      qvec{ij}(:,i)=-k1{ij}(i,:)-[0 -1 0];
      qhat{ij}(:,i)=qvec{ij}(:,i)/norm(qvec{ij}(:,i));
      qhat1{ij}(i,:)=qhat{ij}(:,i);
```

```
        hkl{ij}(:,i)=[reflist{1,ij}(i,3) reflist{1,ij}(i,4) reflist{1,ij}(i,5)];
        hkl1{ij}(:,i)=hkl{ij}(:,i)/norm(hkl{ij}(:,i));

        theta1{ij}(i,:)=acosd(dot([0 -1 0],-qhat{ij}(:,i)));
        a1(:,:,ij)=qhat{ij}/hkl1{ij};
        B(:,:,ij)=FormB([table(ij,5:7)*10 table(ij,8:10)]);
        B1(:,:,ij)=B(:,:,ij)/norm(B(:,:,ij));
        a2(:,:,ij)=a1(:,:,ij)/B1(:,:,ij);
        usim(:,:,ij)=rot1'*a2(:,:,ij);

        usimN(:,1,ij)=usim(:,1,ij)/norm(usim(:,1,ij));
        usimN(:,2,ij)=usim(:,2,ij)/norm(usim(:,2,ij));
        usimN(:,3,ij)=usim(:,3,ij)/norm(usim(:,3,ij));
        usimCor(1,:,ij)=usimN(1,:,ij);
        usimCor(2,:,ij)=-usimN(3,:,ij);
        usimCor(3,:,ij)=usimN(2,:,ij);

        gnew{ij}(:,i)=rot1*usim(:,:,ij)*FormB([table(ij,5:7)*10 table(ij,8:10)])*hkl1{ij}(:,i);
        gnew1{ij}(:,i)=rot1*usimN(:,:,ij)*FormB([table(ij,5:7)*10 table(ij,8:10)])*hkl1{ij}(:,i);
        qhatsim{ij}(i,:)=gnew{1,ij}(:,i)/norm(gnew{ij}(:,i));


        qhatsimN{ij}(i,:)=gnew1{ij}(:,i)/norm(gnew1{ij}(:,i));
        theta2{ij}(i,:)=acosd(dot([0 -1 0],-qhatsimN{ij}(i,:)));
        %rot1%*ab(:,:,ij)%*FormB([table(ij,5:7)*10 table(ij,8:10)])%*hkl1{ij};
    end
end
```

A5.2. Read Strain Files

This code reads µSXRD strain file and outputs the information about each orientation found. The strain file (*filen*) is read by the code and the orientation matrices, lattice parameters of each grain is tabulated in *table* and the reflection information is created in *reflist* as cell each column containing x(exp), y(exp), h, k, l, xdev, ydev, energy, dspace, intens, integr, xwidth, ywidth, tilt, rfactor, pearson, xcentroid, ycentroid. This code also exports the deviatoric strain matrix.

```
function [table,reflist]=readSTRv4(filen)

% Read the µSXRD strain file and outputs the information in the strain text file.
% Developed from the readtextfile.m file available at http://www.phon.ucl.ac.uk/courses/spsci/matlab/lect6.html website.
% Mesut Varlioglu, January 28th, 2007

% USAGE: [table,reflist]=readSTR('BTO_RT0036.str')
% OUTPUT: The output file (TABLE) contains the following:
% image g_number g_indice peak_number a b c alpha beta gamma dev1 dev2
% pixdev M11 M12 M13 M21 M22 M23 M31 M32 M33 DD Xcent YCent S11 S12 S13 S21
% S22 S23 S31 S32 S33
%
% (REFLIST) contains the following columns:
%
% x(exp) y(exp) h k l xdev ydev energy dspace intens integr xwidth ywidth tilt rfactor pearson xcentroid ycentroid
%
%

tab=readtextfile(filen);

 sz=size(tab);

idd=zeros(1,sz(1));
```

```
for i=1: sz(1);
    id{i}=find(strcmp(strcat(tab(i,1:10)),'Grain no:'));%&&&str2num(tab(ID(i)+RefID(ij)+26,:))~=0);
    id1{i}=find(strcmp(strcat(tab(i,1:18)),'latticeparameters='));%&&&str2num(tab(ID(i)+RefID(ij)+26,:))~=0);
    if id{i}~=NaN;%((id{i}~=NaN)& (id1{i}~=NaN)&(str2num(tab(id1{i}+24,:))>0));
        idd(i)=1;
    end;
    if id1{i}~=NaN%str2num(tab(id1{i}+24,:))>0;
        idd1(i)=1;
    end
    %      if id1{i}~=NaN;  idd1(i)=id1{i};
    %     end;
end

% Finding the information on each grain
% (IDA for finding line starting with Grain No
% and ID1 for finding line starting with Lattice Parameters)

IDA=find(idd>eps);
ID1=find(idd1>eps);

for i=1:length(IDA)
    aa(i,:)=str2num(tab(ID1(i)+25,:));
end

finID=find(aa(:,1)~=0);
ID=IDA(finID);

table=zeros(length(ID),34);

for ij=1:length(ID)
    IM=strcat(tab(1,:));
    %Inputting strain file number
    table(ij,1)=str2num(IM(end-7:end-4));
    %Inputting grain number;
    table(ij,2)=ij;

    %Finding the number of the reflections
    cc=strcat(tab(ID(ij),:));
    RefID(ij)=str2num(cc(end-2:end));
    table(ij,4)=RefID(ij);
    latID=tab(ID(ij)+RefID(ij)+2,:);
    latt(ij,:)=str2num(strcat(latID(:,22:end)));
    %
    table(ij,5:10)=latt(ij,:);

    devID=tab(ID(ij)+RefID(ij)+7,:);
    dev(ij,:)=str2num(devID(20:end));

    table(ij,11:13)=dev(ij,:);

    u1=str2num(tab(ID(ij)+RefID(ij)+26,:));
    u2=str2num(tab(ID(ij)+RefID(ij)+27,:));
    u3=str2num(tab(ID(ij)+RefID(ij)+28,:));
    om(ij,:)=[u1 u2 u3];

    table(ij,14:22)=om(ij,:);

    CentDDID=tab(ID(ij)+RefID(ij)+4,:);
    CenD(ij,:)=str2num(strcat(CentDDID(:,20:end)));
    table(ij,23:25)=CenD(ij,:);

    s1=[str2num(tab(ID(ij)+RefID(ij)+13,1:10)) str2num(tab(ID(ij)+RefID(ij)+13,11:20)) str2num(tab(ID(ij)+RefID(ij)+13,21:30))];
    s2=[str2num(tab(ID(ij)+RefID(ij)+14,1:10)) str2num( tab(ID(ij)+RefID(ij)+14,11:20)) str2num(tab(ID(ij)+RefID(ij)+14,21:30))];
    s3=[str2num(tab(ID(ij)+RefID(ij)+15,1:10)) str2num(tab(ID(ij)+RefID(ij)+15,11:20)) str2num(tab(ID(ij)+RefID(ij)+15,21:30))];
```

```
    sm(ij,:)=[s1 s2 s3];
    table(ij,26:34)=sm(ij,:);

    reff=str2num(tab(ID(ij)+2:ID(ij)+RefID(ij)+1,:));
    reff(:,18)=ij;
    %[ic, id]=sort(reff,1);
    reflist{ij}= reff;%(id(:,1),:);
    clear reff;
end
```

A5.3. Read Indexation Files

This code reads µSXRD indexation file and outputs the information about each orientation found. The lattice parameters and components of the orientations are collected in one table while strain matrix components are collected in another table.

```
function [refList,u]=readIND(filen)

%filen='C:\research\xmas\jan08\ebsd\ebsd0220.IND';
%filen='C:\research\ALS_Jan08\xmas\strainFiles\BaTORT_0220.str';

%filen='C:\research\ALS_Jan08\xmas\EBSD\param\ebsd0005.STR';
%filen='C:\research\ALS_Jan08\bto_3dxrd_0001.STR';
% Read the µSXRD indexation file and outputs the information in the indexation text file.
% Developed from the readtextfile.m file available at http://www.phon.ucl.ac.uk/courses/spsci/matlab/lect6.html website.
% Mesut Varlioglu, January 28th, 2007

% USAGE: [reflist,u]=readIND('C:\research\xmas\jan08\ebsd\ebsd0220.IND')
% OUTPUT: The output file (TABLE) contains the following:
% image g_number g_indice peak_number a b c alpha beta gamma dev1 dev2
% pixdev M11 M12 M13 M21 M22 M23 M31 M32 M33 DD Xcent YCent S11 S12 S13 S21
% S22 S23 S31 S32 S33
%
% (REFLIST) contains the following columns:
%
% x(exp) y(exp) h k l xdev ydev energy dspace intens integr xwidth ywidth tilt rfactor pearson xcentroid ycentroid
%
%

tab=readtextfile(filen);

sz=size(tab);

idd=zeros(1,sz(1));

for i=1: sz(1);
    id{i}=find(strcmp(strcat(tab(i,1:10)),'grain no:'));%&&&str2num(tab(ID(i)+RefID(ij)+26,:))~=0);
    id1{i}=find(strcmp(strcat(tab(i,1:25)),'matrix X  Y  Z -> h  k  l'));%&&&str2num(tab(ID(i)+RefID(ij)+26,:))~=0);
    if id{i}~=NaN;%((id{i}~=NaN)& (id1{i}~=NaN)&(str2num(tab(id1{i}+24,:))>0));
        idd(i)=1;
    end;
    if id1{i}~=NaN%str2num(tab(id1{i}+24,:))>0;
        idd1(i)=1;
    end
%      if id1{i}~=NaN;  idd1(i)=id1{i};
%     end;
end

% Finding the information on each grain
% (IDA for finding line starting with Grain No
% and ID1 for finding line starting with Lattice Parameters)
```

```
IDA=find(idd>eps);
ID1=find(idd1>eps);

%
for i=1:length(IDA)
    refList{i}=str2num(tab((IDA(i)+3):ID1(i)-2,:));
   u(:,:,i)=str2num(strcat(tab((ID1(i)+1):(ID1(i)+3),:)));
end
```

A5.4. Convert U Matrix

It converts the XMAS orientations to direction cosine matrices.

```
function [rmat,OM1] = convertU2rmat(data1)

% It converts the XMAS orientations to direction cosine matrices.
% USAGE: [uxmas,OM1] = convertU2rmat(table);

om1 = data1(:,14:22);

%OM2=zeros(3,3,20);

for i=1:size(om1,1)
    OM1(:,:,i)=reshape(om1(i,:),3,3)';
    OM2(1,:,i)=OM1(1,:,i)/data1(i,5);
    OM2(2,:,i)=OM1(2,:,i)/data1(i,6);
    OM2(3,:,i)=OM1(3,:,i)/data1(i,7);
end

rmat=OM2;
```

Appendix 6. Computer codes used in EBSD analysis

This macro reads the OIM software outputs and creates an orientation map from the orientations.

```
%function [table,misOr,mis,rmat1,rmat2,Dom90,Dom180,x,y,z] = readEBSDfile(filename,CILim)
% Manipulates the EBSD experiment data files and orientation matrices.
% Plots the orientation map with rgb color mode where
% 100-->Red
% 010-->Green
% 001-->Blue
%USAGE: [table,misOr,mis,rmat1,rmat2,Dom90,Dom180,x,y,z] = readEBSDfile('C:\research\EBSD\Mesut\BaTiO3-run3.b.ang',0.2)
%
% Mesut Varlioglu, December 19th, 2007

filename='C:\research\EBSD\Mesut\BaTiO3-run3.b.ang';
table=textread(filename,'','headerlines',58);

% x=table(:,4);
% y=table(:,5);
% x=unique(table(:,4));
% y=unique(table(:,5));

% aa=find(table(:,7)~=-1&table(:,7)>=CILim);
% table=table(aa,:);


rmat=RMatOfBunge([table(:,1) table(:,2) table(:,3)]');

rmat1=convertU2FundaRegion(rmat,TetSymmetries);

 for i=1:size(rmat1,3); or(i,:)=rmat1(:,3,i); end


% %%% Make the grain map
% figure;
% multicomb([table(:,5) table(:,4) zeros(1,5372)'],or,'honeym')

%%
r=[table(:,5) table(:,4) zeros(1,5372)'];
U=or;

figure;set(gcf, 'color', 'white');
warning off


Umax=max(max(U));
Umin=min(min(U));
[n,m]=size(r);
x = r(:,1);
y = r(:,2);
z = r(:,3);
%c = (U-Umin)/(Umax+Umin);
c = abs(U);
d=sqrt((r(1,1)-r(2,1))^2+(r(1,2)-r(2,2))^2);

honeyrad=(d/2)/cos(pi/6);

tita =linspace(0,2*pi,7);
Rx =  honeyrad*cos(tita);
Ry =  honeyrad*sin(tita);
```

```
zo = extract(z);
nz = length(zo);
zini = zo(1);
ni=1;

%figure(fignum)
hold off
if (max(c)~=min(c)),

   for ii=1:n,
      if (z(ii)~=zini),
         zini=z(ii);
         ni=ni+1;
         xlabel('X [mm]')
         ylabel('Y [mm]')
         colorbar('v')
         % colormap hot
         axis tight
         shading flat
      end;
      subplot(nz,1,ni),
      %title(strcat('Z=',num2str(zini)))
      hold all;
      fill(x(ii)+Rx,y(ii)+Ry,c(ii,:))
      hold on
   end;
   colorbar('v')
   xlabel('X [microns]')
   ylabel('Y [microns]')
   %colormap hot
   axis tight
   shading flat

else;

   for ii=1:n,
      if (z(ii)==zini),
         fill(x(ii)+Rx,y(ii)+Ry,'g')
         hold on
      end;
   end;


  % hold off
end

%axis([2.1 3.5 2 2.6]); axis square;
```

Appendix 7. Rotation of polarization vectors with spontaneous deformation

The mechanism on how ferroelectric domains form during the cooling from cubic to tetragonal structure has been a major research interest in ferroelastic and ferroelectric materials [Sapriel, J. (1975)]. Sapriel, J. (1975) discussed that the domain boundaries are oriented during the phase transformation to maintain the strain compatibility between two neighbor domains. Nepochatenko, V.A. (2006) also discussed that the mismatch between the lattice parameters of the local domains result in the creation of the spontaneous deformation during the cooling process. This deformation creates a mismatch in the domain walls and results in the rotation of the domains to reduce the spontaneous strain between domains. The rotation mechanism proposed by Nepochatenko, V.A. (2006) is revisited in the following section.

During cooling from cubic to tetragonal phase, the polarization vectors can develop along 6 major tetragonal crystal directions. From these directions, the polarization vectors along the major tetragonal crystal axes are:

$$P(1) = P_0(1,0,0)^T \qquad P(2) = P_0(0,1,0)^T \qquad P(3) = P_0(0,0,1)^T \qquad \text{(A7.1)}$$

where P_0 is the spontaneous polarization of the tetragonal ferroelectric. During the cooling, the tetragonal-to-cubic phase transformation takes place and the lattice parameters for cubic phase (a_0) change to tetragonal (a, c) by creating a spontaneous strain within the body. Due to change in the lattice parameters, $BaTiO_3$ exhibit spontaneous deformation during the phase transformation from cubic to tetragonal structure. During the phase transformation, the resultant spontaneous strain tensors can be obtained for the polarization vectors above:

$$\varepsilon(1) = \begin{pmatrix} \varepsilon_{22} & & \\ & \varepsilon_{11} & \\ & & \varepsilon_{11} \end{pmatrix} \qquad \varepsilon(2) = \begin{pmatrix} \varepsilon_{11} & & \\ & \varepsilon_{22} & \\ & & \varepsilon_{11} \end{pmatrix} \qquad \varepsilon(3) = \begin{pmatrix} \varepsilon_{11} & & \\ & \varepsilon_{11} & \\ & & \varepsilon_{22} \end{pmatrix} \qquad \text{(A7.2)}$$

where $\varepsilon_{11} = (a - a_0)/a_0$ and $\varepsilon_{22} = (c - a_0)/a_0$ represent the spontaneous deformation during the phase transformation. Any of these polarization directions can intersect with 90° domain walls. The number of the maximum possible 90° domain walls is 4. For instance, for a domain with a [001] cubic direction (P(3)) can intersect with 90° domain walls of (101), (-101), (011) and (0-11). (110) and (1-10) domain walls will be equivalent to 180° domain walls. To considering all the major cube axes, 4 domains in each cube axis and 24 domains in all cube axes can form. Due to ambiguity of the directions in x-rays where the positive and negative directions are not detectable, the total 12 domains can be detected. The domain walls separating two domains must have mechanical compatibility with the neighboring domains. Let's consider (101) domain walls at paraelectric phase and select noncollinear directions $a_o[0,1,0]$ and $b_o[1,0,1]$ in plane of (101) domain wall. In the ferroelectric phase, these directions transform into $\mathbf{a_1}$ and $\mathbf{b_1}$ vectors under thermal expansion. Under homogeneous deformation, the change in any vector can be calculated as:

$$\Delta r_j = e_{ij} r_i \tag{A7.3}$$

Applying the corresponding spontaneous strain tensor to the directions above, we can obtain the change in these vectors as: $a_1[0,1+e_{11},0]$ and $b_1[1+e_{11},0,1+e_{22}]$. The normal to the domain wall plane in the ferroelectric phase can be found as:

$$n = a_1 \times b_1 \tag{A7.4}$$

The corresponding normal of the domain wall will be $[-(1+\varepsilon_{11})(1+\varepsilon_{22}),0,(1+\varepsilon_{11})^2]$. The direction cosine of the normal of the domain wall (n) denotes to the mismatching angle between the paraelectric and ferroelectric phase. The angle between the domain walls during the phase transformation will be:

$$\psi = \cos^{-1}\left(\frac{2+e_{11}+e_{22}}{\sqrt{2}\sqrt{(1+e_{11})^2+(1+e_{22})^2}}\right) = \cos^{-1}\left(\frac{a+c}{\sqrt{2}\sqrt{a^2+c^2}}\right) \tag{A7.5}$$

Considering the lattice parameters for the $BaTiO_3$ sample were measured as a=0.39836 and c=0.40198 nm, the phase matching angle can be calculated as 0.2592°. Table 1 summarizes the possible domains and their 90° domain walls separating the neighboring domains and the angles between the domains. The relations between mismatching angles correspond to A=90-ψ, B=90+ψ.

The mismatch angle can be calculated as:

$$\Psi = \cos^{-1}\left(\frac{a+c}{\sqrt{2(a^2+c^2)}}\right) \qquad \text{(A7.6)}$$

where *a* and *c* correspond to lattice parameters of the domains. Considering the lattice parameters for the $BaTiO_3$ sample were measured as a=0.39836 and c=0.40198 nm, the phase matching angle can be calculated as 0.2592°.

Table A7. 1. Possible spontaneous polarization directions and their 90° domain walls separating the neighboring domains and the mismatching angles between the domains. The relations between mismatching angles correspond to A=90-ψ, B=90+ψ

Polarization Vector along Crystal Direction	Possible 90° Domain Walls	In-plane Noncollinear paraelectric vectors (a_0, b_0)	In-plane Noncollinear ferroelectric vectors (a, b)	Normal of 90° Domain Plane ($a \times b$)	Phase Matching Angle**
[1 0 0]	(101)	[101][010]	$[1+\varepsilon_{33},0,1+\varepsilon_{11}][0,1+\varepsilon_{11},0]$	$-(1+\varepsilon_{11})^2,0,(1+\varepsilon_{11})(1+\varepsilon_{33})$	ψ
	(10-1)	[10-1][010]	$[1+\varepsilon_{33},0,-(1+\varepsilon_{11})][0,1+\varepsilon_{11},0]$	$(1+\varepsilon_{11})^2,0,(1+\varepsilon_{11})(1+\varepsilon_{33})$	A
	(110)	[110][001]	$[1+\varepsilon_{33},1+\varepsilon_{11},0][0,0,1+\varepsilon_{11}]$	$(1+\varepsilon_{11})^2,-(1+\varepsilon_{11})(1+\varepsilon_{33}),0$	ψ
	(1-10)	[1-10][001]	$[1+\varepsilon_{33},-(1+\varepsilon_{11}),0][0,0,1+\varepsilon_{11}]$	$-(1+\varepsilon_{11})^2,(1+\varepsilon_{11})(1+\varepsilon_{33}),0$	A
[0 1 0]	(011)	[011][100]	$[0,1+\varepsilon_{33},1+\varepsilon_{11}][1+\varepsilon_{11},0,0]$	$0,(1+\varepsilon_{11})^2,(1+\varepsilon_{11})(1+\varepsilon_{33})$	ψ
	(01-1)	[01-1][100]	$[0,1+\varepsilon_{33},0,-(1+\varepsilon_{11})][1+\varepsilon_{11},0,0]$	$0,-(1+\varepsilon_{11})^2,(1+\varepsilon_{11})(1+\varepsilon_{33})$	ψ
	(110)	[110][001]	$[1+\varepsilon_{11},1+\varepsilon_{33},0][0,0,1+\varepsilon_{33}]$	$(1+\varepsilon_{33})^2,-(1+\varepsilon_{11})(1+\varepsilon_{33}),0$	ψ
	(-110)	[-110][001]	$[-(1+\varepsilon_{11}),1+\varepsilon_{33},0][0,0,1+\varepsilon_{33}]$	$(1+\varepsilon_{33})^2,(1+\varepsilon_{11})(1+\varepsilon_{33}),0$	ψ
[0 0 1]	(011)	[011] [100]	$[0,1+\varepsilon_{11},1+\varepsilon_{33}][1+\varepsilon_{11},0,0]$	$0,(1+\varepsilon_{11})(1+\varepsilon_{33}),-(1+\varepsilon_{11})^2$	ψ
	(0-11)	[0-11] [100]	$[0,-(1+\varepsilon_{11}),1+\varepsilon_{33}][1+\varepsilon_{11},0,0]$	$0,(1+\varepsilon_{11})(1+\varepsilon_{33}),(1+\varepsilon_{11})^2$	B
	(101)	[101][010]	$[1+\varepsilon_{11},0,1+\varepsilon_{33}][0,1+\varepsilon_{11},0]$	$-(1+\varepsilon_{11})(1+\varepsilon_{33}),0,(1+\varepsilon_{11})^2$	ψ
	(-101)	[-101][010]	$[-(1+\varepsilon_{11}),0,1+\varepsilon_{33}][0,1+\varepsilon_{11},0]$	$-(1+\varepsilon_{11})(1+\varepsilon_{33}),0,-(1+\varepsilon_{11})^2$	B

* $\varepsilon_{11}=(a-a_0)/a_0$, $\varepsilon_{33}=(c-a_0)/a_0$

** $\psi=\dfrac{2+\varepsilon_{11}+\varepsilon_{33}}{\sqrt{2}\sqrt{(1+\varepsilon_{11})^2+(1+\varepsilon_{33})^2}}$, $A=\dfrac{\varepsilon_{33}-\varepsilon_{11}}{\sqrt{2}\sqrt{(1+\varepsilon_{11})^2+(1+\varepsilon_{33})^2}}$, $B=\dfrac{\varepsilon_{11}-\varepsilon_{33}}{\sqrt{2}\sqrt{(1+\varepsilon_{11})^2+(1+\varepsilon_{33})^2}}$,

The mismatching angle due to rotation of the polarization vectors during the phase transformation is in the resolution limit of the most common characterization techniques. The most commonly used characterization techniques such as TEM, SEM and optical microscopy have less than 1μm penetration depth [Poulsen, H. F. *et al* (2004)] depending upon the photon energy of the constituents of the material investigated. Several techniques such as Atomic Force Microscopy [Balakumar, S. *et al* (1997)], White Beam Topography [Huang, X. R. *et al* (1996)] and Electron Back Scattering Diffraction [Ernst, F. *et al* (2001)] have been employed to ferroelectrics to study the texture evolution of the domains. Considering the ferroelectrics are extremely sensitive to surface preparation [Chen, J-H, (2005)], the information obtained from the surface can be influenced by residual stress development. With its superior penetration (up to 100 mm in Al and 1 mm in $BaTiO_3$ at 80.72 keV), 0.04° orientation resolution and the microfocusing capability, 3D-XRD technique has been a promising tool to investigate the evolution of the grains embedded in polycrystalline materials. The technique was further capable of studying the texture evolution of the grains and domains as response to external stimuli. The recent implementation of the GE detector reduced the acquisition time to 10 orders of magnitudes. With the superior penetration power and unique orientation resolution made 3D-XRD as a possible characterization tool to investigate the evolution of the ferroelectric domains embedded in polycrystalline $BaTiO_3$.

BIBLIOGRAPHY

Ahart M., Somayazulu M., Cohen R. E., Ganesh P., Dera P., Mao H-K, Russell J.H., Hemley R. J., Ren Y., Liermann P., Wu Z. (2008). Nature 451, 545-548.

Altmann S. L. (1986). *Rotations, quaternions, and double groups*, Clarendon Press.

Amoros J.L., Buerger M.J., Amoros M.C. (1975). The Laue Method. *Academic Press*, New York.

Arlt G. (1990). Review Twinning in ferroelectric and ferroelastic ceramics: stress relief. *Journal of Materials Science*, 25, 2655-2666.

Balakumar S., Xu J.B., Ma J.X., Ganesamoorthy S., Wilson I.H. (1997). Surface Morphology of Ferroelectric Domains in $BaTiO_3$ Single Crystals: An Atomic Force Microscope Study. *Jpn. J. Appl. Phys.*, 36, 5566-5569.

Berlincourt D., Krueger H.A. (1959). Domain Processes in Lead Titanate Zirconate and Barium Titanate Ceramics. *Journal of Applied Physics*, 30(11).

Blair D. and Dufresne E. (2008). The Matlab Particle Tracking Code Repository. (2008). Retrieved from http://physics.georgetown.edu/matlab/index.html

Bryne T.A., Cann D.P. (2004). Effects of Silver on Barium Titanate as a Function of Stoichiometry, *J. Am. Ceram. Soc.*, 87(5), 875–880.

Busing W.R., H.A. Levy. (1967). Angle Calculations for 3- and 4- Circle X-ray and Neutron Diffractometers, *Acta Cryst.*, 22, 457.

Buttner R. H., Maslen E. N. (1992). Structural Parameters and Electron Density in $BaTiO_3$. *Acta Cryst.*, B48, 764-769.

Cao W., Cross L.E. (1991). Theory of tetragonal twin structure in ferroelectric perovskites with a first-order phase transition. *Physical Review B*, 44(1), 5-12.

Chang W., King A. H., Bowman K. J. (2007). Thermal effects on mechanical grinding-induced texture in tetragonal piezoelectrics. *Journal of Materials Research*, 22, 2845.

Chen J-H, Hwang B-H, Hsu T-C, Lu H-Y. (2005). Domain switching of barium titanate ceramics induced by surface grinding. *Materials Chemistry and Physics,* 91, 67–72.

Chung J-S, Ice G. E. (1999). Automated indexing for texture and strain measurement with broad-bandpass x-ray microbeams. *Journal of Applied Physics,* 86(9), 5249-5255.

Dahms M. (1992). The lterative Series-Expansion Method for Quantitative Texture Analysis. II. Applications", *J. Appl. Cryst.* 25, 258-267

Danielson G. C. (1949). Domain Orientation in Polycrystalline $BaTiO_3$. *Acta Cryst*, 2 (90).

Dawson P., Boyce et al. (2005). The DPLAB Polycrystal Library at Cornell. Retrieved from http://anisotropy.mae.cornell.edu.

Doukhan N., Doukhan J.C. (1986). Dislocations in Perovskites $BaTiO_3$ and $CaTiO_3$. *Phys Chem Minerals,* 13, 403-410.

Ernst F., Mulvihill M. L., Kienzle O., Ruhle M. (2001). Preferred Grain Orientation Relationships in Sintered Perovskite Ceramics. *J. Am. Ceram. Soc.*, 84(8), 1885–90

Esin A., Jones W. J. D., A Statistical Approach to Micro-Plastic Strain in Metals. *Journal of Strain Analysis*, I(5), 1966.

Euclid. (2007). The information was retrieved from *http://www.euclideanspace.com/maths/geometry/ rotations/ conversions/angleToMatrix/index.htm*

Floquet N., Valot C. M., Mesnier M. T., Niepce J. C., Normand L., Thorel A., Kilaas R. (1997). Ferroelectric Domain Walls in $BaTiO_3$: Fingerprints in XRPD Diagrams and Quantitative HRTEM Image Analysis. *J. Phys. III France 7*, 1105-1128.

Frank F.C. (1988). Orientation Mapping. *Metallurgical Transactions A*, 19A, 403-408.

Fu H., Cohen R. (2000). Polarization rotation mechanism for ultrahigh electromechanical response in single-crystal piezoelectrics. *Nature*, 403(20).

Goudeau P., Tamura N., Spolenak R. Padmore H.A. (2005). Application of the white/monochromatic X-ray m-diffraction technique to the study of texture and triaxial strain at the submicron level. *Materials Science Forum*, 490-491, 672-677.

Hammersley A. P. (1997). ESRF Internal Report, ESRF97HA02T.

Haertling G. H. (1999). Ferroelectric Ceramics: History and Technology. *Journal of the American Ceramic Society*, 82(4), 797-818.

Hahn T., Klapper H., "Twinning of crystals", International Tables of Crystallography (2006), Vol. D, Chapter 3.3, pp. 393-448.

Harada J., Pedersen T., Barnea Z. (1970). *Acta Cryst.* A 26, 336.

Heinz A., Neumann P. (1991). *Acta Cryst.* A47, 780-789

Hertzberg R. W. (1995). Deformation and Fracture Mechanics of Engineering Materials. *John Wiley & Sons, Inc.*

Hlinka J. and Márton P. (2006). Phenomenological model of a 90° domain wall in $BaTiO_3$-type ferroelectrics, *Physical Review B,* 74(104104).

Hu Y. H., Chan H. M., Wen Z. X. (1986). Scanning Electron Microscopy and Transmission Study of Ferroelectric Domains in Doped $BaTiO_3$. *J. Am. Ceram. Soc. Soc.*, 69(8), 594-602.

Huang X. R., Jiang S. S., Liu W. J., Wu X. S., Feng D., Wang Z. G., Han V., Wang J. Y. (1996). Contrast of Ferroelastic and Ferroelectric Domains in White-Beam X-ray Topographs. *J. Appl. Cryst.* 29, 371-377.

Huber J., Fleck N.A., Landis C.M., McMeeking R.M. (1999). A constitutive model for ferroelectric polycrystals. *Journal of Mechanics and Physics of Solids*, 47, 1663-1697.

Huber J.E., Fleck N.A. (2001). Multi-axial electrical switching of a ferroelectric: theory versus experiment. *Journal of the Mechanics and Physics of Solids*, 49, 785 – 811

Huo Y., Jiang Q. (1997). Modeling of domain switching in polycrystalline ferroelectric ceramics. *Smart Mater. Struct.*, 6, 441–447.

Jaffe B. (1971). Piezoelectric Ceramics. *Academic Press*, London.

Jona F., Shirane G. (1962). Ferroelectric Crystals. *Oxford: Pergamon Press*, 402p.

Jordan T.L., Ounaies Z. (2001). Piezoelectric Ceramics Characterization, *NASA Technical Reports, Langley Research Center.*

Kalinin S.V., Bonnell D.A. (2001). Temperature dependence of polarization and charge dynamics on the $BaTiO_3$(100) surface by scanning probe microscopy, *Appl. Phys. Lett.*, 78, 1116

Kamlah M. (2001). Ferroelectric and ferroelastic piezoceramics –modeling of electromechanical hysteresis phenomena. *Continuum Mech. Thermodynamics*, 13: 219–268.

Keeble D. S., Thomas A. T. (2009). " On the tetragonality of the room-temperature ferroelectric phase of barium titanate, BaTiO3", *Journal of Applied Crystallography*. 42, 480–484.

Larson B. C. et al. (2000). *Mater. Res. Soc. Symp. Proc.*, 590, 247-52

Lauridsen E. M., Jensen D. J., Poulsen H.F. (2000). Kinetics of Individual Grains During Recrystallization. *Scripta Materialia*, 43, 561-566.

Lauridsen E. M., Schmidt S., Suter R. M., Poulsen H. F. (2001). *J. Appl. Cryst.*, 34, 744–750.

Lauridsen E. M., Schmidt S., Poulsen H. F. (2001). Manual for GRAINDEX version 3.01, *Risø National Laboratory*, Roskilde, .

Lee C-C. (2004). An analysis of hexagonal phase retention in $BaTiO_3$. *M.S. Thesis*, Materials Science and Engineering, National Sun Yat-Sen University, Kaohsiung, Taiwan.

Li F. X., Fang D. N., Soh A. K. (2006). Theoretical saturated domain-orientation states in ferroelectric ceramics. *Scripta Materialia*, 54, 1241–1246

Lienert U., Han T.S., Almer J., Dawson P.R., Leffers T., Margulies L., Nielsen S.F., Poulsen H.F., Schmidt S. (2004). Investigating the effect of grain interaction during plastic deformation of copper. *Acta Materialia.* 52, 4461-4467.

Liu J. M., Liu Z. G. (1998). A Monte Carlo approach of domain switching in ferroelectric Potts lattice under external electric field. *Materials Letters*, 36, 17-23.

Lines M. E., Glass A. M. (1977). *Principles and applications of ferroelectrics and related materials.* Oxford, Clarendon Press.

Margulies L., Winther G., Poulsen H.F. (2001). In Situ Measurement of Grain Rotation During Deformation of Polycrystals, *Science*, 291, 2392-2394.

Margulies L., Poulsen H.F. (2004). Three-Dimensional X-Ray Diffraction (3DXRD) Analysis. *Proceedings of the 25th Risoe International Symposium on Materials Science,* 61-77.

Merz W. J. (1952). Domain Properties in $BaTiO_3$. *Phys. Rev.*, 88, 421 - 422.

Merz W. J. (1954). Domain Formation and Domain Wall Motions in Ferroelectric $BaTiO_3$ Single Crystals. *Physical Review*, 95(3).

Morawiec A. (1995). Misorientation-Angle Distribution of Randomly Oriented Symmetric Objects, *J. Appl. Cryst*, 28, 289-293

Motahari M. S., (2007). Study of Constitutive Behavior of Ferroelectrics via Self-Consistent Modeling and Neutron Diffraction", PhD Thesis, California Institute of Technology.

Nepochatenko V.A. (2006). Structure of Thin Pseudo-90° Domain Walls in $BaTiO_3$. *Ferroelectrics*, 341(1), 97-102.

Nielsen S.F., Lauridsen E.M., Juul Jensen D., Poulsen H.F. (2001). A three-dimensional X-ray diffraction microscope for deformation studies of polycrystals, *Materials Science and Engineering A*, 319-321, 179-181.

Offerman S.E., Van Der Zijden A.C.P., Van Dijk N.H., Sietsma J., Lauridsen E.M., Margulies L., Grigull S., Poulsen H.F., Van Der Zwaag S. (2004). Evolving Microstructures in Carbon Steel Studied by 3DXRD Studies. *Proceedings of the 25th Risoe International Symposium on Materials Science,* 471-480.

Pecharsky V. K., Zavalij P. Y. (2005). *Fundamentals of Powder Diffraction and Structural Characterization of Materials.* Springer, 2005

Poulsen H.F. (2002). 3DXRD microscopy- a comparison with neutron diffraction. *Applied Physics A*, 74, S1673-S1675.

Poulsen H.F. (2003). A six-dimensional approach to microtexture analysis. *Philosophical Magazine*, 83(24), 2761–2778.

Poulsen H.F., Bowen J.R., Gundlach C. (2004). Characterizing the dynamics of individual embedded dislocation structures, *Scripta Materialia*, 51, 783-788

Poulsen H.F., Fu X., Knudsen E., Lauridsen E.M., Margulies E.M., Schmidt S. (2004). 3DXRD-Mapping Grains and their dynamics in 3 dimensions, *Materials Science Forum*, 467-470, 1363-1372

Poulsen H. F., Lienert U., Pantleon W. (2005). Characterization of orientation distributions of individual grains within deformed metals. *Materials Science and Technology* (2005), 21(12), 1397-1400.

Rogan R. C., Tamura N., Swift G. A., Ustundag E. (2003). Direct measurement of triaxial strain fields around ferroelectric domains using X-ray microdiffraction. *Nature Materials*, 379-381.

Sapriel J. (1975). Domain-wall orientations in ferroelastics. *Physical Review B*, (12(11), 5128-5140.

Savytskii D. I., Trots D. M., Vasylechko L. O., Tamura N. and Berkowskic M. (2003). Twinning in $La_{0.95}Sr_{0.05}Ga_{0.9}Mg_{0.1}O_{2.92}$ crystal studied by white-beam (Laue) X-ray microdiffraction. *J. Appl. Cryst.*, 36, 1197-1203.

Schmidt S. (2007). Farfield Simulation Package, Risoe National Laboratory, Roskilde, Denmark. The package can be retrieved from *http://fable.sourceforge.net/index.php/Farfield_Simulation*

Schönau K.A., Knapp M., Kungl H., Hoffmann M.J., Fuess H. (2007). In situ synchrotron diffraction investigation of morphotropic Pb[Zr1-xTix]O3 under an applied electric field. *Physical Review B*, 76(14).

Simmons G., Wang H. (1971). *Single crystal elastic constants and calculated aggregate properties: a handbook*. Cambridge, Mass., M.I.T. Press.

Steinkopff T., (1999). Finite-element Modeling of Ferroic Domain Switching in Piezoelectric Ceramics. *Journal of the European Ceramic Society*, 19, 1247-1249.

Subbarao E.C., McQuarrie M.C., Buessem W.R. (1957). Domain Effects in Polycrystalline Barium Titanate. *Journal of Applied Physics*, 28(10).

Sundararaghavan S., Zabaras N. (2007). *Acta Materialia*, 55, 1573.

Tamura N., MacDowell A. A., Spolenak R., Valek B.C., Bravman J.C., Brown W.L., Celestre R.S., Padmore H.A., Batterman B.W., Patel J.R. (2003). Scanning X-ray microdiffraction with submicrometer white beam for strain-stress and orientation mapping in thin films. *Journal of Synchrotron Radiation*, 10, 137-143.

Tamura N. (2007). Personal communication, Advanced Light Source, Lawrence Berkeley National Laboratory, Berkeley, CA.

Tan X., Shang J. K. (2004). Field-induced domain interpenetration in tetragonal ferroelectric crystal. *Journal of Applied Physics*, 95(2).

Tan X. (2007). Unpublished work on the domain intersection.

Valek B. C. (2003). X-Ray Microdiffraction Studies of Mechanical Behavior and Electromigration in Thin Film Structures. *PhD Thesis*, Stanford University.

Vaughan G. B. M., Schmidt S., Poulsen H. F. (2004). Multicrystal approach to crystal structure solution and refinement. *Z. Kristallogr.*, 219, 813–825

Wang J., Li Y., Chen L-Q, and Zhang T-Y. (2005). Domain Structures and Phase Diagram in 2D Ferroelectrics under Applied Biaxial Strains - Phase Field Simulations and Thermodynamic Calculations. *Mater. Res. Soc. Symp. Proc.*, 881E.

Warren B. E. (1990). *X-ray diffraction*. New York : Dover Publications.

ACKNOWLEDGEMENTS

I would like to express my deepest gratitude to my academic and research advisor Dr. Ersan Ustundag for his guidance and constant support in helping me to conduct and complete this work. This project was funded by APS which is supported by the US-DOE under contract no. W-31-109-ENG-38. 3D-XRD experiments were performed at Sector 1-ID of Advanced Photon Source at Argonne National Laboratory. I would also like to thank Dr. Ulrich Lienert for his continuous courage and discussion during this research and Dr. Dean Haeffner, Dr. John Elmer, and Ali Mashayekhi providing me an excellent research environment at Sector 1-ID. I would like to thank of the support from Dr. Jacob Jones and Joel Bernier who are the experts on Matlab®, and texture. μXRD experiments were performed at Microdiffraction 12.3.2 of Advanced Light Source at Lawrence Berkeley National Laboratory, Berkeley, CA. I thank Dr. Nobumichi Tamura for teaching me the scanning microdiffraction technique and many useful discussions over the microdiffraction results. I appreciate all help and discussions from Dr. Xiaoli Tan and Xiaohui Zhao on ferroelectric materials, committee members, Dr. Vitalij K. Pecharsky, Dr. Matthew J. Kramer, Dr. Ashraf Bastawros and Dr. Alan Russell, Dr. Richard LeSar and Carmen Garcia for their help and my research group colleagues, Maziar Motahari, Seung-Yub Lee, Goknur Tutuncu, Sarah Shiley Haubrich, Li Li, Baris Denizer on many helpful discussions, Wonje Jeong, Tim Mauldin and Louis Charles for being excellent and fun officemates in 3114 Gilman Hall.

Many thanks to all the people I have come to know in Iowa State University, whose friendship and companionship I will always enjoy. I owe my sincere appreciation to my dear brother, electric engineer Mehmet Varlioglu and my family for supporting me in all steps of my life. During the summer of 2007, my dear father left our family without saying goodbye in his very young age and he will always be remembered with his friendship, care and love. My final and biggest gratitude goes to my dear wife Melissa Ann Varlioglu for her continuous support, patience and understanding throughout this research.